Department of Aeronautics
Imperial College London
London, SW7 2AZ

Turbulence generated by multiscale inhomogeneous and anisotropic grids

Shaokai Zheng

This thesis is submitted for in partial fulfillment for
the degree of Doctor of Philosophy
at Imperial College London

October 2017

I hereby declare that the work presented in this thesis is my own and that contributions from other authors are appropriately acknowledged and referenced.

Acknowledgments

First and foremost, I would like to thank my supervisors Professor Christos Vassilicos, Professor Mike Graham, and Dr. Paul Bruce for their supervision during the entire course of my PhD study. This work would not have been possible without their help. I am grateful for their valuable insights and numerous comments and ideas towards the finish of this work. Their patience in reading and commenting this thesis have been extremely important to me in the final stage of my PhD study. I would like to thank Professor Christos Vassilicos especially for keeping me on track, and for sharing his knowledge of not only turbulence but science in general.

I would also like to thank the Aeronautics workshop for their technical support. To Ian James for the help of setting up the Honda wind tunnel at the beginning of my study. To Rolland Hutchins for coordinating jobs, and printing my probe supports. To Alan Smith for cutting my grid support and foam blocks for the 3 and Lille experiments. To Ian Parfew and Keith Wolstenholme for preparing the apparatuses needed for my Lille experiment.

There are also many to thank during my secondments. To Professor Jean-Marc Foucaut and Dr. Jean-Philippe Laval at Lille Mechanical Laboratory (LML), for their scientific and casual discussions during my stay. To Dr. Christophe Cuvier, for showing me their facility and for his help and discussions during the experiments. I would also like to thank the PhD students during my stay their who helped me with mounting/dismounting the fractal grid everyday. The experiments at Lille would not have been possible without them.

I would also like to thank the crew at Mel Consultants in Melbourne, Australia. To Dr. Bill Melbourne, Dr. Michael Eaddy, and Dr. Jim Kostas for hosting my experiments in the first place, for the many discussions of experiments. To Jim and Michael for teaching me the 101 of wind engineering experiments, and for the tea breaks and talks during my stay. I would also like to thank the other members of their fantastic team, especially to Eric Chong, for his help in cutting the grids and many rides to the train station. The time I spent with them is truly memorable.

I am grateful to my examiners Dr. George Papadakis from Imperial College, and Dr. Joachim Peinke from University of Oldenburg, for an intense and inspiring two-hour discussion during my Viva Voce which I will never forget. Last but not least, I thank my mother for her love and support throughout my study and life. I would also like to thank my colleagues in the MULTISOLVE group for their accompany during the study, and I gratefully acknowledge the support from Marie Curie FP7 through the MULTISOLVE project, grant number 317269, without which none the experiences in the past four years would have been possible.

Abstract

In this thesis two classes of inhomogeneous multiscale grids are proposed and investigated experimentally. These studies provide further understandings of the idea to generate bespoke turbulence field using fractal grids as proposed by Vassilicos and colleagues.

The first part of the work introduces the rectangular fractal grid (RFG). Due to the inhomogeneous grid geometry, the streamwise location of turbulence intensity peak appears different from the wake interaction length scale calculated from the grid bar dimensions, and a region of decreasing length scales with decreasing Reynolds number is observed. This region is shown to be inhomogeneous and anisotropic. Nevertheless, the non-equilibrium scaling is found in this region, where the ratio between the integral length scale and Taylor microscale remains constant.

From the second part of the work, turbulent flows with different mean shear rates are studied using the new inhomogeneous multiscale grids. By designing the local blockage ratio and the bar dimensions, this new type of shear generating grid is capable of producing different mean velocity and turbulence intensity profiles at the same time. The mean velocity profiles are shown to match the predictive mean velocity model, and a scaling relation of turbulence intensity is proposed based on the wake interaction length scale. The streamwise evolution of the Reynolds stress is studied, and a new dimensionless time scale is proposed.

Finally, the design and scaling methods of the turbulent shear flow generated by the inhomogeneous multiscale grid are tested in a low-fidelity engineering wind tunnel with different size and background flow quality, and the results are consistent. These results perhaps

provide a general methodology to produce various types of turbulent flows through the design of one single passive grid, which is desirable for both fundamental studies of turbulence and engineering applications such as the wind engineering experiments.

Contents

List of Tables

List of Figures

Chapter 1

Introduction

The word *turbulence* is used to describe a range of phenomena that can be observed or felt almost everywhere in nature. From the water running in a river to the clouds drifting in the sky; from the smoke coming out of a chimney to the swirls behinds bridge piers; from the solar wind to the interstellar clouds, it is the universality of turbulence phenomena that makes it difficult to solve, but essential to understand at the same time. The necessity is perhaps twofold, (i) to explore the fundamental physics of turbulence phenomena to fulfill the curiosity of human nature, and (ii) to apply new theories and/or mathematical models to benefit the daily activities of human beings. As our understanding of the subject progresses, questions will be raised requiring more understanding of the problem so that improvements of existing theories/models can be implemented with more efficiency and/or accuracy. The study of turbulence is therefore still on going, and will continue for a foreseeable time frame.

Systematic study of the subject of turbulence generally relies on either computational or experimental methods. One approach of the computational methods is to solve reduced versions of the Navier-Stokes (N-S) equations, such as Reynolds-Averaged N-S equations (RANS) or Large Eddy Simulations (LES). Both methods have been favored by engineers for their relatively lower costs. Another approach is Direct Numerical Simulation (DNS)

of the N-S equations, which is capable to resolve all scales of the turbulence, at the cost of considerably longer computational hours. As a result, the Reynolds number in DNS studies is usually limited. With the development of supercomputers in recent decades, larger Reynolds numbers have been achieved in DNS simulations (e.g. Laizet and Vassilicos, 2011; Eitel-Amor et al., 2014). However, even the most advanced supercomputer cannot afford to perform DNS of large scale turbulent flows at realistic Reynolds numbers. For this reason, experimental approaches have also been widely used to study various types of turbulent flows.

In order to study large scale turbulent flows, it is ideal to have the same order of Reynolds number. However, for topics in geophysics such as the Atmospheric Boundary Layer (ABL), or large scale industrial flows such as the turbulence generated by a wind turbine, it is still difficult to perform experiments at realistic Reynolds numbers. Although full scale wind tunnels have been built, the access is extremely limited. Therefore, experiments in a relatively smaller wind tunnel with properly scaled turbulence characteristics are desirable, which constitutes the main idea of this study, i.e. to explore the possibility to generate turbulent flows with desired characteristics.

A topic of specific interest is wind tunnel simulation of the ABL, which requires correct representations of mean velocity, turbulence intensity, and length scale at the same time, and is therefore difficult to produce in wind tunnels. It is also the part of atmosphere that most human activities occur, so the study of the subject is of great importance. In the following, a brief review is given first on the different methods simulate the ABL in wind tunnels. Following a manner of reductionism, wind tunnel simulation of the ABL might be reduced to two subtopics, i.e. *homogeneous isotropic* turbulence and turbulent shear flows (the analogy is further discussed in section 1.1). Therefore, previous experiments of the fractal generated turbulence are reviewed in section 1.2, and various methods to produce turbulent shear flows are reviewed in section 1.3. The outline of this thesis is given at the end of this chapter.

1.1 Wind tunnel simulation of the ABL

The ABL is defined as the lowest part of the troposphere that directly interacts with the earth's surface and responds to the surface forcing (Stull, 2012). The size (or thickness) of the ABL, being its height away from the surface, is rather complex. It depends on a range of meteorological and geological factors, such as wind intensity and direction, air properties, terrain roughness type, latitude, etc, and is affected by the presence of clouds. As a result, the thickness of the ABL varies from the order of 100 m to 1000 m. Even at the same site, its thickness exhibits diurnal cycles due to thermal forcing from the earth's surface (see e.g. McNider and Pielke, 1981; Svensson et al., 2011).

The study of the ABL is important because it is the layer of atmosphere that most human activities interact with. The knowledge of turbulent characteristics within the ABL is critical in the practice of wind load testing of large scale civil structures, pollutant disposal, weather forecasting, etc. Reviews on studies of the ABL over the past few decades have been given by Monin (1970); Panofsky (1974); Garratt (1994); Garratt et al. (1996); Cermak (2003). Both numerical and experimental advances have been made, and this introduction will focus on the experimental techniques.

The most straightforward way to study the ABL experimentally is to conduct field measurements. Although such measurements are possible (e.g. Clarke et al., 1971; Readings et al., 1974; Kaimal et al., 1976; Driedonks, 1982; Kader and Yaglom, 1990; Lohou et al., 1998; Cuxart et al., 2000; Svensson et al., 2011; Pea et al., 2014), it often involves complex set up of large scale anemometer towers or balloons, and greatly depends on the weather conditions on the measurement site. Wind tunnel simulations of the ABL are therefore much desired, but the physics has to be simplified to an extent such that it can be generated using various devices installed in a wind tunnel.

Davenport (1963) proposed that a neutral atmosphere can be obtained in high winds. In a neutral boundary layer, the buoyancy effects, the variation of wind direction, and the

Coriolis effect due to the earth's rotation are all neglected. It is therefore an essential step to simulate the natural atmospheric boundary layer Armitt and Counihan (1968). Cook (1978) also suggested that the ABL can be considered adiabatic for strong winds with $U \geq 10\,\mathrm{m/s}$, where U is the local mean velocity. The simulation of a neutral boundary layer by a *standard* turbulent boundary layer is then possible as long as the geometric similarity is maintained, the surface roughness is reduced in proportion, and the Reynolds number is comparable to the real case.

With such simplifications, a direct approach to simulate a turbulent boundary layer in a wind tunnel is to let it grow naturally over a very long test section up to 30 m (e.g. Jensen and Franck, 1963; Cermak et al., 1966; Davenport, 1966; Cermak, 1971; Robins, 1975). However, the thickness of the boundary layer developed in such a manner has been limited by practical considerations. Here we introduce the scale factor, which is interpreted as the ratio between the real boundary layer size and the simulated one. This ratio consequently determines the size of the model to be fitted into the simulated ABL. Ideally one would try to have as large a model as possible to fully utilize the wind tunnel dimensions to have more realistic results, and thus generating a thick turbulent boundary layer in a given wind tunnel is crucial. Different types of wall roughness elements have been used for such purpose. For example, with a wind tunnel of 25 m long, Davenport (1967) produced a boundary layer with thickness of 380 mm over a rural terrain (simulated by carpet) and 900 mm over an urban terrain (simulated by arrays of 25 mm to 100 mm high blocks), whereas a representative boundary layer thicknesses for these two types of terrains with 1:400 scale factor would be 610 mm and 1200 mm, respectively. Therefore, more efficient methods to artificially thicken the boundary layer in wind tunnels are needed.

Several methods have been proposed to produce thick turbulent boundary layers in wind tunnels, for example, the tripping grid tested by Davenport (1967), the grid-barrier arrangement used by Cook (1973), and the tripping devices proposed by Rodríguez-López et al. (2016). One of the most popular methods was proposed by Armitt and Counihan

(1968). Their experiments were carried out in a wind tunnel with cross section measuring 4.5 m × 1.5 m, and 11 m in length, which is significantly shorter than that used by Cermak et al. (1966) and Davenport (1967). The authors proposed a system with a barrier of height 0.15 m at the beginning of the working section, followed by four triangular vortex generators of 1.2 m high and placed 1.2 m apart. Downstream of the vortex generators, a surface of Lego blocks measuring 31.75 mm × 15.88 mm × 9.53 mm was placed on the bottom floor to simulate surface roughness, over a streamwise extent up to the leading edge of the turn table. With such arrangement, Armitt and Counihan (1968) were able to generate a turbulent boundary layer with thickness of order 1 m (which is similar to the height of the vortex generators), and concluded that the simulated ABL could facilitate model tests at a scale of 1:250.

The results of Armitt and Counihan (1968) were, however, unsatisfactory in several ways. The mean velocity profiles of their results exhibited excessive velocity deficit close to the floor due to the barrier, but not enough in the outer part of the velocity profile. A square rod of diameter 50.8 mm was then added 635 mm horizontally above the barrier as an effort to remedy the difference, although the results showed unintended variations in the mean velocity profile. Transverse inhomogeneity was also observed, which was attributed to the existence of the vortex generators. Armitt and Counihan (1968) then studied the effects of the incident angle of the vortex generators, and concluded that reducing the angle of incidence from 10° to 5° would add unrealistic irregularities in both mean velocity and turbulence intensity profiles.

Following on from this study, Counihan (1969) redesigned the triangular vortex generators to redistribute the area into elliptical shapes with a 2:1 major to minor axis ratio as an effort to correct the unrealistic velocity deficit in the mean velocity profile. Counihan (1969) tested this improved arrangement in a smaller wind tunnel with test section dimensions 0.6 m × 0.2 m × 1.5 m. The height of the generators was 152 mm, placed 76.2 mm apart, and the boundary layer thickness was about the same as the generator height (152 mm). The

relative position between the barrier and the generators was decided by trial-and-error through comparisons with theoretical data. It took four to five boundary layers heights to develop the simulated flow. Counihan (1969) concluded that such a method was suitable for producing a neutral ABL. The integral length scale, however, was not studied at that time.

At the end of the paper from Armitt and Counihan (1968), they proposed the idea of a two vortex generator system with different heights as a means to mix the vortical systems more effectively. This idea was tested by Cook (1978) using a barrier with serrated or castellated edge together with two arrays of Counihan-type elliptical vortex generators. Two types of roughness were also tested. A layer of 14 mm gravel, and a fetch of blocks of 100 mm × 50 mm × 50 mm, with the 100 mm edge aligned with the transverse direction. The castellated barrier was placed at the beginning of the test section with height from 58 mm to 267 mm. Two arrays of elliptical vortex generators were mounted downstream of this barrier. The smaller vortex generators of height 400 mm were placed first, and then the taller generators of height 800 mm. Their results suggested that the boundary layer can be thickened by increasing the barrier height, provided that the mean height of the barrier was smaller than twice the height of the blocks or fivefold the gravel. Cook (1978) also comments that completely natural grown boundary layers give the best simulation of the ABL, but the thickness is limited, which limits the scale factor, and artificial ways to thicken the simulated boundary layer would inevitably cause unrealistic results so that one has to prioritize certain characteristics to optimize.

This type of barrier, mixing-device, and roughness method was widely used and further developed in the subsequent experimental studies by many researchers. Gartshore and De Croos (1977) proposed a semi-empirical method to calculate the dimensions of the wall roughness. Farell and Iyengar (1999) applied this method in their wind tunnel simulation of an urban terrain boundary layer. The boundary layer thickness was the same as the vortex generators (1.2 m), and achieved a good representation of the boundary layer over

city centers with a scale factor of 1:500. Balendra et al. (2002) further modified the setup with a different arrangement of roughness elements. In their study, Balendra et al. (2002) first placed a 12 m long fetch of 28 mm cubes, and then a 0.75 m long fetch of mixed elements consisting of 28 mm cubes and taller cubes of 28 mm × 28 mm × 56 mm to simulate the scenario of wind blowing over an area with gradually built-up constructions before reaching a city. The reproduced mean velocity and turbulence intensity profiles were generally satisfactory, but the integral length scale showed scattering of roughly 20% around the modeled values as proposed by Walshe (1972).

All of these previous studies have achieved appreciable success of wind tunnel simulation of boundary layers over different terrain types, yet the implementation involves a considerable amount of trial-and-error, and optimization of the setup is mostly empirical. Even if the mean velocity profiles are satisfied, the turbulence intensity and integral length scales suffer from large deviations from realistic values, especially the integral length scales, which are usually insufficient in artificially thickened turbulent boundary layers. Consequently new methods that provide some level of control over the turbulence generating process especially the turbulence intensities and length scales are desired.

There have been some ideas such as the jet grid, which consists of 2D arrays of individually controlled jets (e.g. Gad-El-Hak and Corrsin, 1974; Tassa and Kamotani, 1975; Teunissen, 1975), and the oscillating grids (e.g. Ling and Wan, 1972). The jet grid was not widely used due to its complexity (as it requires modification of the wind tunnel section) and considerable power requirements (Teunissen, 1975). The agitated grid was later developed into the idea of active grids, which was perhaps first published by Makita (1991), and then further studied by many (Mydlarski and Warhaft, 1996b; Kang et al., 2003a; Cekli and van de Water, 2010; Knebel et al., 2011; Stefan et al., 2013; Thormann and Meneveau, 2014).

An active grid consists of horizontal and vertical arrays of oscillating rods with agitator wings. These rods are connected to stepping motors installed outside the wind tunnel

walls. The motion of each rod is controlled by feeding electric pulses to the stepping motor, which generates different mean velocity and turbulence intensity. The active grids have also been used in combination with mesh grids to produce mean velocity and turbulence profiles as described by e.g. Zhu et al. (2006); Thormann and Meneveau (2015). Even though the method of active grid has shown promising progress in producing turbulence fields, the grid itself is complicated to set up, and the control protocol is usually determined through some level of trial-and-error. A passive device that is capable of producing certain turbulence fields without the need for extensive trial-and-error is therefore highly desirable.

As mentioned by Cook (1978), it is impossible to simulate every aspect of flow characteristics of the ABL through artificial methods, and some parameters have to be neglected for wind tunnel simulations. For example, the boundary layer can be simplified to a homogeneous turbulent flow with high turbulence intensities and large length scales, e.g. for wind load testing of a bridge, where the vertical span of the flow is small such that the local velocity gradient can be neglected. Or it can be simplified to a turbulent shear flow with desired profiles of mean velocity and turbulence intensities in the vertical direction with proper length scales. In fact, in the cornerstone paper by Armitt and Counihan (1968), the authors argued that the three primary aims of wind tunnel simulation of the ABL are in fact the turbulence intensities, the relevant length scales, and varying mean velocity with height.

Following this idea, we look at possibilities of tailoring turbulent flows using passive grids. To continue the introduction, we first review the multiscale grids proposed by Vassilicos and colleagues, referred to as fractal grids, which have been shown to produce bespoke homogeneous isotropic turbulent flows with high turbulence intensity and large integral length scales. The review focuses on both the scaling of turbulence statistics, and the evolution of various turbulence characteristics such as length scales and dissipation.

1.2 Fractal generated turbulence

Grid generated turbulence has been studied extensively over the past decades. In most cases, planar grids with regular mesh sizes were used to produce flows close to a *homogeneous isotropic* turbulence. This series of work dates back to Simmons and Salter (1934) and Taylor (1935), and contributions have been made by many (e.g. Comte-Bellot and Corrsin, 1966, 1971; Gad-El-Hak and Corrsin, 1974; Mohamed and Larue, 1990; Sreenivasan, 1984; Mydlarski and Warhaft, 1996a; Cardesa et al., 2012) to study the evolution of various turbulence characteristics. For the past decade, research into space-filling fractal square grids, henceforth referred to as FSG (Seoud and Vassilicos, 2007) has shown the existence of a non-equilibrium region where turbulence characteristics (such as various length scales and the dissipation coefficient) evolve differently from the predictions of classical theory. These observations have been confirmed in studies using conventional regular and bi-planar grids (Isaza et al., 2014; Valente and Vassilicos, 2014). The following discussion focuses mainly on the one point statistics and characteristic length scales of turbulence. The results of the current experiments are presented in the same manner in Chapter 2, with a few cases of two-point correlation measurements to look at the integral length scale. The scaling laws of the dissipation is also discussed in this chapter and investigated further in Chapter 2. Here and for the discussion, x, y, z represent the streamwise, vertical, and transverse direction, respectively.

1.2.1 Scaling of turbulence statistics

The very first study of fractal-generated turbulence was on turbulence generated by three dimensional fractal objects Vassilicos (2001). This work was followed by simulations of periodic turbulence subjected to fractal/multi-scale forcing (Mazzi et al., 2002; Mazzi and Vassilicos, 2004). The concept of fractal-generated turbulence was further developed by Hurst and Vassilicos (2007), where two-dimensional grids with three types of fractal-

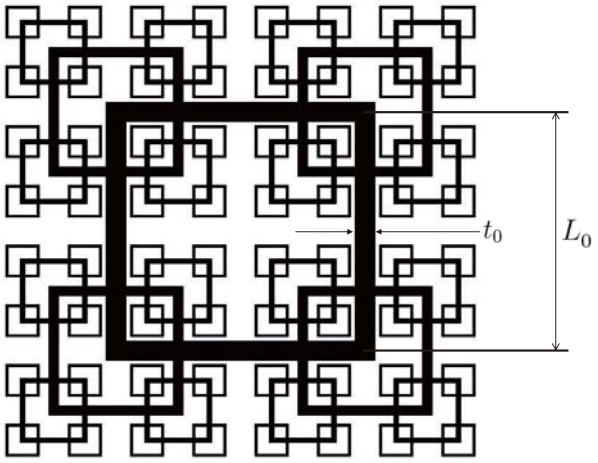

Figure 1.1: Example of space-filling square fractal grid, where L_0 and t_0 give the length and thickness of the bar at first iteration, respectively.

generating patterns were proposed, i.e. cross, I-shaped, and squares. Each pattern can be completely characterized by the fractal iteration number N_f, the length L_j and width t_j (where $j = 0, 1, ...N_f - 1$) of the grid bars, and the number of patterns at each iteration. With relatively low blockage ratios of approximately 25%, these grids exhibited large turbulence intensities and Reynolds numbers in comparison to classical grids with blockage ratios of 44%. The best decaying turbulence homogeneity was returned by space-filling fractal square grids (FSG), i.e. grids with square patterns. The FSG, as shown in figure 1.1, also have a protracted production region where the turbulence builds up reaching a maximum value at a streamwise position x_{peak} beyond which the turbulence decays. The authors commented that it might be possible to control the distance where the turbulence intensity peaks by controlling the geometry of the grids and Mazellier and Vassilicos (2010) followed by Gomes-Fernandes et al. (2012) showed how both this distance and the turbulence intensity at the peak can indeed be predicted given the dimensions of the grid.

The homogeneity of such space-filling fractal generated turbulence was found satisfactory by Seoud and Vassilicos (2007) in the decay region, i.e. $x > x_{peak}$ (where x_{peak} is the streamwise location with maximum turbulence intensity), and improved by increasing the ratio of $t_r = t_{max}/t_{min}$, where t_{max} and t_{min} is the width of the bar in the first and

last iteration of the grid, respectively, according to Hurst and Vassilicos (2007); Seoud and Vassilicos (2007). The large scale isotropy was achieved at streamwise distance large enough where $U/U_\infty \leq 1.1$ (U_∞ is the free stream velocity) such that the ratio of u'/v' reached values between 1.2 and 1.3, and $L_u/L_v \approx 2$, where $L_u = L_{uu,x}$ and $L_v = L_{vv,x}$ are the longitudinal integral length scales of the fluctuating velocities u and v, respectively. A thorough study of homogeneity and isotropy in turbulence generated by FSG was conducted by Valente and Vassilicos (2011) which revealed the presence of significant transverse turbulent energy and pressure transport in the region up to $x \approx 3x_{peak}$ that they studied.

Mazellier and Vassilicos (2010) conducted further experiments on four different FSGs. By relating the wake width l with the bar width t_j ($j = 0, 1, ..., N_f - 1$) and the streamwise distance x from the bar via $l \sim \sqrt{xt_j}$ (Townsend, 1980), they introduced the wake interaction length scale $x_* = L_0^2/t_0$, where L_0 is the length of the largest bar and t_0 is the corresponding width, both shown in figure 1.1. Mazellier and Vassilicos (2010) were then able to collapse data from their four grids such that the streamwise location of the peak turbulence intensity was approximately

$$x_{peak} \approx 0.45x_* = 0.45\frac{L_0^2}{t_0}. \tag{1.1}$$

Both mean velocities and turbulence intensities from these four different FSGs collapsed with such scaling. The flow homogeneity was measured by the ratios U_c/U_d and u'_c/u'_d, where U_c and u'_c are the mean velocity and streamwise turbulence rms (root mean square), respectively, along the centerline of the grid, and U_d and u'_d are along the streamwise line behind the corner of the square of second iteration. Both of these ratios approached $1 \pm 10\%$ by $x/x_* = 0.6$. This point $x/x_* = 0.6$ sets apart different behaviors of various properties as well. For example, the streamwise fluctuating velocity skewness S_u showed large negative values in the region $x/x_* < 0.6$, but was approximately zero where $x/x_* > 0.6$.

Although the scaling relation of equation 1.1 successfully collapsed streamwise developments of various properties, it failed, however, when Gomes-Fernandes et al. (2012) compared data from wind tunnels and a water tunnel, i.e. with different incoming flow conditions. By taking into account the incoming flow turbulence level and the drag coefficient C_d of the grid bars, Gomes-Fernandes et al. (2012) proposed a length scale

$$x'_* = \frac{L_0^2}{\alpha C_d t_0}, \tag{1.2}$$

where α was determined as 0.287 and 0.231 (after Symes and Fink, 1977) for incoming flows with moderate and negligible free-stream turbulence, respectively, and C_d was evaluated from the aspect ratio (defined as $AR = d_0/t_0$, where t_0 and d_0 are the width and streamwise thickness of the largest grid bar, respectively), following Bearman and Trueman (1972) and Nakamura and Tomonari (1976). After plotting turbulence intensities against x/x'_*, they finally proposed a revised wake interaction length scale

$$x_*^{peak} = \phi x'_* = 0.21 x'_* = 0.21 \frac{L_0^2}{\alpha C_d t_0}, \tag{1.3}$$

where $\phi = 0.21$ was determined empirically so that $x_*^{peak} = x_{peak}$. Starting from the mean momentum equation of wake flows, the authors also proposed a scaling relation for the centerline turbulence intensity level

$$\frac{u'}{U_\infty} = \frac{1}{\beta}\Big(\frac{C_d t_0}{x_*^{peak}}\Big)^{1/2} g\Big(\frac{x}{x_*^{peak}}; *\Big), \tag{1.4}$$

where β is a constant of 2.88 and 2.68 (after Symes and Fink, 1977) for incoming flows with moderate and negligible free-stream turbulence, respectively, and the function g incorporates any residual dependencies that might exist on the boundary or inlet conditions. The scaled turbulence intensity $u'/U_\infty \beta (C_d t_0/x_*^{peak})^{-1/2}$ collapsed as a function of x/x_*^{peak} for six different inlet conditions.

1.2.2 Turbulence dissipation

The study of turbulence dissipation has initiated numerous works on different types of turbulent flows over the past few decades. The cornerstone of classical turbulence theory proposed by Taylor (1935) states that $\epsilon = C_\epsilon k^{3/2}/L_u$ (where ϵ is the dissipation rate, C_ϵ is the dissipation coefficient, k is the turbulent kinetic energy, and L_u is the longitudinal integral length scale), with $C_\epsilon = const$, i.e. independent of Reynolds number, for turbulent flows with large local Reynolds numbers $Re_\lambda \gg 1$, where $Re_\lambda = u'\lambda/\nu$, u' is the streamwise turbulence rms, λ is the Taylor micro scale, and ν is the kinematic viscosity. This relation is referred to as the equilibrium dissipation scaling, and is explained by the Richardson-Kolmogorov cascade mechanism (see e.g. Pope, 2001). By assuming $\epsilon = 15\nu u'^2/\lambda^2$, which holds exactly for isotropic turbulence, it follows directly that $L_u/\lambda \sim C_\epsilon Re_\lambda$. This implies that a larger range between L_u and λ is required for the turbulent energy to be dissipated with increasing Reynolds number, or simply, L_u/λ grows proportionally with Re_λ.

The dependence or independence of C_ϵ on boundary/inlet/initial conditions, has been controversial over the decades of turbulence research, with evidence from both experimental and numerical results. Gad-El-Hak and Corrsin (1974) showed a dependency of $C_\epsilon = \epsilon L_u/u'^3$ on the initial condition (i.e. injection rate of their jet grid), and seemed to suggest a smoothly varying C_ϵ with different initial conditions. Sreenivasan (1984) summarized several data sets up to that time, and showed that for certain grids C_ϵ approached a constant value for $Re_\lambda > 100$ when the Reynolds number was varied by varying the inlet flow velocity. These observations were also included in the review by Lumley (1992).

After that time, new data and evidence from a number of experimental and numerical works contributed further to the understanding of the behavior of C_ϵ. A summary can be found in Vassilicos (2015). It was not until the work on fractal grids by Vassilicos and coworkers, that the dependency of C_ϵ on flow conditions and Reynolds number could be studied more comprehensively and systematically. One outcome was the discovery of a region with a new non-equilibrium dissipation scaling such that the dependency of C_ϵ on

Reynolds numbers is given by $C_\epsilon \sim Re_0^m/Re_L^n \sim Re_0^{m/2}/Re_\lambda^n$, where $m \approx n \approx 1$, Re_0 is a global Reynolds number such that $Re_0 = (U_\infty L_0)/\nu$, and Re_L is a local Reynolds number given by $Re_L = (u'L_u)/\nu$. Note that $m = n = 1$ is equivalent to $L_u/\lambda \sim \sqrt{Re_0}$. This non-equilibrium dissipation scaling has now been found in various types of turbulent flows (Hurst and Vassilicos, 2007; Mazellier and Vassilicos, 2010; Valente and Vassilicos, 2011; Gomes-Fernandes et al., 2012; Stefano et al., 2013; Valente and Vassilicos, 2014; Goto and Vassilicos, 2015, 2016a; Obligado et al., 2016).

Valente and Vassilicos (2012) studied the non-equilibrium dissipation law by comparing measurements behind fractal and regular grids and both confirmed and generalized the finding of Mazellier and Vassilicos (2010) that L_u/λ increases with Re_0 showing, in fact, that $L_u/\lambda \propto \sqrt{Re_0}$. Their results showed two distinct regions for C_ϵ such that $C_\epsilon \sim Re_0^m/Re_L^n$ held for $x_{peak} < x < 5x_{peak}$, where $C_\epsilon \sim Re_0^m/Re_L^n$ with $m \approx n \approx 1$, and $C_\epsilon \approx const$ for $x > 5x_{peak}$ with a rather abrupt transition at $x = 5x_{peak}$. The streamwise extents of these two regions correspond to about the same number of turnover times, which is in fact a few. This dissipation behavior was confirmed by Hearst and Lavoie (2014); Valente and Vassilicos (2014). Valente and Vassilicos (2014) also ruled out the dependency of such a scaling law on the choice of length scales by showing that both longitudinal and transverse length scales follow this non-equilibrium scaling relation, regardless of the inhomogeneity and anisotropy of different flows.

To close this section, it is worth mentioning that the aforementioned works were all carried out with regular grids, single square grids and FSGs (or variants of FSGs such as the grid used by Hearst and Lavoie (2014)). In all these grids, all corresponding bars, whether vertical (in the y direction) or horizontal (in the z direction) had the same lengths and thicknesses, i.e. L_0 and t_0 are defined irrespective of orientation. In the current study, we introduce the rectangular fractal grid (RFG). This grid is stretched in the transverse direction, and consequently two distinctive lengths and thicknesses are present at each iteration. A detailed description of the grid is presented in section 2.1.2.

1.3 Turbulent shear flows

Many efforts have been made to develop different types of devices to produce shear flows in wind tunnel experiments. Some of the most popular methods are briefly discussed here, and reviews of the earlier methods can be found in Lawson (1968) and Laws and Livesey (1978). In this section, various methods to generate turbulent shear flows over the past few decades are briefly discussed first. The evolution of turbulence statistics, length scales and other turbulent characteristics in turbulent shear flows are reviewed in the second part. Here and for the rest of the discussion, x, y, z represent the streamwise, vertical, and transverse direction, respectively.

1.3.1 Shear generating methods

Several methods have been proposed to generate shear flows in laboratories. One of the methods is to use wire gauze to modify the local solidity, and consequently produce a mean velocity gradient. The effect of flow passing through wire gauze was described in detail by Taylor et al. (1949). Then by using resistance and deflection coefficients as grid properties, a theoretical method of grid design was offered by Owen and Zienkiewicz (1957) relating the downstream mean velocity profile to the spacing of the wires, and a uniform shear flow was produced in their study using parallel wires of diameter $d = 3.175\,\mathrm{mm}$. This method was further generalized by Elder (1959) to non-uniform gauze with arbitrary shapes. Elder (1959) tested his theory on linear and parabolic gauze, and proposed a gauze shape to generate a linear shear flow. Rose (1966) followed the same method and showed that the shape of the generated downstream mean velocity profile was persistent at different streamwise locations. The later studies of Livesey and Laws (1973) on flow through shaped gauze proposed a modification of the theory to exclude a higher order term, which seemed to cause discrepancies between theoretical solutions and experimental data from two-dimensional and axisymmetric cases. The most obvious drawback of a method using

gauze and wires is, as commented by Lawson (1968), that the turbulence characteristics cannot be varied once the wire is chosen, and it is therefore impossible to generate mean velocity and turbulence profiles independently.

The parallel wire method relies mostly on the spacing of the wires, and it is therefore hard to adjust the elements locally. Another type of shear generator was tested by Champagne et al. (1970), where the authors used plates of 609.6 mm long, and 3.175 mm thick separated by 25.4 mm to form parallel channels with adjustable internal screens to control the local solidity. The same method was then used by many, e.g. Harris et al. (1977); Tavoularis and Corrsin (1981); Karnik and Tavoularis (1987); Rohr et al. (1988); Garg and Warhaft (1998); Nedić and Tavoularis (2016), with different configurations such as the size of internal grid size, and the separation distance of the plates. A honeycomb with uniform cell diameter but varying lengths in the streamwise direction was also tested by Rose (1970) to generate shear flows. Rose (1970) studied the combination of such a honeycomb and a grid placed downstream with different sizes and geometries, and the downstream grid was shown to reduce the mean shear rate. Richards and Morton (1976) produced a quadratic mean velocity profile using such a honeycomb and grid combination. Mulhearn and Luxton (1975) used a similar setup where a grid of non-uniform parallel rods was placed upstream of the honeycomb with uniform length to produce a uniform sheared flow. Note that no relation between the shear flow and the geometry of the setup was concluded from these parallel plate methods since all of them were tuned by trial-and-error. Even though they offer the possibility of local adjustments of the device, which is an improvement of the previous method, they lack theoretical support to relate the grid geometry to the generated shear flow. Experiments involving extremely high shear rates, e.g. $\partial U/\partial y > 400\,\mathrm{s}^{-1}$ (see Souza et al., 1995), are excluded from our discussion.

The active grid proposed by Makita (1991) and subsequent works by e.g. Mydlarski and Warhaft (1996b); Shen and Warhaft (2000a); Cekli and van de Water (2010); Knebel et al. (2011) provided another option to tailor turbulent flows. It is typically used to produce

a higher turbulence level, and is sometimes combined with other passive devices to produce shear flows (see e.g. Zhu et al., 2006; Bai et al., 2012; Thormann and Meneveau, 2015). Hearst and Ganapathisubramani (2017) proposed the possibility to obtain independent control of the mean flow and turbulence intensity using the active grid. They produced shear flows with small shear rates ranging approximately $6.25\,\mathrm{s}^{-1}$ to $12.5\,\mathrm{s}^{-1}$ over a physical domain of 0.32 m and generated profiles of varying turbulence intensity and high Reynolds numbers. Hearst and Ganapathisubramani (2017) claimed that such shear flows would be directly applicable in wind turbine experiments. Amongst many advantages, the methodology of active grid generated turbulence, however, is rather costly to implement, and the establishment of control protocols is largely empirical. The work of Hearst and Ganapathisubramani (2017) did not provide quantitative relations between the control parameters and the turbulence characteristics. Therefore we explore the possibility of a type of passive grid design for producing desired turbulence fields. This idea is also supported by the conclusion of Roach (1987) that the turbulence energy scales on the bar dimensions rather than the mesh size, which suggests that it is possible to manipulate the turbulence intensity through the design of the grid bars.

In this context we attempt to combine the known methodology for producing mean shear with fractal/multiscale ways to produce scalable high turbulence intensities at the same time. For this reason, we exploit to the studies of fractal grids proposed by Hurst and Vassilicos (2007), especially the space filling fractal square grids (e.g. Seoud and Vassilicos, 2007; Mazellier and Vassilicos, 2010; Valente and Vassilicos, 2011; Gomes-Fernandes et al., 2012; Hearst and Lavoie, 2014; Isaza et al., 2014) where the development of downstream turbulence has been quantitatively related to the grid geometries. These fractal square grids are characterized by repeated square patterns of different sizes, and the blockage ratio is usually small ($\sigma \approx 25\%$ to 30%). Detailed descriptions can be found in Seoud and Vassilicos (2007); Hurst and Vassilicos (2007); Mazellier and Vassilicos (2010).

Mazellier and Vassilicos (2010) studied the fractal generated turbulence, and proposed the

wake interaction length scale $x_* = L_0^2/t_0$, where L_0 is the largest length of the bars, and t_0 is the largest width. This scaling relation succeeded in collapsing both the centerline mean velocity and turbulence intensity profiles. The peak of the turbulence intensity was found at $x_{peak} \approx 0.45x_*$ with maximum level of approximately $15\%U_\infty$. Later, Gomes-Fernandes et al. (2012) extended the study to include the effects of the aspect ratio of the bars and the free stream turbulence level, and proposed the improved scaling relation $x_*^{peak} = 0.21L_0^2/(\alpha C_D t_0)$, where $\alpha = 0.231$ is a constant associated with the wake development for flows with minimal inlet free stream turbulence intensity, and C_D is the drag coefficient of the bar. This x_*^{peak} provided better collapse of the streamwise turbulence intensity profiles from different grids, and was taken to be an important parameter for designing the grids. Gomes-Fernandes et al. (2012) also proposed a scaling relation for the turbulence intensity levels, and the scaled turbulence intensity $(u'/U_\infty)\beta(C_D t_0/x_*^{peak})^{-1/2}$ (where $\beta = 2.88$ is a constant for laminar free stream, and U_∞ is the inlet free stream velocity) collapsed six different inlet conditions as a function of x/x_*^{peak}. These scalings are adapted and discussed further in the design process of our new multiscale inhomogeneous grids in section 3.1.2.

1.3.2 Shear flow characteristics

The development of turbulence intensity in a grid generated shear flow was perhaps first discussed by Rose (1966). Rose (1966) generated a homogeneous turbulent shear flow with a mean shear rate $S = \partial U/\partial y = 13.69\,\mathrm{s}^{-1}$ which retained its value up to $x/H = 9.76$, where H is the height of the grid. The streamwise and vertical turbulence rms u' and v' were found nearly uniform along the mean shear direction y at $x/H = 1.33$, but the two edges were affected by the growing boundary layers on the tunnel walls and the turbulence intensities were significantly larger on the sides. Along the centerline, u' and v' decayed to values of $u'/U_c = 1.2\%$ and $v'/U_c = 0.8\%$, where U_c is the centerline mean streamwise velocity.

Champagne et al. (1970) produced a mean shear rate $S = 12.9\,\mathrm{s}^{-1}$ using parallel plates with internal screens, and the shear rate was maintained in the range $x/H = 3$ to 9.5. The centerline turbulence intensity u'/U_c reached a constant value of 1.8% after $x/H = 6.5$. Rose (1970) created shear flows using different combinations of honeycomb and wire grid, and produced mean shear rates in the range $S = 6\,\mathrm{s}^{-1}$ to $12\,\mathrm{s}^{-1}$. The streamwise turbulence intensity level u'/U_c in the range $x/H = 7$ to 9 was shown to be constant, with a value increased from 0.2% to 2% with increasing grid size.

Harris et al. (1977) improved on the work of Champagne et al. (1970) and produced a larger mean shear rate $S = 44\,\mathrm{s}^{-1}$ which remained almost constant up to a dimensionless time scale $\tau^* = 12$, where $\tau^* \equiv (x/U_c)(\partial U/\partial y)$. Their hot-wire results showed a larger normalized turbulence intensity compared to that in Champagne et al. (1970), and the turbulence intensity was found to grow with streamwise distance after $\tau^* \approx 4$. The growth of turbulence intensity along the streamwise direction was then studied by Rohr et al. (1988) for several cases, where the grid size, centerline velocity, and mean shear rate were varied. The results clearly showed a region of increasing streamwise turbulence intensity u'/U_c. The critical point τ_c^*, where u'/U_c reached its minimum was studied by several authors, and interestingly the turbulence intensity beyond τ_c^* remained constant in some cases (e.g. Rose, 1966; Champagne et al., 1970; Rose, 1970), but grew in others (e.g. Harris et al., 1977; Tavoularis and Corrsin, 1981; Rohr et al., 1988; Nedić and Tavoularis, 2016). For the cases where u'/U_c stayed constant, the development was fairly fast, reaching constant values at $\tau_c^* = 1.6$ to 3, whereas for those cases exhibiting growing u'/U_c the critical point was observed at roughly $\tau_c^* = 4$ to 5. Tavoularis and Karnik (1989) studied this more systematically and suggested that when the shear is *weak*, i.e. $\epsilon/P \sim 1$, the turbulent kinetic energy will remain constant after τ_c^*, whereas for *strong* shears, where $\epsilon/P < 1$, the turbulence kinetic energy will grow exponentially after τ_c^*.

Regarding the Taylor microscale λ, Harris et al. (1977) reported a constant value of λ in the range $\tau^* = 6$ to 11, with $S = 44\,\mathrm{s}^{-1}$. Rohr et al. (1988) also reported a constant λ

from $\tau^* = 6$ with approximately $S = 1\,\mathrm{s}^{-1}$, while Tavoularis and Karnik (1989) showed in their experiments that λ approached a constant value at $\tau^* \approx 16$ for mean shear rates $S = 44\,\mathrm{s}^{-1}$ and $84\,\mathrm{s}^{-1}$. More recently Nedić and Tavoularis (2016) reported a constant λ downstream of their shear generating plates at $\tau^* \approx 9.25$ in a uniformly sheared flow with $S = 62\,\mathrm{s}^{-1}$. By comparing the results from HGC and Rohr et al. (1988), it can be concluded that the location where λ stops growing is not only a function of the mean shear rate, but other factors as well.

In terms of integral length scales, all of the previous results showed monotonic increases with streamwise distance. Results by Nedić and Tavoularis (2016) also showed a decrease of growth rate of the longitudinal integral length scale $L_{uu,x}$ beyond roughly $\tau^* = 9$. Some studies reported relations between longitudinal and transverse integral length scales such that $L_{uu,x} = 2L_{uu,y}$, indicating a large scale isotropy (e.g. Rose, 1966; Champagne et al., 1970; Harris et al., 1977). Further discussion on length scales is provided in section 3.2.5.

1.4 Outline

Contributions of this thesis will be presented in three chapters. In Chapter 2 the results of experiments with the rectangular fractal grids are presented from three different wind tunnels using hot-wire anemometry and Particle Image Velocimetry (PIV). The use of three different facilities provides an opportunity to study the turbulence generated by these RFGs in different regions of the decaying turbulence, and gives confidence in the observed patterns of evolution of various length scales. The mean velocity and turbulence intensity profiles are studied first to discuss the previous scaling relations for the wake interaction length scale. The evolution of different length scales is examined, and the homogeneity and isotropy of the flow is studied. The results show regions where the non-equilibrium scalings are present in all three experiments. Finally the spectra are presented, demonstrating the single length scale spectra corresponding to the non-equilibrium

scaling relation. In Appendix A, a simple temperature calibration is proposed for easy implementations in large wind tunnels without thermal controls, which was the case in one of the facilities used in this study. Some discussions on calculating the integral length scale are also given in Appendix B.

In Chapter 3 a group of new multiscale inhomogeneous grids is introduced that offers the ability to produce desired mean velocity profiles and near-field turbulence intensity profiles simultaneously. Details of the grid design is given first, and measurements of the mean velocity profiles are presented. It is shown that predictions using the mean velocity model derived from Taylor et al. (1949) and McCarthy (1964) are in good agreement with the experimental data. By modifying the grid thickness, the aspect ratio of the grid bars are changed, and consequently the drag coefficients. The effect of drag coefficient on the local mean velocity gradient is discussed. Results on the evolution of turbulence intensities and length scales are presented, and finally a simplified model is proposed to describe the downstream development of the turbulence field generated by our grids. Finally, it is concluded that the proposed inhomogeneous multiscale grids might be used to tailor the characteristics of turbulent shear flows in a more systematic way.

Two different versions of the grids proposed in Chapter 3 were made for measurements in a low-fidelity engineering wind tunnel in Mel Consultants to test the robustness of the methodology. These results are presented in Chapter 4. A detailed setup of the grid is given first, and the quality of the base flow is examined. Results of mean velocities and turbulence rms confirm the model and scaling method proposed in Chapter 3. The integral length scales along the x and y directions are also presented, and the evolution is shown to be the same as the results from 3. These results all together suggest the possibility to use the multiscale inhomogeneous grids for further studies to generate different combinations of mean velocity and turbulence profiles.

Finally, Chapter 5 gives a summary of the main results, and some possible ideas of future work are proposed.

Chapter 2

Fractal generated turbulence

In this chapter we present works on the modified fractal grid, referred to as the rectangular fractal grid (RFG), which produces turbulence with large integral length scales and high turbulence intensities. The experiments were carried out in three facilities, i.e. the Honda and 3×3 wind tunnels at Imperial College London, and the Lille wind tunnel at Lille Mechanics Laboratory at Lille-1 University. Since the Honda experiments revealed unusual length scale evolution patterns in the decay region (as discussed in section 2.2.3), the Lille experiments were conducted to verify this behavior by extending the streamwise measurement domain. However, the turbulence at further downstream is inevitably affected by the growing boundary layer at the walls, so the 3×3 experiments were designed using a repeated pattern of the same grid (as shown in section 2.1.2) to compare the effect of different boundary conditions.

Hot-wire anemometry is used in all three campaigns, and some Stereo-PIV measurements were taken in the Lille experiments. The wake interaction length scale x_*^{peak} is shown to be dependent of the grid geometry, but independent of the inlet Reynolds number. Due to the inhomogeneous grid geometry, there are two distinct x_*^{peak} in the y and z directions, giving a region where $L_u \propto Re_\lambda$ and $\lambda \propto Re_\lambda$ is observed, where L_u is the longitudinal integral length scale, and λ is the Taylor micro scale. Calculated 2D swirling

strength λ_{ci} from the PIV measurement shows strong vortex interactions in this region. The non-equilibrium scalings are shown to be present for some part of the decay region. The self-similarity of spectra are also given, which follows the energy dissipation scalings in various streamwise regions. Here and for the rest of the discussion, x, y, z represent the streamwise, vertical, and spanwise directions, respectively.

2.1 Experiments

2.1.1 Facilities and experiments

The Honda wind tunnel experiments

The Honda closed return wind tunnel in the Department of Aeronautics at Imperial College London has a test section of 3 m in width, 1.5 m in height, and a working length of 8 m. The air is driven by two 40 hp axial fans with vanes installed in a twin duct to straighten the flow. Before entering the test section, the flow passes through a honeycomb followed by a mesh screen mounted before the 9:1 contraction chamber. A turbulence level of 0.2% for the incoming flow is achieved at free stream velocity of $U_\infty = 10\,\mathrm{m/s}$. Control of the air velocity was accomplished by a MATLAB script with PID controller, using pressure readings from a Furness Controls FCO510 flow meter. The pressure tubes are connected on the walls before and after the contraction chamber, and the readings are calibrated before each experiment using a Pitot tube placed at the center of the beginning of the test section.

A computer-controlled traversing system is mounted on the ceiling of the test section. Two rails are laid on each side of the ceiling, and a moving platform is suspended on the rails allowing movements in the x direction. On the platform, another traversing system (referred to as z-traverse) is installed so that spanwise movements can be achieved. Consequently, the measurement domain for the present study ranges from 2 m to 8 m in

the streamwise direction, and -1 m to 1 m in the spanwise direction. A y-traversing beam was also mounted to the z-traverse, allowing position adjustments in the y direction in the range of approximately 0 m to 0.3 m. The tip of the y traverse was strengthened by four piano wires attached to the moving platform to avoid vibrations.

For the Honda experiments, a single hot-wire was used for all measurements. The Hot Wire Anemometry (HWA) system consists of a DANTEC Streamline anemometer operated at constant temperature mode, two DANTEC 55H21 probe supports, and two DANTEC 55P01 probes with Wollaston wires of 5 micron in diameter. The effective length of the wire is approximately 1 mm, and the frequency response is measured to be approximately 30 kHz by a square wave test. The hot wire data were acquired using MATLAB through a 16-bit NI-6229(USB) data acquisition board. All data were sampled at 100 kHz for 200 s, and a 30 kHz low pass filter was applied in the Streamline anemometer before the data was recorded.

Two types of experiments were performed, i.e. single point measurements and two point correlation measurements. The inlet velocity U_∞ was varied from 5 m/s to 17 m/s. For single point measurements, one hot wire was mounted on the y-traverse, which is attached to the z-traverse, allowing position adjustments in all directions. Data points were taken along the centerline of the wind tunnel with $\Delta x = 0.4$ m at $y = z = 0$ m, and along the streamwise direction at $y = 330$ mm, $z = 0$ m, henceforth referred to as *center* and *bar*330, respectively. In the $y - z$ plane at $x = 2$ m, the flow was probed across the span for $-1\,\text{m} < z < 1\,\text{m}$ with $\Delta z = 0.1$ m at $y = 0.1, 0.2, 0.3$ m, respectively, whereas at $x = 8$ m, measurements were taken for $0\,\text{m} < z < 1\,\text{m}$ with $\Delta z = 0.1$ m at $y = 0.1, 0.2, 0.3$ m, respectively. These arrays of points are assembled into two-dimensional planes for $-0.3\,\text{m} < y < 0.3\,\text{m}$ and $-1\,\text{m} < z < 1\,\text{m}$ by assuming symmetry to look at the mean statistics in the production and the decay region, defined as before and after the turbulence peak location x_{peak}, respectively.

Two point correlation measurements were also taken to study the integral length scales in

the y direction. The fixed wire was placed on the center plane at $(x, z) = (8\,\mathrm{m}, 0\,\mathrm{m})$, and $(x, z) = (6\,\mathrm{m}, 0\,\mathrm{m})$, respectively, with $\Delta y = 20\,\mathrm{mm}$ up to a separation of 360 mm to look at the correlation functions $R_{uu,y}$. Note that all data with two hot wires were acquired using non-adjacent channels to reduce the crosstalk to $-90\,\mathrm{dB}$.

The 3×3 wind tunnel experiments

The 3×3 closed loop wind tunnel in the Aeronautics Department at Imperial College London has a cross sectional area of $0.91\,\mathrm{m} \times 0.91\,\mathrm{m}$, and a test section length of 4.2 m. The flow goes through a set of perforated screens and a 9:1 contraction before reaching the test section. The background turbulence intensity without the grid was measured to be $\sim$0.1% at $U_\infty = 10\,\mathrm{m/s}$. A computer controlled traversing system is mounted on top of the working section, allowing movements in the range $0.83\,\mathrm{m} < x < 4.13\,\mathrm{m}$, $-0.28\,\mathrm{m} < y < 0.14\,\mathrm{m}$, and $-0.15\,\mathrm{m} < z < 0.15\,\mathrm{m}$.

A Furness Controls FCO510 micro-manometer was used to monitor the tunnel inlet velocity U_∞ and the temperature. The system also has a PID controller that stabilizes the inlet velocity U_∞. Velocity signals were measured using an in-house etched platinum Wollaston cross wire powered by a Dantec Streamline CTA system. The diameter of the wire was $d_w = 5\,\mathrm{micron}$ with length to diameter ratio approximately 200. The cross wire was mounted on a servo motor, allowing accurate control of the pitching angle during calibration, and the servo motor was cased in a plastic holder attached to the traverse. The cross wire was mounted in the holder to align with the $x - y$ plane. The output voltage was recorded by MATLAB through a 16-Bit National Instruments NI-6229 (USB) board. All data sets consist of 2 packets of samples recorded at 125 kHz for 300 s, and a low pass filter of 30 kHz was applied before the data was recorded.

The hot wire was calibrated at the beginning and end of every data set acquired using the look-up table method by Lueptow et al. (1988) for five velocities from 3 m/s to 19 m/s and seven angles ranging from $-27°$ to $27°$. The temperature was monitored during

acquisitions, and the data was discarded if temperature variation $\Delta T_a = T_{a,max} - T_{a,min}$ was larger than 0.1 °C. The inlet velocity U_∞ was maintained within ±1.5% of the target value for all data sets.

Streamwise profiles are taken at $U_\infty = 6\,\mathrm{m/s}$ and $U_\infty = 10\,\mathrm{m/s}$ along x on the centerline, and behind the largest horizontal bar of the grid, referred to as *center* and *bar*, respectively.

The Lille wind tunnel experiments

The Lille experiments were carried out in collaboration with the Lille Mechanics Laboratory (LML) in their boundary layer wind tunnel at Lille-1 University. The tunnel's test section has a 2 m wide 1 m high cross section, and is 21 m in length. Before entering the test section, the flow passes through two honeycombs, a screen, and a 5:1 contraction chamber. The maximum free-stream velocity is 9.4 m/s at the tunnel entrance with a free stream turbulence level no bigger than 0.2%. Note that at the tunnel entrance there is a 93 mm long grit 40 sandpaper (mean roughness 425 μm) attached to the bottom and the top of the tunnel walls which is not removable, and the turbulence far downstream is inevitably affected by the boundary layer, especially for measurements behind the horizontal bar, which is roughly 0.17 m above the bottom wall.

The test section is transparent on all sides with high quality 10 mm thick glass for the purpose of optical access. All the glasses and surfaces at the bottom wall are adjusted so that there is no step bigger than 0.1 mm. The top and bottom walls were also adjusted so that they are perfectly parallel (locally less than ±0.1°), so were the lateral walls.

During acquisition, the free stream pressure was measured by a Pitot tube through a Furness Controls FCO14 micro-manometer to control the inlet velocity. The wind tunnel is driven by a 37 kW blade fan controlled through MATLAB. The fluctuation of incoming velocity was monitored at all times to be within $\pm 0.5\% U_\infty$. The wind tunnel is also

equipped with a temperature regulator. The fluctuation of ambient temperature was monitored at all times to be within $\pm 0.15\,^{\circ}\mathrm{C}$ of the calibration temperature, which was $17\,^{\circ}\mathrm{C}$. The data acquisition or calibration was restarted if either the velocity or temperature variations exceeded these limits.

For hot-wire calibrations, the local pressure was used, measured by a Pitot tube placed next to the hot-wire ($\Delta z = 5\,\mathrm{cm}$) through a Furness Controls FCO560. Due to the upper limit of the free stream velocity, the hot-wire was calibrated with the grid in as an accelerator, but placed very close to the grid (equivalent to $x/x_{peak} = 0.05$) on the centerline so the turbulence intensity is smaller than 0.5%. Between 25 to 60 packets of 4 s samples were taken with decreasing velocities to reduce the error during calibration.

For the hot wire experiments, one DANTEC 55P15 wire was used with $5\,\mu$m diameter and 1.25 mm long tungsten wire sensor. The hot-wire was mounted on a DANTEC 55H22 right-angled probe support, which was fixed inside a streamlined probe holder extending from the top of the test section. The whole probe holder was installed on a y (vertical) traverse on top of the test section. A Lektronix Micro Control TL78 was used to control the traverse, allowing accurate positioning in the y direction. The traverse was moved manually in the x direction to complete the streamwise profiles.

The hot-wire was powered by a TSI IFA 300 Constant Temperature Anemometer, and the voltage signal was recorded by MATLAB through a NI-cDAQ 9188 board, acquiring at 50 kHz with a low-pass filter of 30 kHz. Two enterline profiles were measured from $x = 0.86\,\mathrm{m}$ to $18.6\,\mathrm{m}$ at $U_\infty = 6\,\mathrm{m/s}$ and $9\,\mathrm{m/s}$, respectively, referred to as *center*. Another two streamwise profiles were taken behind the horizontal bar at $y = -0.327\,\mathrm{m}$ for the same x locations with $U_\infty = 6\,\mathrm{m/s}$ and $9\,\mathrm{m/s}$, referred to as *bar*. For each data set, 3 packets of 600 s samples were acquired, and the results are averaged over these packets to have a better convergence.

Some Particle Image Velocimetry (PIV) experiments were also performed as part of the Lille experiments to look at the region just behind x_{peak} where turbulence intensity is

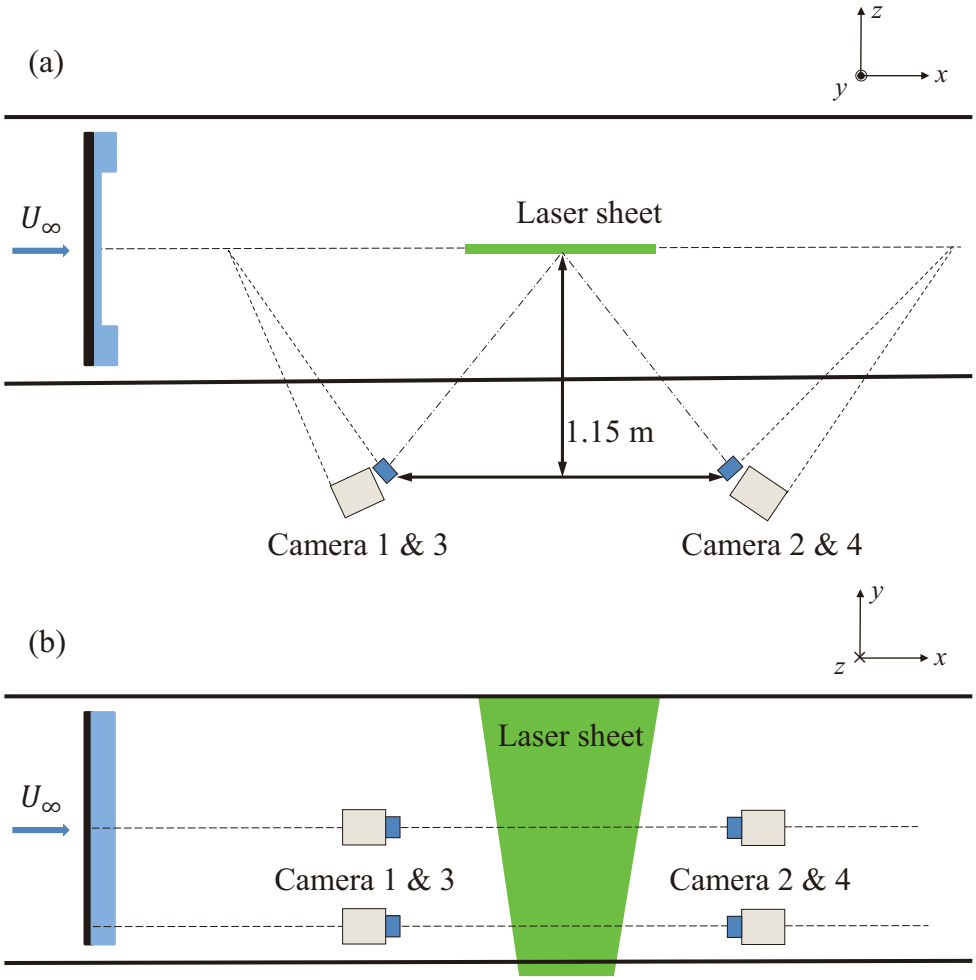

Figure 2.1: Schematic sketch of the PIV setup from (a) top view, and (b) side view. Dimensions not in scale.

highest. Four 16-bit LaVision sCMOS cameras with 2160 × 2560 pixels were used to set up two Stereoscopic PIV systems. Four Nikon Micro-Nikkor 105 mm lenses and four 200 mm lenses were used to facilitate large and small field of view (FOV) respectively. All experiments used $f^{\#} = 8$. The cameras were mounted on custom designed Scheimpflug adapters, allowing independent fine adjustment in all aspects of the camera positioning. During the PIV measurements, the glass side walls at measurement location were replaced with coated glasses to allow more light. The cameras were all mounted 1.15 m away from the center plane of the tunnel, and oriented at 45 degrees to the measurement plane. Figure 2.1 gives a schematic sketch of the setup.

The laser was B.M. Industries custom made dual-cavity Nd:YAG operated at 532 nm

with an output power of 200 mJ/pulse. The flow was seeded with a smoke generator from Hazebase using Base L Smokefluid. The liquid consists of a mixture of glycol (1%) and water (99%), and has a mean diameter of order 1 μm with a specific gravity of 1.058 g/cm^3 at 20 °C.

A set of cylindrical ($f = -150$ mm for small FOV, and $f = -100$ mm for large FOV) and spherical lenses ($f = 5$ m) were used to generate a light sheet through the bottom of the wind tunnel. The thickness of the light sheet was 0.6 mm for the small FOV and 1 mm for the large FOV. The resulting FOVs have sizes of 17×11 cm and 33×21 cm, centered at $x = 3.55$ m on the centerline of the grid.

A calibration target of size 34×74 cm was installed at the center plane of the tunnel, and it was traversed for ± 5 mm with 0.5 mm steps during the calibration. The target consists of "+" marks with size 6×6 mm spaced 0.916 cm and 0.917 cm in the x and y direction, respectively.

Synchronization was achieved by a LaVision PTU 9 control box using DaVis 8 software. The Q-switch delay of laser was set to 150 ms to maximize the output power. Particle images were acquired at 4 Hz, and a total of 20000 images were acquired for each data set with 10 separate runs of 2000 images.

2.1.2 Grid design

The original idea to design such a rectangular fractal grid, or RFG, was to (i) stretch the size in z and therefore increase the integral length scale, (ii) maximize the drag coefficient C_D by giving a depth to each one of the grid bars to obtain a higher turbulence intensity in the downstream turbulence, and (iii) test the non-equilibrium dissipation scaling (Vassilicos, 2015) when two length scales of the grid are present.

The first of such grids was designed to fit in the Honda wind tunnel (see figure 2.2). Detailed dimensions of this grid are given in table 2.1. The grid was designed with a third

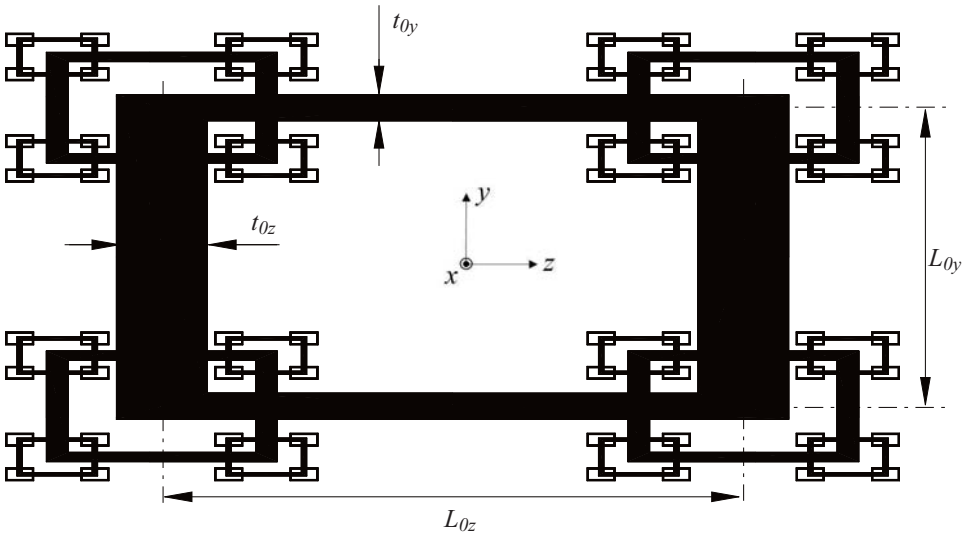

Figure 2.2: Rectangular fractal grid for the Honda wind tunnel. Dimensions mark the first iteration of the grid.

dimension d, which is the depth of the bar in the streamwise direction. These dimensions were chosen to give each bar an aspect ratio AR (equal to the streamwise thickness d over the transverse width t) of 0.61, so that the drag coefficient C_d of each bar could be maximized (see Bearman and Trueman, 1972). The last two iterations of the grid, however, have larger aspect ratios of approximately $AR = 1$ and $AR = 3.75$, respectively, due to durability concerns during manufacturing.

The grid was made from CNC routed plywood sheets, and the depth was modified using foam blocks (illustrated in figure 2.1 in blue color). During the experiments, it was mounted with two supporting aluminum profiles attached to the lee of the two largest vertical bars. The gap between the tunnel wall and the edge of the smallest grids was approximately 3 cm on the top and bottom, and 5 cm on the sides.

The same grid was scaled down by a ratio of 1.54 to fit in the Lille wind tunnel. The Lille grid was also made of plywood and foam. The thickness of the grid bars were adjusted using foam blocks to match $AR = 0.61$. Due to the glass surface of the Lille wind tunnel, it was mounted on two horizontal aluminum profiles with rubber pads at each end to hold on the side walls, attached to the lee of the largest horizontal bars of the grid.

j	0	1	2	3
L_{jz} (mm)	1954	703	253	91
L_{jy} (mm)	1004	341	116	39
t_{jz} (mm)	305	73	18	4
t_{jy} (mm)	88	31	11	4
d_{jz} (mm)	184	45	15	15
d_{jy} (mm)	54	19	15	15

Table 2.1: Dimensions of the rectangular fractal grid, where L, t, d correspond to length, width and depth of the bar, respectively, and $j = 0, 1, ...N_f - 1$, where $N_f = 4$ is the number of fractal iterations. The subscript y and z gives the direction of the dimension, e.g. L_{0y} means the length of the bars of the first iteration in the y direction.

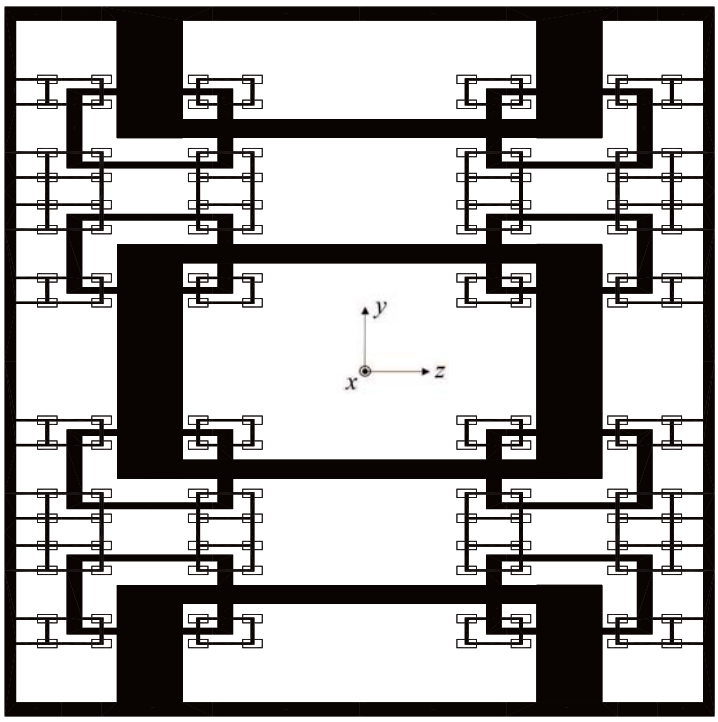

Figure 2.3: Rectangular fractal grid for the 3×3 wind tunnel with frame.

	L_{0z}(m)	t_{0z}(m)	x_{z*}^{peak}(m)	L_{0y}(m)	t_{0y}(m)	x_{y*}^{peak}(m)	σ(%)
Honda	1.954	0.308	3.924	1.004	0.088	3.591	33.4
Lille	1.272	0.199	2.557	0.654	0.057	2.339	34.3
3×3	0.558	0.087	1.123	0.287	0.025	1.032	33.8

Table 2.2: Largest bar size, wake interaction length scales, and the total blockage ratios of the rectangular fractal grids in all experiments, where $x_{y*}^{peak} = 0.21(L_{0y}^2)/(\alpha C_d t_{0y})$ and $x_{z*}^{peak} = 0.21(L_{0z}^2)/(\alpha C_d t_{0z})$.

For the 3×3 experiments, the grid was scaled down by a ratio of 3.5, and was repeated by half at both ends in the vertical direction to fit in the square test section, as shown in figure 2.3. The grid was made of laser cut acrylic sheets, and it was fitted on a wooden frame to support the largest bars. The frame was flush with the tunnel walls. As with the other grids, the bar thickness were adjusted to achieve $AR = 0.61$ using foam blocks attached to the lee of the grid bars. Table 2.2 gives a comparison of the dimensions of the largest bars in each experiment. Since there are two large scales, there are also two wake interaction length scales $x_{y*}^{peak} = 0.21(L_{0y}^2)/(\alpha C_d t_{0y})$ and $x_{z*}^{peak} = 0.21(L_{0z}^2)/(\alpha C_d t_{0z})$, calculated using the two corresponding dimensions marked by subscripts y or z. Note that $x_{y*}^{peak} \neq x_{z*}^{peak}$ due to the difference of grid bar dimensions in the y and z directions, and the impact of this difference is discussed in section 2.2.2. The blockage ratios, taking into account the mounting/supporting elements, are approximately 33.8%, which is only slightly larger than $\sigma = 25\%$ to 32% for the square fractal grids used by Valente and Vassilicos (2011).

2.1.3 Data processing

Hot-wire processing

Due to the lack of thermal control in the Honda wind tunnel, temperature variations as large as 5 °C were frequently detected, so a practical temperature correction method was

developed for the Honda experiments. Based on the assumption that $E_0^2 = A' + B'T_a$, where E_0 is the output voltage from the anemometer, A' and B' are constants, and T_a is the ambient temperature, this method successfully collapsed several calibration curves taken at different ambient temperatures, and then uses an iterative processing method to correct the output voltages. The details are explained in Appendix A.

Another issue frequently encountered in experimental works is that the largest scales of the flow are often insufficiently resolved due to limited sample size. In order to calculate the longitudinal integral length scale L_u, several methods are compared. The method of integrating auto-correlation functions is not used here due to the ambiguity in the choice of integration limit (see O'Neill et al., 2004). These results are also affected by the piecewise sample size if one takes average of shorter samples (see appendix B). Based on the Wiener-Khinchin theorom, the auto-correlation function and the power spectral density is a Fourier pair, and therefore the power spectral density provides another option to calculate L_u. In practice, the inertial range of the power spectrum density is first fitted to a model to extrapolate the low wavenumber range of the spectrum, and the integral length scale is calculated using $L_u = \pi E_{11}(k = 0)/(2u'^2)$, where k is the wavenumber defined as $k = 2\pi f/U$ (f is the frequency in time), and u' is the streamwise turbulence r.m.s. velocity. To calculate wavenumber k, the spatial signal is converted from the time series using the Taylor's hypothesis, where the local mean velocity U is taken as the convection velocity.

One of the frequently used spectrum models is the von Kármán model (von Kármán, 1937), which can be written in a one-dimensional form as

$$E_{11}^{+}(k) = \frac{2u'^2 L_{uu,x}}{\pi} \frac{1}{\{1 + [kL_{uu,x}B(1/2, 1/3)/\pi]^2\}^{5/6}}, \tag{2.1}$$

where u' is the streamwise turbulence r.m.s. velocity, k is the wave number, and B is the beta function related to the Γ function by $B(1/2, 1/3) = \Gamma(1/2)\Gamma(1/3)/\Gamma(5/6)$. More recently, another form of spectrum model is proposed by Wilson (1998) based on the

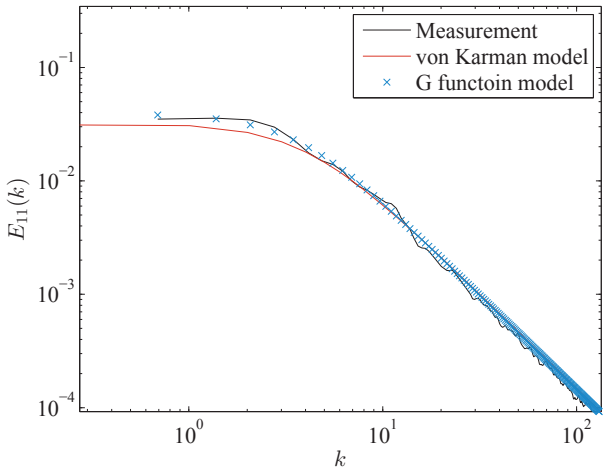

Figure 2.4: Comparison of two spectra models against experimental data taken from Honda wind tunnel, in the decay region of RFG generated turbulence.

Meijer's G-function (referred to as the G-model in this text), namely

$$E_{11}^{*}(k) = \frac{2u'^2 l}{3B(1/2, 1/3+b)}(k^2l^2)^{-5/6}B_{k^2l^2/(1+k^2l^2)}(5/6, b), \tag{2.2}$$

where B is the beta function, u' is the streamwise turbulence r.m.s. velocity, k is the wavenumber, and B_x is the incomplete beta function. This model includes two fitting variables l and b, and is therefore more accurate than the von Kármán model (see Wilson, 1998) in terms of adjusting the energy level for the inertial sub-range and energy-containing range separately. This G-model is therefore used for spectrum correction in the current discussion.

Figure 2.4 shows an example to compare these two models with experimental data, fitted using nonlinear regression. It is clear that the von Kármán model underestimates the spectra levels in the energy-containing range, as reported by Wilson (1998). The sum of squared residuals for the G-model is also smaller. Therefore the G-model is used to correct the spectra in the energy-containing range and to calculate integral length scales in the following discussion. Note that the G-model might introduce unwanted error if the Reynolds number is small, such that the inertial sub-range does not show a definite $-5/3$ slope. In that case, the von Kármán model might be a better choice.

While the inertial range of spectra can be corrected by the G-model method, the dissipation range of spectra is also of concern. This part of a spectrum usually suffers from electrical noise which shows up as spurious rises at the end of the spectrum proportional to k^2 (Seyed and Srinivas, 1996; Antonia, 2003). This rise can lead to overestimation of the dissipation rate ϵ because of the k^2 term in the integrand. Furthermore, at sufficiently large Reynolds number, the Kolmogorov length scale sometimes cannot be resolved due to limited resolution of the hot wire, so it is desired to extrapolate the spectra to obtain higher wavenumber components. There have been many discussions on spectrum models for the high wavenumber range (see Sanada, 1992; Antonia et al., 1996). Here we refer to the method discussed by Pearson (1999) and Zhou et al. (2002), such that for sufficiently large k, the spectrum $E_{11}(k)$ has the form $k^{-5/3}\exp(\alpha k+\beta)$, where α and β are constants. Thus a linear extrapolation can be applied to $\mathrm{In}[k^{5/3}E_{11}(k)]$ with respect to k. Antonia (2003) improved the form to have $E_{11}(k) \sim k^m\exp(\alpha k+\beta)$, where the constant $-5/3$ was substituted by the variable m as they found that the magnitude of m increases with Re_λ. The actual value of m is chosen first by trial and error to give the best fit, and the value for current experiments are in the range $m = -8/3$ to -2.

The dependence of this method on the choice of fitting wavenumber range was found to be negligible. Extrapolations performed based on ranges from 2 kHz to 5 kHz and 3 kHz to 6 kHz, respectively, give 1.8% difference in the dissipation rate ϵ calculated by integrating the corrected and re-sampled spectrum. One example of the corrected result is given in figure 2.5. It can be observed that the re-sampled spectrum correctly represents the original one in the inertial sub-range. For calculations using fluctuating velocity signals, the cutoff frequency is chosen to be $f_c = 2.3f_{noise}$, where f_{noise} is the frequency where $f^2E(f)$ has a minimum in the high frequency range. The constant 2.3 compensates for the Nyquist limit, and the transition band (the region between pass band and stop band) of the filter.

The iterative filtering method proposed by Mi et al. (2011) and used by Hearst and Lavoie

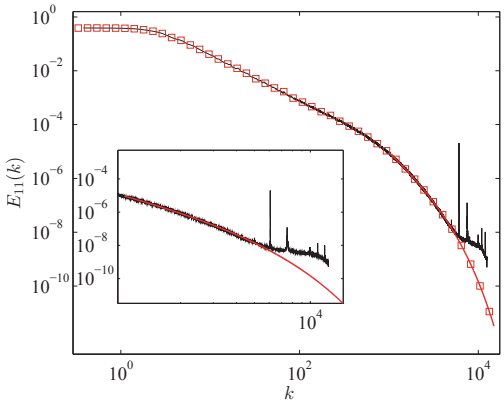

Figure 2.5: Re-sampled spectra (squares) after the extrapolation (red lines) from the Honda centerline data at $x/x_{peak} = 1.08$, $U_\infty = 10\,\mathrm{m/s}$.

(2014) was also tested. This method uses the Kolmogorov frequency f_η as a reference to check the selection of the cutoff frequency f_c, and recursively reduces f_c until the small scale properties such as η and f_η converge. The results, however, depend theoretically on the parameters of the filter, such that the filtered spectrum is always attenuated by the transfer function of the digital filter itself, and the converged results do not necessarily represent the true values of small scale properties. For these reasons, the extrapolation method is used to correct for the high frequency range of signals.

Finally, the results of different calculation methods at select locations are summarized in table 2.3. The uncertainties of the turbulence intensities calculated using the fluctuating velocity signals and corrected spectra are all well within $1\%U_\infty$ difference. The longitudinal integral length scales are computed by $L_u^+ = \pi E_{11}^+(0)/(2u'^2)$ (using the spectrum $E_{11}^+(k)$ corrected by the von Kármán spectrum model), and $L_u^* = \pi E_{11}^*(0)/(2u'^2)$ (using the spectrum $E_{11}^*(k)$ corrected by the G-function model), and their differences are within approximately 5%. However, there is always an underestimation by the von Kármán spectrum model, which is in agreement with the discussions found in Wilson (1998).

To estimate the dissipation rate, we first calculated both $\tilde{\epsilon}_{iso} = 15\nu\overline{(du/dx)^2}$ and $\epsilon_{iso}^* = 15\nu \int k^2 E_{11}^*(k)dk$ using the isotropic assumption, where $E_{11}^*(k)$ is the spectrum corrected by the G-function model. It is noticed that ϵ_{iso}^* is always larger than $\tilde{\epsilon}_{iso}$, which comes

Data set	Honda		Lille			3×3			Valente11
x/x_{peak}	1	1.54	1	1.65	2.73	1	1.48	2.62	1.04
U_∞(m/s)	10	10	9	9	9	10	10	10	15
$\tilde{u'}/U_\infty$	0.152	0.118	0.167	0.111	0.073	0.149	0.121	0.080	0.053
u'^*/U_∞	0.145	0.117	0.166	0.110	0.072	0.149	0.121	0.079	–
L_u^+(m)	0.26	0.23	0.19	0.18	0.22	0.08	0.08	0.10	0.05
L_u^*(m)	0.30	0.26	0.20	0.19	0.23	0.08	0.08	0.10	–
$\tilde{\eta}$(mm)	0.17	0.19	0.16	0.19	0.25	0.12	0.14	0.18	0.15
η^*(mm)	0.17	0.19	0.14	0.18	0.24	0.12	0.13	0.18	–
$\tilde{\lambda}$(mm)	11.5	10.9	9.6	9.0	10.2	5.8	5.7	6.9	4.8
λ^*(mm)	10.6	10.3	7.8	8.0	9.6	5.4	5.4	6.5	–
$\tilde{Re_\lambda}$	1161	849	949	593	443	570	458	364	253
Re_λ^*	1015	802	773	522	414	532	431	341	–
$\tilde{\epsilon}_{iso}(\mathrm{m^2\,s^{-3}})$	3.9	2.7	5.6	2.8	0.9	15.1	10.1	3.0	6
$\tilde{\epsilon}_{XW}(\mathrm{m^2\,s^{-3}})$	–	–	–	–	–	9.2	6.2	1.9	4.7
$\epsilon_{iso}^*(\mathrm{m^2\,s^{-3}})$	4.6	2.9	8.3	3.5	1.0	17.3	11.3	3.3	–
$\epsilon_{XW}^*(\mathrm{m^2\,s^{-3}})$	–	–	–	–	–	10.5	7.0	2.1	–

Table 2.3: Comparison of turbulence characteristics in different experiments along the centerline using different methods. The integral length scale are calculated as $L_u^+ = \pi E_{11}^+(0)/(2u'^2)$ and $L_u^* = \pi E_{11}^*(0)/(2u'^2)$, where the superscript $+$ and $*$ indicates the use of the von Kármán spectrum model and the G-function model, respectively. The Taylor microscale $\tilde{\lambda}$ is calculated by $\lambda = u'/\sqrt{\overline{(du/dx)^2}}$, where the velocity gradient is calculated from the filtered fluctuating velocity signal, and the velocity gradient $\overline{(du/dx)^2}$ for λ^* is calculated by integrating the G-model corrected spectrum. The dissipation is calculated as $\epsilon_{iso} = 15\nu\overline{(du/dx)^2}$, and $\epsilon_{XW} = 3\nu\overline{(du/dx)^2} + 6\nu\overline{(dv/dx)^2}$. Quantities with tilde hat are calculated directly from the filtered fluctuating velocity samples. Quantities with superscript $*$ are calculated by integrating the G-function model corrected spectrum such that $\overline{(du/dx)^2} = \int k^2 E_{11}^*(k)dk$, and $\overline{(dv/dx)^2} = \int k^2 E_{22}^*(k)dk$, where $E_{11}^*(k)$ and $E_{22}^*(k)$ are calculated by assuming the Taylor hypothesis for the instantaneous u, v velocity, respectively, with the local convection velocity equals to the local mean streamwise velocity U. The last column is reproduced from Valente and Vassilicos (2011) for comparison.

from the filtering of the signal and extrapolation method discussed above. For the Honda and 3×3 experiments, the results exhibit deviations of $\pm4\%$ to $\pm7\%$ from the mean value, and the difference between $\tilde{\epsilon}_{iso}$ and ϵ^*_{iso} decreases with downstream distance for all cases.

For the Lille experiment, however, this discrepancy is $\pm19\%$ at $x/x_{peak} = 1$, and decreases to $\pm6\%$ at $x/x_{peak} = 2.73$. This large error comes partly from the lower sampling frequency $f_s = 50\,\mathrm{kHz}$ (due to hardware limitation), versus $f_s = 125\,\mathrm{kHz}$ for the other two experiments, such that the higher frequency components are less well-resolved. The filtering method proposed by Mi et al. (2011) is also tested, and it gives a smaller value, e.g. $\epsilon^*_{iso} = 6.845\,\mathrm{m^2\,s^{-3}}$ at $x/x_{peak} = 1$ in the Lille experiment, due to the attenuation in the higher frequency range, which makes the discrepancy seem smaller between $\tilde{\epsilon}_{iso}$ and ϵ^*_{iso}. But as discussed before, the result may not be trustworthy. For these reasons, the corrected spectra using the extrapolation method are used to calculate the small scale properties for the Lille experiment.

Another issue is the validity of the isotropic assumption used in calculating the dissipation rates. Comparisons are made between ϵ_{iso} and $\epsilon_{_{XW}} = 3\nu\overline{(du/dx)^2} + 6\nu\overline{(dv/dx)^2}$ from the 3×3 experiments. To calculate the dissipation rate $\epsilon^*_{_{XW}}$ from the spectrum, it is assumed that $\overline{(du/dx)^2} = \int k^2 E^*_{11}(k)dk$, and $\overline{(dv/dx)^2} = \int k^2 E^*_{22}(k)dk$, where $E^*_{11}(k)$ and $E^*_{22}(k)$ are calculated by assuming the Taylor hypothesis for the instantaneous u, v velocity, respectively, with the local convection velocity equals to the local mean streamwise velocity U. It seems that the isotropy assumption in both methods causes an overestimation of the values of ϵ_{iso}, and the difference is roughly $\pm24\%$ at $x/x_{peak} = 1$, whereas Valente and Vassilicos (2011) give a $\pm12\%$ difference for the square fractal grid at $x/x_{peak} = 1.04$. Note, however, the value of $\epsilon_{_{XW}}$ might be underestimated for cross wires since the 1 mm separation of the two wires is approximately 10η (see Valente and Vassilicos, 2011). The isotropy assumption is further discussed in section 2.2.4.

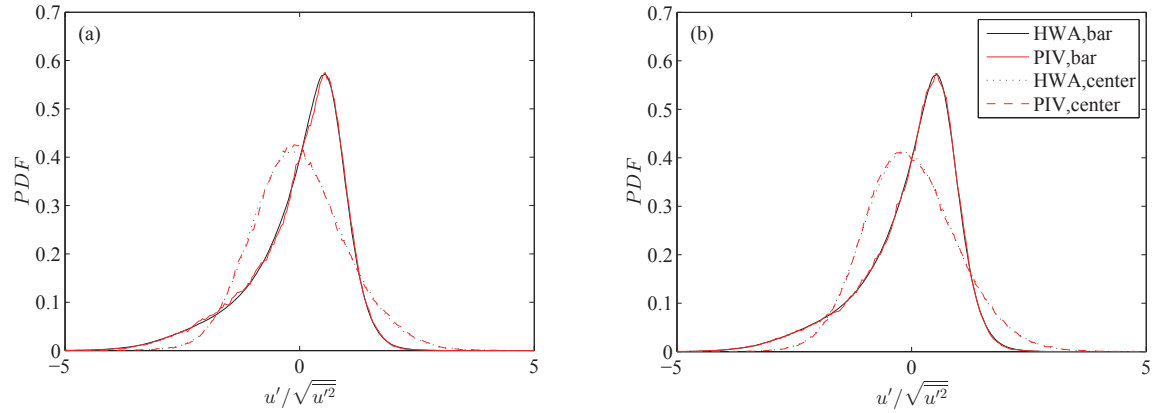

Figure 2.6: Probability density function of u' at $x/x_{peak} = 1$ on the centerline and behind the bar, from the Lille experiments, with $U_\infty = 9\,\mathrm{m/s}$ for (a) small FOV, and (b) large FOV cases.

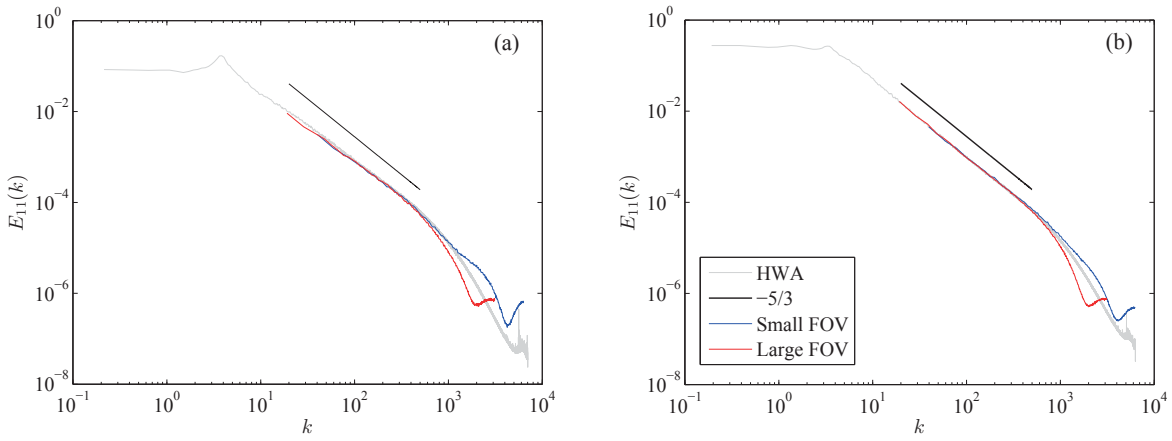

Figure 2.7: Spectrum comparison at $x/x_{peak} = 1$ on the centerline, from the Lille experiments, with $U_\infty = 9\,\mathrm{m/s}$ for small and large FOV PIV cases with HWA result at (a) behind the bar, and (b) on the centerline.

PIV processing

During the PIV processing, a self-calibration similar to that proposed by Wieneke (2005) was performed to establish the mapping function. Four passes were used starting with an interrogation window of size 64×64 pixels, then 32×48 pixels, then 26×32 pixels for two times. The overlap was 70% for all passes. The final interrogation window size is 1.65 mm for the small FOV, and 3.3 mm for the large FOV.

Probability density functions (pdfs) from PIV results are compared with the hot-wire

data in figure 2.6. It can be observed that the PIV results collapse well with the hot-wire measurements. Small discrepancies at the large scale end are observed for the case behind the horizontal bar. The spectra are also computed from the PIV results at the center of each FOV, as shown in figure 2.7, to compare with the HWA data. The small scales of the PIV spectra show the limit of resolution, which is expected, but they agree well in the inertial subrange of the spectra with a clear $-5/3$ slope. This also validates the use of Taylor's hypothesis in the hot-wire data processing.

The uncertainty for the PIV comes from several aspects. According to Westerweel et al. (1997), the interrogation error of a 2D vector field is typically $\sigma_0 \approx 0.1\,\text{px}$. For the current set-up with cameras aligned 45° to the measurement plane, the error carried on to the reconstructed 3C vector field can be estimated as $\sigma(\Delta x) \approx M\sigma_0$, $\sigma(\Delta y) \approx 1/\sqrt{2}M\sigma_0$, $\sigma(\Delta z) \approx M\sigma_0$, where M is the magnification $M = f/(f - d_o)$ with the lens focal length f, and the distance between the lens to the object d_o (van Doorne and Westerweel, 2007). For the large FOV, these values are calculated to be $\sigma(\Delta x) = \sigma(\Delta z) \approx 0.01\,\text{px}$, and $\sigma(\Delta y) \approx 0.007\,\text{px}$, while for the small FOV these values are estimated as $\sigma(\Delta x) = \sigma(\Delta z) \approx 0.02\,\text{px}$, and $\sigma(\Delta y) \approx 0.014\,\text{px}$. The y component bears the smallest error because it is an average of the two cameras. Comparing to a general displacement of approximately 8 px of individual particles, the interrogation error seems negligible.

The sampling uncertainty of the mean velocities can be evaluated as $\sigma = \pm 1.96S/\sqrt{N_s}$, where S is the standard deviation of the velocity fluctuation, and $N_s = 20000$ is the total number of samples. The errors for each component are given in table 2.4 for the $U_\infty = 9\,\text{m/s}$ case on the centerline. The results suggest the sampling uncertainties are all small, and the value of y component appears to be the smallest, which agrees with the discussions above.

Finally, the mean statistics calculated from PIV and HWA at the same location are compared together in figure 2.8. Discrepancies of approximately 3% are observed for the mean velocity, and 1% for the turbulence intensity. Note that the free stream velocity

	σ_u/u' (%)	σ_v/u' (%)	σ_w/u' (%)
Large FOV	1.37	1.05	1.21
Small FOV	1.39	0.97	1.16

Table 2.4: Estimated sampling error for PIV measurements at $U_\infty = 9\,\mathrm{m/s}$.

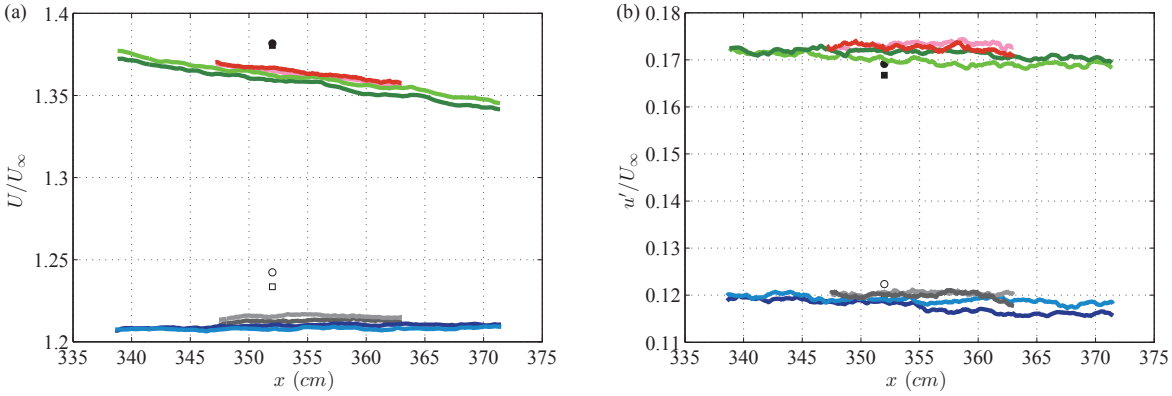

Figure 2.8: (a) Mean velocities and (b) turbulence intensities from PIV (lines) and HWA (symbols) results along the centerline (green and red lines), and behind the bar (blue and purple lines).

during the PIV measurement is not monitored during acquisition (for HWA measurements, it is monitored to be within $\pm 0.5\% U_\infty$), so the 3% error seems reasonable.

2.2 Results

In this section the results are presented in the following order. First of all, the Reynolds number effect is checked using the Honda data. Then the streamwise evolution of turbulence statistics are examined using the wake interaction length scale, followed by discussions on the evolution of various length scales and flow homogeneity and isotropy. The PIV data is used to look at the vortical structures of the flow at the turbulence peak location $x/x_{peak} = 1$. Finally, the non-equilibrium scaling relation is presented.

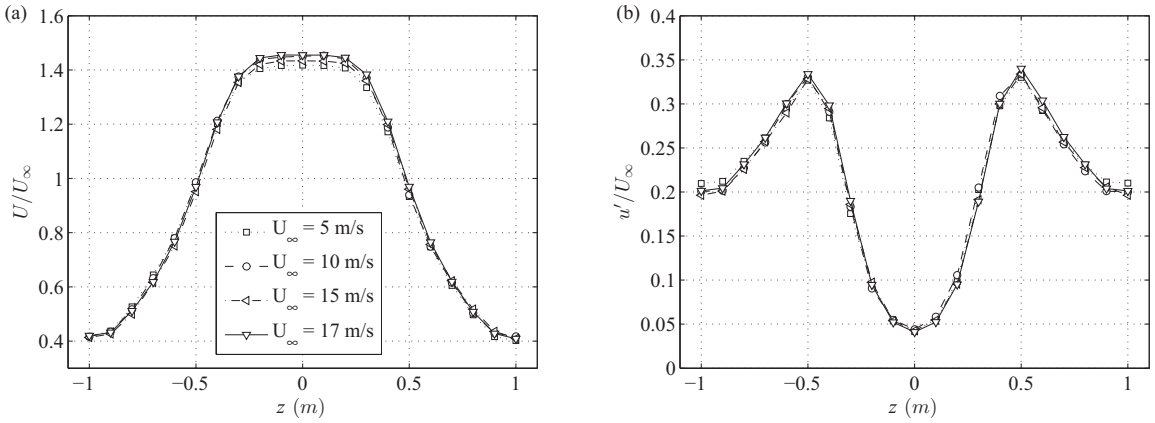

Figure 2.9: Transverse profiles of (a) mean velocity, and (b) turbulence intensity from the Honda experiments, at different inlet velocities U_∞ at $x/x_{peak} = 0.38$, $z = 0\,\mathrm{m}$.

2.2.1 Reynolds number effect

To study the Reynolds number effect of the turbulence wake, the flow is probed across the span at $x = 2\,\mathrm{m}$ (or $x/x_{peak} = 0.38$) $y = 0\,\mathrm{m}$ to see if there are any differences in the wake separation for different inlet Reynolds number $Re_0 = U_\infty L_{0y}/\nu = 6.5 \times 10^5$ to 1.9×10^6. Figure 2.9 gives the results for mean velocity and turbulence intensity at $U_\infty = 5, 10, 15, 17\,\mathrm{m\,s^{-1}}$. It is obvious that the normalization by inlet velocity U_∞ collapses both mean velocity and turbulence intensity profiles. This suggests that the separation, and consequently the shape of the wake is independent of the inlet Reynolds number Re_0.

2.2.2 Wake interaction length scales

The wake interaction length scale x_*^{peak1} was originally introduced by Gomes-Fernandes et al. (2012) to characterize the location where the wakes generated by the largest grid bars meet, and this length scale successfully collapsed turbulence intensity profiles from several experiments with FSG. It is defined as $x_*^{peak} = 0.21L_0^2/(\alpha C_d t_0)$, which incorporates

[1]The notation x_*^{peak} is taken after Gomes-Fernandes et al. (2012) for consistency. In the original paper this wake interaction length scale physically gives the turbulence intensity peak location x_{peak} such that $x_{peak} = x_*^{peak}$, but this is not the case for the current study, as the actual turbulence intensity peak location is further downstream such that $x_{peak} > x_*^{peak}$. One should not confuse with the actual turbulence intensity peak location x_{peak}.

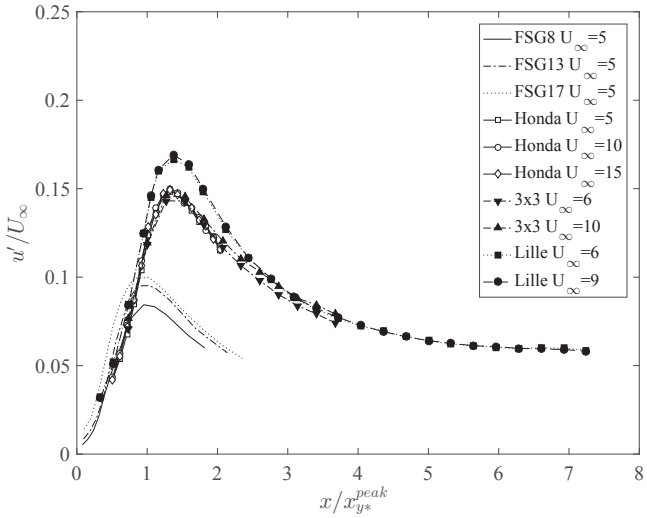

Figure 2.10: Turbulence intensity profiles at centerline versus x/x_{y*}^{peak} from all experiments. FSG data reproduced from Mazellier and Vassilicos (2010).

the incoming flow turbulence condition via α, the length L_0, the width t_0, and the drag coefficient C_D of the largest grid element. Since the RFG consist of two distinct large scales, the wake interaction length-scale can be calculated in either direction, as shown in table 2.2. For the current discussion, x_{z*}^{peak} is used to normalize the streamwise development as it is assumed that the largest vertical bars generate most of the turbulent energy. The result is shown in figure 2.10 together with profiles reproduced from Mazellier and Vassilicos (2010) at $U_\infty = 5.2\,\mathrm{m/s}$.

The length scale x_{z*}^{peak} fails to collapse the data from FSGs and RFGs. All of the turbulence intensity profiles from Mazellier and Vassilicos (2010) peak at $x/x_*^{peak} = 1$ as previously shown. But for the RFGs, this peak location is at $x/x_{z*}^{peak} = 1.40$, which corresponds to $x/x_{y*}^{peak} = 1.53$.

This discrepancy can be explained by a review of the scaling proposed by Gomes-Fernandes et al. (2012), who followed the results from Symes and Fink (1977) to derive their scaling for the evolution of the wake half width and intensity. The effect of the free stream turbulence was studied, as reproduced in figure 2.11, and was characterized by the constant

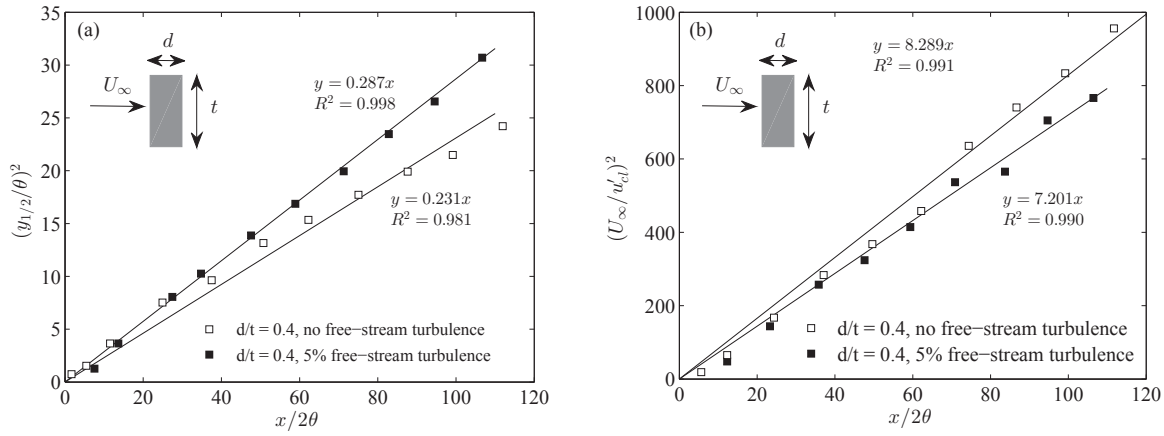

Figure 2.11: Influence of external turbulence on the development of (a) wake half-width, and (b) turbulence intensity. Reproduced after Symes and Fink (1977).

coefficients α and β as in

$$\left(\frac{y_{1/2}}{\theta}\right)^2 = \alpha\frac{x}{2\theta}, \left(\frac{U_\infty}{u'_{cl}}\right)^2 = \beta\frac{x}{2\theta}, \tag{2.3}$$

where $y_{1/2}$ is the wake half width, θ is the momentum thickness, and u'_{cl} is the turbulence intensity at the centerline of the wake. The parameters α and β are functions of the free stream turbulence intensity and were used by Gomes-Fernandes et al. (2012) in their derivation of $x^{'}_{*} = L_0^2/(\alpha C_D t_0)$ assuming that $L_0 = 2y_{1/2}$ and $2\theta = C_D t_0$. The final definition of $x^{peak}_{*} = \phi x^{'}_{*}$ incorporates a constant $\phi = 0.21$ to scale the peak turbulence intensity at $x/x^{peak}_{*} = 1$, and the value was chosen empirically based on results from Mazellier and Vassilicos (2010).

The free stream turbulence is not the only factor that affects the streamwise development of the wake. This is in agreement with the discussions made by Wygnanski et al. (1986), where they showed the effect of different initial conditions on the spreading rate of different types of wakes. Since u'_{cl} is defined in relation with the wake half width $y_{1/2}$, it also suggests a dependency of u'_{cl} on the initial conditions. George (1989) also commented that the spreading rate of the plane wake depends on initial conditions. The value of $\phi = 0.21$ seems to characterize this effect for the FSGs, but not necessarily for other

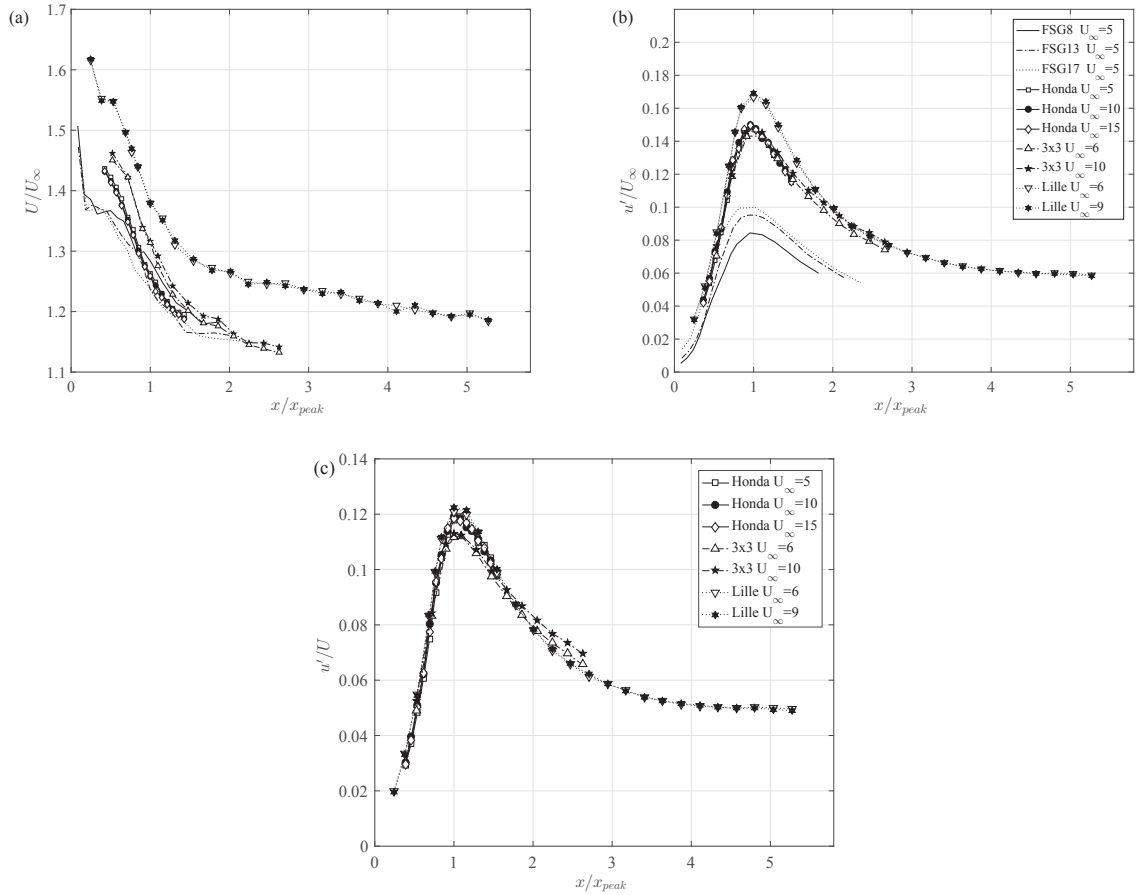

Figure 2.12: (a) Mean streamwise velocity profiles normalized by U_∞, (b) turbulence intensity profiles normalized by U_∞, and (c) turbulence intensity profiles normalized by local mean velocity U along the centerline against x/x_{peak} from all experiments. The data from fractal square grids (FSG) is reproduced from Mazellier and Vassilicos (2010).

fractal-like grids once the geometry is changed, as suggested by the RFG results.

In fact, Zhou et al. (2014) studied the streamwise evolution of the turbulence intensity behind a FSG and a single square grid (or SSG), which consists of only the first iteration of the fractal grid, and they showed a clear discrepancy between the peak locations x_{peak} of their results. It was noted that the blockage ratio of the two grids studied by Zhou et al. (2014) was $\sigma_{FSG} = 36\%$ and $\sigma_{SSG} = 11\%$, respectively.

The reason for such discrepancies lies most likely in the geometry of the grid. Firstly, the spreading rate varies by a scale factor related to the normalized centerline mean velocity U_c/U_∞ on the grid plane due to the effect of the local shear. Secondly, there

are two distinctive wake interaction length-scales in the flow, and the wakes from both sides interact and modify the actual turbulence peak location. This modification cannot be quantified at the moment, so the measured physical turbulence peak location x_{peak} is used henceforth to normalize the streamwise distance. Again, one should not confuse x_*^{peak} with x_{peak}.

The streamwise mean velocity and turbulence intensity profiles for all experiments are given in figure 2.12. The mean profiles collapse well except for the Lille experiments, where both the mean velocity and turbulence intensity are notably higher. The difference in the mean velocity might be explained by the different measurement methods of U_∞. A Pitot tube is used in the Lille experiments (roughly 10 cm off the centerline and 20 cm upstream of the grid), and wall pressure across the contraction is used in the other two experiments, as described in section 2.1.1. Therefore, the exact incoming velocity U_∞ is slightly different due to the inhomogeneous grid geometry. This effect is also seen in the turbulence intensity, which is normalized as u'/U_∞. In fact, when the turbulence intensity is normalized with the local mean velocity U, the collapse from all experiments clearly improves (figure 2.12 c). The discrepancies are within 1%, which supports the discussion above.

2.2.3 Length scales

Integral length scales

The length scales of the RFG-generated turbulence are of interest. Previously, it has been shown that the longitudinal integral length scale L_u ($L_u = L_{uu,x}$ is the streamwise integral length scale of fluctuating velocity u) in the FSG-generated turbulence has a magnitude roughly comparable to $0.2L_0$ in the decay region, i.e. $x/x_{peak} > 1$, where L_0 is the length of the largest grid bar, and that the ratio of L_u/λ remains roughly constant in the non-equilibrium decay region (Mazellier and Vassilicos, 2010; Gomes-Fernandes et al., 2012;

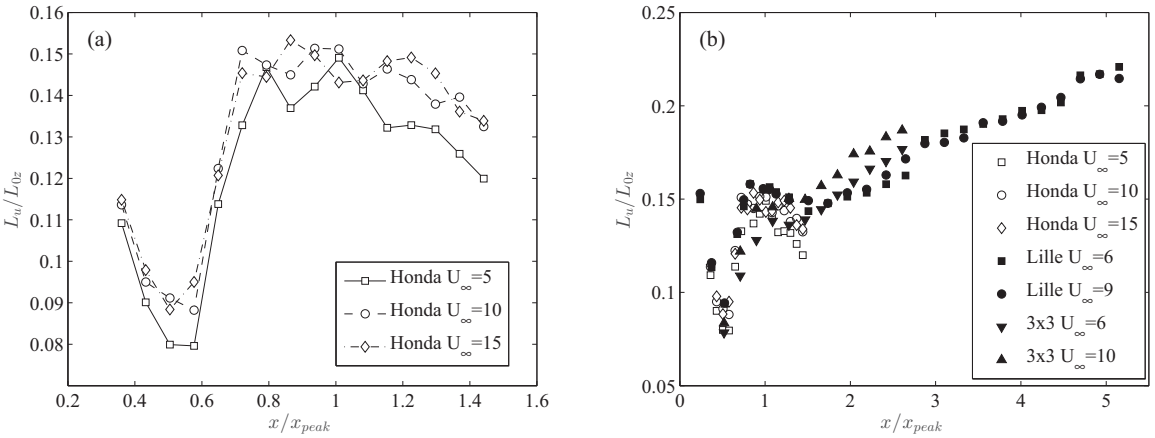

Figure 2.13: Longitudinal integral length scale profiles L_u/L_{0z} along the centerline from (a) the Honda experiment, and (b) all three experiments.

Hearst and Lavoie, 2014).

The integral length scale L_u measured from the Honda experiments is given in figure 2.13 (a), where the length scale L_u/L_{0z} appears to decrease in the decay region from $x/x_{peak} = 1$ to 1.5. This is surprising as the integral length scale is expected to grow in decaying turbulence. However, results from the 3×3 and Lille experiments (figure 2.13 b) revealed that this decrease exists only in the beginning of the decay region. The value of L_u increases monotonically after $x/x_{peak} = 1.5$.

Note that L_u in figure 2.13 is normalized as L_0/L_{0z}, and this ratio is doubled if L_0/L_{0y} is used. The average values of L_u/L_{0z} and L_u/L_{0y} in the region from $x/x_{peak} = 1$ to 1.5 are 0.14 and 0.28 respectively. This ratio has been previously reported as $L_u/L_0 \approx 0.2$ in the FSG generated turbulence (Mazellier and Vassilicos, 2010). If the FSG were to fit in the rectangular wind tunnel, the longest bar length L_0 would be equivalent to the L_{0y} of RFG. Therefore, the rectangular fractal geometry seems to have extended the integral length scale as expected in the design.

The streamwise profiles of L_u with y offsets are shown in figure 2.14. The Honda case shows the streamwise profile at $y = 0.33\,\mathrm{m}$, which is approximately at the height of the smallest grid bars closest to the center. It seems that the value of L_u decreases slightly

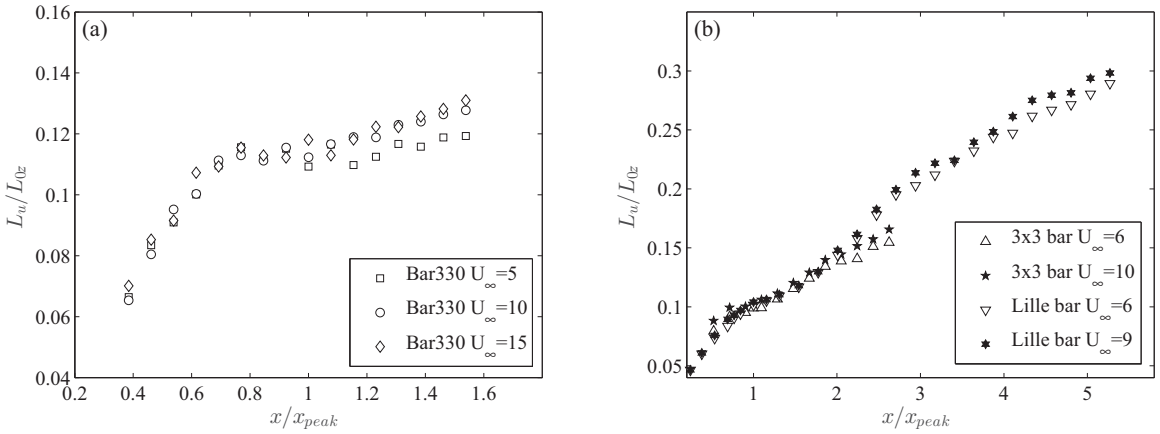

Figure 2.14: Longitudinal integral length scale profiles L_u/L_{0z}, (a) from the Honda experiment along the streamwise direction at $y = 0.33\,\mathrm{m}$, and (b) from the 3×3 and Lille experiments behind the horizontal bar.

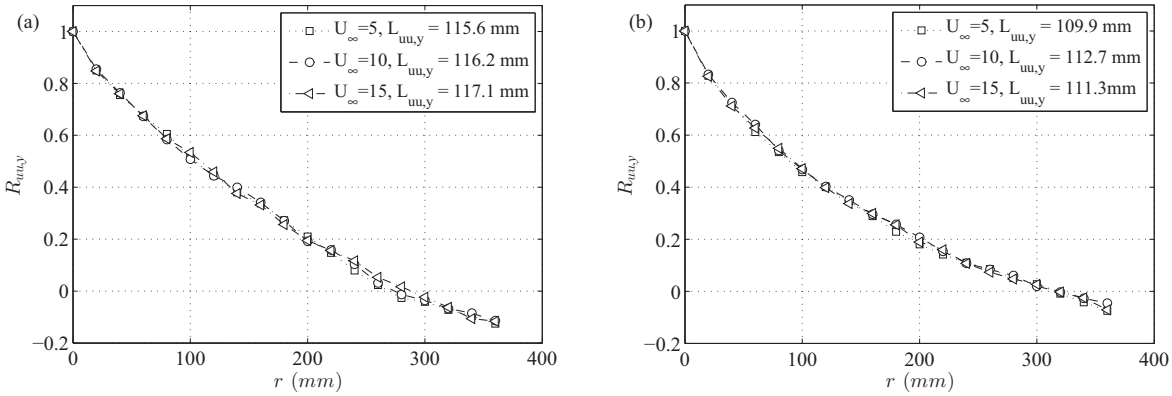

Figure 2.15: Two-point correlation functions $R_{uu,y}$ for different inlet velocities U_∞ in the Honda experiments with fixed wire at (a) $x/x_{peak} = 1.15$ ($x = 6\,\mathrm{m}$), and (b) $x/x_{peak} = 1.54$ ($x = 8\,\mathrm{m}$) on the centerline.

in the region from $x/x_{peak} = 0.8$ to 1 before monotonically increasing afterward. All of the profiles behind horizontal bars from the 3×3 and Lille experiments in figure 2.14 (b) show a monotonic increase throughout the measurement domain. The increasing rate seems perhaps reduced slightly in the region of $0.8 < x/x_{peak} < 1.5$, which is recovered at $x/x_{peak} = 2$.

To confirm the decrease of integral length scale in the region $1 < x/x_{peak} < 1.5$, two-point correlations are also measured at $x = 6\,\mathrm{m}$ and $8\,\mathrm{m}$, or $x/x_{peak} = 1.15$ and 1.54 in the Honda experiments. The correlation coefficients are given in figure 2.15. The values

of $L_{uu,y}$ are calculated by integrating up to the first zero-crossing point, which shows a decrease in their values from $L_{uu,y} \approx 116\,\text{mm}$ at $x/x_{peak} = 1.15$ to $L_{uu,y} \approx 111\,\text{mm}$ at $x/x_{peak} = 1.54$. This supports our discussion of the decreasing integral length scale L_u in the beginning of the decay region.

Taylor microscales

The evolution of the Taylor microscale is given in figure 2.16 for each experiment with streamwise profiles along the centerline and along the streamwise direction with y offset. The Taylor microscale λ is calculated by $\lambda = u'/\sqrt{\overline{(du/dx)^2}}$, where the velocity gradient is calculated by integrating the G-model corrected spectrum assuming Taylor's hypothesis. It shows a similar trend to the integral length scales, where their values decrease in the region of $x/x_{peak} = 1$ to 1.5 along the centerline, and grow monotonically elsewhere. The Taylor microscale also shows a dependency on the Reynolds number Re_0. The value of λ at two y locations becomes similar after approximately $x/x_{peak} = 1.8$.

We now follow Mazellier and Vassilicos (2010) and Gomes-Fernandes et al. (2012) by plotting $\lambda/(\nu x_{peak}/U_\infty)^{1/2}$ as a function of x/x_{peak} in figure 2.17. The normalized data does not collapse well. The values of λ are roughly constant in the region of $1 < x/x_{peak} < 1.5$, before monotonically increasing afterwards. These observations agree with the results of Gomes-Fernandes et al. (2012), where their normalized Taylor micro scale λ stays roughly constant in the range $0.9 < x/x_{peak} < 1.3$. It is also interesting to note that λ grows proportionally to x for $x/x_{peak} \geq 2$ and that $\lambda/(\nu x_{peak}/U_\infty)^{1/2} \propto x/x_{peak}$ collapses the Lille data in this streamwise range. The collapse is not so good for the 3×3 data where the local Re_λ is lower and presumably not high enough for the $(\nu x_{peak}/U_\infty)^{1/2}$ dependence to collapse the data. This collapse is related to the non-equilibrium dissipation scaling discussed in section 3.5 which was found by Goto and Vassilicos (2015, 2016a,b) to be valid for high enough values of Re_λ.

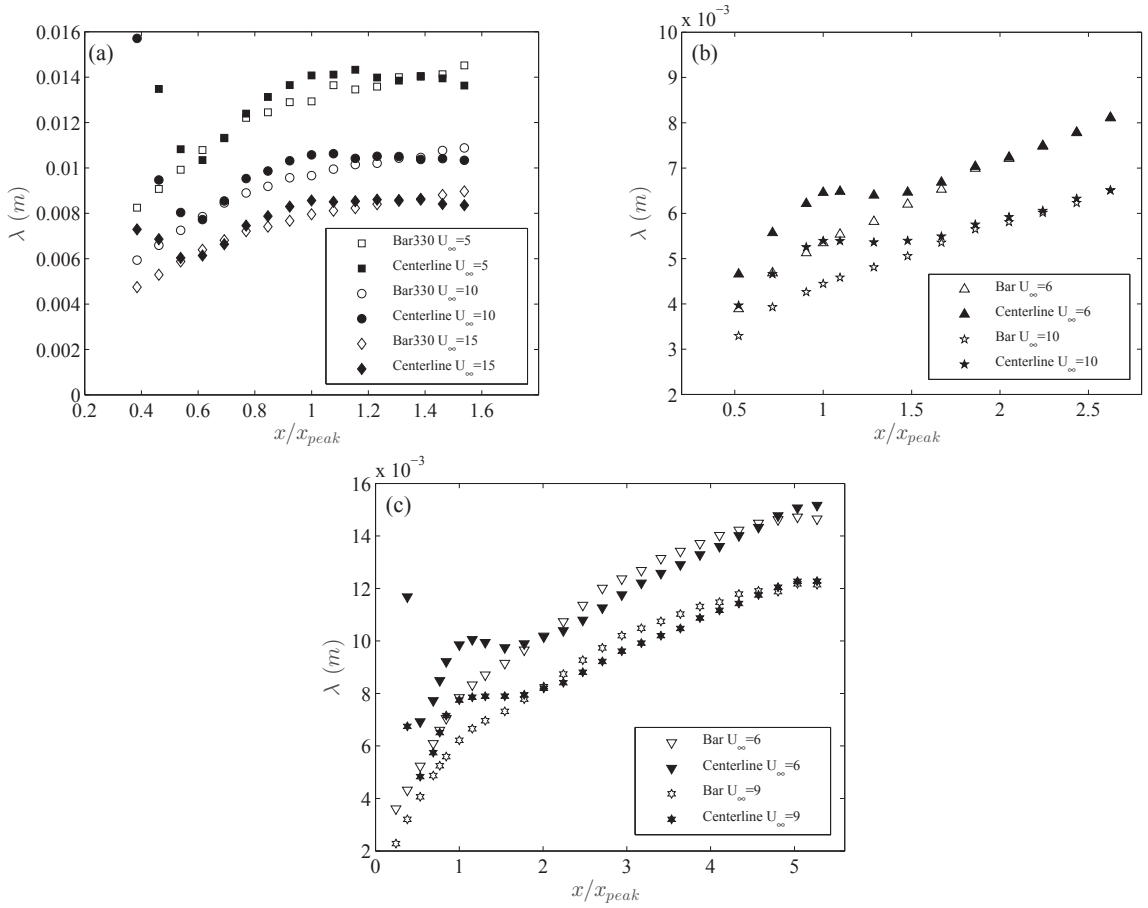

Figure 2.16: Streamwise profiles of the Taylor microscale λ from (a) Honda experiments, (b) 3×3 experiments, and (c) Lille experiments.

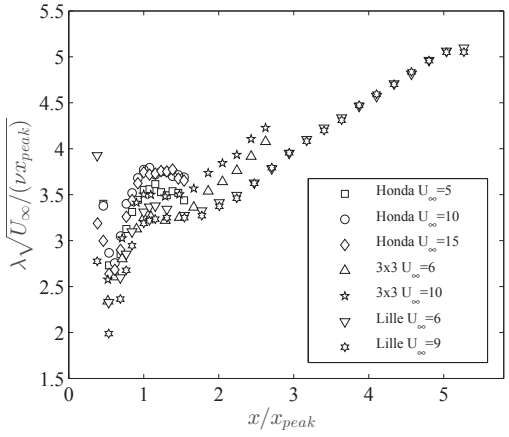

Figure 2.17: Taylor microscale λ, normalized by $(\nu x_{peak}/U_\infty)^{1/2}$, as a function of x/x_{peak} along the centerline from three experiments.

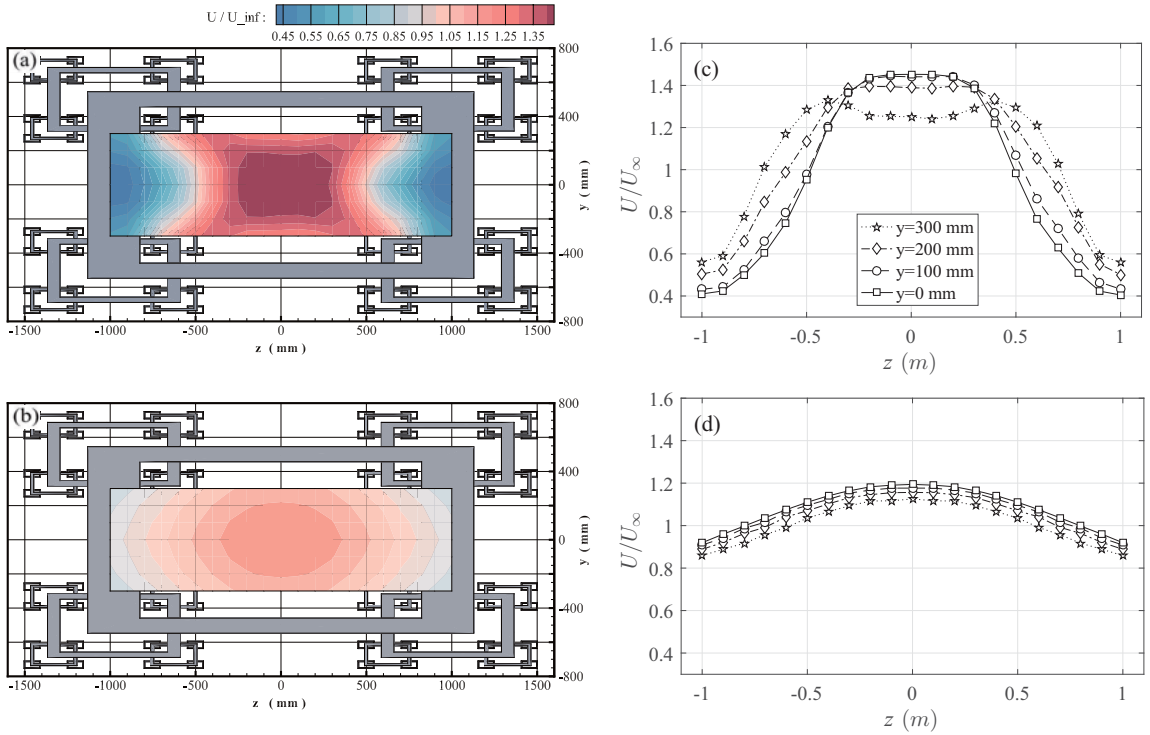

Figure 2.18: Contours of U/U_∞ at $x/x_{peak} = 0.38$ (a), and $x/x_{peak} = 1.54$ (b) at $U_\infty = 10\,\mathrm{m/s}$ From the Honda experiments. Contour plots (a) and (b) are assembled from (c) and (d), respectively.

2.2.4 Homogeneity, isotropy and Gaussianity

Homogeneity

The homogeneity of the RFG-generated turbulent flow is assessed first using the mean statistics from the Honda wind tunnel experiments. The transverse profiles at different y locations and the two-dimensional assembly contours are given in figure 2.18 and 2.19.

At $x = 2\,\mathrm{m}$ ($x/x_{peak} = 0.38$), the mean velocity contour was plotted assuming z symmetry of the flow, and it suggests that there is a rectangular jet-like structure in the middle of the grid with higher mean velocities. The shape of the wake of the largest bars is altered by the small grids in the corners. In figure 2.18 (c), the mean velocity profile at $y = 300\,\mathrm{mm}$ appears different. This difference is attributed to the presence of the smaller grids and the horizontal bar.

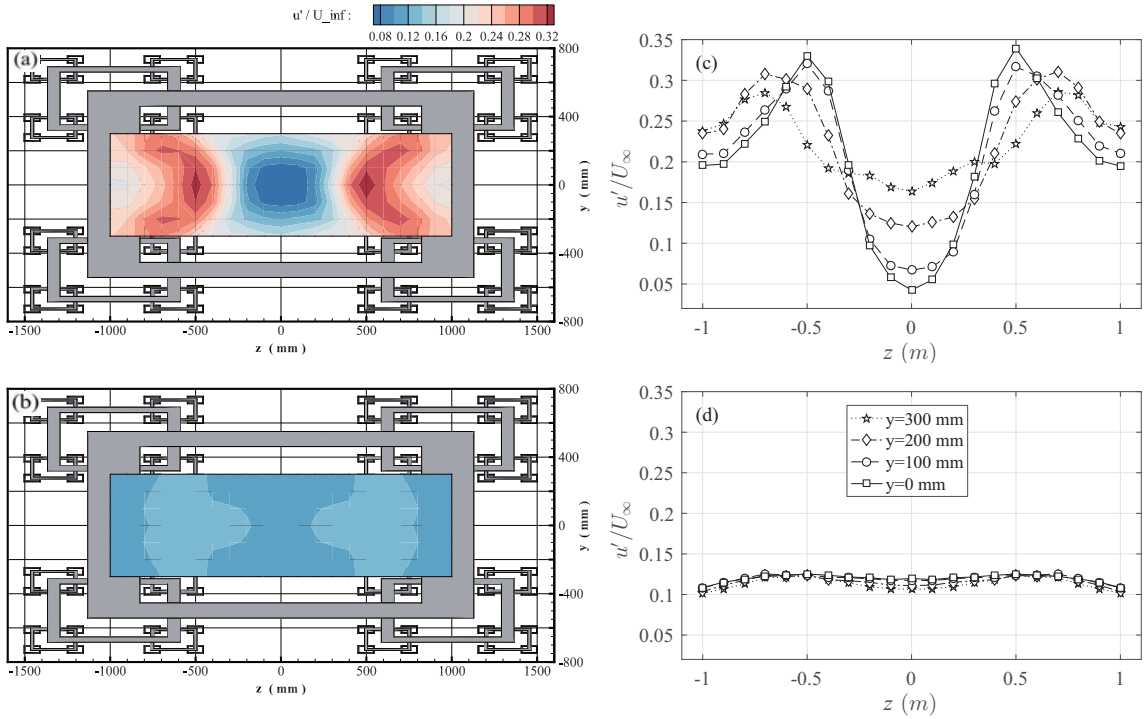

Figure 2.19: Contours of u'/U_∞ at $x/x_{peak} = 0.38$ (a), and $x/x_{peak} = 1.54$ (b) at $U_\infty = 10\,\mathrm{m/s}$ From the Honda experiments. Contour plots (a) and (b) are assembled from (c) and (d), respectively.

At $x = 8\,\mathrm{m}$ ($x/x_{peak} = 1.54$), the flow was measured across half of the span and symmetry was assumed in both y and z directions to produce figure 2.18 (b). The variations are much reduced, which suggests that the flow is approaching a homogeneous state. The velocity contour in figure 2.18 (b) show an oval shape at $x/x_{peak} = 1.54$, in contrast to the rectangular shape at $x/x_{peak} = 0.38$. This is different from the FSG results where axisymmetric shapes are observed in the decay region (Zhou et al., 2014; Laizet et al., 2015).

The turbulence intensity profiles and the assembled contours are given in figure 2.19. The turbulence intensity has its minimum near the centerline, and it peaks just off the side of the biggest bars, where the gradient of the mean velocity is largest as seen in figure 2.18. This peak location moves aside with increasing height corresponding to the shape of the wake, which is altered by the smaller grids. In general, the turbulence intensity profiles becomes more homogeneous with increasing y, which seems to support the idea

that the smaller grids tend to homogenize the flow. At $x/x_{peak} = 1.54$, the variation of u'/U_∞ across the span is reduced to approximately 3%, as shown in figure 2.19.

To further quantify the homogeneity in the streamwise direction, we refer to the criteria proposed by Corrsin (1963), namely

$$\partial L_u/\partial x \ll 1, \tag{2.4a}$$

$$(L_u/\lambda)\partial\lambda/\partial x \ll 1, \tag{2.4b}$$

$$(L_u/\overline{u^2})\partial\overline{u^2}/\partial x \ll 1. \tag{2.4c}$$

The results for relations 2.4 from all experiments are presented in figure 2.20. The values of $\partial L_u/\partial x$ and $(L_u/\lambda)\partial\lambda/\partial x$ are all approximately 0 in the decay region. The results for $(L_u/\overline{u^2})\partial\overline{u^2}/\partial x$, however, show a larger deviation from 0. The minimum appears to occur at $x/x_{peak} \approx 1.5$, which corresponds to the start of the growth of L_u in the decay region. The maximum deviation is approximately 0.075, which is larger than the reported value of 0.05 from the FSG generated turbulence (Hearst and Lavoie, 2014). The results along the streamwise direction with y offset are also given in figure 2.20, which appear similar to that along the centerline, and the most obvious deviation from homogeneity is observed in figure 2.20 (f). In previous figures 2.13 and 2.14, the length scales are shown to increase along the streamwise direction, which might seem to contradict figure 2.20 where the gradients are almost zero in the decay region. These results are in fact consistent with each other as the increase of the integral length scales L_u is indeed small, as presented in figure 2.21, where non-normalized integral length scale profiles from different cases are plotted. These results seem to suggest that the turbulence in the beginning of the decay region $1 < x/x_{peak} < 1.5$ is not strictly homogeneous, but the rest of the decay region can be considered homogeneous under the criteria of relations 2.4.

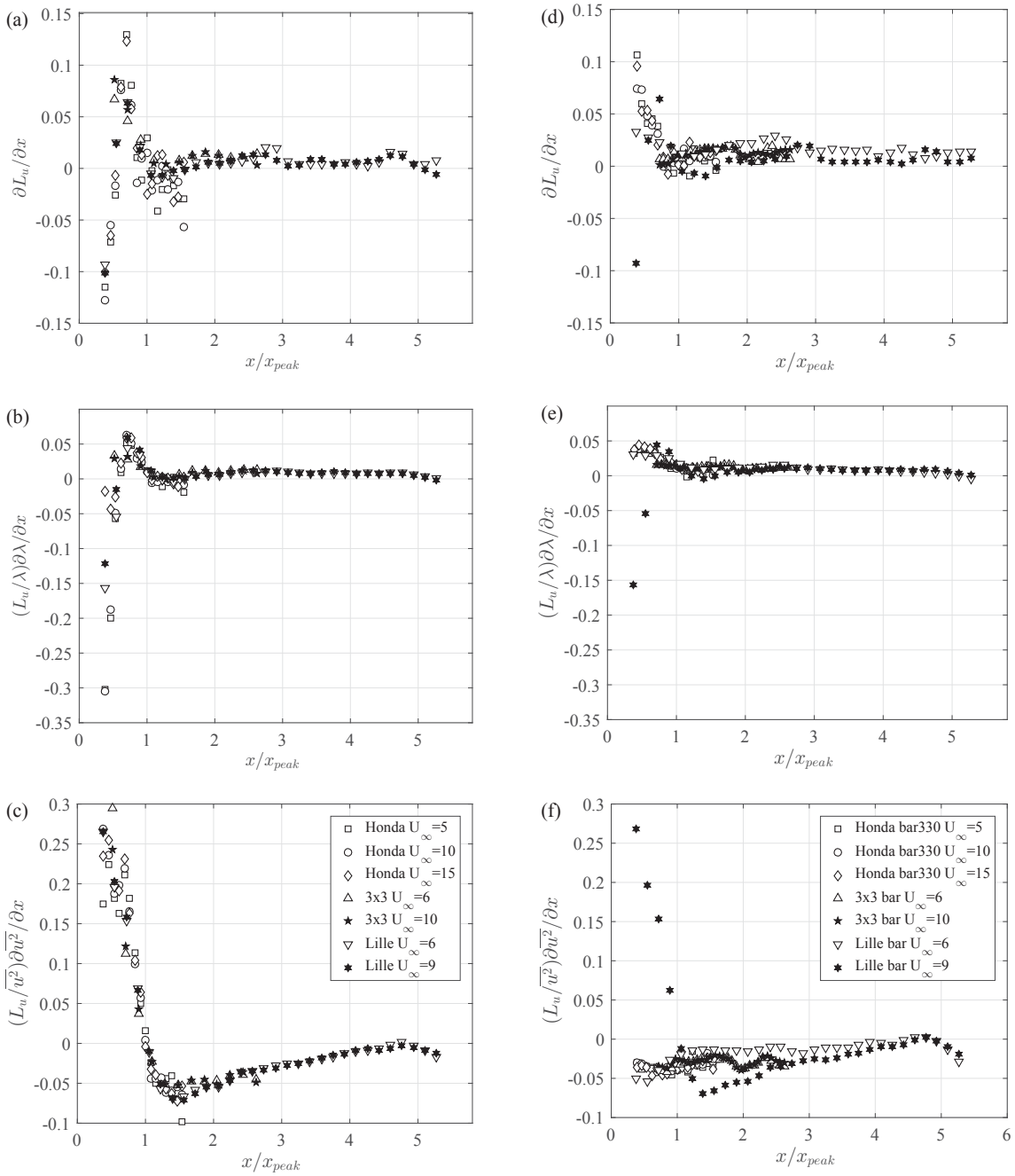

Figure 2.20: Streamwise homogeneity of (a, d) $\partial L_u/\partial x$, (b, e) $(L_u/\lambda)\partial\lambda/\partial x$, and (c, f) $(L_u/\overline{u^2})\partial\overline{u^2}/\partial x$ from three experiments along the centerline (left) and along the streamwise direction with y offset (right).

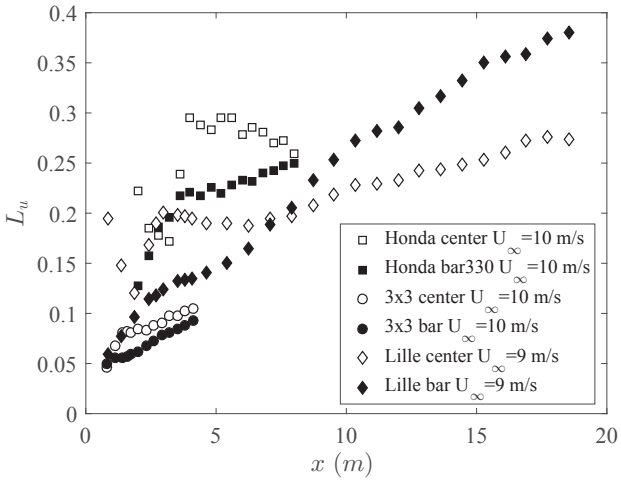

Figure 2.21: Longitudinal integral length scale profiles L_u from all experiments along the centerline and along streamwise direction with y offset.

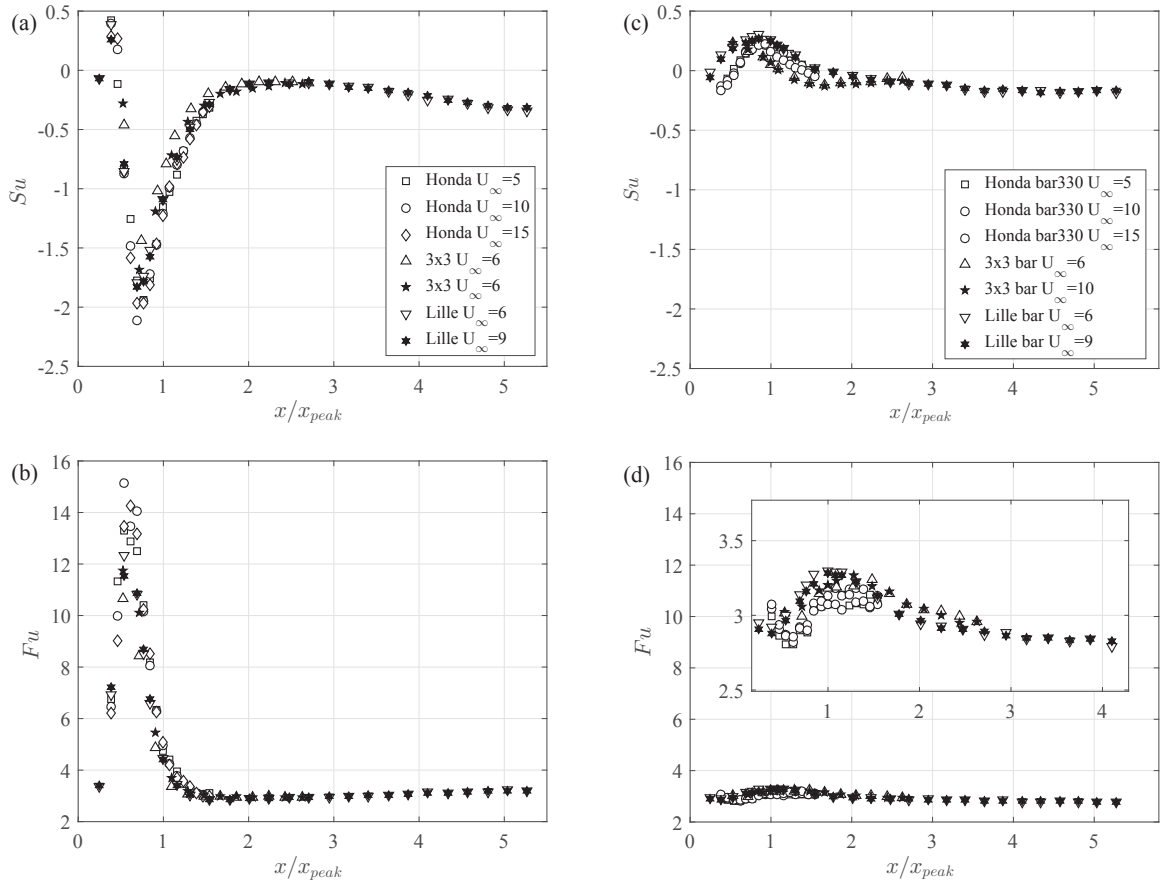

Figure 2.22: Profiles of (a, c) skewness, and (b, d) flatness along the centerline (left) and along the streamwise direction with y offset (right).

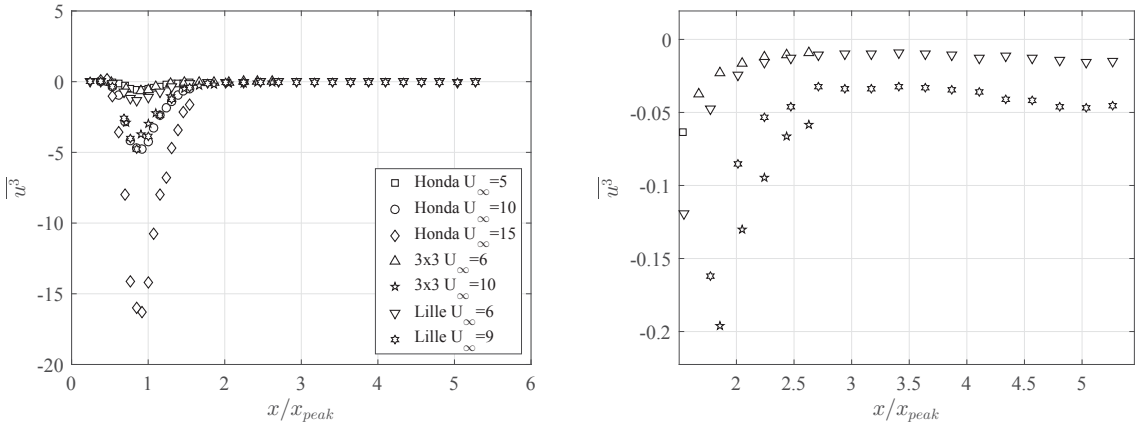

Figure 2.23: Profiles of $\overline{u^3}$ along the streamwise direction against x/x_{peak} for all experiments. The figure on the right is exactly the same data, only zoomed in over the range $x/x_{peak} > 2$.

Gaussianity

The skewness and flatness for different experiments are presented in figure 2.22 along the centerline and along the streamwise direction with y offset. In figure 2.22 (a), the skewness approaches zero only after $x/x_{peak} \approx 0.9$ along the centerline, but stays negative throughout the measurement domain, which corresponds to a prevalence of negative velocity fluctuations. After approximately $x/x_{peak} = 2.7$, the value of S_u decreases away from 0 to -0.35 at $x/x_{peak} = 5.3$ (the end of the measurement domain). These observations are quite different from those reported by Mazellier and Vassilicos (2010); Melina et al. (2016), where S_u crosses zero at $x/x_{peak} = 1.5$ in the FSG-generated turbulence, and then stays positive.

In figure 2.22 (b), the flatness F_u returns to 3 at $x/x_{peak} \approx 1.5$, whereas Mazellier and Vassilicos (2010) and Melina et al. (2016) reported $F_u = 3$ at $x/x_{peak} \approx 1$, and remained at 3 throughout the measured decay region. In the current data, the value of F_u after $x/x_{peak} = 3$ in fact increases slightly, although the deviation from Gaussianity is not as obvious as that of S_u. Figure 2.22 (c) and (d) give the results along the streamwise direction with y offset. It is observed that the streamwise variation is much smaller off the centerline.

These observations are quite interesting, especially the decreasing values of S_u away from 0, as shown in figure 2.22 (a). However, the streamwise profiles of $\overline{u^3}$, as shown in figure 2.23, seem to give a rather constant value of $\overline{u^3}$ after $x/x_{peak} \approx 2$. The value of $\overline{u^3}$ in the region $x/x_{peak} > 2$ is decreasing from roughly -0.01 to -0.05. Note however, even though it looks constant over the decay region, the actual variation is large (see figure 2.23). On the other hand, the term u'^3 monotonically decreases towards 0, which leads to the exaggerated decrease of $S_u = \overline{u^3}/u'^3$ as observed in figure 2.22 (a). This suggests that the decrease of S_u is indeed caused by the decreasing triple correlation $\overline{u^3}$ term. In fact, Maxey (1987) has showed the importance of the triple correlation term in determining the Skewness. Based on analysis of homogeneous and isotropic turbulence, Maxey (1987) reported positive non-zero values of $\overline{u^3}$. This does not necessarily contradicts the current results as it has been shown above that the flow is not strictly homogeneous or isotropic. Furthermore, the decreasing $\overline{u^3}$ might have to do with the growing boundary layers on the Lille wind tunnel walls such that negative velocity fluctuations are induced as the flow becomes a channel flow towards the end of the measurement domain, which is $x = 18\,\mathrm{m}$. Maxey (1987) also concluded that the decay of turbulent energy has stronger effects on the odd-order moments than on the even-order moments, which seems to explain the smaller variations observed in the Flatness profiles, as shown in figure 2.22 (b) and (d).

These results also relate to the probability density functions (*pdf*) of the streamwise fluctuating velocity. Figure 2.24 (a) shows the *pdf* of u/u' at the peak location $x/x_{peak} = 1$ from different experiments with different inlet Reynolds numbers. The collapse of the *pdf* confirms the independence on inlet Reynolds number. The distribution is clearly non-Gaussian, and skewed to the left, which means more negative velocity fluctuations, in agreement with the negative velocity skewness. From the 3×3 experiments, the *pdf* from different streamwise locations along the centerline are shown in figure 2.24 (b). In the production region $x/x_{peak} = 0.5$, the distribution is clearly non-Gaussian. The *pdf* at $x/x_{peak} = 1.4$ and $x/x_{peak} = 2.6$ are both representative of a Gaussian distribution, and the latter is slightly better (figure 2.24 b). As demonstrated in figure 2.24 (c), the *pdf*

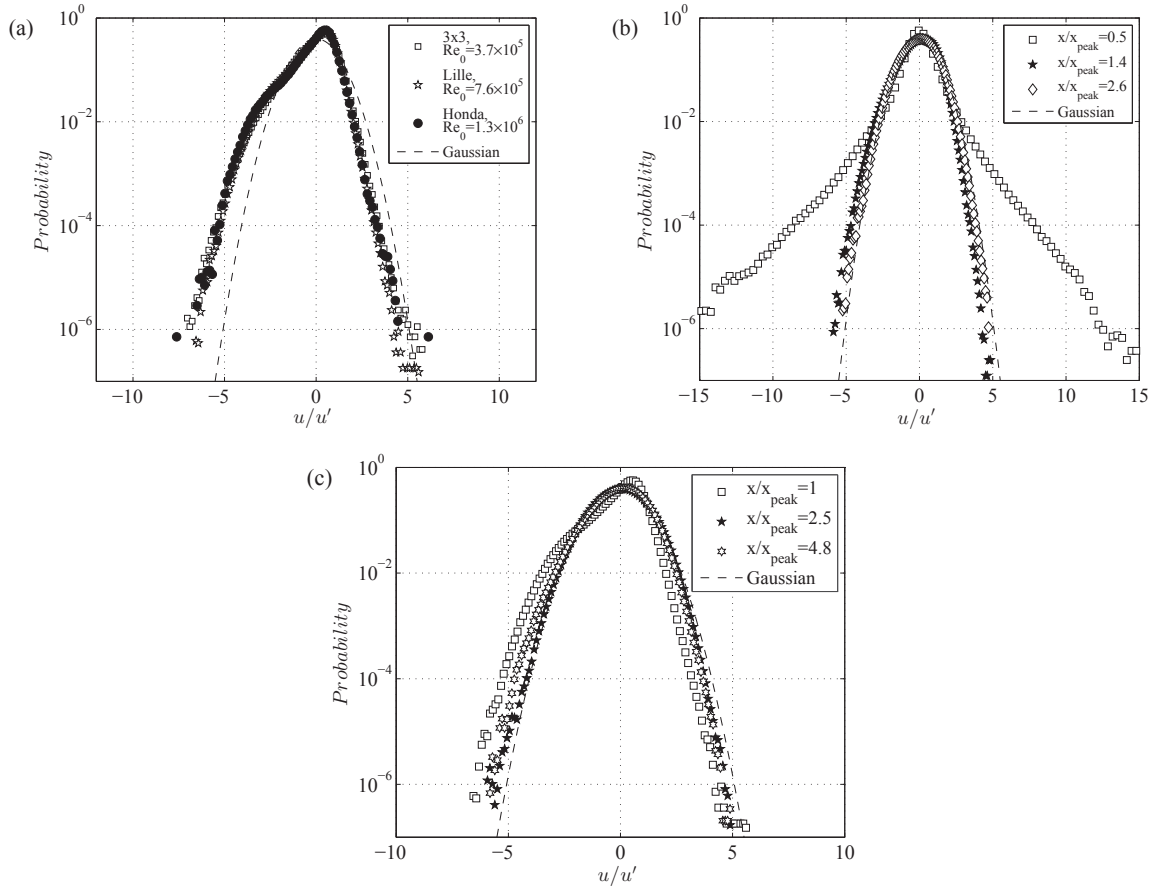

Figure 2.24: Probability density function of u/u' (a) at $x/x_{peak} = 1$ with different inlet Reynolds numbers $Re_0 = U_\infty L_{0z}/\nu$, (b) at different streamwise locations along the centerline in the 3×3 experiment with $U_\infty = 10\,\mathrm{m/s}$, and (c) at different streamwise locations along the centerline in the Lille experiment with $U_\infty = 9\,\mathrm{m/s}$. The dashed lines give the Gaussian distribution.

of u/u' beyond $x/x_{peak} = 2.6$ from the Lille experiments are skewed to the left again, suggested by the deviation of Skewness S_u.

Isotropy

To look at the isotropy of the flow, we use the data from the 3×3 experiments where both u and v components of the velocity were measured. Ideally, large scale isotropy of turbulent flow requires $u'/v' = u'/w' = 1$ and $L_u/L_v = L_u/L_w = 2$ (where $L_v = L_{vv,x}$ is the streamwise integral length scale of fluctuating velocity v). The results from the 3×3 experiments are presented in figure 2.25. In figure 2.25 (a), the ratio of u'/v' behind the centerline and behind the bar are both larger than 1, and gradually converges to $u'/v' = 1.35$. This value is larger than the previously reported values of e.g. $u'/v' = 1.14$ for regular grid generated turbulence (Kang et al., 2003b), and $u'/v' = 1.1 \sim 1.25$ for fractal grid generated turbulence (Valente and Vassilicos, 2011; Hearst and Lavoie, 2014).

This anisotropy is also evident in figure 2.25 (b), where the integral length scale ratio L_u/L_v is everywhere well above 2 on the centerline. This is comparable to the results of Hearst and Lavoie (2014), where they reported values of L_u/L_v of 2.4 to 2.5 in the decay region. These observations of large scale anisotropy seem to come from the two distinct length scales L_{0y} and L_{0z}, such that the largest eddy scales in these two directions are different.

The large scale isotropy indicators u'/v', and v'/w' are presented in figure 2.26 from PIV data. The centerline value of u'/v' is roughly 1.5 at $x/x_{peak} = 1$, and decreases downstream, which is consistent with the HWA results as shown in figure 2.25 (a). Figure 2.26 (b) shows that the value of v'/w' increases from roughly 0.8 to 0.86 along the centerline. The fact that $v'/w' < 1$ also indicates that the turbulence intensity is larger in the z direction so that $v' < w'$. It seems to correspond to the grid geometry as the largest bars are separated in the z direction. The ratio of u'/w' (implied by the ratios of u'/v' and v'/w'), is approximately 1.2, which is similar to that reported for the FSG experiments.

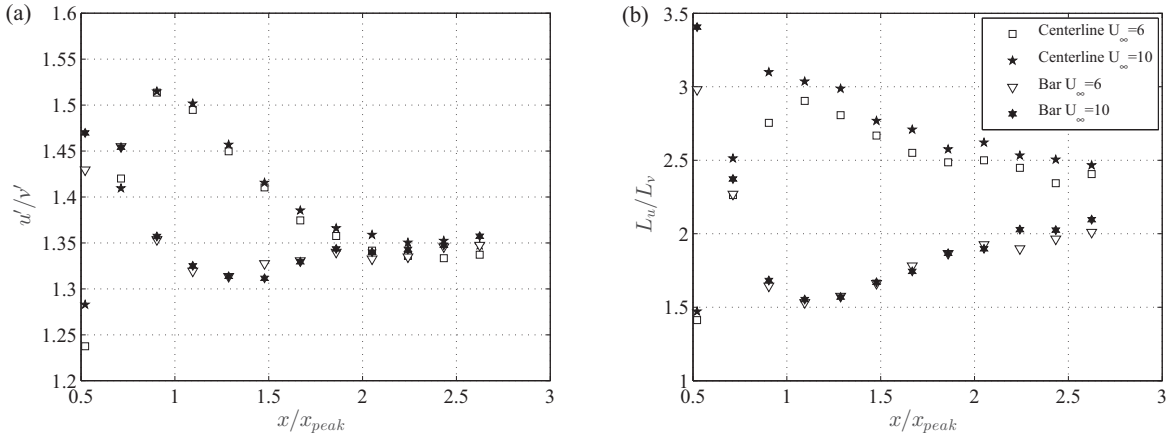

Figure 2.25: Large scale isotropy criteria of (a) u'/v', and (b) L_u/L_v from the 3×3 experiment.

Behind the horizontal bars, the value of u'/v' is roughly 1.2 (at $y = -0.33\,\mathrm{m}$) in the Lille experiment, as shown in figure 2.26 (a), which is similar to that 1.3 observed in the 3×3 experiment around $x/x_{peak} = 1$, as shown in figure 2.25 (a). As shown in figure 2.26 (b), the ratio of v'/w' is approximately 1 behind the horizontal bar. These observations seem to suggest that the isotropy level of the flow is better behind the horizontal bars than that on the centerline in the region $x/x_{peak} \approx 1$, and it is consistent with the HWA results given in figure 2.25.

The small scale isotropy indicator $\overline{(dv/dx)^2}/\overline{(du/dx)^2}$ is shown in figure 2.27. It is clear that this ratio is much smaller than the isotropic value of 2, even though the values are increasing monotonically. The values behind the horizontal bars are slightly larger (closer to 2 that indicates isotropy) than that on the centerline, which is in agreement with the previous observation on the large scale isotropy. The ratio of $\overline{(dv/dx)^2}/\overline{(du/dx)^2}$ is smaller than that from the FSG-generated turbulence reported by Valente and Vassilicos (2011), where they showed $\overline{(dv/dx)^2}/\overline{(du/dx)^2} \approx 1.4$ in the decay region. The anisotropy partly explains the discrepancies of the dissipation rate ϵ calculated with different methods, as discussed in section 2.1.3.

Finally, to further evaluate the isotropy assumption in discussing the decaying turbulence, the advection is computed as $\mathcal{A}_{iso} = (3/2)U(\partial\overline{u^2}/\partial x)$, assuming $\overline{u^2} = \overline{v^2} = \overline{w^2}$, and

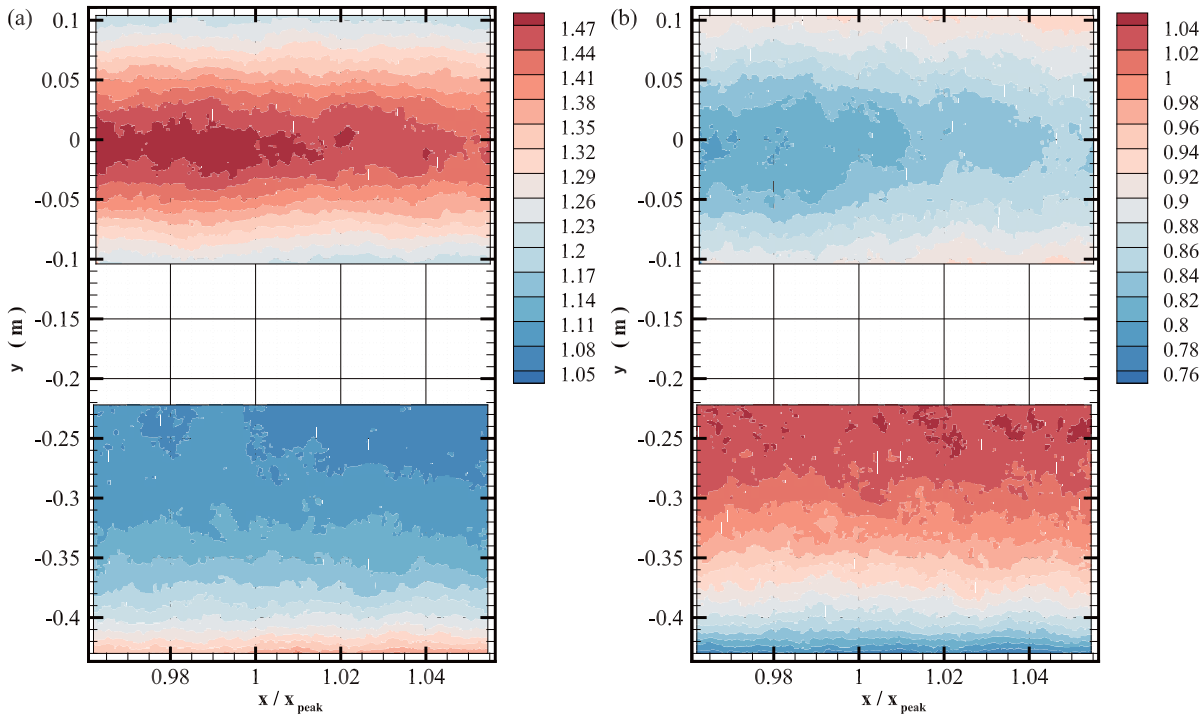

Figure 2.26: PIV measurements of the large scale isotropy criteria of (a) u'/v', and (b) v'/w' from the Lille experiments.

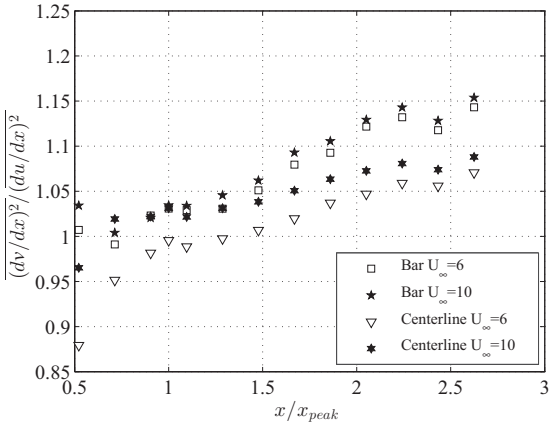

Figure 2.27: The small scale isotropy $\overline{(dv/dx)^2}/\overline{(du/dx)^2}$ along the streamwise direction from the 3×3 experiments.

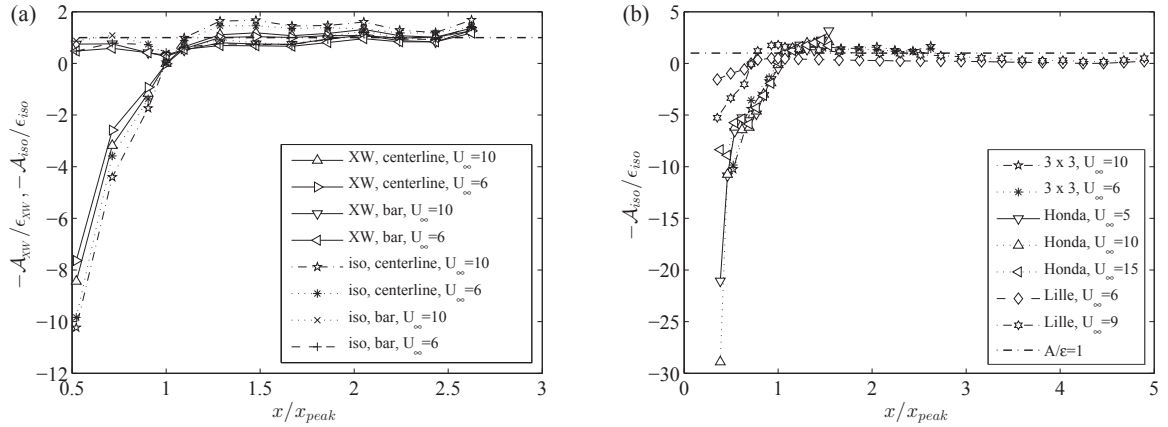

Figure 2.28: Ratios of (a) $-\mathcal{A}_{XW}/\epsilon_{XW}$ and $-\mathcal{A}_{iso}/\epsilon_{iso}$ at different locations using the XW measurements from the 3×3 experiments, and (b) $-\mathcal{A}_{iso}/\epsilon_{iso}$ from all three experiments using the isotropy assumption. The dashed line marks ratio of 1.

$\mathcal{A}_{XW} = U(\partial k/\partial x)$, where $k = (\overline{u^2} + 2\overline{v^2})/2$, and the ratios $-\mathcal{A}_{iso}/\epsilon_{iso}$ and $-\mathcal{A}_{XW}/\epsilon_{XW}$ are examined. Results from the 3×3 experiments are given in figure 2.28 (a). It can be seen that the ratio collapses for both cases with and without the isotropy assumption, and stays roughly constant in the region $x/x_{peak} > 1.1$. This is slightly different from the results discussed by Valente and Vassilicos (2011) as the ratio in their case becomes constant at $x/x_{peak} \approx 0.8$, which indicates that the turn to isotropy of the FSG-generated turbulence is faster. To evaluate the consistency, the ratio of $-\mathcal{A}_{iso}/\epsilon_{iso}$ for the Honda and Lille measurements along the centerline are also given in figure 2.28 (b). It is observed that this ratio evolves in the same pattern, and stays close to 1 in the decay region. Following these discussions, we might argue that, although the flow is not strictly isotropic, the isotropy assumption can be used to look at the evolution of the dissipation rate, although care must be taken in the region $x/x_{peak} < 1.1$, which is roughly the production region of the flow.

2.2.5 Vortical structures

Some PIV data are presented to look at the vortices generated by the RFG around the turbulence peak location $x/x_{peak} = 1$. Here the 2D swirling strength λ_{ci} is used to extract

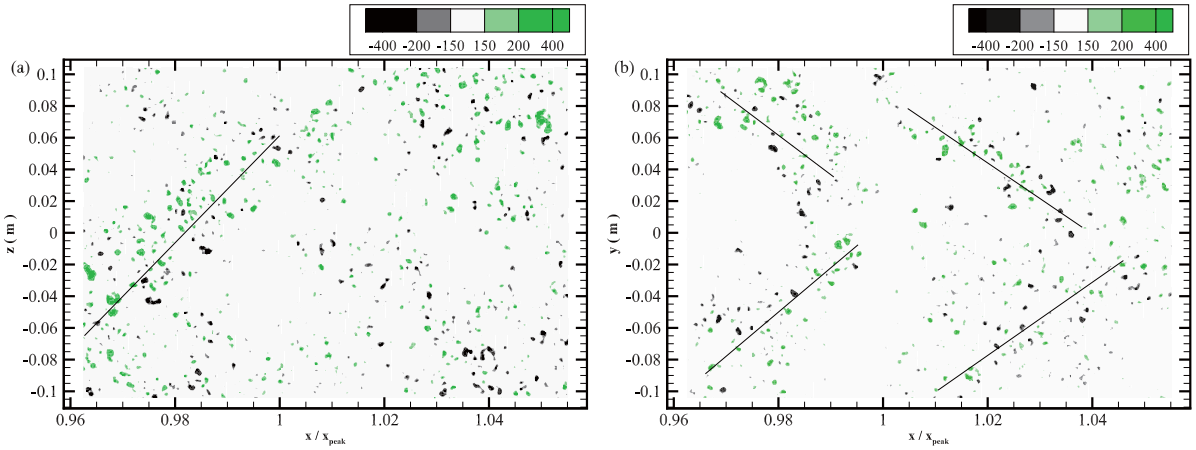

Figure 2.29: Examples of instantaneous 2D swirling strength λ_{ci} in the $x-y$ plane at $U_\infty = 9\,\mathrm{m/s}$. Data taken from the Lille experiment. Black lines indicate possible alignments of the vortices.

the vortical structures from the PIV data. It is defined as the imaginary part of the eigenvalues of the velocity gradient, which eliminates the effects of local shear (Zhong et al., 1998; Zhou et al., 1999). In practice, the two dimensional velocity gradient $\mathcal{D}$ matrix is calculated from the PIV velocity field, and the eigenvalue problem is written as $D = V\lambda_e V^{-1}$, where V is the eigenvector, and λ_e is the eigenvalue matrix. If the eigenvalue is complex, the imaginary part of the complex conjugate is extracted and the absolute value is stored as λ_{ci}, which is the 2D swirling strength. The value of λ_{ci} is then signed by the local vorticity to give direction of the swirl. Two instantaneous fields are given as examples in figure 2.29. Small values are shown in white to highlight only the stronger swirling structures. It seems that each group is packed with counter-rotating swirls, and they are oriented towards the center of the grid. This is a signature of vortices shed from the horizontal bars.

The averaged results over 20000 instances are given in figure 2.30 around the centerline and behind the horizontal bar. The averaged magnitude of the swirl is much smaller than that of the instantaneous ones. The swirling strength is observed on both sides of the centerline with opposite signs in figure 2.30 (a). Figure 2.30 (b) gives the mean swirling strength behind the horizontal bar, which suggests that the vortices in this region is more Gaussian so the mean goes to zero, which is in agreement with the observations in the

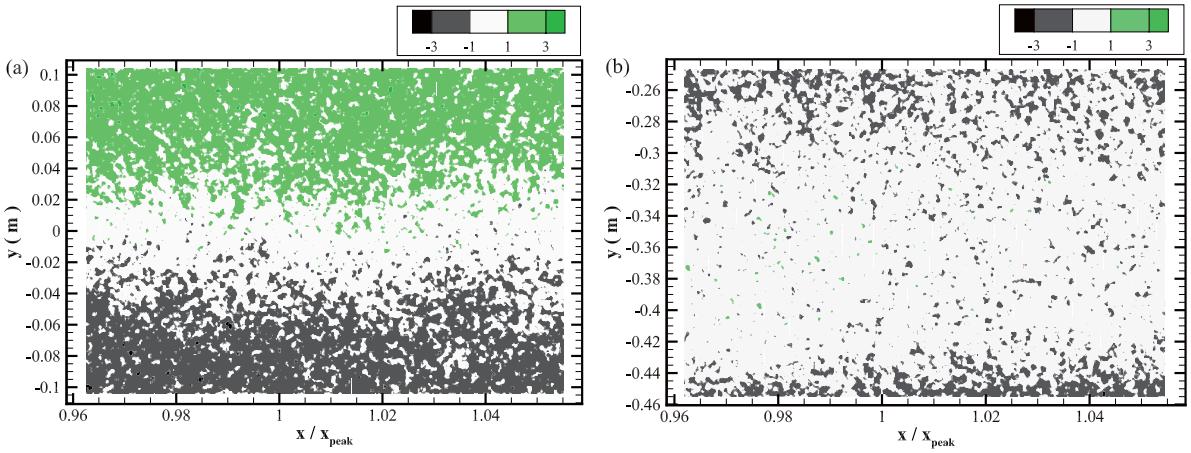

Figure 2.30: Averaged 2D swirling strength λ_{ci} in the $x-y$ plane centered (a) around the centerline, and (b) behind the horizontal bar at $U_\infty = 9\,\mathrm{m/s}$. Data taken from the Lille experiment.

previous sections.

It has been shown in table 2.2 that there are two different interaction length scales, i.e. x_{y*}^{peak} and x_{z*}^{peak} (again, this is not to be confused with the physical turbulence intensity peak location x_{peak}, as discussed in section 2.2.2), due to the two length scales in the grid geometry. The calculated value gives $x_{z*}^{peak} > x_{y*}^{peak}$, suggesting that the vortices shed from the vertical bars would meet later than those from the horizontal bars. The results computed here are in the $x-y$ plane, and therefore the vortices observed around the centerline are predominantly associated with the horizontal bars. It follows that vortices shed from the vertical bars should meet on the centerline at a later streamwise location $x/x_{peak} > 1$. This suggests that the shedding vortices from the rectangular fractal grid interact over a wide range of x locations due to the different anisotropic length scales. For a FSG generated turbulence, the shedding vortices from the largest bars are expected to meet at the peak location x_{peak} only. This difference seems to be the cause of the inhomogeneity and anisotropy, and consequently affect the evolution of length scales L_u, λ, the Skewness S_u, and Flatness F_u.

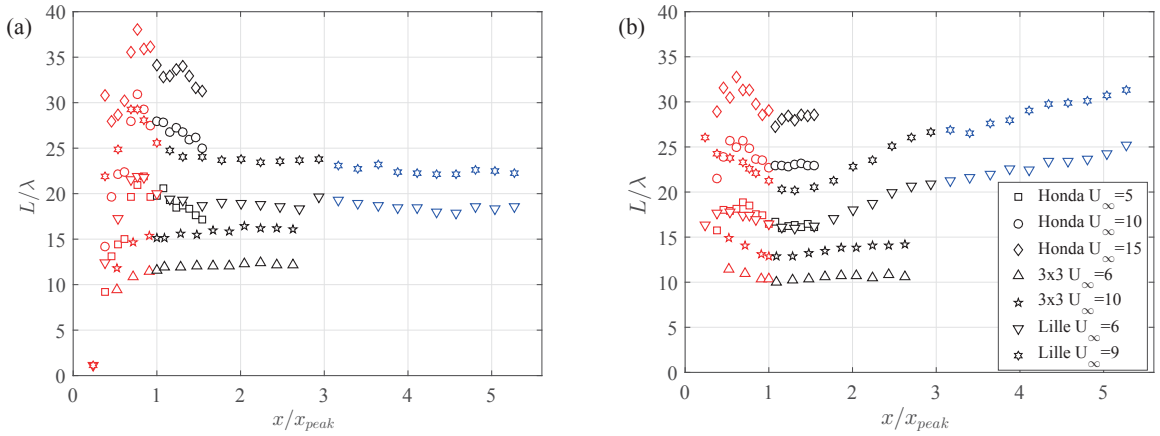

Figure 2.31: Streamwise profiles of L_u/λ for different inlet velocities (a) along the centerline, and (b) along the streamwise direction for the *bar*330 data set from Honda experiments and the *bar* data set from other experiments. Red and black colors mark the production and decay region, respectively. Blue marks the region in Lille experiments where $x/x_{peak} > 3$.

2.2.6 Non-equilibrium energy dissipation scaling

The values of L_u and λ are shown to have increasing values along the streamwise direction except for a regional decrease between $x/x_{peak} = 1$ to 1.5 along the center lines, as discussed in section 2.2.3. The ratio L_u/λ along the centerline and the streamwise direction with a y offset are shown in figure 2.31.

Along the centerline, it seems that the ratio L_u/λ stays roughly constant in the decay region. The results from the Honda experiments seem to decrease slightly along the centerline. It is noted that the local Reynolds number is the highest amongst all cases, and both length scales have a estimated error of $\sim 5\%$. Therefore the slight decrease of L_u/λ in the Honda experiment might be attributed to measurement error. In the region of $x/x_{peak} = 1.5$ to 3, the invariance of L_u/λ is consistent with the non-equilibrium scalings from fractal generated turbulence (see Mazellier and Vassilicos, 2010; Gomes-Fernandes et al., 2012; Hearst and Lavoie, 2014). The blue data points in figure 2.31 (a) mark the region where Re_λ stays roughly constant, as shown in figure 2.32 (a) and (b), and therefore should not be interpreted as evidence for the non-equilibrium scaling relation. With the y offset, as shown in figure 2.31 (b), the value of L_u/λ seems roughly constant in

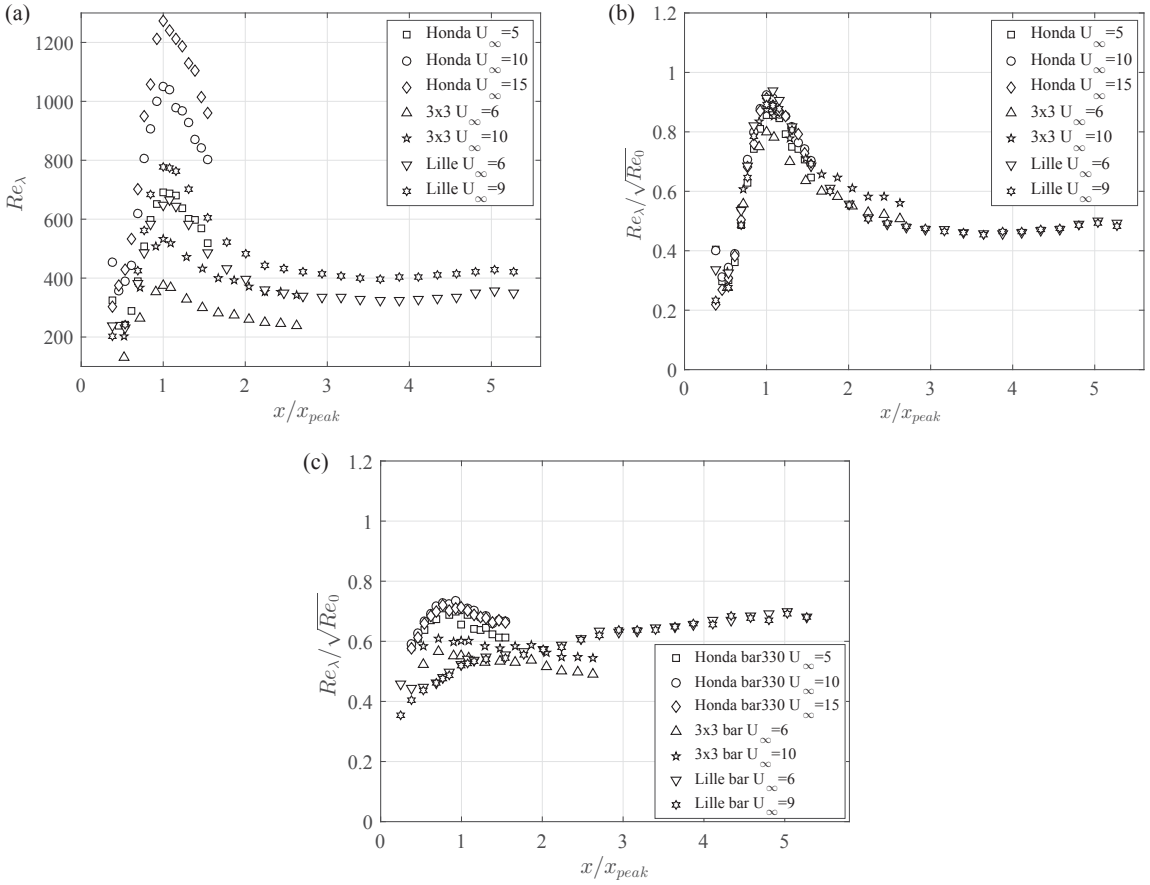

Figure 2.32: Streamwise profiles of Re_λ (a) along the centerline from different experiments, (b) normalized by the inlet Reynolds number $Re_0 = U_\infty L_0/\nu$ along the centerline, and (c) normalized along the streamwise direction with y offset.

the decay region for data from Honda and 3×3 experiments, but increases monotonically in the Lille experiment. The reason for such observations can be partly explained by the growing of Re_λ as shown in figure 2.32, which might be caused by the growing boundary layer.

The profiles of Taylor Reynolds number $Re_\lambda = u'\lambda/\nu$ from different experiments with different U_∞ are given in figure 2.32 (a). The values of Re_λ increase with inlet Reynolds number $Re_0 = U_\infty L_{0z}/\nu$, and figure 2.32 (b) shows the collapse of $Re_\lambda/Re_0^{1/2}$ for all the experiments along the centerline. Note that the value of $Re_\lambda/Re_0^{1/2}$ stays roughly constant in the region of $x/x_{peak} > 3$, which corresponds to the blue data points in figure 2.31 (a). These data points are therefore not to be interpreted as the non-equilibrium scaling relation.

Along the streamwise direction with y offset, the normalization $Re_\lambda/Re_0^{1/2}$ does not collapse the data as shown in figure 2.32 (c). It suggests that the streamwise evolution of $Re_\lambda/\sqrt{Re_0}$ varies differently along the streamwise direction off the centerline of the grid. The values of $Re_\lambda/\sqrt{Re_0}$ does not vary as much as that along the centerline, and the data from the Lille experiment grows monotonically.

For turbulence generated by various grids, the Reynolds number Re_λ usually decreases along the streamwise direction x in the decay region (see e.g. Melina et al., 2016). The constant or increasing Reynolds numbers Re_λ observed in these experiments suggest that the decreasing rate of u' is similar or smaller than the growth rate of λ. From figure 2.16, it can be observed that in the decay region $x/x_{peak} > 2$, the growth rate of λ is the same as they collapse in the figure. Therefore, the main reason for the differences in the evolution of Re_λ perhaps lies in the wall effects on the turbulence intensity u'.

This might make sense as the growing boundary layer would increase the turbulence intensity level of the flow. The turbulence intensities on the centerline would then decrease slower than the power law usually observed in a free decaying turbulence, which explains the slower decay rate of u' at $x/x_{peak} > 3$ as shown in figure 2.12 (b) and (c). Behind the horizontal bar, especially in the Lille experiment, the measurement location would be inside the wall boundary layer as the boundary layer thickness grows in the x direction. The turbulence intensity at given height is therefore expected to grow. This would imply that, in the Lille experiment, the decay of u' behind the bar would be much slower than that along the centerline. The results are given in figure 2.33. In figure 2.33 (a), the data along the centerline and those with y offset become closer with increasing x/x_{peak} distance in the Honda and 3×3 experiments. These two cases are free from the wall effects. In figure 2.33 (b), the decay rate of the centerline data decreases from approximately $x/x_{peak} > 3$, and the difference between the centerline data and those behind the bar is visible. This shows the increased turbulence intensity due to the growing boundary layer from the wall of the Lille wind tunnel, which explains the unusual observations made above.

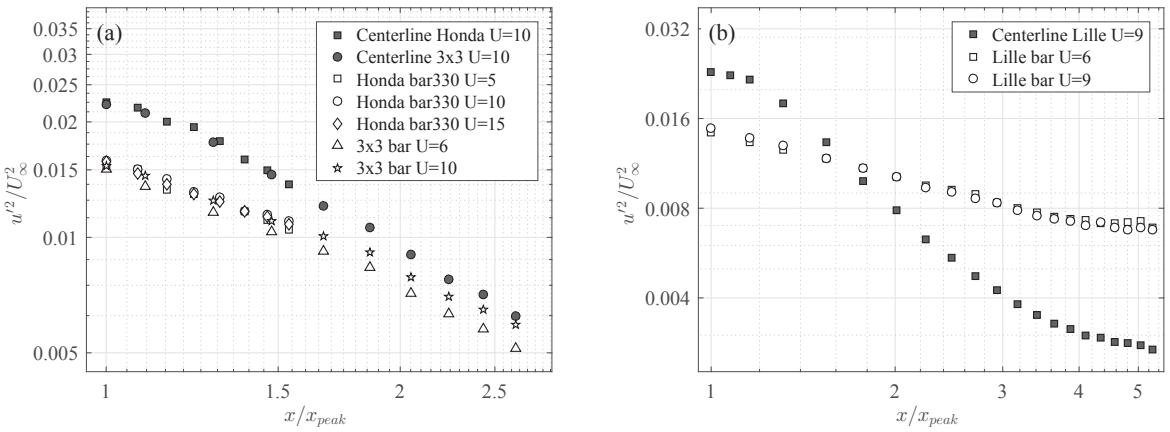

Figure 2.33: Profiles of u'^2/U_∞^2 against x/x_{peak} from (a) Honda and 3×3 experiments, and (b) Lille experiments, plotted in log scale.

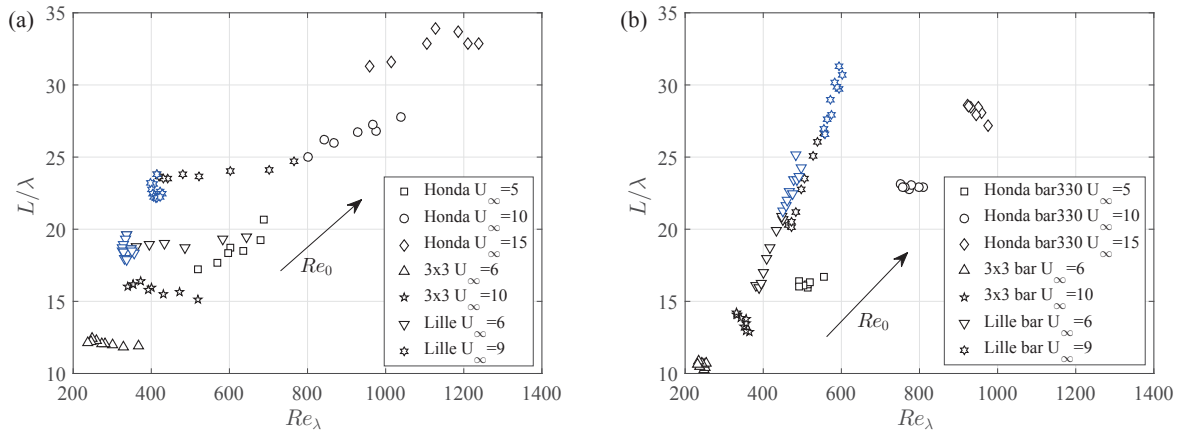

Figure 2.34: Profiles of L_u/λ as a function of Re_λ (a) along the centerline, and (b) along the streamwise direction with y offset. Blue marks the region in Lille experiments where $x/x_{peak} > 3$.

The dependence of L_u/λ on Re_λ is $L_u/\lambda \propto Re_\lambda$ according to the equilibrium energy dissipation scaling. But more and more evidence has shown that there exists a region where L_u/λ remains roughly constant while Re_λ decreases (Valente and Vassilicos, 2011, 2012; Hearst and Lavoie, 2014). The results from the current measurements along the centerline are given in figure 2.34 (a). The clear constancy of L_u/λ is observed in the decay region of 3×3 and Lille experiments, with increasing values as Re_0 increases.

The ratio of L_u/λ from the Honda experiments in the region of $x/x_{peak} = 1$ to 1.5 seems to vary as $L_u/\lambda \propto Re_\lambda$, as shown in figure 2.34 (a). However, this might be attributed to the measurement error due to the large Reynolds number of $Re_\lambda \approx 1000$ in the Honda experiments. Indeed, the uncertainty of the length scales from the Honda experiments is about 5%, and the variation of L_u/λ is within this range. The data from Honda experiments are therefore interpreted as constant values. The data marked in blue come from the region of $x/x_{peak} > 3$, where $Re_\lambda \approx const$ and consequently $L/\lambda \approx const$, as shown in figure 2.34 (a).

Along the streamwise direction with y offset, as shown in figure 2.34 (b), the value of L_u/λ from Honda and 3×3 experiments seems to be constant at different Reynolds numbers, which is also evident in figure 2.31 (b), and the value of L_u/λ increases with increasing Re_0. The data from Lille experiments follows $L_u/\lambda \propto Re_\lambda$, corresponding to the monotonic growth of L_u/λ as shown in figure 2.31 (b). This is not further interpreted as the region is expected to be affected by the boundary layer in the Lille wind tunnel.

The dissipation coefficient is calculated as $C_\epsilon = \epsilon L_u/u'^3$. If we assume $\lambda^2 = \nu u'^2/\epsilon$, it implies that $L_u/\lambda \sim C_\epsilon Re_\lambda$. For regions with $L_u/\lambda \approx const$, it follows that $C_\epsilon \propto Re_\lambda^{-1}$. Results along the centerline and along the streamwise direction off the centerline are given in figures 2.35 and 2.36, respectively.

Figure 2.35 (a) shows that the decreasing rate of C_ϵ decreases with increasing Reynolds number Re_λ, and that the values collapse with the non-equilibrium scaling such that $C_\epsilon \propto Re_0^{1/2}/Re_\lambda$, as the data collapse in figure 2.35 (b). Figure 2.36 gives the results off

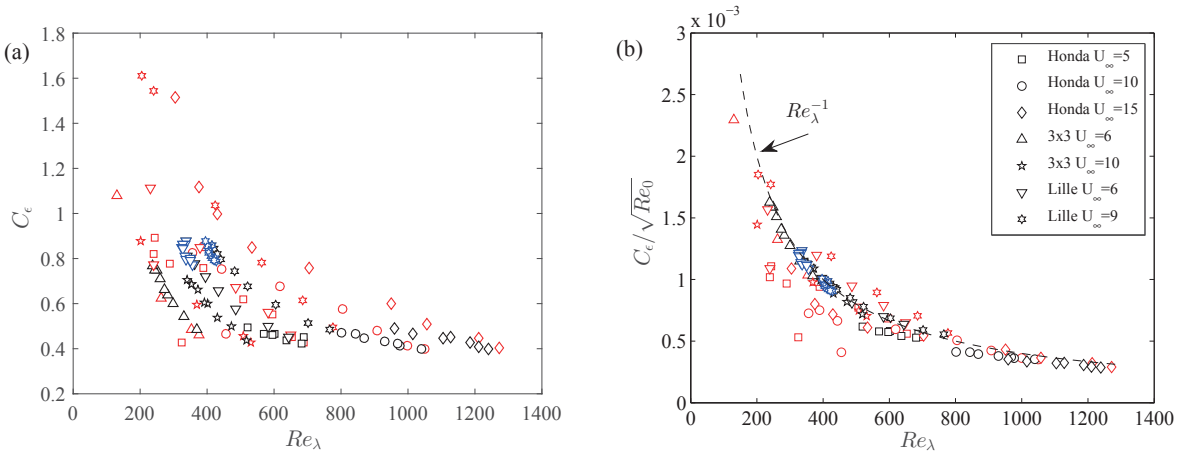

Figure 2.35: Reynolds number dependence of (a) C_ϵ, and (b) $C_\epsilon/\sqrt{Re_0}$ along the centerline. Red and black colors mark the production and decay region, respectively. Red and black colors mark the production and decay region, respectively. Blue marks the region in Lille experiments where $x/x_{peak} > 3$.

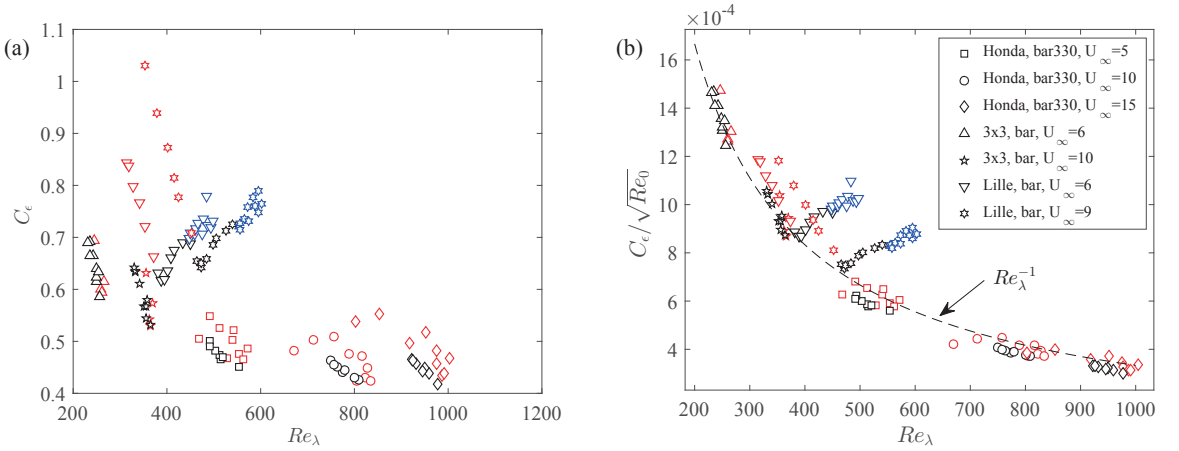

Figure 2.36: Reynolds number dependence of (a) C_ϵ, and (b) $C_\epsilon/\sqrt{Re_0}$ along the streamwise direction with y offset. Red and black colors mark the production and decay region, respectively. Red and black colors mark the production and decay region, respectively. Blue marks the region in Lille experiments where $x/x_{peak} > 3$.

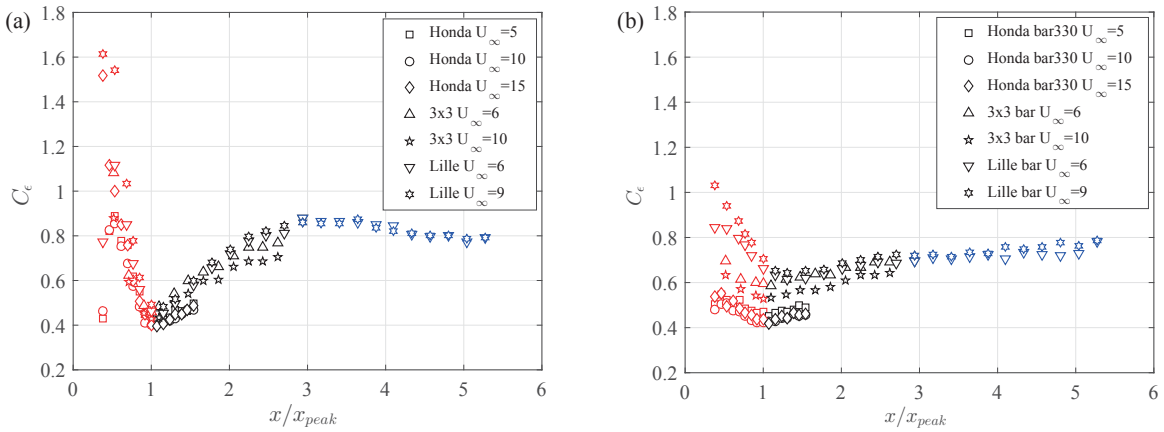

Figure 2.37: Dissipation coefficient C_ϵ as a function of x/x_{peak} (a) along the centerline, and (b) along the streamwise direction with y offset. Red and black colors mark the production and decay region, respectively. Blue marks the region in Lille experiments where $x/x_{peak} > 3$.

the centerline, and a clear deviation from the scaling relation can be observed in the Lille data, where the local Reynolds number Re_λ increases as discussed regarding figure 2.32.

Finally, the dissipation coefficient C_ϵ is plotted as a function of x/x_{peak} in figure 2.37. Figure 2.37 (a) has been shown in previous works (e.g. Hearst and Lavoie, 2014; Vassilicos, 2015), demonstrating the non-equilibrium scaling. However, the data from Lille experiments at $x/x_{peak} > 3$ should be interpreted with caution as $Re_\lambda \approx const$ was observed in this region, so this constancy of C_ϵ may not be depicted as the non-equilibrium scaling relation. Nevertheless, the values of C_ϵ collapse well in the production region and the beginning part of the decay region, which agrees with the non-equilibrium scalings. Figure 2.37 (b) shows the results along the streamwise direction with y offset. Note the relative measurement location in Honda experiments ($bar330$) and the other two is not the same, so the grouped collapse is not surprising. The evolution of C_ϵ seems to suggest $C_\epsilon \sim Re_\lambda^{-1}$ as well, and different slopes are clearly observed in different offset locations relative to the centerline.

2.2.7 Self-similarity of spectra

In the decaying homogeneous and isotropic turbulence, the classical equilibrium theory depicts that the spectra are expected to collapse at small scales when normalized using inner variables (ϵ and η), and at large scales using outer variables ($\overline{u^2}$ and L_u). For turbulent flows with the non-equilibrium scaling such that $L_u/\lambda \approx const$, it has been shown that either L_u or λ can be used to collapse the entire range of spectra, corresponding to a single-length scale spectra $E_{11}(k) = u'^2 l F_{11}(kl)$, where l is a characteristic length scale (Mazellier and Vassilicos, 2010; Valente and Vassilicos, 2011; Hearst and Lavoie, 2014). Mazellier and Vassilicos (2010) also showed a dependance of the spectra on the initial conditions, such that $E_{11}(k) = u'^2 l F_{11}(kl, Re_0, *)$, where the initial condition is characterized by Re_0, and $*$ represents any other possible factors. To evaluate this scaling, the compensated spectra $E_{11}(k) = u'^2 l F_{11}(kl)$ at given Re_0 are plotted at different streamwise locations, as shown in figure 2.38.

The spectra are compensated with the $-5/3$ slope, and the inertial subrange shows a clear plateau in all cases. For the Honda experiments, the ratio of L_u/λ shows a slight decrease in the region $1 < x/x_{peak} < 1.5$, as shown in figure 2.31, which was attributed to measurement error as the difference is within the uncertainty. In figure 2.38 (a) and (b), this slight variation of L_u/λ is also observed, such that the small scales are not collapsed exactly when normalized using u' and L_u. For the current discussion, this is attributed to the measurement error as the local Reynolds number is of order 1000. In the 3×3 experiments, it has been shown that, even though L_u and λ decreases individually in the beginning of the decay region, the ratio of L_u/λ is roughly constant. This corresponds to the well collapsed spectra in the entire range as shown in figure 2.38 (c) and (d). For the Lille experiments, the constancy of L_u/λ is only observed throughout the decay region, which is consistent with figure 2.38 (e) and (f). Note that the collapse of spectrum at $x/x_{peak} > 3$ is mainly due to the roughly constant Reynolds number Re_λ as discussed in the previous section.

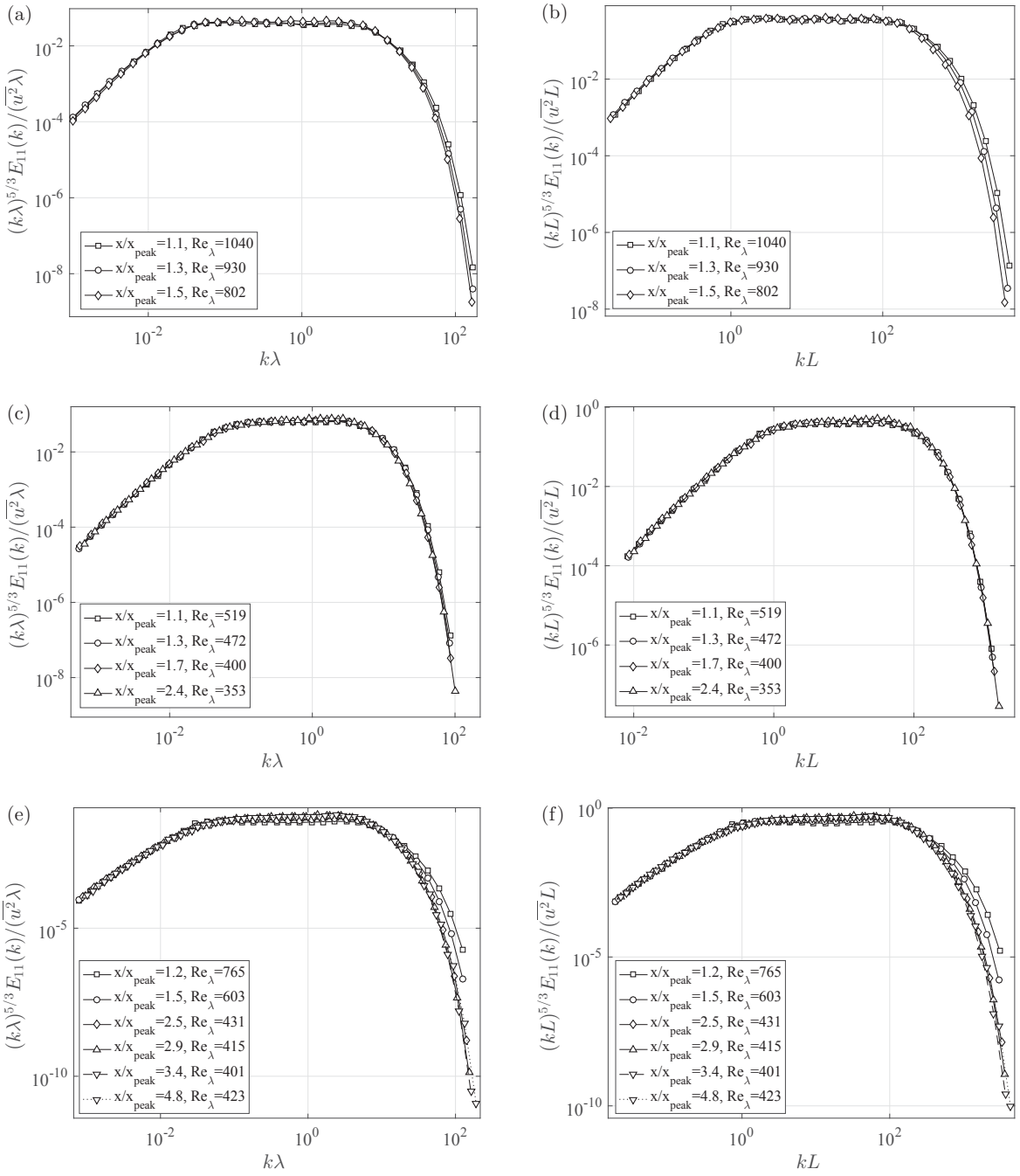

Figure 2.38: Compensated one-dimensional spectra along the centerline using the inner variables (left) and outer variables (right) at different streamwise locations normalized as x/x_{peak} from Honda experiments with $U_\infty = 10\,\mathrm{m/s}$ (a, b), 3×3 experiments with $U_\infty = 10\,\mathrm{m/s}$ (c, d), and Lille experiments with $U_\infty = 9\,\mathrm{m/s}$ (e, f).

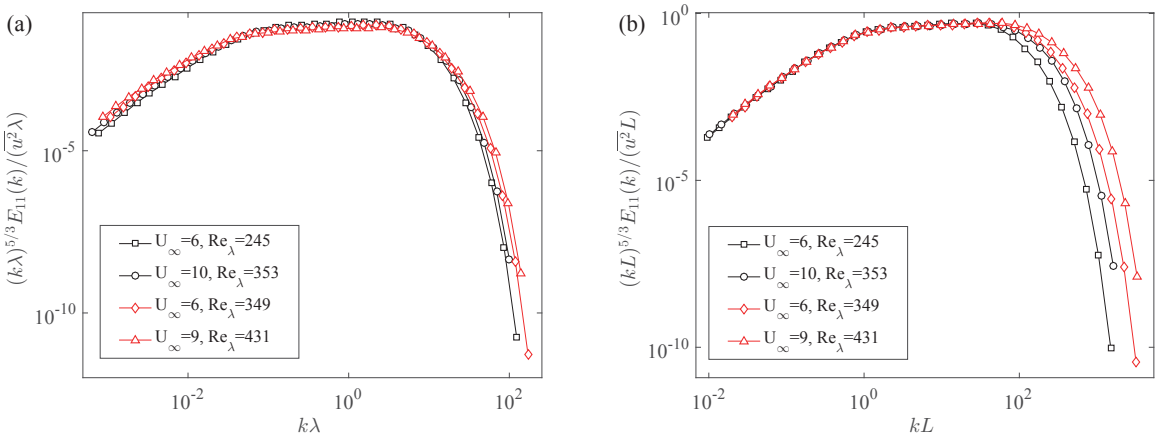

Figure 2.39: Compensated one-dimensional spectra along the centerline using (a) inner variables and (b) outer variables at $x/x_{peak} \approx 2.45$ with different Re_0 from 3×3 experiments with $U_\infty = 6\,\mathrm{m/s}$ and $10\,\mathrm{m/s}$, and Lille experiments with $U_\infty = 6\,\mathrm{m/s}$ and $9\,\mathrm{m/s}$.

To examine the dependency on Re_0, and to avoid the effect of the region $1 < x/x_{peak} < 1.5$, selected data from 3×3 and Lille experiments at $x/x_{peak} \approx 2.45$ are plotted in figure 2.39. The spectra in figure 2.39 do not collapse as expected. Note that the spread of spectra in the dissipative range is smaller for normalization using the inner variables. This also agrees with the analysis proposed by Valente and Vassilicos (2011), such that for a given Reynolds number ratio $Re_{\lambda_1}/Re_{\lambda_2}$ the spread using outer variables are about 3 times larger than that using inner variables.

2.3 Summary

In this chapter, a variation of the classical space-filling fractal grid (FSG) was designed, referred to as the rectangular fractal grid (RFG), and tested in three different facilities to document the turbulence field.

The wake interaction length scale was examined first, which failed to collapse the FSG and RFG data. There are two reasons for this observation. First, the spreading rate of the wake generated by grid bars varies by a scale factor related to the normalized centerline

mean velocity U_c/U_∞ on the grid plane due to the effect of the local shear. Secondly, there are two distinctive length scales in the RFG generated turbulence, and the wakes meet at different streamwise locations on the centerline and influence the actual turbulence peak locations.

The homogeneity of the flow was examined using different criteria, and results suggest that the beginning part of the decay region is more inhomogeneous, but the homogeneity for the rest of the flow is similar to previously reported FSG generated turbulence. The conclusions are also supported by the probability density functions at different locations. The velocity Skewness gives negative values, and decreases with x distance. It was shown that this was mainly caused by the triple correlation term $\overline{u'^3}$, which behaves differently from the predictions for homogeneous isotropic turbulence.

The anisotropy level in both large and small scales was shown to be greater than that for FSG generated turbulence. Nevertheless, it was shown that the ratio of $\epsilon/\mathcal{A}$ with and without the isotropy assumption is similar, and therefore the isotropy assumption can be used to study the turbulence characteristics during decay.

Due to the existence of two length scales, the beginning of the decay region exhibits interesting turbulence characteristics. Both the integral length scale L_u and Taylor microscale λ decrease in this part of the decay region. This might relate to the interaction of the two vortex systems from the two pairs of largest grid bars. The 2D swirling strength λ_{ci} calculated from the PIV measurement seems to support this scenario.

The ratio of L/λ remains constant in most of the data examined, except for the data acquired behind the bar in the Lille experiment. It was explained by showing the decay of turbulence intensity at these locations, which seems to be affected by the growing boundary layer from the wall. The evolution of C_ϵ in the decay region generally follows $C_\epsilon \sim Re_0^{1/2}/Re_\lambda$. The spectra also demonstrates the single-length scale solution, and shows a dependency on the initial conditions.

The geometry of the RFG has shown interesting features in turbulence characteristics, and further work to examine the interaction between the wakes might be interesting in several ways. First of all, by varying the ratio of the two lengths of the largest grid bars, the spreading rate of the wakes can be revisited (with the opening in the center of the grid, and consequently a local shear). The results can be used to update the definition of the wake interaction length scale, which can be used to predict the turbulence peak location x_{peak}. This will benefit a large number of experiments that requires high turbulence intensity at specific downstream location. Further measurement of the terms in the turbulent kinetic energy equation in the beginning of the decay region may reveal the interactions between the two different scales, and perhaps contribute to the understanding of the evolution of turbulence length scales in a more general way.

Chapter 3

Turbulent shear flow

In this chapter a new class of turbulence generating grid is designed and tested to find the possibility to scale the mean velocity and turbulence intensity profiles to the geometry of the grid, which might provide the ability to produce desired mean velocity and near-field turbulence intensity profiles simultaneously. The details of the grid design is given first, and measurements of the mean velocity profiles are presented. It is shown that predictions using the mean velocity model derived from Taylor et al. (1949) and McCarthy (1964) are in good agreement with our experimental data. By modifying the grid thickness, the aspect ratio of the grid bars are changed, and consequently the drag coefficients. The effect of drag coefficient on the local mean velocity gradient is discussed. The turbulence intensity profiles at given streamwise location x are found to scale with the geometry of the grid bars. The scaling relations between the turbulence field and the geometry of the grid might be used in the future to generate other types of turbulence flows of interest. A general procedure of the grid design method is proposed in section 3.2.3. Results on the evolution of turbulence intensities and length scales are presented, and finally a simplified model is proposed to describe the downstream development of the turbulence field generated by our grids. Finally, it is concluded that the proposed inhomogeneous multiscale grids might be used to tailor the characteristics of turbulent shear flows in a

more systematic way. Again, x, y, z represent the streamwise, vertical, and transverse directions, respectively.

3.1 Experiments

3.1.1 Facility

All experiments in this chapter were conducted in the 3×3 closed loop wind tunnel in the Aeronautics Department at Imperial College London. The test section has a cross sectional area of $0.91\,\mathrm{m} \times 0.91\,\mathrm{m}$, and a measurable length of $4.2\,\mathrm{m}$. The flow goes through a set of perforated screens and a 9:1 contraction before reaching the test section. The background turbulence intensity without the grid was measured to be $\sim$0.1% at $U_\infty = 10\,\mathrm{m/s}$. A computer controlled traversing system is mounted on top of the working section, allowing movements in all three directions. The origin of the coordinate system is set at the bottom of the grid on the windward side.

3.1.2 Grid design

In this section we outline the design principles of our new multiscale grids. A schematic sketch is given in figure 3.1. Three such grids were made for the current investigation producing flows with different shear rates and different turbulence profiles, even though the geometries are very similar. The first grid was designed to generate a turbulent flow without mean shear, and a non-uniform turbulence intensity, while the other two were designed to generate turbulent flows with gradients in both mean velocity and turbulence intensity. The grids are numbered in order of increasing shear rates. They were laser cut in acrylic with a uniform thickness (in the x direction) of $D = 10\,\mathrm{mm}$.

There are several parameters involved in the design process, and a summary is given

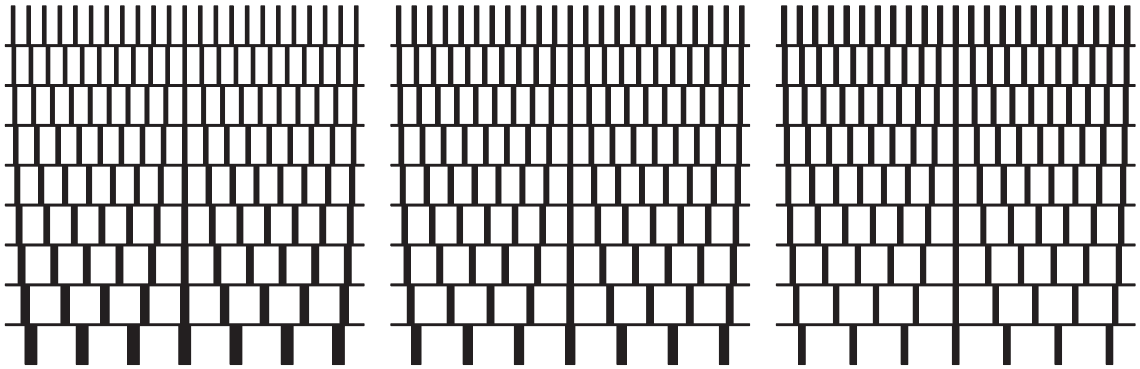

(a) (b) (c)

Figure 3.1: Schematic sketch of (a) grid 1, (b) grid 2, and (c) grid 3, respectively, in $z - y$ (horizontal-vertical) plane with $N = 9$ layers numbered from bottom to top as $n = 1, 2, ...N$.

H, W	External height and width of grid
D	Thickness of the original grid (in x), and the horizontal supporting bars
N	Number of layers
h_n	Height of layer n
σ_n	Blockage ratio at layer n
c_n	Number of vertical bars in layer n
w_n	Width of the vertical bars (in z) at layer n
g_n	Distance between two adjacent vertical bars at layer n
d_n	Thickness of the vertical bars (in x) at layer n
a_n	Aspect ratio of the vertical bars, defined as $a_n = d_n/w_n$, at layer n
t_b	Width of horizontal bars (in y)

Table 3.1: Design parameters of multiscale shear grids.

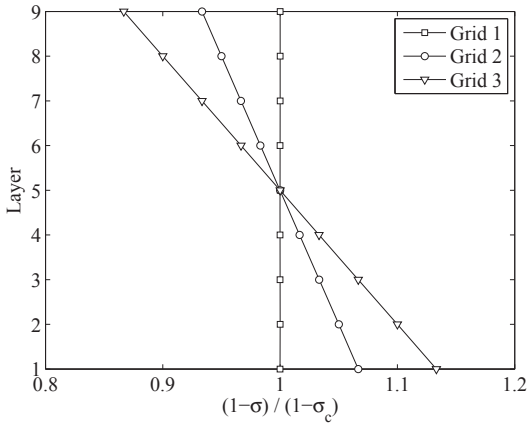

Figure 3.2: Profiles of $(1 - \sigma)/(1 - \sigma_c)$ for grid 1, 2 and 3, respectively, where σ_c is the blockage ratio at layer 5, the center of the grid, i.e. $\sigma_c = \sigma_5$.

in table 3.1. The external height H and width W of the grid are determined by the dimensions of the wind tunnel test section in the y and z directions, respectively. For the current study we have $H = W = 0.91\,\mathrm{m}$. The number N of horizontal layers is chosen to be $N = 9$ for all three grids in the current study. This number can be increased to obtain finer control over the local velocity gradient. The height of each layer h_n is set here to be $h_n = constant = 101.67\,\mathrm{mm}$. There are also eight horizontal supporting bars. Their width (in the y direction) for the present grids is $t_b = 5\,\mathrm{mm}$, and an aspect ratio of $D/t_b = 2$ was achieved to minimize the wake shed from them.

The most important parameters for the design of the mean flow profile are the blockage ratios σ_n of each layer. The normalized blockage ratio profiles for each grid are given in figure 3.2. The mean blockage ratio $(\sigma_1+\sigma_2+...+\sigma_n)/N$ (with $N = 9$ here) was set to 25% for all three grids, while the maximum local blockage ratio was set as $\sigma_9 = \sigma_{max} = 35\%$ to avoid flow recirculation. This is consistent with the observations of Rose (1966), who limited the maximum local solidity to $\sigma_{max} = 40\%$ for this reason.

While the blockage profile controls the mean velocity of the flow, the lateral widths and spacing of the vertical bars in each layer of the grid are tailored to vary the wake interaction mechanisms in order to generate different turbulence characteristics. Three parameters are introduced here, namely c_n the number of vertical bars, w_n the lateral width of each individual bar, and a_n the aspect ratio of the bars (defined as $a_n = d_n/w_n$). Note that since the thickness of the original grid is constant, i.e. $d_n = D = 10\,\mathrm{mm}$, a_n varies with vertical bar width w_n, and the drag coefficient C_D of each bar therefore varies with n, which affects the wake characteristics. The number of bars for each layer is set to be $c_n = 2(n + M) + 1$ for $n = 1, 2, ...N$, where $M = 2$ is a control parameter for the current

grids. The width of the bars are calculated from

$$w_n = \begin{cases} \dfrac{W}{c_n}\Big(\dfrac{h_n\sigma_n - t_b}{h_n - t_b}\Big), & n = 2, 3, ...N-1 \\ \\ \dfrac{W}{c_n}\Big(\dfrac{h_n\sigma_n - 0.5t_b}{h_n - 0.5t_b}\Big), & n = 1, N. \end{cases} \tag{3.1}$$

As shown in figure 3.1, there are no horizontal bars at the top and bottom edges of the grids, and the area is distributed in the vertical bars at layer 1 and N using the second equation in 3.1. At each layer, the vertical bars are evenly separated by a distance g_n, and are placed symmetrically about $z = 0$.

Note that the uniform thickness of the original grid inevitably causes variable aspect ratios $a_n = d_n/w_n$ of the vertical bars as the width w_n varies. Figure 3.3 (a) gives the C_D profiles of the three grids evaluated using the relation between C_D and the aspect ratio a_n given by Bearman and Trueman (1972). The Reynolds number of the vertical bars with $U_\infty = 10\,\mathrm{ms}^{-1}$ is within the range $6,000$ to $20,000$, and the Reynolds number dependence of the drag coefficient C_D is therefore negligible. The grids were also modified by attaching blocks behind the vertical bars to achieve a uniform aspect ratio a_n by effectively varying d_n, and hence a uniform C_D. Due to the dimensions of the vertical bars, the aspect ratio is set equal to that of the eighth layer a_8. For grid 3, however, the modification was only applied to the bottom layer $n = 1$, because the additional thicknesses to be attached to the other layers were all smaller than 1 mm, and therefore difficult to manufacture. The drag coefficient profiles after the modificaction are given in figure 3.3 (b).

Now if we refer to the scalings for grid-generated turbulence proposed by Vassilicos and colleagues as outlined in the introduction, we can calculate the wake interaction length scale for each layer n as $x_*^{peak}(n) = 0.21g_n^2/(\alpha C_D w_n)$ by substituting $L_0 = g_n$ and $t_0 = w_n$ in their original equation (Gomes-Fernandes et al., 2012). The results for the original and modified grids are plotted in figure 3.4 (a) and (b), respectively. It can be observed that

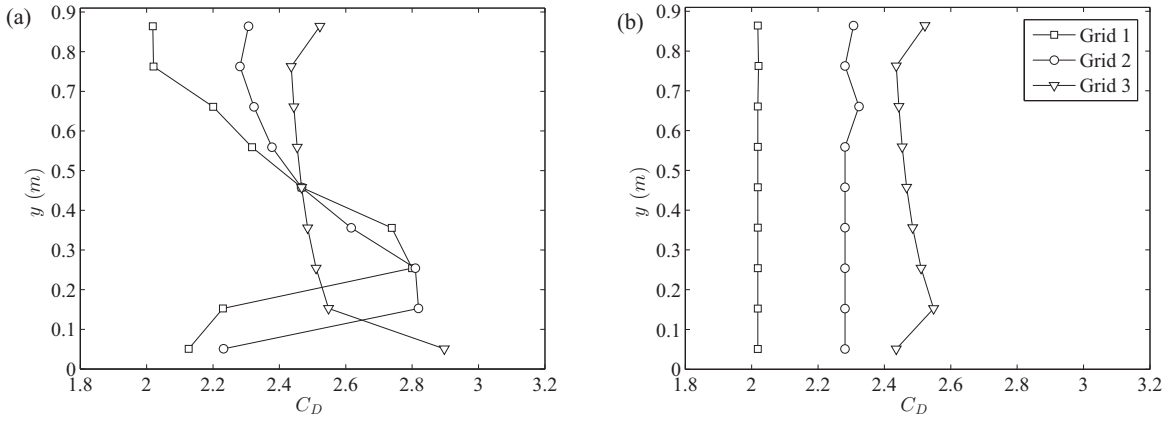

Figure 3.3: Vertical drag coefficient profiles of (a) original grids with uniform thickness $D = 10\,\text{mm}$, and (b) modified grids with variable thickness but uniform aspect ratio.

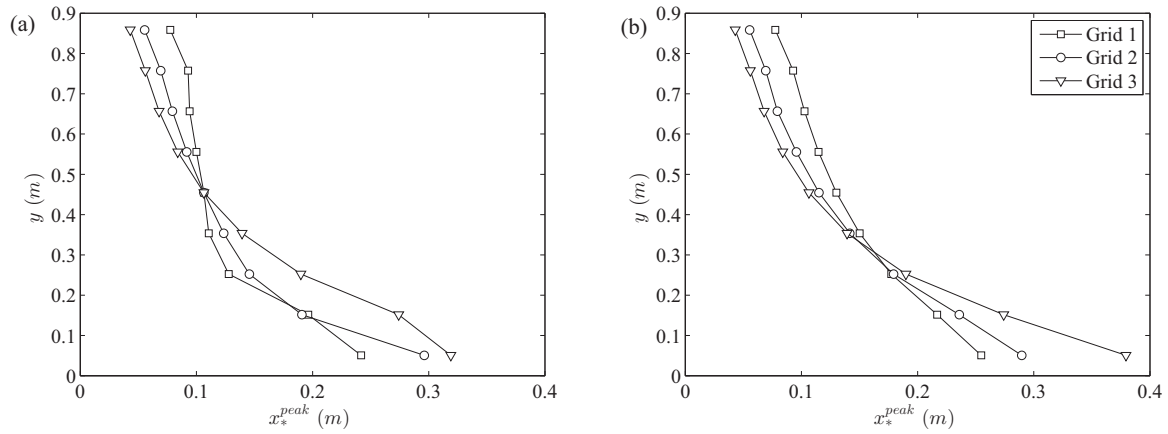

Figure 3.4: The wake interaction length scale $x_*^{peak}(n)$ for (a) original grids, and (b) modified grids.

the variation of x_*^{peak} with n becomes much more smooth due to the modification of C_D, and the maximum x_*^{peak} is about $x = 0.38\,\text{m}$ from the grid. From the results of Gomes-Fernandes et al. (2012), where the turbulence intensity profiles from several experiments and different grids collapsed against x/x_*^{peak}, it can be expected (see Gomes-Fernandes et al., 2012) that the streamwise turbulence intensity at level n scales with $(x_*^{peak})^{1/2}$. Further results and discussions on this scaling relation are presented in section 3.2.2.

3.1.3 Experimental set-up and method

The tunnel inlet velocity U_∞ was monitored using a Furness Controls FCO510 micro-manometer which measures the static pressure head across the contraction and the temperature. The inlet velocity U_∞ was maintained using a PID controller to be within $\pm 1.5\%$ of 10 m/s for all data sets in the current study. Only one inlet velocity is tested as previous studies showed that the turbulence statistics produced by grid with square bars is independent of the Reynolds number (see Roach, 1987). Data was then acquired with MATLAB, using a 16-Bit National Instruments NI-6229(USB) board. Instantaneous velocity signals were measured using an in-house etched platinum Wollaston cross wire powered by a Dantec Streamline CTA system. The diameter of the wire was $d_w = 5\,\mu$m with length to diameter ratio approximately 200. Resolution of the wire are estimated to be $l/\eta = 2.6$ to 7.2, where the Kolmogorov length scale η was estimated using $\eta = (\nu^3/\epsilon)^{1/4}$. To calculate ϵ, we compute $\epsilon_* = 15\nu\overline{(\partial u/\partial x)^2}$ and $\epsilon_{**} = 3\nu\overline{(\partial u/\partial x)^2} + 6\nu\overline{(\partial v/\partial x)^2}$, and then use the average $\epsilon = (\epsilon_* + \epsilon_{**})/2$ in this paper.

The hot-wire probe was mounted on a servo motor to allow accurate control of the pitching angles. It was calibrated at the beginning and end of every data set acquired using the look-up table method for five velocities from 3 m/s to 19 ms^{-1} and seven angles ranging from $-27°$ to $27°$. The temperature was monitored during acquisitions, and the data was discarded if temperature variation $\Delta T_a = T_{a,max} - T_{a,min}$ was larger than $0.1°C$. Two packets of $t_s = 300$ s samples were acquired to ensure convergence in mean statistics. Longer samples ($t_s > 300$ s) were not possible as the drift of the ambient temperature during acquisition will add artificial large scale variation. The acquisition rate was 125 kHz, and a low pass filter of 30 kHz was applied before the data was recorded to avoid aliasing. The data is also low-pass filtered before the processing to eliminate high frequency noise.

To calculate the longitudinal integral length scales $L_{uu,x}$, one either integrates the correlation function $R_{uu,x}$ or uses the streamwise turbulence kinetic energy spectrum $E_{11}(k)$ as $L_{uu,x} = \pi E_{11}(0)/(2u'^2)$ (see Tennekes and Lumley, 1972). It is noted that the spec-

trum and the correlation function is a Fourier pair. Yet the zero frequency asymptote of the digitally acquired spectrum has large uncertainty and the integral length scale is usually extrapolated from a number of the low frequency spectral estimates. For the other method, the integral of the correlation function cannot be taken to infinity, and thus an upper limit of the integration has to be chosen. Moreover, this upper limit of the integration is not well defined, and the integration result using different upper limit varies as large as 20% (ONeill et al.). We therefore seek a way to correct the lower frequency range of the spectra before estimating the longitudinal integral length scale $L_{uu,x}$.

Several models have been proposed for estimating the power spectra density $E(k)$, and the most frequently used is the von Kármán model, which can be written in a one-dimensional form as

$$E_{11}(k) = \frac{2u'^2 L_{uu,x}}{\pi} \frac{1}{\{1 + [kL_{uu,x}B(1/2, 1/3)/\pi]^2\}^{5/6}}, \tag{3.2}$$

where u' is the turbulence r.m.s. velocity, k is the wavenumber defined as $k = 2\pi f/U$ (f is the frequency in time), and B is the beta function related to the Γ function by $B(1/2, 1/3) = \Gamma(1/2)\Gamma(1/3)/\Gamma(5/6)$. The previously mentioned G-model (in Chapter 2) is not used because the Reynolds number in this study is relatively small, and the extent of the inertial sub-range is less definite. Therefore, the extra degree of freedom in the G-model introduces undesired errors sometime. In practice, an average of the spectra of two packets of data is taken first, and use equation 3.2 to fit the data in a least square sense. One example is given in figure 3.5, where it is shown that the small wavenumber range of the original spectrum (black) is slightly tilted upward leading to a larger value of $E_{11}(0)$. This effect is most obvious at locations close to the grid where $x = 0.83\,\mathrm{m}$, but much less further downstream. This method is used in section 3.2.5 to correct the lower frequency part of the spectrum.

It is acknowledged that most spectrum models have potential flaws in the low frequency range. There have been other models, e.g. Wilson (1998), where a two parameter spectrum model is proposed that allows more freedom in fitting the inertial range and inertial

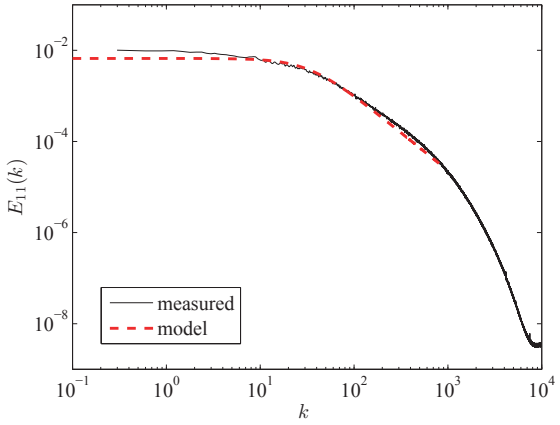

Figure 3.5: Example spectrum for grid 2 at centerline $x = 0.83\,\mathrm{m}$.

sub-range of the spectrum. However, that model works well only in turbulent flows with sufficiently large Reynolds numbers that has more decades of -5/3 slope, otherwise the extra parameter causes large uncertainties in the fitted spectrum. For the current study, the Reynolds number is moderate so that models such as Wilson's (1998) are not considered.

3.2 Results

3.2.1 Mean velocity

Before showing the measured vertical mean velocity profiles produced by the grids, we refer to previous works that used wire gauzes to produce non-uniform mean flow profiles. Following Taylor et al. (1949); McCarthy (1964), the streamwise velocity near the grid (upstream denoted by "-0"and downstream denoted by "$+0$") can be related by

$$\frac{U_{+0}}{U_{-0}} = \frac{1 + \alpha_n - \alpha_n K_n}{1 + \alpha_n + K_n}, \tag{3.3}$$

where the subscript n denotes the layer number, α_n is the refraction coefficient at layer n, and K_n is the resistance coefficient of the grid, which can be calculated from

$$K_n = \frac{r\sigma_n}{(1-\sigma_n)^2}, \tag{3.4}$$

where σ_n is the local blockage ratio of the grid at layer n, and r is an empirical constant in the range $0.65 < r < 1$ (see McCarthy, 1964). Cornell (1958) reported a constant value of $r = 0.7$ for the range $2,000 < Re < 40,000$. For the current grids, the Reynolds number based on $U_\infty = 10\,\mathrm{ms}^{-1}$ and bar width w is calculated to be in the range $6,000$ to $20,000$. The value of r is therefore chosen to be $r = 0.7$ in this work. Although there are other ways to calculate the value of K_n (as summarized in Karnik and Tavoularis, 1987), equation 3.4 seems to give the best result at least for the current cases.

Finally, an empirical expression of the refraction coefficient at layer n of the grid is given in both Taylor et al. (1949) and McCarthy (1964) as

$$\alpha_n = 1.1(1+K_n)^{-1/2}, \tag{3.5}$$

which was also concluded by these authors to be insensitive to Reynolds number.

In figure 3.6 (left), we present the vertical profiles of streamwise velocity U measured at $x = 0.83\,\mathrm{m}$ and $x = 4.13\,\mathrm{m}$ for the original grids (i.e. with non-uniform C_D as shown in figure 3.3 a), together with the profiles calculated using equations 3.3 to 3.5 with $r = 0.7$. Measurements were taken from the middle of the second layer up to the middle of the seventh layer. Note that there was no trial-and-error involved in generating the velocity profiles. The normalized profiles U/U_c (where U_c is the centerline mean velocity) are presented because the measured incoming velocity (at the beginning of the test section) is different from U_{-0} in equation 3.3 by a constant factor.

A wave-like deviation of the mean velocity profiles across these original grids is observed, especially for grid 1 where the variation of C_D is the largest. The non-uniform drag

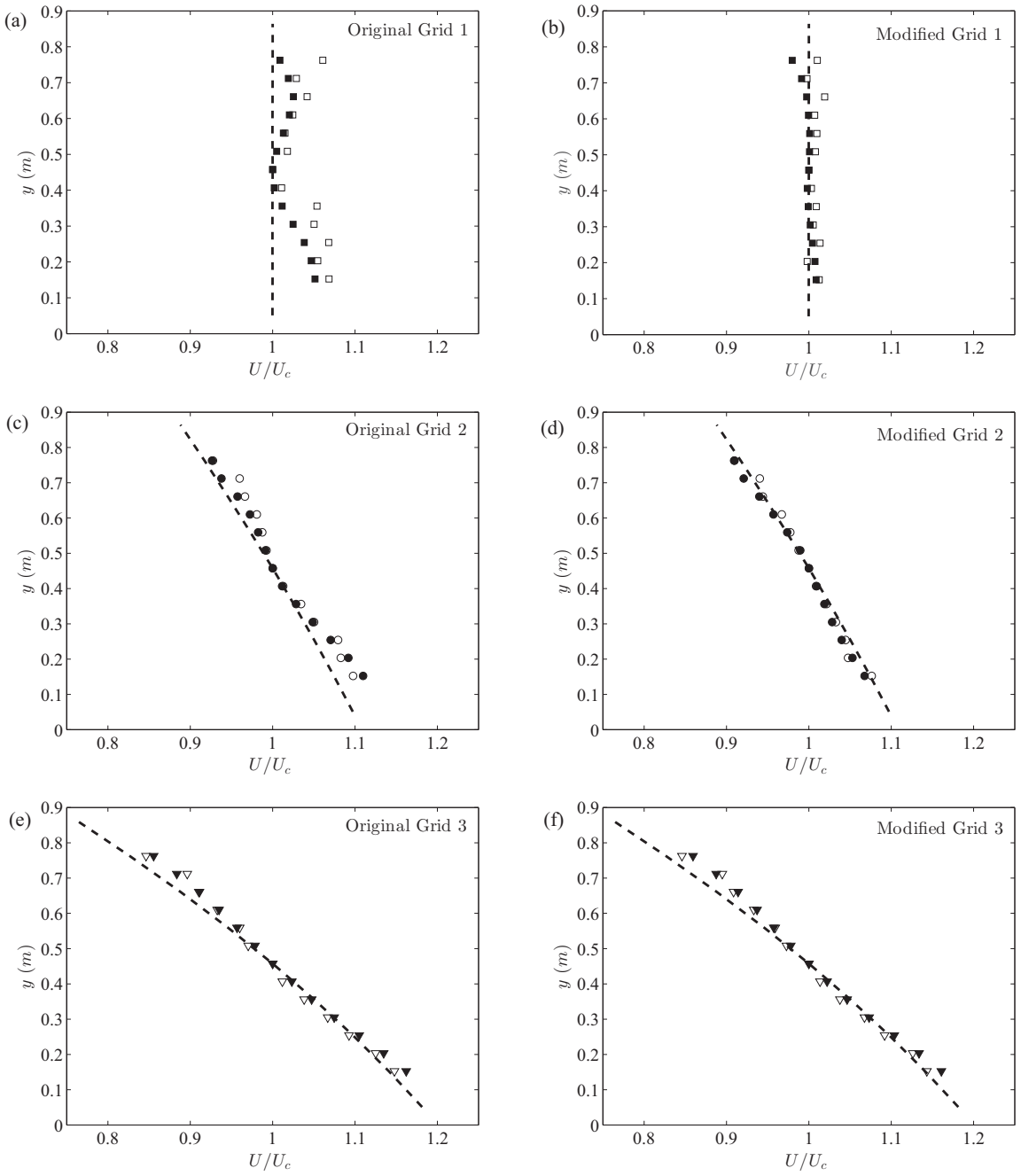

Figure 3.6: Vertical profiles of the normalized streamwise velocity U/U_c (symbols) and equation 3.3 (dashed lines) for original (left column) and modified (right column) grids. Empty symbols, $x = 0.83\,\mathrm{m}$; filled symbols, $x = 4.13\,\mathrm{m}$.

coefficient C_D of the vertical bars in the grid at each layer effectively modifies the local blockage ratio and consequently the local mean velocity. Other than that, the shapes of the velocity profiles generally follow the model, and the shape of the mean profiles is maintained within the measurement range of approximately $x/H = 1$ to 4.5. This is consistent with previous conclusions from the parallel wire-generated or plate-generated shear flows (e.g. Rose, 1966; Champagne et al., 1970; Shen and Warhaft, 2000a).

The measurements behind the modified grids, as described in section 3.1.2, are given in figure 3.6 (right). It is obvious that both grid 1 and 2 collapse better with the predicted profile when the non-uniformity of C_D is eliminated. This shows that the drag coefficient indeed affects the mean velocity profile quite significantly. As for grid 3, the only modified layer is the bottom one, which is outside the measurement range, and thus the mean velocity profiles of the original and modified grids are almost identical. Again, these results are obtained without trial-and-error, suggesting that equations 3.3 to 3.5 can serve as a guideline for bespoke design of desired mean velocity profiles using our proposed inhomogeneous multiscale geometries.

For the modified grids, the shape of the mean profiles is also maintained, in fact better than that for the original grids. The absolute values of the averaged mean shear rate $|\overline{\partial U/\partial y}|$ are $0.29\,\mathrm{s}^{-1}$, $2.97\,\mathrm{s}^{-1}$, and $4.99\,\mathrm{s}^{-1}$ for grids 1, 2, and 3, respectively. These shear rates are rather small compared to those of Champagne et al. (1970) and Harris et al. (1977). Nevertheless, higher shear rates could in theory be achieved by increasing the gradient of blockage ratio σ_n of the grid, as long as σ_{max} does not exceed the limit required to avoid recirculations, e.g. $\sigma_{max} = 35\%$ for the current case.

Figure 3.7 shows the mean velocity profiles along the streamwise direction downstream of the modified grids measured at $y = 0.25\,\mathrm{m}$, $y = 0.46\,\mathrm{m}$ and $y = 0.66\,\mathrm{m}$ with streamwise step of $\Delta x = 0.3\,\mathrm{m}$. The difference between the profiles at each y position indicates the shear rate of the flow. The linear fit of the centerline profiles along x gives slopes of 0.0092, -0.043, and -0.067, respectively, and it is concluded that the mean velocity

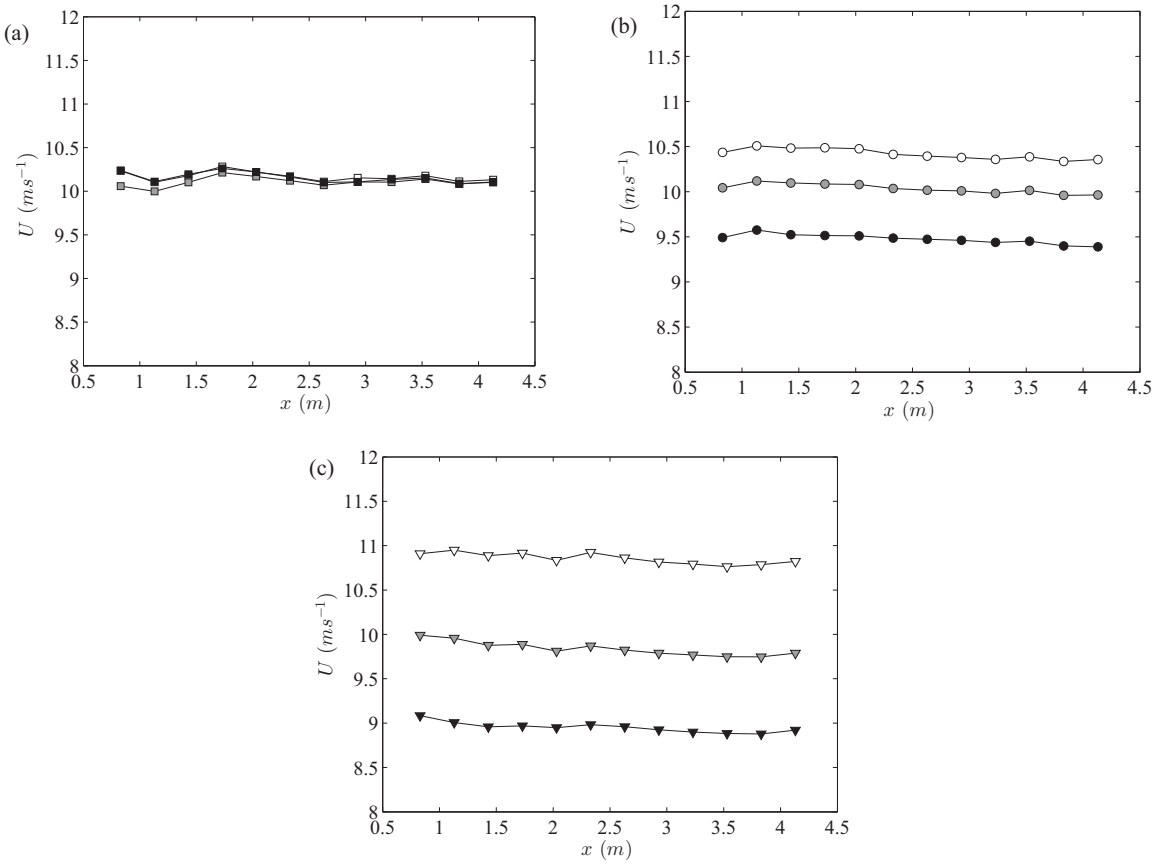

Figure 3.7: Streamwise velocity profiles for modified (a) grid 1, (b) grid 2 and (c) grid 3, at $y = 0.25\,\mathrm{m}$ (white), $y = 0.46\,\mathrm{m}$ (grey) and $y = 0.66\,\mathrm{m}$ (black).

is roughly constant along the streamwise direction. This also coincides with the self-preserved velocity profiles observed in figure 3.6.

In the rest of the paper, only modified grids are discussed to exclude the unwanted velocity variations caused by the non-uniform C_D of the original grids.

3.2.2 Turbulence intensities

To begin this section, we present the turbulence intensities measured at different streamwise locations. The profiles of u'/U_∞ and v'/U_∞ are plotted along the centerline at $y = 0.46\,\mathrm{m}$ in figure 3.8 (a). The decay of both u' and v' is obvious, and the value of v' is always smaller than u' for each individual grid at all locations, and approximately follows

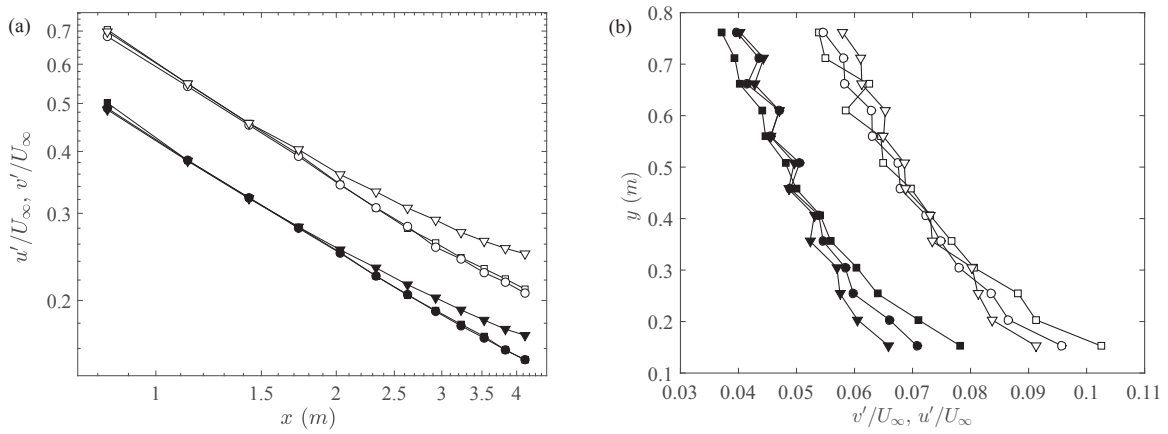

Figure 3.8: Profiles of turbulence intensity u'/U_∞ (empty symbols), v'/U_∞ (filled symbols) along (a) streamwise direction x at the centerline $y = 0.46\,\mathrm{m}$, and (b) vertical direction at $x = 0.83\,\mathrm{m}$ for grid 1 (square), grid 2 (circle), and grid 3 (triangle).

$u'^2 = 2v'^2$, which is consistent with many previous observations in various turbulent shear flows (e.g. Champagne et al., 1970; Tavoularis and Corrsin, 1981; Garg and Warhaft, 1998; Vanderwel and Tavoularis, 2014). The averaged ratio of u'^2/v'^2 throughout all x locations along the centerline for grid 1, 2, 3 is 1.93, 1.90, 2.07, respectively. The value of u'/U_∞ for all grids at different y locations drops from approximately 7% to 2% along the streamwise direction, and it seems for grid 3 that the streamwise turbulence level u' remains higher than the others. This might be explained by the higher drag coefficient C_D as shown in figure 3.3, and the larger mean shear rate of grid 3, which generates turbulence intensity through production and keeps the turbulence level higher than the other grids.

In figure 3.8 (b), we plot u'/U_∞ and v'/U_∞ along the shear direction y at $x = 0.83\,\mathrm{m}$. Both components of the turbulence profiles show a gradient along the shear direction, and the largest value of u'/U_∞ reaches above 10% even at $x = 0.83\,\mathrm{m}$ (or $x/H = 0.9$). This is quite large compared to conventional grid generated turbulence, where the turbulence decays rapidly downstream of the grid, and it suggests that it is possible to increase the turbulence level using the vertical bars. This can be of practical importance for experiments that require large turbulence intensities at a distance downstream of the grid. From this point of view, it is desired to have a quantitative scaling relation for $u'(x, y)$.

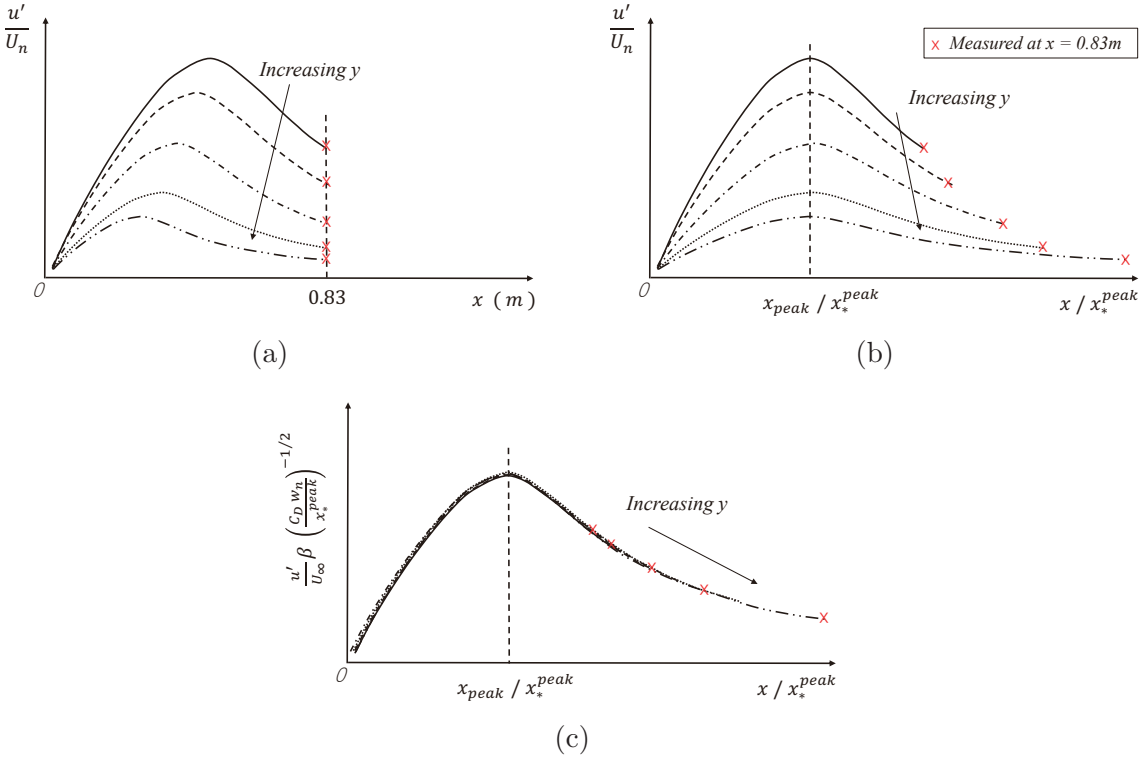

Figure 3.9: Schematic sketch to show the scaling method of the normalized turbulence intensities along y. Different lines in (a) and (b) represent the streamwise turbulence intensity developments behind different layers of the grid.

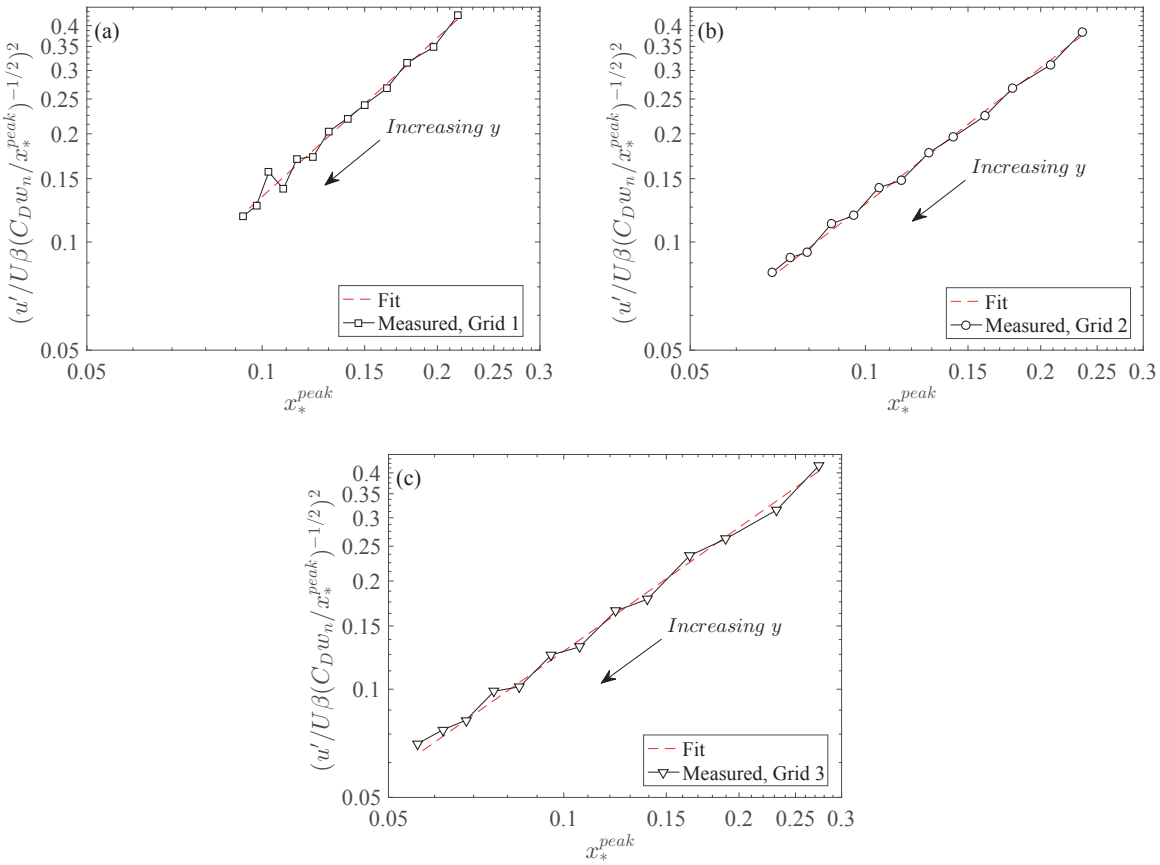

Figure 3.10: Scaling of the normalized turbulence intensity profiles $u'(y)$ measured at $x = 0.83\,\mathrm{m}$ for (a) grid 1, (b) grid 2, (c) grid 3, respectively.

To scale the turbulence intensity profiles $u'(y)$ at given x closely downstream of the grid, we refer to the work of Gomes-Fernandes et al. (2012) mentioned in the introduction. The streamwise turbulence intensity level therefore depends on the streamwise development of the turbulence behind each layer of the grid, as shown in figure 3.9 (a), where the turbulence level and peak location varies from layer to layer. This peak location x_{peak} is different for different layers but scales with the wake interaction length scale x_*^{peak}, which is itself different at different layers n, as illustrated in figure 3.9 (b). Note that the ratio of x/x_*^{peak} is not necessarily one as discussed in the previous chapter, but the fact that the vertical bars at different layers are self-similar guarantees the ratio of x/x_*^{peak} is the same at different layers. The results of (Gomes-Fernandes et al., 2012) also suggest that the turbulence intensity at the peak location can be collapsed in the form $(u'/U_n)\beta(C_D w_n/x_*^{peak})^{-1/2}$, where $\beta = 2.88$ is a constant corresponding to the wake development with laminar incoming flow condition, and U_n is the mean velocity at layer n. Figure 3.9 (c) shows how the streamwise turbulence intensities $u'(x,y)/U_n$ can be collapsed.

The current grids are designed such that the x_*^{peak} at all levels n are smaller than the first measurement location $x = 0.83\,\mathrm{m}$ (see figure 3.4 b), and all the data are therefore in the decay region $x/x_*^{peak} > 1$. We now attempt to use the scalings given in figure 3.9 (c) to establish the y-profile of u' at $x = 0.83\,\mathrm{m}$.

For a streamwise location $x = x_m$, $(u'/U_n)\beta(C_D w_n/x_{*,n}^{peak})^{-1/2}$ is a function of $x_m/x_{*,n}^{peak}$, where $x_{*,n}^{peak}$ varies along the y direction, as shown in figure 3.4. If we assume this function to be a power law, i.e. $(u'/U_n)^2\beta^2(C_D w_n/x_{*,n}^{peak})^{-1} \sim (x_m/x_{*,n}^{peak})^b$, and fit our measurements of $u'(y)/U_n$ obtained at $x_m = 0.83\,\mathrm{m}$, we have $b = 1.47$, 1.26, and 1.14 for grids 1, 2, and 3, respectively. It can be observed in figure 3.10 that the fitted power law functions (dotted line) matches our measurements quite well.

This scaling method quantitatively relates the downstream turbulence intensities with the geometry of the grid bars, i.e. C_D, w_n, and g_n. When the mean shear rate is weak and the streamwise location $x = x_m$ is not too far downstream of the grid but $x_m/x_*^{peak} > 1$,

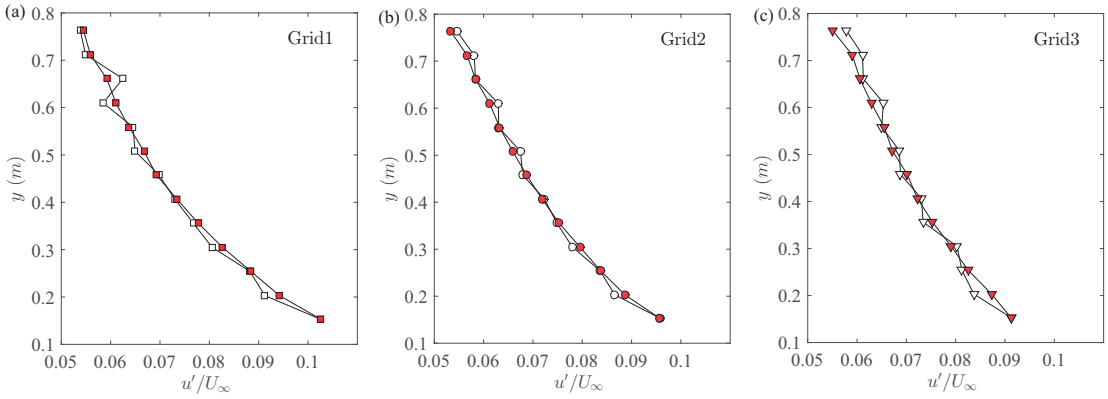

Figure 3.11: Measured (white symbols) $u'(y)/U_\infty$ at $x = 0.83\,\mathrm{m}$ for (a) grid 1, (b) grid 2, (c) grid 3, respectively. Red symbols are calculated values of $u'(y)/U_\infty$ using the top, center and bottoms measurements.

this scaling method allows us to estimate the vertical profile at a streamwise location x_m with three $u'(y)$ measurements to fit the power law function. As an example, we take three points from the bottom ($y = 0.15\,\mathrm{m}$), center ($y = 0.46\,\mathrm{m}$), and top ($y = 0.76\,\mathrm{m}$) of our turbulence intensity profile $u'(y)$ at $x_m = 0.83\,\mathrm{m}$, and then apply the scaling method mentioned above to calculate the turbulence intensity u' at other y locations. The fitted exponents b are 1.49, 1.3, and 1.18 for grid 1, 2, and 3, respectively, similar to the values fitted using all measurement points. The y profiles of u'/U_∞ calculated from $(u'/U_n)^2\beta^2(C_D w_n/x_{*,n}^{peak})^{-1} \sim (x_m/x_{*,n}^{peak})^b$ are shown in figure 3.11, and the difference from measured values are all small.

3.2.3 A general grid design approach

Based on the mean velocity model from section 3.2.1, and the turbulence intensity scaling from section 3.2.2. We now outline a possible procedure to design a grid to produce a flow with bespoke mean velocity and turbulence profiles.

First, the desired mean velocity profile $U_{target,n}$ is used as an input for equation (3.3), (3.4), and (3.5) to solve for the blockage ratio σ_n, subject to $\sigma_n < 0.4$ to prevent recirculation. The average blockage ratio $\overline{\sigma_n}$ can be set to limit the pressure drop, which is $\overline{\sigma_n} =$

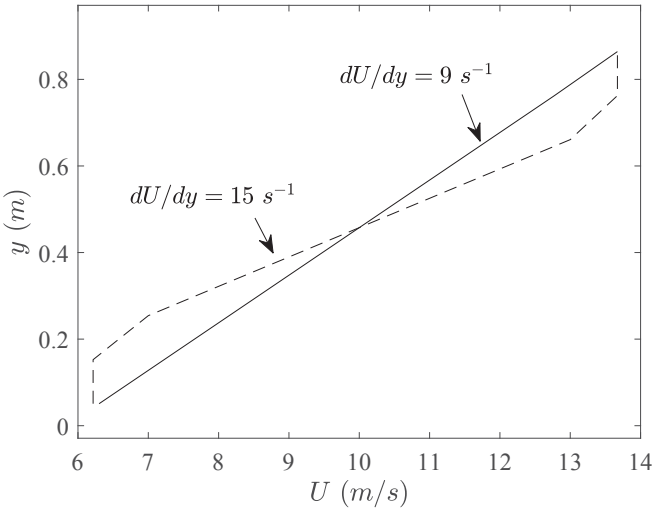

Figure 3.12: Calculated mean velocity profile to demonstrate the maximum mean shear rates achievable in a wind tunnel test section for the case of a uniform shear flow (solid line), and the case where only part of the test section is of interest (dashed line).

0.25 in this case. The problem can be solved by minimizing the error E_1 between the calculated value of U_n and the desired value $U_{target,n}$, which can be defined as $E_1 = \sum [U_n(\sigma_n) - U_{target,n}]^2$. Therefore the problem becomes to find

$$\begin{aligned} &min\ E_1(\sigma_n), \\ &s.t.\ \sigma_n < 0.4,\ \overline{\sigma_n} = 0.25. \end{aligned} \tag{3.6}$$

This can be realized using the $fmincon$ routine in MATLAB$^{\text{TM}}$. For a uniform shear flow across the test section, the maximum mean shear rate one can achieve using this method depends on the physical size of the wind tunnel because the maximum blockage ratio is always limited by $\sigma \leq 0.4$, and the maximum variation of blockage ratio is $(\Delta\sigma)_{max} = 0.4$, which constrains the maximum variation of the mean velocity ΔU. The mean shear rate dU/dy will therefore become larger for a smaller physical domain. For example, for a uniform shear flow, the maximum mean shear rate could be achieved in the current facility (with test section of height $H = 0.91\,\text{m}$) is approximately $9\,\text{s}^{-1}$, but higher mean shear rates could be achieved if only part of the test section is of interest, as demonstrated in figure 3.12.

	S_n	a	b
Grid 1	0.29	3.93	1.47
Grid 2	2.97	2.32	1.26
Grid 3	4.99	1.78	1.14

Table 3.2: Variation of the fitting constants a and b at different mean shear rates, fitted using measurements at $x = 0.83\,\mathrm{m}$ along the y direction.

Secondly, as shown in the previous section, at a streamwise location $x = x_m$, such that $x_m/x_*^{peak} > 1$, we have the scaling relation for the turbulence intensity profile along the y direction $u'(y)$ that $(u'/U_n)^2\beta^2(C_D w_n/x_{*,n}^{peak})^{-1} = a(x_m/x_{*,n}^{peak})^b$, where $\beta = 2.88$, and $C_D = 2.9$ for the current study. The turbulence intensity along the y direction can be therefore expressed as $u'/U_n = f_1(\beta, C_D, w_n, x_m, x_{*,n}^{peak}, a, b)$, where w_n is the width of the vertical bars at layer n, a and b are constants, and $x_{*,n}^{peak}$ is the interaction length scale at layer n. The width of the grid bar w_n is determined by $w_n = f_2(\sigma_n, c_n, *)$ (where c_n is the number of the grid bars at layer n, and $*$ stands for other geometry details of the grid such as the overall width W and thickness of the horizontal bars, see equation 2.1). Since the gap between adjacent vertical bars is defined by $g_n = W/c_n$, the interaction length scale $x_{*,n}^{peak} = 0.21g_n^2/(\alpha C_D w_n)$ (α is a constant characterizing the incoming flow condition) can be written as $x_{*,n}^{peak} = f_3(c_n, C_D, *)$. Finally, we have $u' = f(U_n, \beta, C_D, \sigma_n, c_n, x_m, a, b, *)$. Given a target shape of the turbulence rms velocity profile $u'_{target,n}$, the solution of the problem might be solved by minimizing the error $E_2 = \sum [u' - u'_{target,n}]^2$. Note that the values of a and b cannot be determined analytically based on the current measurements, but their values seem to vary as a function of the mean shear rate S_n for a profile $u'(y)$ measured at a given streamwise location x_m, as shown in table 3.2. This table gives a possible range of the values of a and b, which might be used as a reference to set up the

optimization problem. The problem becomes the minimization of

$$\begin{aligned} &min\ E_2(\beta, C_D, \sigma_n, c_n, x_m, a, b, *), \\ &s.t.\ a \in \mathcal{R},\ b \in \mathcal{R},\ a = f_a(S_n),\ b = f_b(S_n), \\ &c_n \in \mathcal{Z},\ c_n \in [lb, ub], \end{aligned} \tag{3.7}$$

where a and b are expressed as functions of the mean shear rate. The solution of the problem fully determines the geometry of the grid, and the target turbulence rms velocity profile $u'(y)$ could be achieved at a streamwise location $x_p/x_*^{peak} > 1$. The exact location of x_p cannot be predicted yet, because the exact values of a and b cannot be prescribed explicitly based on the current results. However, this procedure does go some way to ensure that the target profile is produced somewhere downstream of $x_{*,n}^{peak}$. The lower bound lb of c_n, is set to 2, which ensures that each layer has at least two vertical bars. The upper bound ub of c_n is determined using equation (3.1) and varies between setups. For example, assuming a 10 mm streamwise thickness of the grid, the minimum width of the vertical bar is $w_{min} = 0.017$ given an aspect ratio $AR = 0.6$, which gives the maximum possible c_n for each layer.

Since the number of bars c_n is restricted to be integers, the problem is solved by Mixed Integer Non-Linear Programming (MINLP), which is an active subject of research in optimization. There are many solvers available, and the results can be compared between different algorithms to give confidence. In principle, a homogeneous shear seems possible using this method where a linear profile of $U_{target,n}$ and a constant $u'_{target,n}$ are used as input to each one of these steps. This approach gives the framework of the grid design method, and the constraints in the problem can be improved and broadened to a wider range of turbulent shear flows with further studies.

3.2.4 Reynolds shear stress

In preparation of the model that we develop in section 3.2.5 to describe the streamwise evolution of the profiles $u'(y)$ from $x = 0.83\,\mathrm{m}$ to larger values of x, we study in this section the streamwise development of the shear correlation coefficient $\rho \equiv -\overline{uv}/u'v'$ given in figure 3.13 (a). It can be observed that, except for grid 1, all values decrease monotonically with streamwise distance. It is interesting to explore if there is a scaling relation that collapses these data. We first look at the dimensionless time scale $\tau^* \equiv (x/\overline{U_c})\,|S_n| = (x/\overline{U_c})\left|\overline{\partial U_n/\partial y}\right|$ (where $\overline{U_c}$ is the streamwise mean velocity averaged over the x along the centerline at $y = 0.46\,\mathrm{m}$) used in previous studies as this is an important parameter to describe the evolution of shear flows. The results are shown in figure 3.13 (b), and $\overline{U_n}$ and $S_n \equiv \overline{\partial U_n/\partial y}$ are the averages of values measured at $x = 0.83\,\mathrm{m}$ and $x = 4.13\,\mathrm{m}$. It is clear that the data does not collapse, especially for grid 2 and 3. If we use a modified local dimensionless time scale defined as $\tau \equiv [(x - x_*^{peak})/\overline{U_n}]\,|S_n|$, it can be seen that ρ is collapsed fairly well for $\tau \geq 0.8$. This definition of τ replaces $\overline{U_c}$ with $\overline{U_n}$, and includes the wake interaction length scale x_*^{peak} as the virtual origin, since x_*^{peak} marks the starting location of decay that varies from layer to layer for each grid. This new definition of τ is equivalent to a translation of τ^* for regular grids, where x_*^{peak} is constant at all positions. The results can be compared between figure 3.13 (b) and (c), where the profiles of ρ of grids 2 and 3 collapse much better with τ.

In several previous experiments (e.g. Rose, 1966; Harris et al., 1977; Tavoularis and Corrsin, 1981; Tavoularis and Karnik, 1989; Nedić and Tavoularis, 2016) it has been shown that the value of the shear correlation coefficient ρ increases downstream along the centerline and eventually reaches a magnitude of approximately 0.45 to 0.5. For the current results, it is interesting that the shear coefficient ρ changes sign for grids 2 and 3, but not for grid 1. Figures 3.13 (b), (c) suggest that the flow is greatly disrupted by the initial conditions that have an effect up to about $\tau = 0.8$, downstream of which the Reynolds shear stress starts to play a significant role. This makes sense by comparing

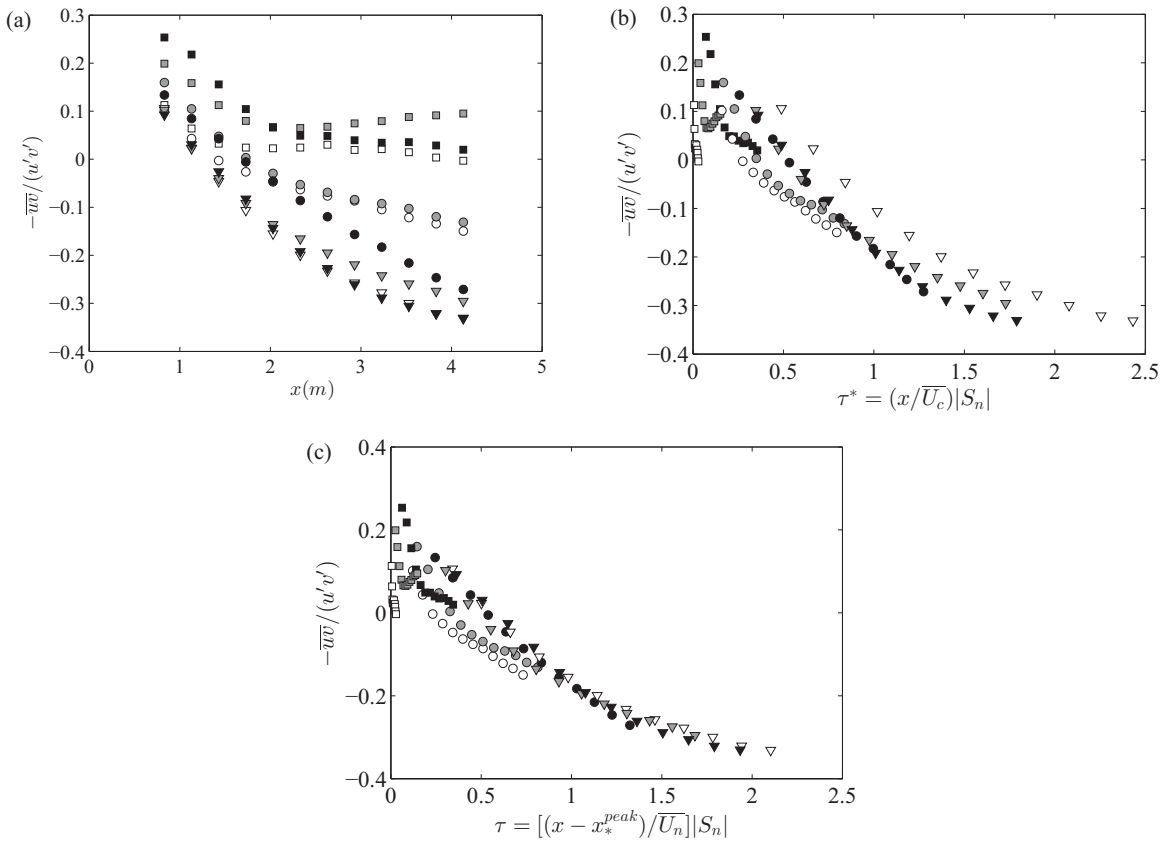

Figure 3.13: Streamwise development of $-\overline{uv}/u'v'$ for grid 1 (square), grid 2 (circle) and grid 3 (triangle) along the streamwise direction at $y = 0.25\,\mathrm{m}$ (white), $y = 0.46\,\mathrm{m}$ (grey) and $y = 0.66\,\mathrm{m}$ (black) versus (a) streamwise location x, (b) local dimensionless time scale $\tau^* \equiv (x/\overline{U_c})\,|S_n|$, and (c) local dimensionless time scale $\tau \equiv [(x - x_*^{peak})/\overline{U_n}]\,|S_n|$ with virtual origin x_*^{peak}.

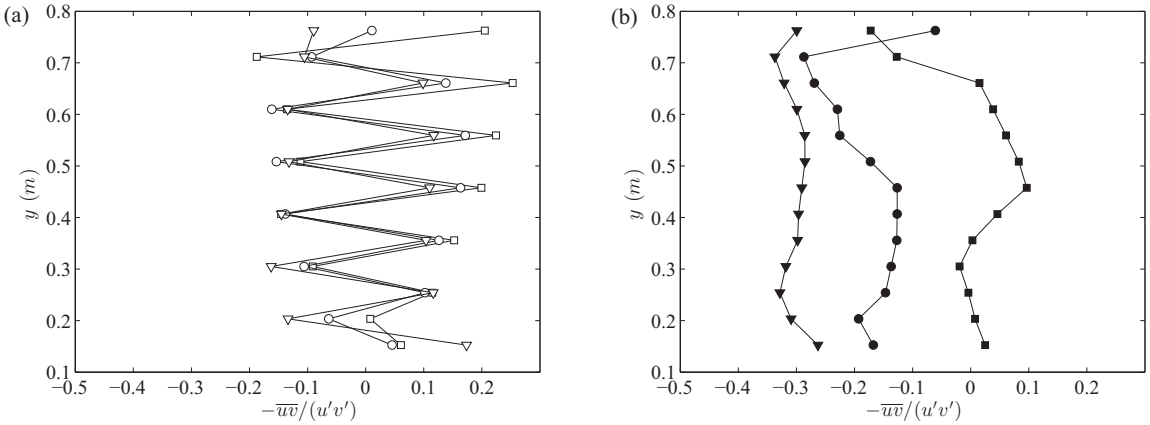

Figure 3.14: Vertical profiles of $-\overline{uv}/u'v'$ for grid 1 (square), grid 2 (circle) and grid 3 (triangle) at (a) $x = 0.83\,\mathrm{m}$ (empty symbols) and (b) $x = 4.13\,\mathrm{m}$ (filled symbols).

	y=0.26m			y=0.46m			y=0.66m		
	ρ_v	ρ_s	CI	ρ_v	ρ_s	CI	ρ_v	ρ_s	CI
Grid 1	0.1146	0.113	0.0016	0.1993	0.1989	0.0004	0.2531	0.2534	0.0003
Grid 2	0.102	0.1017	0.0003	0.1633	0.1594	0.0038	0.1378	0.1335	0.0042
Grid 3	0.1163	0.1058	0.0103	0.1102	0.1021	0.0079	0.0989	0.0923	0.0065

Table 3.3: Comparison of shear correlation coefficients measured from independent expriments at $x = 0.83\,\mathrm{m}$ and different y locations. The 95% confidence interval CI is calculated as $CI = 1.96\mathrm{cov}(\rho_v, \rho_s)/\sqrt{2}$, where ρ_v, ρ_s is the shear correlation coefficient measured from the vertical and streamwise profiles, respectively, and $\mathrm{cov}(\rho_v, \rho_s)$ is the covariance of ρ_v, ρ_s.

with grid 1 whose shear coefficient remains positive all the time and close to zero. Even though the time scale τ is not large enough to show the expected constant value of ρ in the range $0.45 < |\rho| < 0.5$, it can be nevertheless observed that the decrease of ρ with increasing τ slows down after $\tau = 1$, which is consistent with previous literature.

The shear correlation coefficients $-\overline{uv}/u'v'$ along the y direction at $x = 0.83\,\mathrm{m}$ and $x = 4.13\,\mathrm{m}$ are shown in figure 3.14. The oscillatory behavior at $x = 0.83\,\mathrm{m}$ around $-\overline{uv}/u'v' = 0$ is most obvious as the probe moves behind the horizontal bars of the grid at every other y locations. The large fluctuation of shear correlation coefficients with change of signs were also observed in e.g. Rose (1966) in a streamwise location close to the grid ($x/H = 1.33$).

The positive-valued data points in figure 3.14 (a) are from measurements taken at the center of each layer (i.e. behind the vertical bars), which corresponds to the data at $x = 0.83\,\mathrm{m}$ given in figure 3.13 (a). This also supports the assumption that direct effects of the grid dominate in the region of $\tau < 0.8$ as shown in figure 3.13. Table 3.3 gives the error of the shear correlation coefficients from two independent experiments to give confidence in the measurement, indicated by the 95% confidence interval $CI = 1.96\mathrm{cov}(\rho_x, \rho_y)/\sqrt{2}$, where $\mathrm{cov}(\rho_s\rho_v)$ is the covariance of ρ_s, ρ_v measured from the streamwise and vertical profiles, respectively. In figure 3.14 (b), it is observed that the magnitude of the shear coefficients increases from grid 1 to grid 3 (with increasing shear rate), and the variation of $-\overline{uv}/u'v'$ along the y direction is much reduced comparing to that measured at $x = 0.83\,\mathrm{m}$. This is consistent with the streamwise profiles discussed above, and previous observations made by Rose (1966); Garg and Warhaft (1998); Nedić and Tavoularis (2016).

3.2.5 A simplified model for turbulent kinetic energy

To look at the evolution of the y profiles of u' along the streamwise direction x, we have to consider the turbulence production by the mean shear rate, and we propose a simplified model to describe how $u'(x, y)$ evolves in the x direction downstream of our grids. To begin with, we neglect the pressure, transport, and viscous diffusion terms in the turbulent kinetic energy equation. HGC estimated the significance of the transport term by showing that the ratio $|(\partial\overline{u^3}/\partial x)/(U_c\partial\overline{u^2}/\partial x)|$ is smaller than 0.03 in their experiment, and concluded that the transport term can be omitted. In the current study, this ratio decreases rapidly with streamwise distance away from the grid, and the maximum values on the centerline (at $x = 0.83\,\mathrm{m}$) are 0.0105, 0.0102, 0.0113 for grids 1, 2, 3, respectively. We therefore assume that the transport is relatively small compared to the advection term, and that it can be neglected.

With these assumptions, we keep only the production and dissipation terms in the right hand side of the kinetic energy equation following HGC and Tavoularis and Corrsin (1981),

i.e.

$$U\frac{\partial k}{\partial x} = P - \epsilon. \tag{3.8}$$

Then we write $P \cong -\overline{uv}S_n = \rho S_n u'v' = \rho^* S_n u'^2$, where $S_n \equiv \overline{\partial U_n/\partial y}$ is the local mean shear rate, and $\rho^*(x) = \rho(x)/\sqrt{2}$ because $v' = u'/\sqrt{2}$ as discussed in section 3.2.2. By assuming that the transverse r.m.s. fluctuating velocity w' equals v', i.e. $w' = v'$, the turbulent kinetic energy can then be written as $k = \frac{1}{2}(u'^2 + 2v'^2) = u'^2$. Finally we write the dissipation ϵ as $\epsilon = C_\epsilon \frac{k^{3/2}}{L} = C_\epsilon \frac{u'^3}{L}$, where $L = L_{uu,x}(x)$ is the longitudinal integral length scale.

Equation 3.8, for a given n or y (therefore omitted in the equations for simplicity), now becomes

$$U\frac{\partial u'^2}{\partial x} = \rho^*(x) S u'^2 - \frac{C_\epsilon(x)}{L(x)} u'^3. \tag{3.9}$$

To continue with a quantitative description of $u'(x, y)$, we write equation 3.9 at given n as

$$\frac{\partial k}{\partial x} + \xi(x)k = \zeta(x)k^m, \tag{3.10}$$

where $\xi(x) = -\rho^*(x)\frac{S}{U}$, $\zeta(x) = -\frac{C_\epsilon(x)}{UL(x)}$, and $m = 3/2$.

The solution of equation 3.10 is given by

$$\begin{aligned} k &= \left(\frac{(1-m)\int e^{(1-m)\int \xi(x)dx}\zeta(x)dx + C}{e^{(1-m)\int \xi(x)dx}} \right)^{1/(1-m)} \\ &= \left(\frac{-\frac{1}{2}\int_{x_p}^{x} e^{-1/2\int_{x_p}^{x} -\rho^* S/U dx}(\frac{-C_\epsilon}{UL})dx + C}{e^{-1/2\int_{x_p}^{x} -\rho^* S/U dx}} \right)^{-2}, \end{aligned} \tag{3.11}$$

where we write $x_p \equiv x_*^{peak}$ for simplicity. To close equation 3.11, we need the expressions of $\rho^*(x)$, $L(x)$, $C_\epsilon(x)$, and the integration constant C. Since $\rho(\tau)$ collapses well in the way shown in figure 3.13 (c), we fit $\rho^* = \rho/\sqrt{2}$ using a second order polynomial (dashed lines) as shown in figure 3.15 to calculate $\rho^*(x)$ since x_*^{peak}, U_n, and S_n in τ are known at given

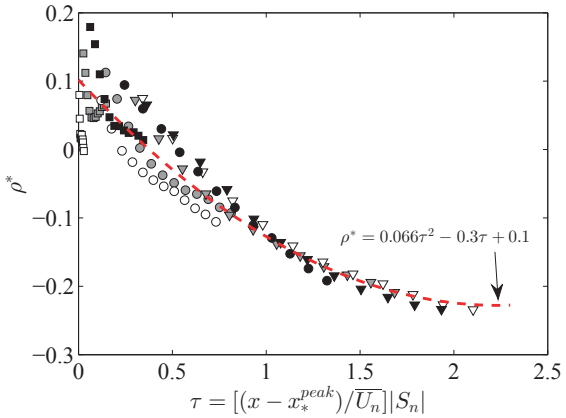

Figure 3.15: Streamwise profiles of ρ^* for grid 1 (square), grid 2 (circle) and grid 3 (triangle) at $y = 0.25\,\mathrm{m}$ (white), $y = 0.46\,\mathrm{m}$ (grey), and $y = 0.66\,\mathrm{m}$ (black) with second order polynomial fit (dashed lines).

y. Here we fit the data with the centerline values of each grid (i.e. grey symbols), and the result captures the evolution of ρ^* quite well. This fitted function is then used to prescribe $\rho^*(x)$ given local constants x_*^{peak}, U_n, and S_n. This fitting method inevitably carries larger error for grid 1 (see figure 3.15) due to the scatter of $\rho^*(x)$ at $\tau \approx 0$. But the mean shear rate produced by grid 1 is approximately 0, and the power $(-0.5S/U \int_{x_p}^{x} -\rho^* dx)$ in the exponential is effectively 0 too, which makes the error for grid 1 insignificant in equation 3.11.

Integral length scale

Now we look at the development of the longitudinal integral length scale L as a function of the streamwise location x for all grids, see figure 3.16. The length scales are calculated using the corrected spectra as discussed in section 3.1.3. It is obvious that L increases with the streamwise location monotonically. The value of L for a given grid at different y locations seems to grow linearly at a rate which is practically similar at all y locations. This also implies that L increases approximately linearly against the local dimensionless time scale τ as well, which is consistent with Champagne et al. (1970) and Harris et al. (1977).

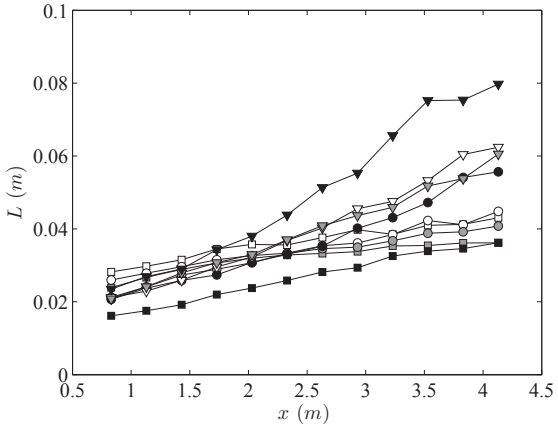

Figure 3.16: Longitudinal integral length scale L profiles for grid 1 (square), grid 2 (circle) and grid 3 (triangle) at $y = 0.25\,\mathrm{m}$ (white), $y = 0.46\,\mathrm{m}$ (grey) and $y = 0.66\,\mathrm{m}$ (black) versus the streamwise location x.

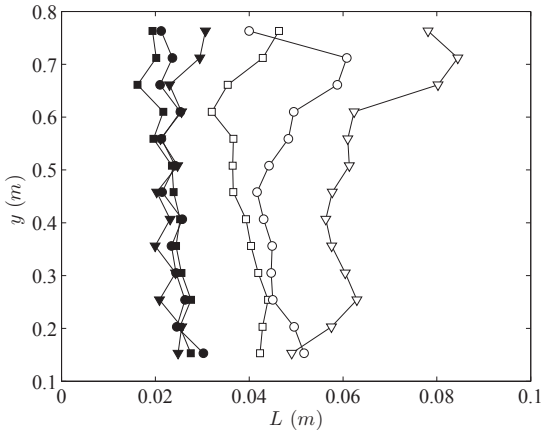

Figure 3.17: Longitudinal integral length scale L profiles for grid 1 (square), grid 2 (circle) and grid 3 (triangle) along the y direction at $x = 0.83\,\mathrm{m}$ (filled symbols) and $x = 4.13\,\mathrm{m}$ (empty symbols).

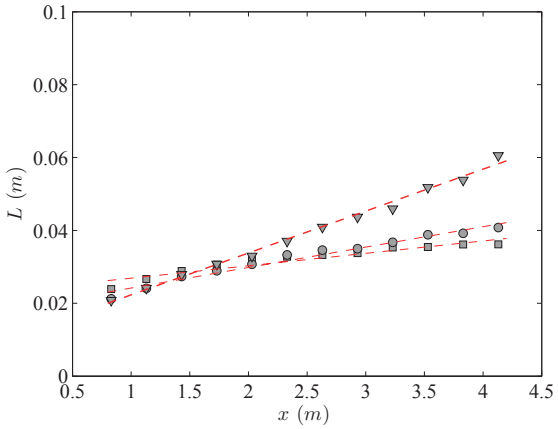

Figure 3.18: Profiles of longitudinal integral length scale L for grid 1 (square), grid 2 (circle) and grid 3 (triangle) along the centerline with linear fitted results (dashed lines).

By looking at the profiles along y in figure 3.17, it seems that L remains roughly constant at $x = 0.83\,\mathrm{m}$. At $x = 4.13\,\mathrm{m}$, the value of L increases from grid 1 (square) to grid 3 (triangle). This makes sense if $L \propto \tau$, as τ increases with the mean shear rate S at given x and U.

From figure 3.16 and 3.17, we notice that the values of L at $y = 0.66\,\mathrm{m}$ are smaller for grid 1 and larger for grid 3, yet the values calculated at this location from the two independent measurements are the same (as shown in figure 3.16 and 3.17), which rules out the possibility of measurement/calculation error. The reason for this larger value is not completely clear, but might have to do with the different inlet grid conditions and the related different mean shear rates.

For the purpose of the current discussion, we ignore this outlier, and assume that the rate of increase of L for a given grid is independent of y. We therefore estimate the streamwise evolution of L based on its centerline profile only. The fitted results are given in figure 3.18, where all three profiles show a linear increase with streamwise distance x away from the grid. This is also consistent with previous works such as Champagne et al. (1970) and Harris et al. (1977). We write $L(x) = px + q$, where p, q are fitting coefficients. The fitted constants are $p = 0.0034$, 0.0056, 0.012, and $q = 0.024$, 0.019, 0.011 for grid 1, 2, 3, respectively.

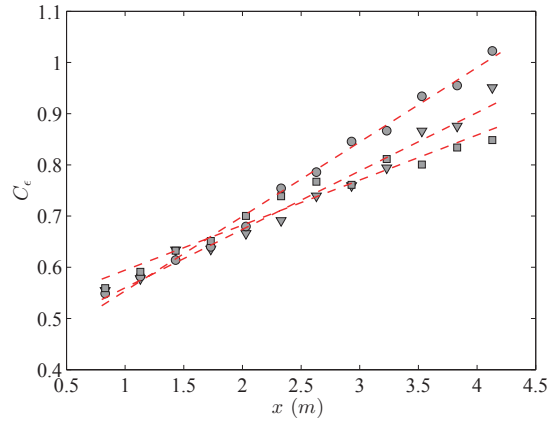

Figure 3.19: Profiles of $C_\epsilon = \epsilon L/u'^3$ for grid 1 (square), grid 2 (circle) and grid 3 (triangle) along the centerline with linear fitted results (dashed lines).

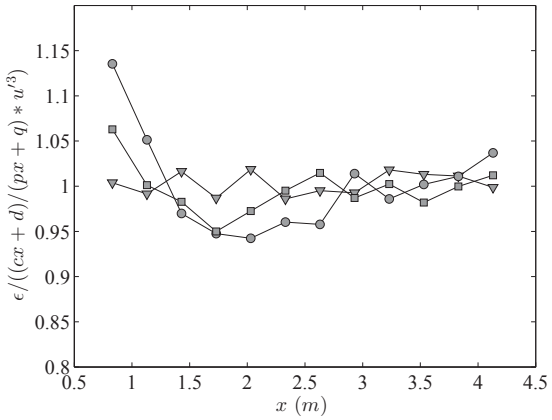

Figure 3.20: Ratio of ϵ and modeled term $(cx+d)/(px+q)u'^3$ grid 1 (square), 2 (circle) and 3 (triangle), respectively, along the centerline.

Dissipation coefficient C_ϵ

The behavior of C_ϵ in turbulent shear flow with uniform mean shear rate has been studied by Nedić and Tavoularis (2016), where they showed different stages of development with respect to τ. In figure 3.19, we show the streamwise development of $C_\epsilon = \epsilon L/u'^3$ along the centerline for all three grids. It can be observed that all three profiles increase linearly as $C_\epsilon = cx + d$, where the coefficients c, d are fitted in a least square sense. The fitted constants are $c = 0.088$, 0.15, 0.11, and $d = 0.51$, 0.41, 0.45 for grids 1, 2, 3 respectively. This linear increase of C_ϵ with x is in agreement with Nedić and Tavoularis (2016) in their initial region.

To check the quality of our linear fits of $C_\epsilon(x)$ and $L(x)$, we plot the ratio $\epsilon/(C_\epsilon u'^3/L)$ as $\epsilon/((cx+d)u'^3/(px+q))$ in figure 3.20. It is observed that this ratio is within $\pm 5\%$ of unity for all three grids, with the exception of the first point.

Predicting streamwise evolution

With the fitted functions of $\rho^*(x)$, $L(x)$, and $C_\epsilon(x)$, we can now rewrite equation 3.11. Using $k = u'^2$ we have

$$\begin{aligned} u' &= \frac{e^{\frac{S}{2U}\int_{x_p}^{x}\rho^*(x)dx}}{\frac{1}{2U}\int_{x_p}^{x} e^{\frac{S}{2U}\int_{x_p}^{x}\rho^*(x)dx}\frac{cx+d}{px+q}dx + C} \\ &= \frac{e^{\frac{S}{2U}[P^*(x)-P^*(x_p)]}}{\frac{1}{2U}e^{\frac{S}{2U}[P^*(x)-P^*(x_p)]}\left[\frac{dp-cq}{p^2}log(\frac{px+q}{px_p+q}) + \frac{c}{p}(x-x_p)\right] + C} \end{aligned} \tag{3.12}$$

where $P^* = \int \rho^* dx$, and the constant $C = C(y)$ in equation 3.12 can be calculated from the vertical turbulence intensity profile $u'(y)$ at $x = 0.83\,\mathrm{m}$.

Figure 3.21 shows the result of both the measured turbulence intensity profiles $u'(x,y)/U_\infty$, and profiles calculated using equation 3.12, where $S = \overline{S_n}$ and $U = \overline{U_n}$. The vertical profile measured at $x = 0.83\,\mathrm{m}$ (where the turbulence intensity is highest, i.e. the first profile on the right) is used as initial values to calculate the constant $C = C(n)$ so the collapse of this profile is perfect. The fitted values of C at selected y locations are given in table 3.4. The measured streamwise profiles are plotted at their corresponding height y, and are used to check the results calculated at different x locations. Each profile is separated by $\Delta x = 0.3\,\mathrm{m}$. Small discrepancies between the measured and calculated values are observed, which might come from the neglected terms in equation 3.9 and the fitting of the centerline profiles. Nevertheless, the results are in appreciable agreement up to $x = 2.33\,\mathrm{m}$, which is equivalent to $x/H = 2.6$, where H is the height of the grid (i.e. height of the tunnel). For grid 3, it is noticed that the discrepancy between measured turbulence intensity and modeled result at $x = 4.13\,\mathrm{m}$ (first profile on the left) is the

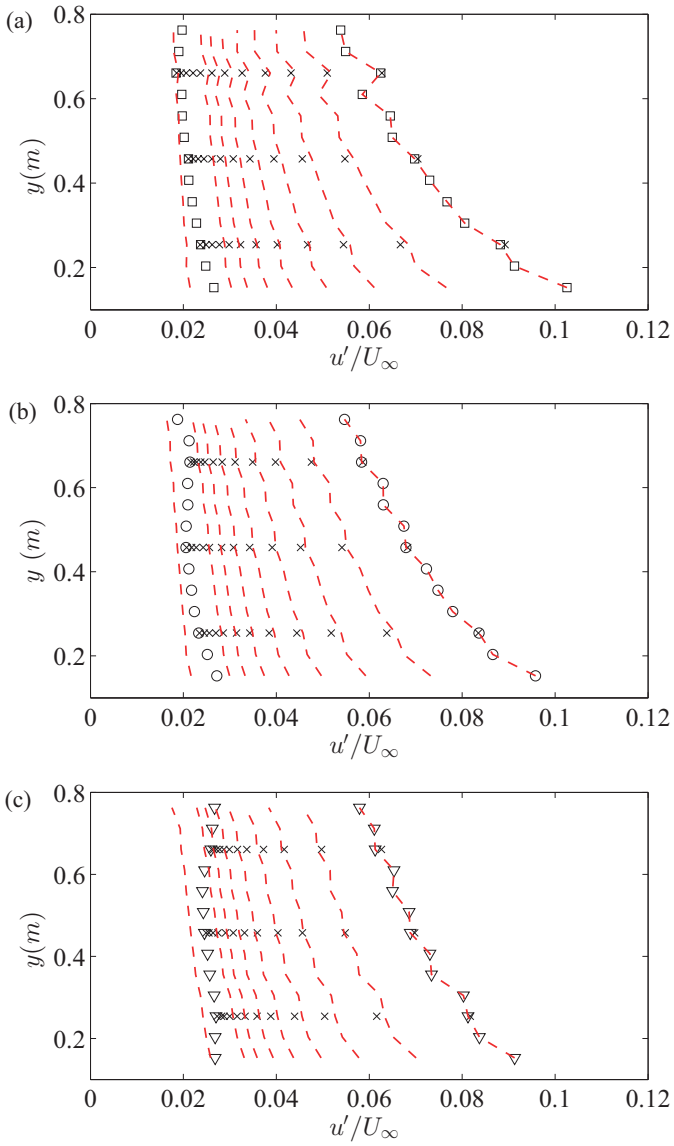

Figure 3.21: Turbulence intensity profiles u'/U_∞ for (a) grid 1 (square), (b) grid 2 (circle), and (c) grid 3 (triangle). Empty symbols are vertical profiles measured at $x = 0.83\,\mathrm{m}$ and $x = 4.13\,\mathrm{m}$. Cross symbols are streamwise profiles measured at given y location. Dashed red lines are predictions calculated using the vertical profile and centerline profile.

$y\ (m)$	Grid 1	Grid 2	Grid 3
0.66	0.82	0.82	0.29
0.46	0.67	0.67	0.31
0.25	0.43	0.50	0.33

Table 3.4: Fitted constant C in equation 3.12 at selected y locations for all grids.

largest, especially at higher y locations. This can be partially explained by the discussion in section 3.2.5 about L increasing faster for grid 3 around $y = 0.7\,\mathrm{m}$. Also, streamwise turbulence intensity developments of shear flows such that u'/U_∞ stops decaying (or starts increasing) at larger τ have been reported by e.g. Rohr et al. (1988); Tavoularis and Karnik (1989). In such case, flow characteristics such as C_ϵ, ρ, and L all evolve in different ways compared to their initial development as discussed by Nedić and Tavoularis (2016). A more comprehensive model of the problem will require measurements at further stages of the turbulent kinetic energy evolution in terms of τ. Nevertheless, the current method provides a practical solution for the near-region turbulent kinetic energy development of our multiscale grid generated shear flow, and can be of practical use in the study of turbulent shear flows and engineering applications.

3.2.6 Taylor microscales

In this section we report Taylor microscale values calculated from $\lambda = u'/((\overline{\partial u/\partial x)^2})^{1/2}$. Figure 3.22 (a) gives the streamwise development of λ versus x. It can be observed that λ increases with x in all cases. This agrees well with several previous experiments such as Rose (1966); Champagne et al. (1970). Tavoularis and Karnik (1989) also showed a region $\tau^* > 16$, where λ remains constant against τ. This is not observed here due to the small mean shear rates. We also report the local Reynolds number $Re_\lambda = u'\lambda/\nu$ along the x direction, where ν is the kinematic viscosity. Their values decrease monotonically for grid 1 and grid 2. For grid 3, a mild increase after $x = 2.5m$ is observed, which corresponds

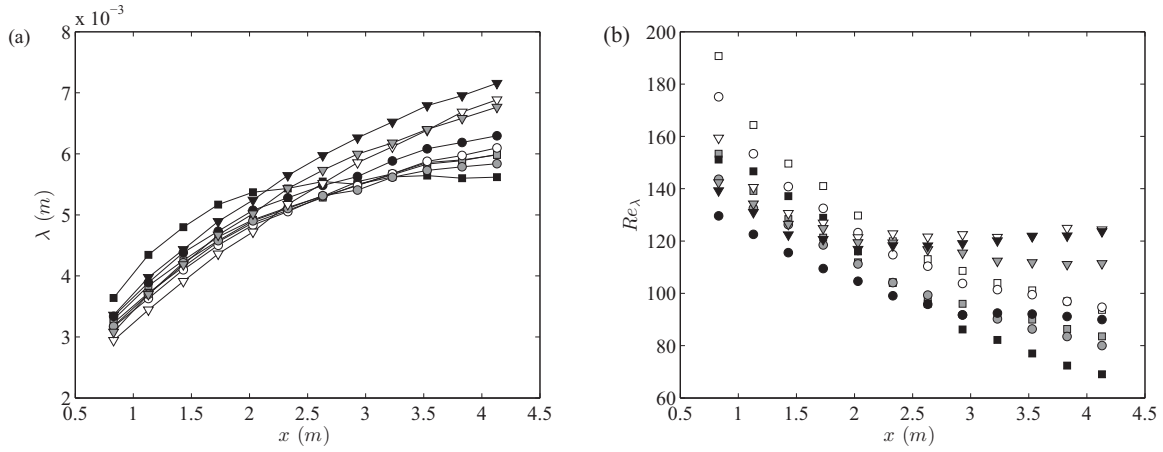

Figure 3.22: Streamwise profiles of (a) Taylor microscale λ, and (b) local Reynolds number Re_λ for grid 1 (square), grid 2 (circle) and grid 3 (triangle) at $y = 0.25\,\mathrm{m}$ (white), $y = 0.46\,\mathrm{m}$ (grey) and $y = 0.66\,\mathrm{m}$ (black).

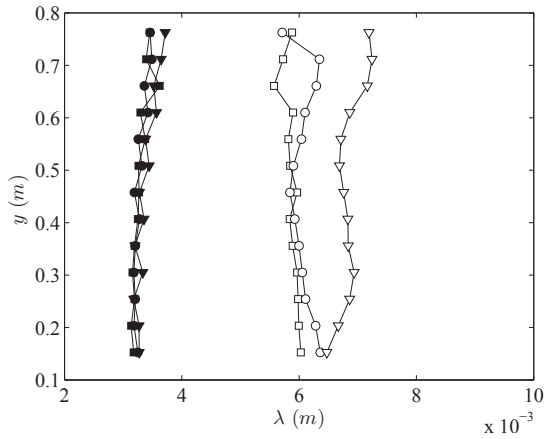

Figure 3.23: Taylor microscale λ profiles for grid 1 (square), grid 2 (circle) and grid 3 (triangle) along the y direction at $x = 0.83\,\mathrm{m}$ (filled symbols) and $x = 4.13\,\mathrm{m}$ (empty symbols).

to its higher turbulence intensity u' (see figure 3.8 a), and the larger value of λ (see figure 3.22 a). This is in agreement with the observation of Nedić and Tavoularis (2016) where they showed an increase of Re_λ after $\tau^* > 4.5$.

Along the shear direction y, Rose (1966) reported decreasing values of λ with increasing local mean velocity, whereas Champagne et al. (1970)showed roughly constant values of λ along the shear direction. The shear rates of the two cases are similar, i.e. $\partial U/\partial y = 13.6\,\mathrm{s}^{-1}$ and $12.9\,\mathrm{s}^{-1}$, respectively, so it seems the shear rate is not the reason for this difference. Note however, Rose (1966) used wire gauze with different spacings along the

	Grid 1			Grid 2			Grid 3		
x(m/s)	0.83	2.33	4.13	0.83	2.33	4.13	0.83	2.33	4.13
x/H	0.91	2.55	4.52	0.91	2.55	4.52	0.91	2.55	4.52
U/U_∞	1.006	1.012	1.011	1.004	1.004	0.996	0.999	0.987	0.979
u'/U_∞	0.07	0.031	0.021	0.068	0.031	0.021	0.070	0.033	0.025
Re_λ	153.4	119.3	111.4	143.6	104.1	80.06	142.3	119.3	111.4
$-\overline{uv}/u'v'$	0.199	0.065	0.095	0.159	-0.053	-0.131	0.102	-0.166	-0.296
u'/v'	1.41	1.37	1.39	1.40	1.37	1.36	1.44	1.42	1.46
$L_{uu,x}/L_{vv,x}$	2.12	1.84	1.58	1.98	1.89	1.67	1.96	1.94	2.12
$\frac{\overline{(\partial v/\partial x)^2}}{\overline{(\partial u/\partial x)^2}}$	0.941	1.071	1.091	0.938	1.074	1.091	0.963	1.099	1.129

Table 3.5: Summary of centerline turbulence characteristics at different streamwise locations for different grids at $Re_D = 8500$ based on the width of the vertical grid bar.

shear direction as a generator, while Champagne et al. (1970) used parallel plates with equal spacing but different local blockage ratios to generate the shear flow. There are no more data available for a more comprehensive conclusion, but the current study is similar to that of Champagne et al. (1970), in that the layer height is constant with varying local blockage ratios, and therefore it might be expected to have a roughly constant y-profile of λ. The results of the Taylor microscale λ along the y direction at $x = 0.83\,\mathrm{m}$ and $x = 4.13\,\mathrm{m}$ are given in figure 3.23, and it indeed seems roughly constant.

3.2.7 Flow isotropy

Having shown the streamwise development of turbulence intensities and length scales, we now examine the isotropy of the flow. Some of the results are given in table 3.5 at different x locations along the centerline at $y = 0.46\,\mathrm{m}$. The small scale isotropy indicator $\overline{(\partial v/\partial x)^2}/\overline{(\partial u/\partial x)^2}$ seems to suggest that the flow is anisotropic as the ratio is much smaller than the isotropic value of 2, even though they are increasing along the x direction. These results are in agreement with previous observations made by Shen and Warhaft (2000b) and Schumacher (2001).

It is interesting that the results close to the grid suggest large scale isotropy of the flow such that $L_{uu,x}/L_{vv,x} = 2$, but $u'/v' \approx 1.4$ on the other hand. These values are maintained best by grid 3 if we compare the values at different streamwise locations in table 3.5. Intuitively, the shearing stress is expected to strain the large scale structure along the mean shear direction and impose anisotropy to the flow, which seems to counter our observation that $L_{uu,x}/L_{vv,x} = 2$. Similar observations have been reported before, for example Rose (1966) showed $L_{uu,x}/L_{uu,y} = 2$ and $u'/v' \approx 1.5$ in a turbulent shear flow generated by a parallel wire grid, and Tavoularis and Corrsin (1981) reported $L_{uu,x}/L_{vv,x} = 4.34$ with $u'/v' \approx 1.4$ in a parallel plate generated turbulent shear flow. These observations seem to suggest that the ratio of $L_{uu,x}/L_{vv,x}$ and u'/v' reflect different aspects of anisotropy of the flow, and do not need to take their isotropic values concordantly.

3.2.8 Transverse homogeneity

The transverse homogeneity of the shear flow is discussed in this section. The mean velocity and turbulence intensity profiles are given in figure 3.24 (a) and (b), respectively, measured at $x = 0.83\,\mathrm{m}$ (or $x/H = 0.91$, open symbols) and $x = 4.13\,\mathrm{m}$ (or $x/H = 4.52$, filled symbols) across the center of the grid at $y = 0.46\,\mathrm{m}$ or $y/H = 0.5$. From figure 3.24 (a), it is observed that the transverse profiles of the streamwise mean velocity are more homogeneous closer to the grid, whereas the vertical mean velocity is more homogeneous further downstream (filled symbol with dashed line in the inserted figure). A sinusoidal variation seems to be present for the streamwise mean velocity profiles measured at $x = 4.13\,\mathrm{m}$, and the profiles seem to be symmetric about the center plane $z = 0\,\mathrm{m}$, although the variations are all within $8\%U_\infty$. For the mean velocity profiles of V/U_∞, the sinusoidal variation is also observed symmetric about the center plane, and the amplitude is smaller (within $5\%U_\infty$). The symmetry is due to the alignment of the vertical bars at $z = 0\,\mathrm{m}$, and might be reduced by arranging the vertical bars in a staggering pattern.

This symmetry is also observed in the transverse profiles of streamwise turbulence inten-

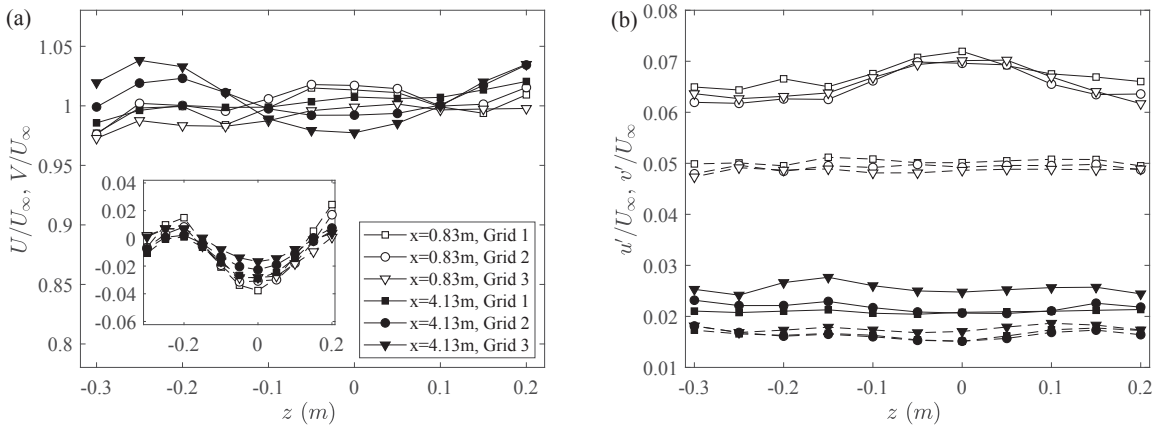

Figure 3.24: Transverse profiles of (a) mean velocity U/U_∞ (symbols with solid line) and V/U_∞ (inserted figure, symbols with dashed line); (b) turbulence intensity u'/U_∞ (symbols with solid line) and v'/U_∞ (symbols with dashed line) across the center of the grid where $y/H = 0.5$.

sity u'/U_∞ at $x = 0.83\,\mathrm{m}$, as shown in figure 3.24 (b) with open symbol and solid line. Nevertheless, the variation of the turbulence intensity is within $1\%U_\infty$. The transverse profiles of v'/U_∞ seems to be more homogeneous in all cases. We therefore further quantify the homogeneity of the streamwise properties in the transverse direction, referring to the criteria proposed by Corrsin (1963), namely

$$\partial L_u/\partial z \ll 1, \tag{3.13a}$$

$$(L_u/\lambda)\partial\lambda/\partial z \ll 1, \tag{3.13b}$$

$$(L_u/\overline{u^2})\partial\overline{u^2}/\partial z \ll 1. \tag{3.13c}$$

The results are given in figure 3.25 for measurements taken at $x = 0.83\,\mathrm{m}$ (open symbols), and $x = 4.13\,\mathrm{m}$ (filled symbols).

The values of the homogeneity criteria, as shown in figure 3.25, are all smaller at the streamwise location closer to the grid. The values calculated at $x = 0.83\,\mathrm{m}$ are all within ± 0.05 as seen in figure 3.25 (a-c). These figures suggest that the transverse homogeneity of the shear flow is better at $x = 0.83\,\mathrm{m}$, or $x/H = 0.91$, which is a nice trait as the turbulence intensity level is higher in this region.

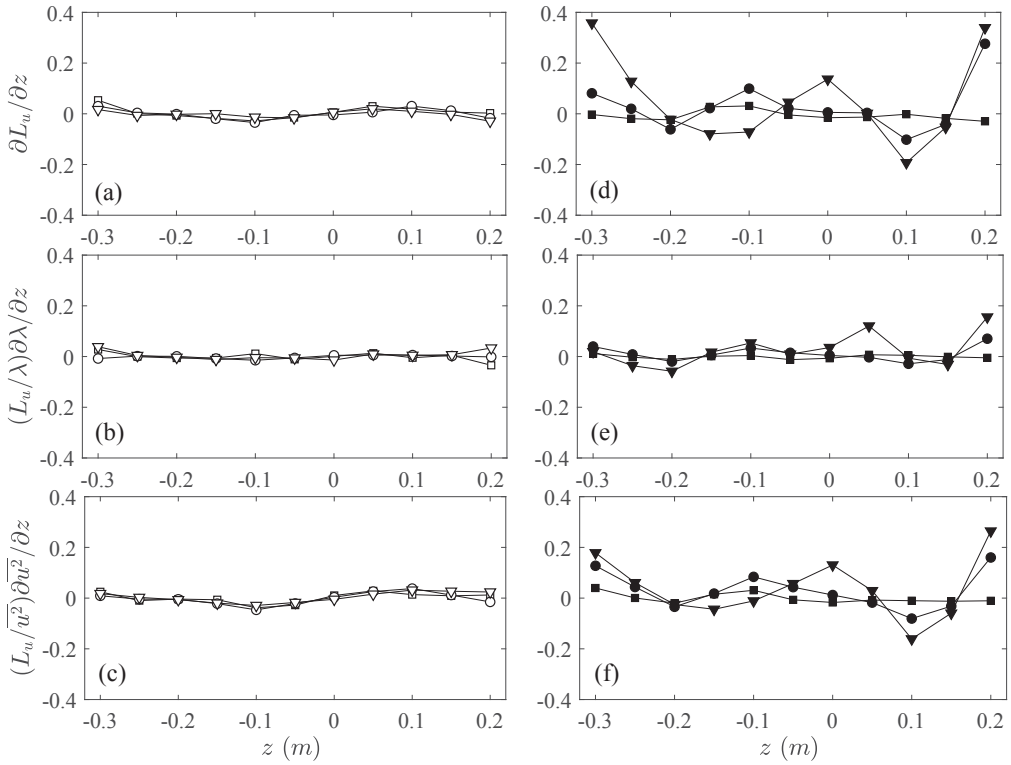

Figure 3.25: Homogeneity of the transverse profiles for grid 1 (square), grid 2 (circle), and grid 3 (triangle) at $x = 0.83\,\mathrm{m}$ (or $x/H = 0.91$, open symbols) and $x = 4.13\,\mathrm{m}$ (or $x/H = 4.52$, filled symbols) across the center of the grid at $y/H = 0.5$.

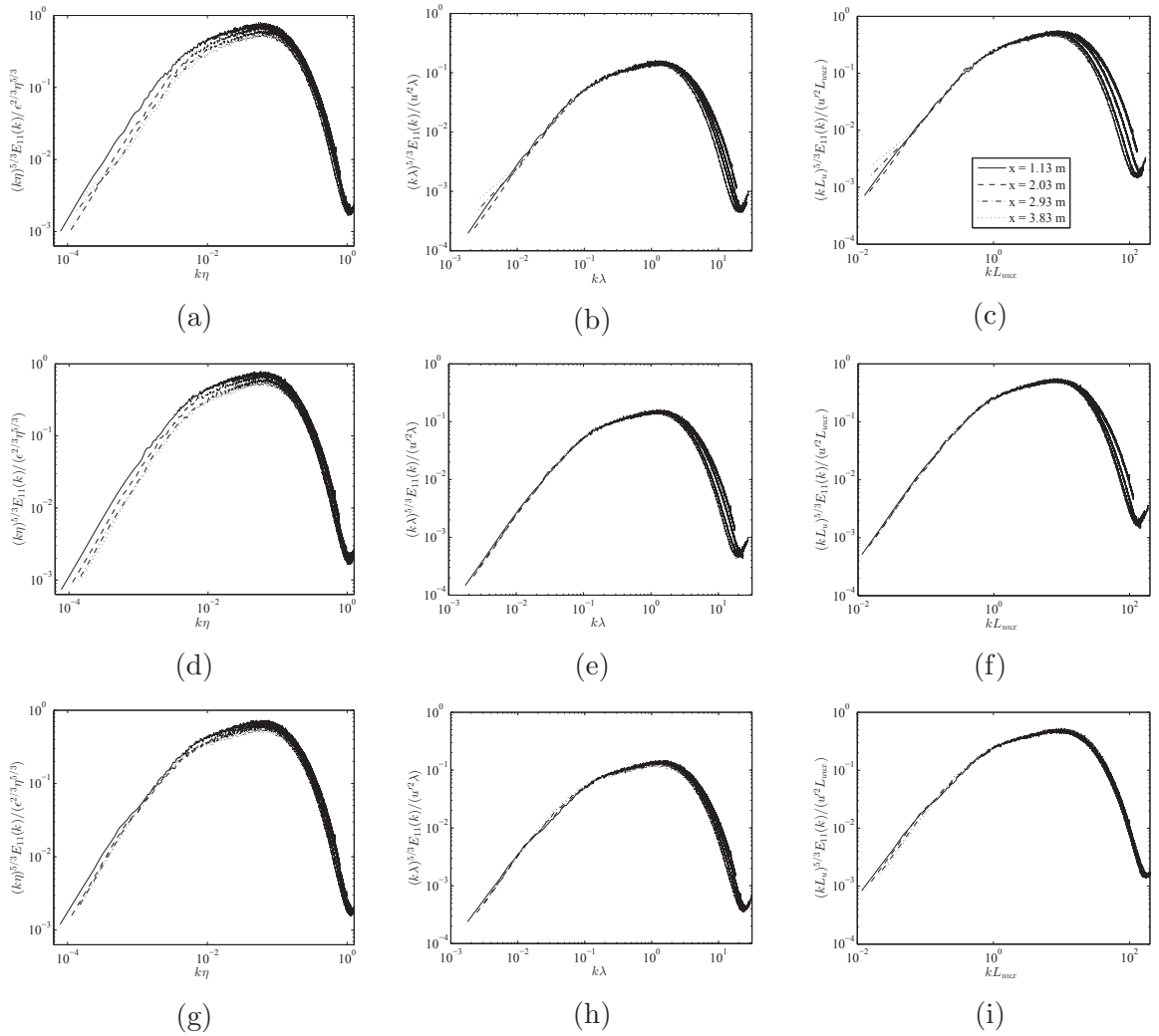

Figure 3.26: Turbulence spectra $E_{11}(k)$ at four x locations along the centerline at height $y = 0.46\,\mathrm{m}$ for grid 1 (a, b, c), grid 2 (d, e, f), and grid 3 (g, h, i), compensated for η, λ, and L, respectively.

3.2.9 Spectra

The spectra for all three grids are presented here at four streamwise locations, namely $x = 1.13\,\mathrm{m}$, $2.03\,\mathrm{m}$, $2.93\,\mathrm{m}$, $3.83\,\mathrm{m}$. The Reynolds number is in the range of $70 < Re_\lambda < 190$. First of all, considering grid turbulence, the one dimensional spectra are expected to collapse at corresponding range when normalized with $L_{uu,x}$, λ, and η, respectively. Figure 3.26 shows the spectra measured at different x locations along the centerline at height $y = 0.46\,\mathrm{m}$. It shows that the spectra collapse well in the small wavenumber range when normalized with L, and in the large wavenumber range when normalized with η.

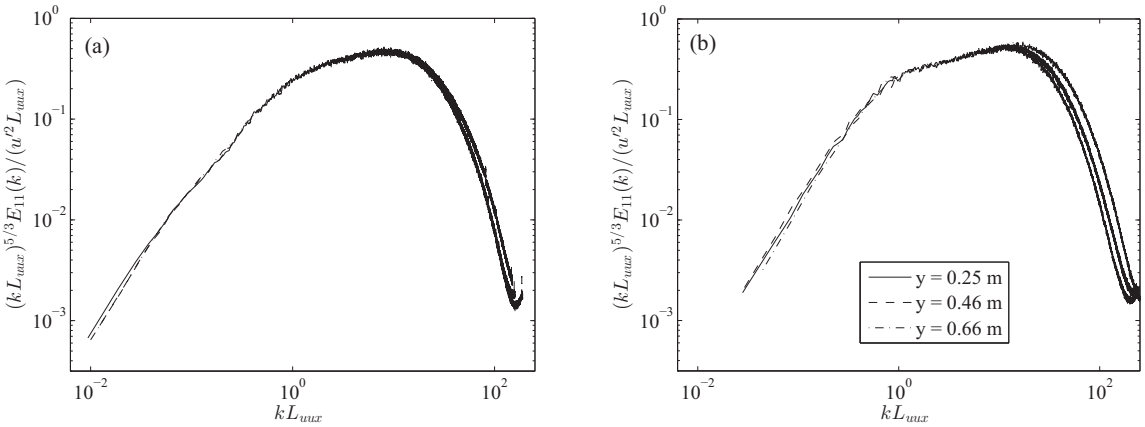

Figure 3.27: Turbulence spectra $E_{11}(k)$ at several y locations compensated for L at (a) $x = 0.83\,\mathrm{m}$, and (b) $x = 4.13\,\mathrm{m}$.

This is consistent with those conclusions for homogeneous isotropic turbulence.

It is also observed from figure 3.26 such that for all scaling methods, the quality of collapse improves from grid 1 to grid 3, and it is interesting that for grid 3, the integral length scale L_{uux} seems to collapse the spectra at all wave numbers. The reason for this is not exactly clear.

When the spectra of grid 3 at different y locations are plotted together, as shown in figure 3.27, the collapse is not observed even when compensated using the longitudinal integral length scale $L_{uu,x}$, and the difference seems to increase with streamwise distance. These observations suggests the dependency of $E(k)$ on the initial conditions of the grid, but this dependency cannot be quantified at the moment.

3.3 Summary

In this chapter a new class of inhomogeneous multiscale grids is proposed and the turbulent shear flows generated by these grids are investigated using hot-wire anemometry. There are three major advantages of such grids in generating turbulent shear flows:

(i) Generation of a desired mean velocity profile is possible by optimizing the blockage

ratio profile σ_n, while maintaining a constant C_D profile of the vertical bars. The drag coefficient of the vertical bars was found to affect the mean velocity profiles significantly, and it is therefore important to maintain a constant C_D. The mean velocity model after Taylor et al. (1949) and McCarthy (1964) based on the local blockage ratio σ_n was shown to agree with our measurements, with mean shear rates of $0.29\,\mathrm{s}^{-1}$, $2.97\,\mathrm{s}^{-1}$, and $4.99\,\mathrm{s}^{-1}$ for grids 1, 2, and 3, respectively. The maximum possible mean shear rate generated by these grids depends on the size of the test facility as the maximum local blockage ratio is always constrained by $\sigma_n < 0.4$.

(ii) High turbulence intensities can be generated simultaneously with the desired mean velocity profile. The maximum turbulence intensities generated by the present grids are of the order $10\%U_\infty$, which is much larger than those generated by previously reported passive shear generators, and it seems possible to prescribe the shape of the turbulence intensity profile. From the scalings proposed by Gomes-Fernandes et al. (2012), and by considering the non-uniform convection velocity, it was shown that at a streamwise location $x = x_m$ such that $x_m/x_*^{peak} > 1$ ($x_m/H = 0.9$ for the current cases), the y-profiles of turbulence intensity $u'(y)$ scale as $(u'/U_n)^2\beta^2(C_D w_n/x_{*,n}^{peak})^{-1} \sim (x_m/x_{*,n}^{peak})^b$, where $\beta = 2.88$ is a constant, U_n is the local (in y or equivalently n) mean velocity, and b is a power law constant. Based on this scaling relation, it seems possible to optimize the grid geometry to produce a desired shape of turbulence intensity profile. From the mean velocity model and the scaling of turbulence intensity, a general approach to the design of multiscale inhomogeneous grids is proposed and briefly discussed in section 3.2.3. The methodology can be improved by adding more constraints to the optimization problem, as new results of such experiments emerge.

(iii) For a given grid, the generated turbulence field can be described using one centerline measurement along the streamwise direction and one vertical profile at $x/x_*^{peak} > 1$. For the current study, the proposed model successfully predicts the y-profiles of u' at different x locations up to $x/H \approx 2.5$ for all cases as shown in figure 3.21. The evolution of various

flow characteristics included in the model was also studied and compared with previous literature.

There are some other interesting observations of the shear flows generated by these multiscale grids such as the spectra, as briefly discussed in the appendix. In terms of future work, the potential of the grid design method should be explored further to establish the range of turbulent shear flows that can be produced. The special case of homogeneous turbulent shear flows could be attempted with our grid design method because of the long standing fundamental interest in such flows. Due to the small mean shear rate, the dimensionless time scale ranges from $\tau = 0$ to 2.3. So it is also interesting to extend the range of measurement to larger dimensionless time scale τ, where the development of various turbulence characteristics and length scales could be further examined. This can be achieved by either extending the measurement distance or increasing the mean shear rate. Measurements with multiple hot-wires will also help to understand the neglected terms in the turbulent kinetic energy model. Such studies, if successful, would provide another option to design a shear flow with desired mean velocity and turbulence intensity profiles, which will benefit both fundamental studies and a wide range of practical applications.

Chapter 4

Engineering wind tunnel testing of the multiscale inhomogeneous grids

In this chapter, a modified version of the inhomogeneous multiscale grids introduced in Chapter 3 is tested in a low-fidelity engineering wind tunnel to verify the mean velocity model, the turbulence intensity scaling, and the evolution of turbulence characteristics as discussed in the previous chapter. The grids were re-engineered to fit in a new completely different wind tunnel, and therefore the robustness of the previously proposed mean velocity model and scaling relation can be tested. A description of the grid is first given in section 4.1.2. In section 4.1.3, the measurement method is introduced, and measurements of the background flow are presented. Some modifications to the flow conditioner were implemented by trial-and-error to improve the incoming flow quality in the wind tunnel. In section 4.2, the mean velocity results are first presented, with comparisons to the mean velocity model discussed in section 3.2.1. The scaling of turbulence intensities along the shear direction is examined according to the relation proposed in section 3.2.2, and the streamwise evolution is discussed. The evolution of the streamwise integral length scale $L_{uu,x}$ is also presented at the end of section 4.2.3.

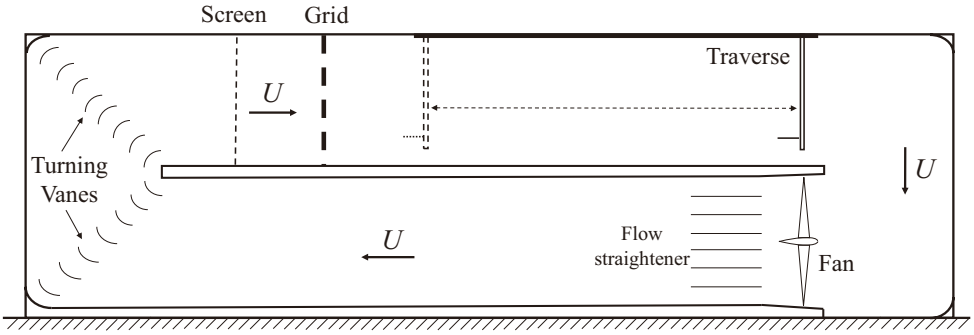

Figure 4.1: Schematic sketch of the Mel Consultants wind tunnel. Dimensions not in scale.

4.1 Experiments

4.1.1 Facility

All experiments in this chapter were performed in the wind tunnel at Mel Consultants Ltd located in Melbourne, Australia. The Mel Consultants wind tunnel is a close return wind tunnel designed for wind engineering testings, which has a lower and upper test section, as shown in figure 4.1. The upper test section, which was used for current experiments, is 4.8 m wide, 2.5 m high, and 25 m in length. The air is driven by a fan at the beginning of the lower test section. Then the flow goes through a flow straightener and a 1.5:1 contraction before entering the lower test section. After the turning vanes on the upper test section, a screen (as illustrated in figure 4.1) is installed to reduce the turbulence intensity and to homogenizes the incoming flow. A second screen was installed on site to improve the flow quality, which is discussed in details in section 4.1.3. In the following discussions, x, y, z represents the streamwise, vertical, and transverse direction, respectively.

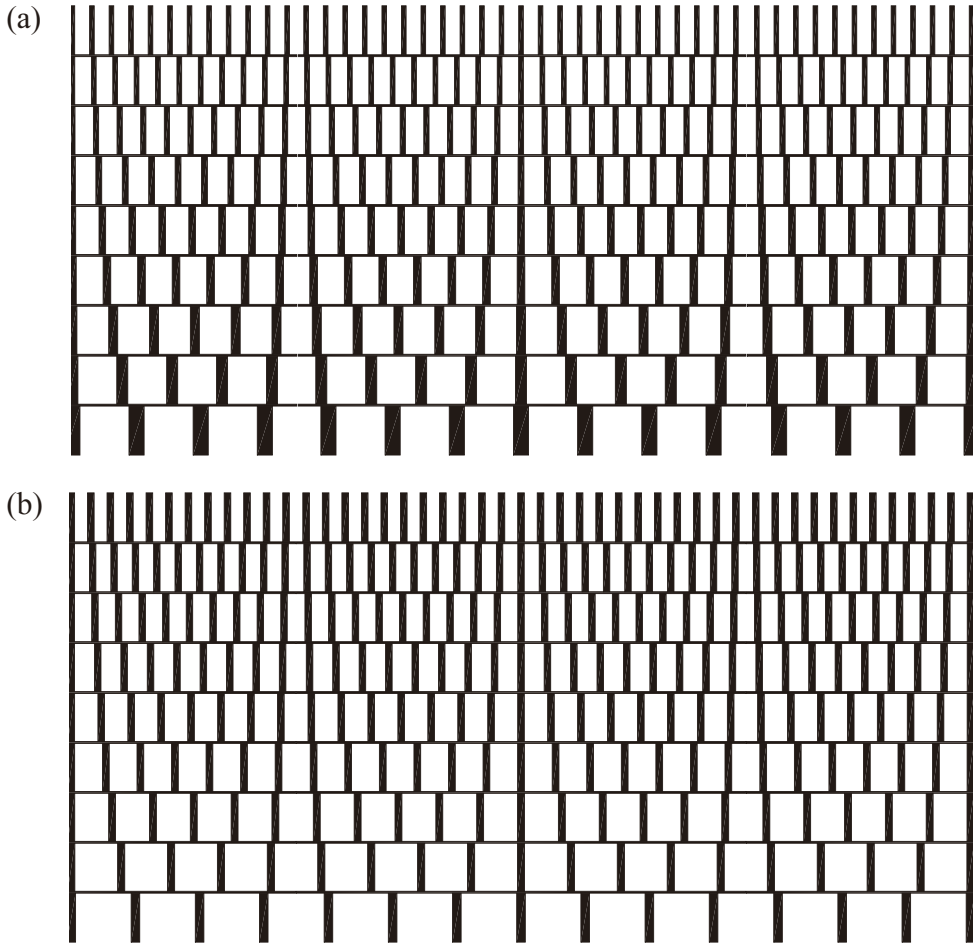

Figure 4.2: The inhomogeneous multiscale grid, (a) Grid 1, and (b) Grid 3, for the Mel Consultants wind tunnel.

4.1.2 Grid design

As discussed in Chapter 3, the inhomogeneous multiscale grid produces mean velocity and turbulence intensity profiles that relate to the geometry of the grid. Two of the grids (Grid 1 and Grid 3, as defined in section 3.1.2), are modified to fit in the Mel Consultants wind tunnel. The grid is repeated in the z direction to cover the entire cross section of the tunnel. The sketches of Grid 1 and Grid 3 are given in figure 4.2.

The grids are cut in plywood sheets of 18 mm thickness. Each grid is made in eight pieces, which are mounted on the walls using L-brackets, and the connections in between are glued and reinforced using aluminum foils rapped around the horizontal bars. The dimensions

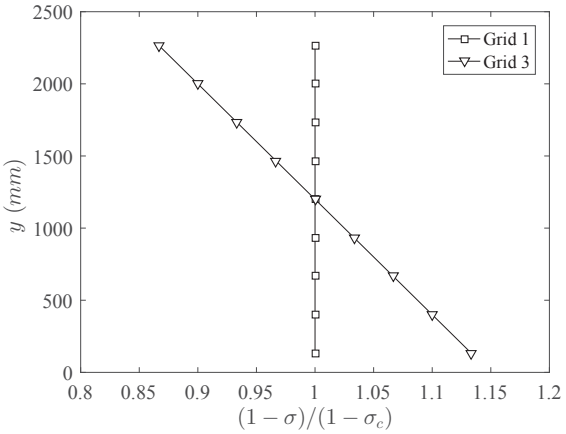

Figure 4.3: Profiles of the normalized blockage ratios of Grid 1 and Grid 3 at different y locations, where σ_c is the blockage ratio at layer 5, the center of the grid.

of the grids were designed to represent the Grid 1 and Grid 3 defined in section 3.1.2 with the same blockage ratio profiles across the wind tunnel height, as shown in figure 4.3. The total height of the grids is $H = 2.4\,\mathrm{m}$. As discussed in section 3.2.1, the aspect ratio of the vertical bars $a_n = d_n/w_n$ is crucial in generating the mean velocity profiles, where d_n is the depth of the bar in the streamwise direction, and w_n is the width of the bar in the transverse direction. The maximum drag coefficient of a rectangular bar is achieved with $a_n = 0.6$ (Bearman and Trueman, 1972). Therefore, the aspect ratio of the grid bars is adjusted by attaching laser cut acrylic pieces to the lee of the grid. For Grid 1, the top three levels are not modified because the aspect ratio is already larger than the target value of 0.6. The local drag coefficients C_D at different y locations of Grid 1 and Grid 3 after the modification are calculated after Bearman and Trueman (1972), and the results are given in figure 4.4. The top three levels of Grid 1 have smaller drag coefficients C_D due to the limits of the modification.

The wake interaction length scale (as defined by Valente and Vassilicos, 2012) is calculated as $x_*^{peak}(n) = 0.21 g_n^2/(\alpha C_D w_n)$, where g_n is the distance between adjacent vertical bars at layer n, α is a constant, and w_n is the lateral width of each individual bar. The constant α characterizes the turbulence intensity of the incoming flow, and $\alpha = 0.287$ is used following Symes and Fink (1977) since the free stream turbulence intensity in the Mel

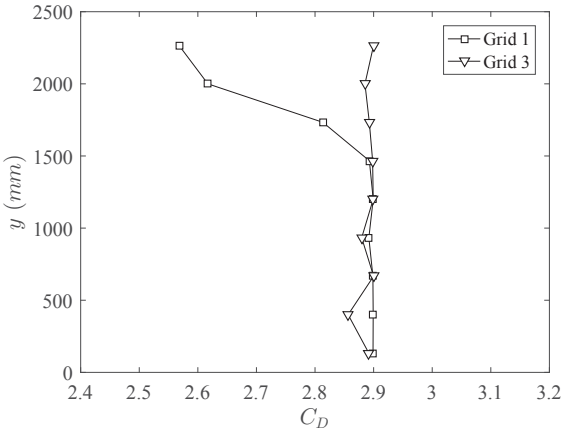

Figure 4.4: Profiles of the drag coefficients of Grid 1 and Grid 3 at different y locations.

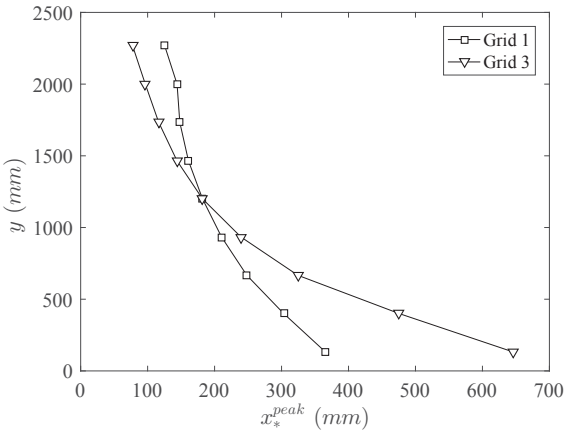

Figure 4.5: The wake interaction length scale x_*^{peak}(n) of Grid 1 and Grid 3 at different y locations.

Consultants wind tunnel is non-negligible (approximately 3%), as opposed to $\alpha = 0.231$ for incoming flows with negligible turbulence intensity.

4.1.3 Experimental setup and methods

All experiments in this chapter were conducted in the upper test section of the wind tunnel, where the only flow conditioner was a mesh screen installed about 5 m downstream of the turning vanes to homogenize the flow. During experiments, the grid was mounted 3 m downstream of the screen, leaving a measurable length of roughly 17 m. The two rails on the ceiling where the traverse is mounted gives a measurable range from 3.5 m to 17.5 m

downstream of the grid. The origin of the coordinate system is set at the lee of the bottom center of the grid. The measurement method is introduced first in the following, and the base flow quality is examined before the description of measurement setup is given.

Cobra probe

For current measurements, a four-hole pressure probe was used referred to as the Cobra probe. This specific type of four-hole pressure probe was perhaps first proposed by Bryer and Pankhurst (1971), and has been subsequently validated and improved by many (see e.g. Shepherd, 1981; Sitaram and Treaster, 1985; Hooper and Musgrove, 1991; Musgrove and Hooper, 1993; Hooper and Musgrove, 1997; Chen et al., 1998, 2000). The Cobra probe from Turbulent Flow Instrumentation (TFI) is a pressure probe designed to measure three-component fluctuating velocities. A sketch of the probe is given in figure 4.6. The overall length of the probe is 155 mm, and 14 mm in body diameter. Figure 4.6 (b) shows the truncated triangular pyramid-shaped head of the probe. Four 0.5 mm diameter pressure tappings are arranged at the center of four faceted faces. The tappings are connected to pressure transducers in the body of the probe via tubing inside the stem. Further details of the probe design can be found in Hooper and Musgrove (1997); Chen et al. (2000).

The specific type of Cobra probe used in the current measurements has a linear frequency response from 0 Hz to more than 2 kHz, with a measurable velocity range from 2 m/s to 100 m/s. A commercial data acquisition interface with proprietary control software from TFI was used. The sampling frequency was $f_s = 5$ kHz, and the signal was re-sampled at $f_s = 3$ kHz to avoid electrical noise.

The calibration of such probes requires rotation of the probe in a range of different pitch and yaw angles. The pressure from each one of the tappings and reference stagnation pressure are recorded to give the calibration function for different flow directions, which makes three dimensional measurements possible. Details of the calibration method can be found in Sitaram and Treaster (1985); Chen et al. (1998).

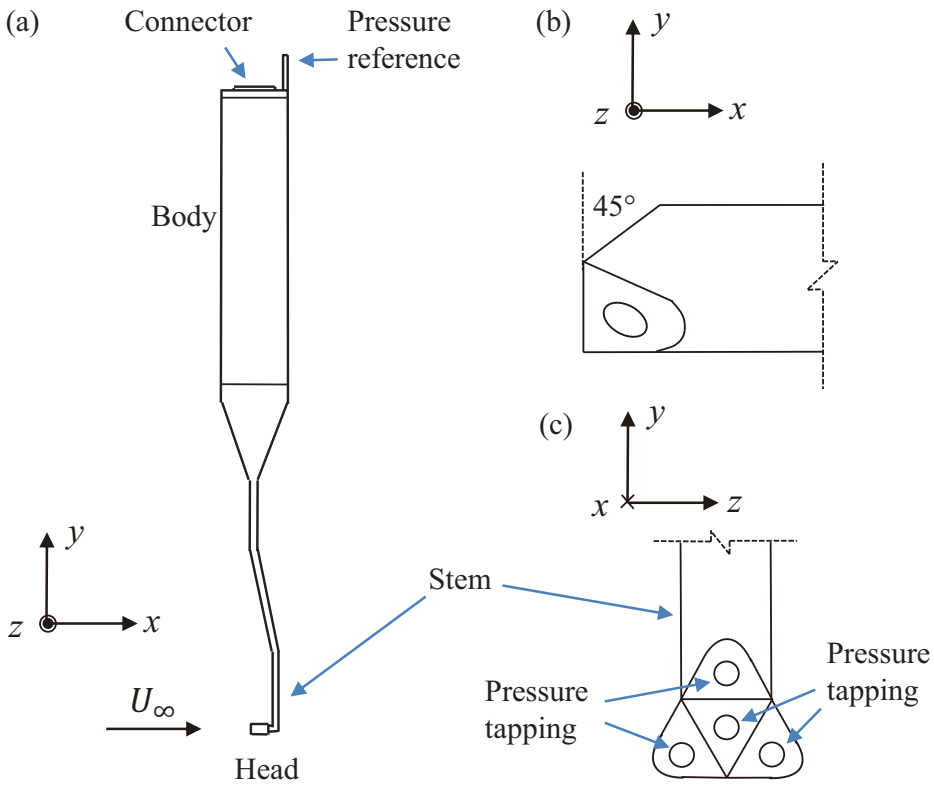

Figure 4.6: (a) Sketch of the entire Cobra probe, (b) side view, and (c) front view of the head of the probe.

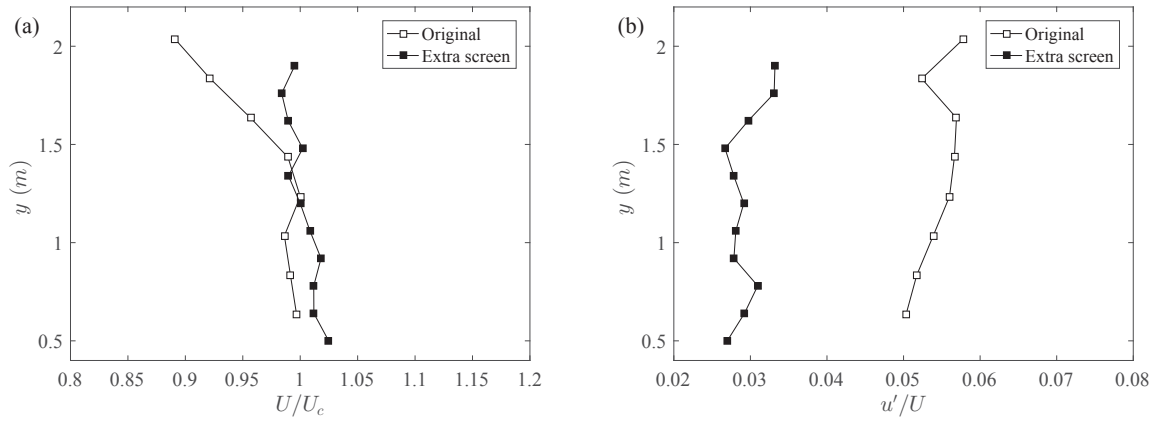

Figure 4.7: Normalized (a) mean velocity and (b) turbulence intensity along the vertical direction before and after fitting the extra screen at $x = 3.5\,\mathrm{m}$ and $z = 0\,\mathrm{m}$, where U_c is the centerline velocity.

Note that the calibration functions provided by the manufacturer were used for each probe, because on-site calibration was not possible. The calibration functions are independent of temperature variations (assuming constant air properties) and Reynolds number effects (assuming the Reynolds number is sufficiently high). However, the v and w components of the velocity are quite sensitive to the pitch and yaw angles of the probe (Sitaram and Treaster, 1985; Chen et al., 1998). Therefore, only the streamwise velocity u is used for further discussions.

The measurement accuracy of the Cobra probe, as provided by the manufacturer, is generally within $\pm 0.5\,\mathrm{m/s}$, but also depends on the turbulence level. By comparing with preliminary measurements using Hot-Wire Anemometry, the uncertainty of u is estimated to be 5% of U_∞ for current experiments. Hot-wire was not used in the measurements because the electrical noise eliminates the advantage of HWA in high frequency measurements of velocity signals, and the on-site temperature measurement was not accurate (by wall temperature gauge) so the temperature correction method proposed in appendix A could not be applied accurately.

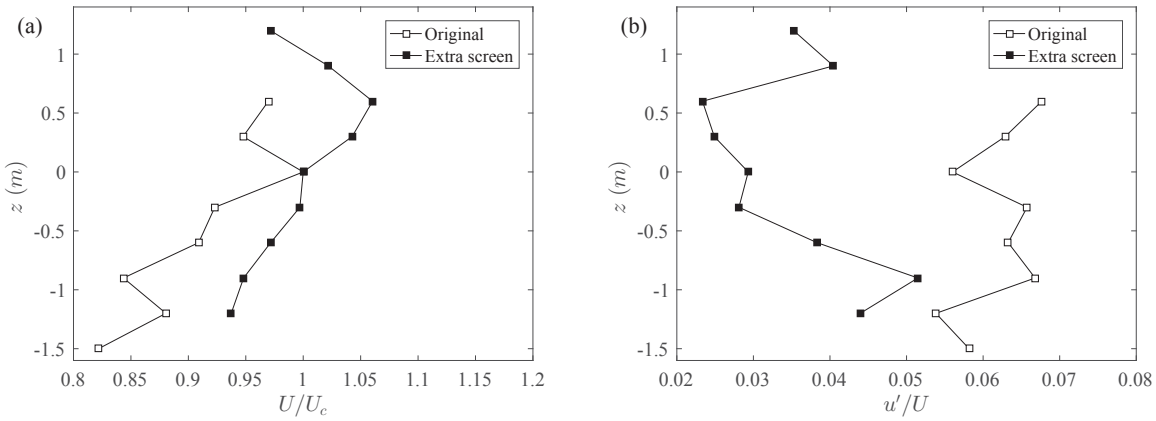

Figure 4.8: Normalized (a) mean velocity and (b) turbulence intensity along the transverse direction before and after fitting the extra screen at $x = 3.5\,\mathrm{m}$ and $y = 1.2\,\mathrm{m}$, where U_c is the centerline velocity.

Base flow

The quality of the base flow in the empty Mel Consultants wind tunnel was examined first as shown in figure 4.7 and figure 4.8, along the the vertical and transverse directions, respectively (empty symbols). From figure 4.7 (a), it can be observed that the mean velocities at $y > 1.5\,\mathrm{m}$ suffer from a velocity deficit as large as 12%, and the turbulence intensities given in figure 4.7 (b) are all larger than 5%, which is significant for a background flow. The transverse profiles from figure 4.8 demonstrate the same problem in the flow homogeneity, where the mean velocity deficit is nearly 20%, and the turbulence intensity reaches up to 7%.

To correct the inhomogeneity of the background flow profiles, and to reduce the turbulence intensity, an extra screen was fitted on to the original screen following some trial and error. The final layout is given in figure 4.9, where the extra screen covers $-1.5\,\mathrm{m} < z < 1.5\,\mathrm{m}$, and $0\,\mathrm{m} < y < 2.5\,\mathrm{m}$. The four blue supports that appear in figure 4.9 are non-removable parts of the wind tunnel to prevent structural deformation.

After the modification, the variation of the mean velocity along the vertical direction is reduced to $\pm 3\%$, as shown in figure 4.7 (a), labeled as 'extra screen'. The turbulence intensities are reduced, as given in figure 4.7 (b), to approximately 3% normalized by

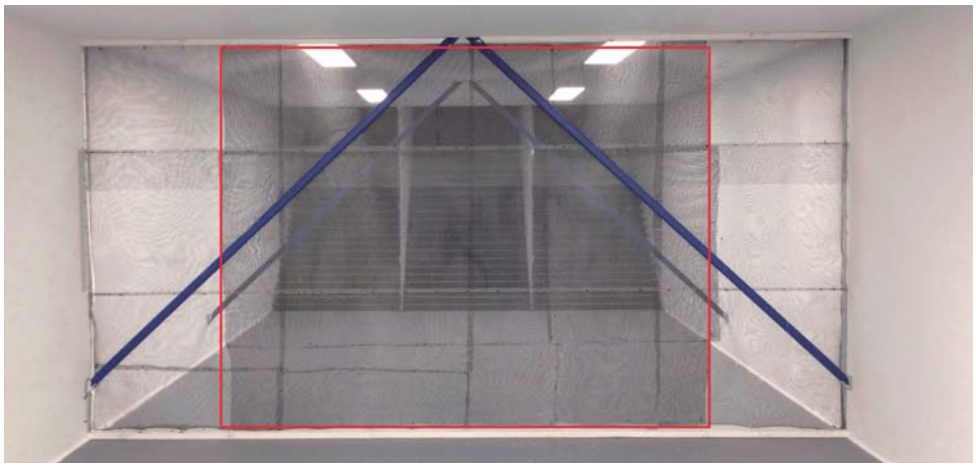

Figure 4.9: Extra screen mesh (marked by red) to improve the quality of the background flow.

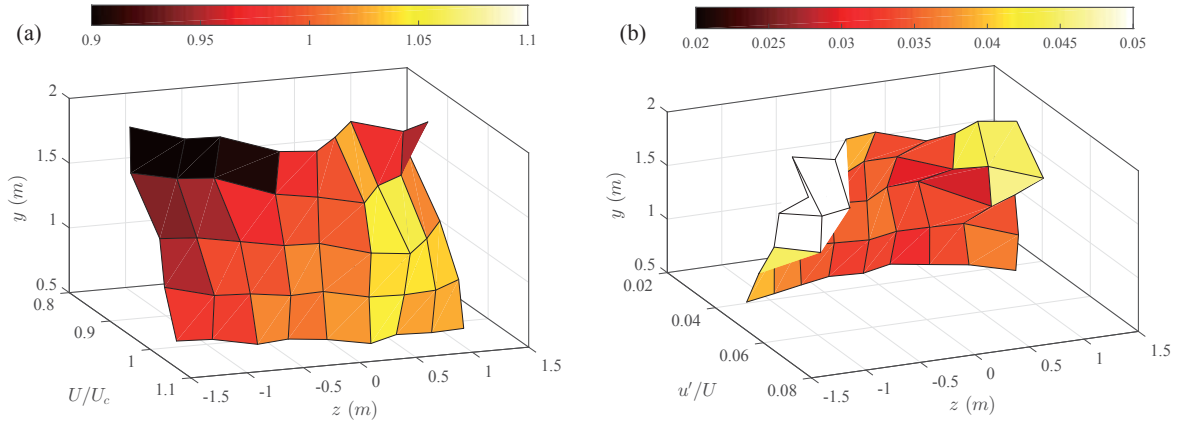

Figure 4.10: Normalized (a) mean velocity and (b) turbulence intensity of the background flow measured in the $y-z$ plane at $x = 3.5\,\mathrm{m}$.

local mean velocity. For the transverse profiles, the mean velocities vary roughly within 5% of the centerline velocity U_c, and the turbulence intensities are reduced from $6\% - 7\%$ to roughly $3\% - 4\%$, as shown in figure 4.8. Figure 4.10 gives the results of mean velocity and turbulence intensity of the base flow measured at $x = 3.5\,\mathrm{m}$ across the $y-z$ plane. It can be observed that the mean velocities are generally within $\pm 10\%$ of the centerline velocity U_c, and the turbulence intensity is in the range of 2.5% to 4% (except the corner at $z = -1.5\,\mathrm{m}$ and $y = 2\,\mathrm{m}$). This will be further discussed in section 4.2 to interpret the measurement results.

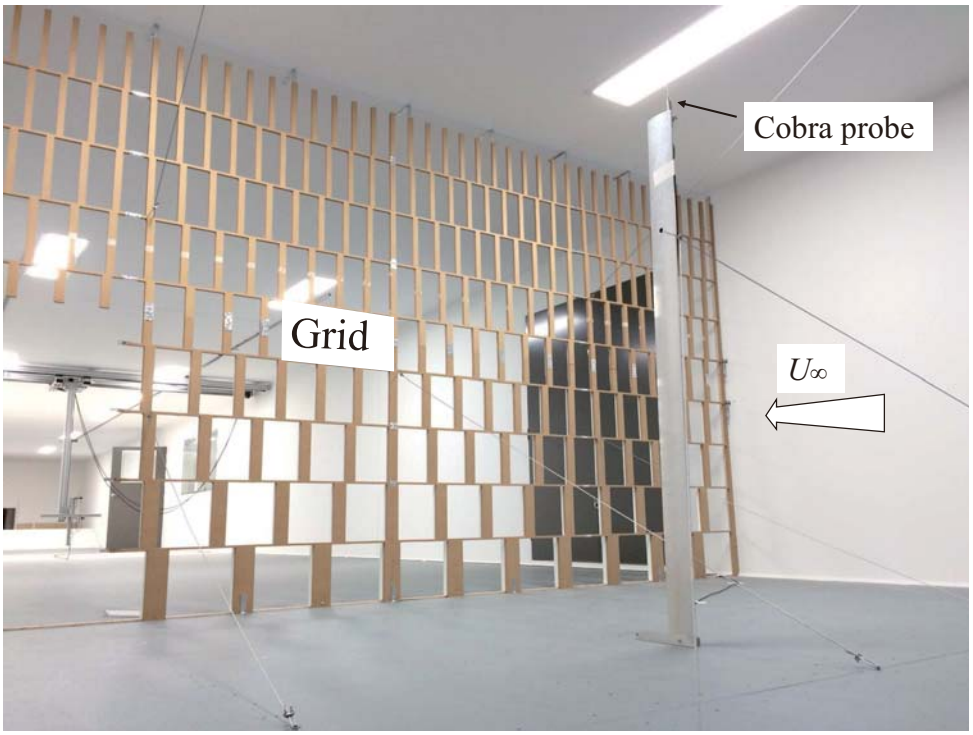

Figure 4.11: Setup of the cobra probe to measure the free stream velocity U_∞. Steel wires are used to reinforce the probe support and the grid. One panel of the grid is temporarily removed in the figure to access the section upstream of the grid.

Measurement setup

During the measurement, the free stream velocity U_∞ is measured by a fixed Cobra probe mounted on a streamlined support extending from the bottom wall of the wind tunnel to a height of 1.5 m as shown in figure 4.11. The probe is fixed at a location 1.8 m upstream of the grid. Steel wires are used to reinforce the support to make sure it is upright, which also reduces the vibration caused by the incoming flow. Wires were also used to strengthen the grid to prevent deformation of the grid under the incoming flow pressure. The wires are fixed during the adjustment of the level of the grid to make sure it is in the same $y - z$ plane.

The free stream velocity was calibrated with and without the grid to determine the fan speed for velocity control, and the results are given in figure 4.12. The calibration data is fitted by a linear function. The free stream velocities chosen for the acquisition are 5.5 m/s and 7 m/s, corresponding to fan speeds of 264 rpm and 330.8 rpm (within the

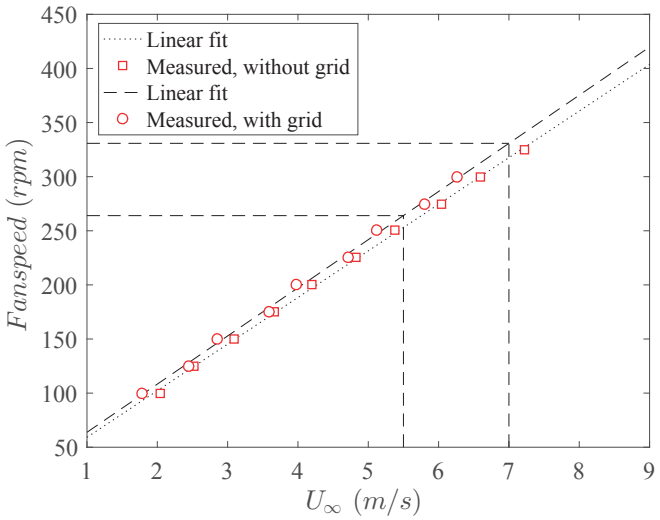

Figure 4.12: Calibration of the free stream velocity of the wind tunnel with and without the grid. The dashed lines give fan speeds of 264 rpm and 330.8 rpm, for free stream velocities of 5.5 m/s and 7 m/s, respectively.

safety limit of 350 rpm), respectively. The Reynolds number based on the width of the grid bars $Re_D = w_n U_\infty/\nu$ range from 10000 to 37000, where w_n is the width of the vertical bar at layer n, U_∞ is the free stream velocity, and ν is kinematic viscosity.

For each grid, streamwise profiles were acquired at $z = 0$ m, $y = 668$ mm, $y = 1200$ mm, and $y = 1732$ mm at a free stream velocity of $U_\infty = 7$ m/s. Another centerline profile at $z = 0$ m and $y = 1200$ mm was acquired at $U_\infty = 5.5$ m/s for comparison at different Reynolds number and different dimensionless time scale $\tau \equiv [(x - x_*^{peak})/\overline{U_n}]\,|S_n|$ as defined in section 3.2.4, where x_*^{peak} is the wake interaction length scale, U_n, S_n are the mean velocity and shear rate at layer n, respectively. At $z = -1.2$ m, two centerline profiles were acquired at $y = 1200$ mm along the streamwise direction at $U_\infty = 7$ m/s to look at the streamwise evolution of the turbulence characteristics behind different grid positions.

Vertical profiles were taken at three different streamwise locations ($x = 3.5$ m, $x = 10.5$ m, and $x = 17.5$ m) at $z = 0$ m with free stream velocities of $U_\infty = 5.5$ m/s, and $U_\infty = 7$ m/s, respectively. For comparison, measurements were also taken at $z = -1.2$ m at the same streamwise locations with $U_\infty = 7$ m/s. The measurement locations relative to the grid

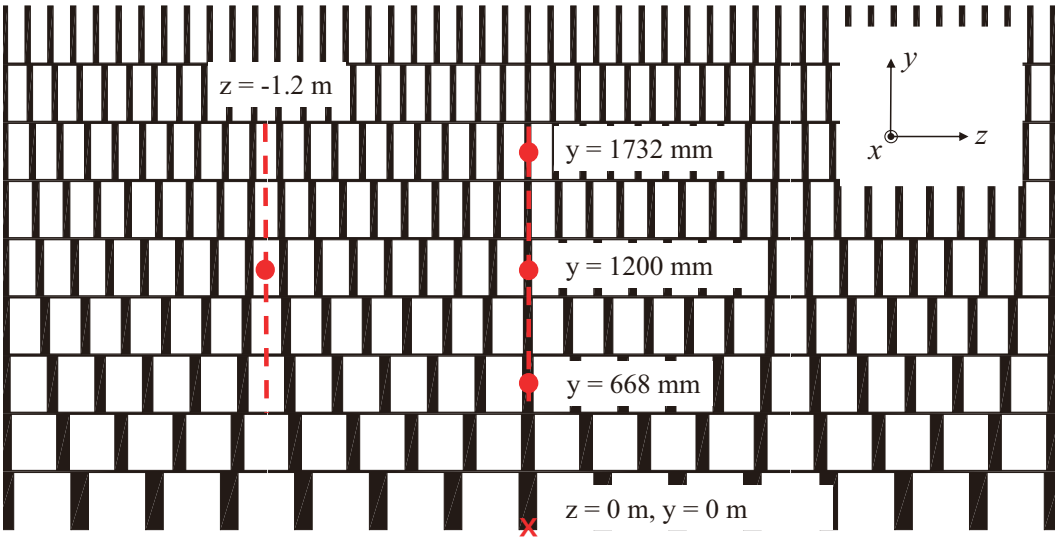

Figure 4.13: Illustration of measurement locations relative to the grid. The dot gives the locations of streamwise measurements, and the dashed lines give the measurement range of the vertical profiles. The red x symbol shows the origin of the coordinate system.

are demonstrated in figure 4.13.

4.2 Results

In this section, the mean velocity profiles are first presented referring to the mean velocity model discussed in section 3.2.1. The turbulence intensities are examined based on the scaling method proposed in section 3.2.2, and the streamwise evolution is studied. This section is then closed by discussions on the streamwise integral length scales and spectra.

4.2.1 Mean velocity

Following the mean velocity model discussed in section 3.2.1, equations (3.3) to (3.5), the mean velocity profiles are first calculated using the blockage ratio profiles of the grids, and the results are shown in figure 4.14 (dashed lines).

The vertical profiles measured behind grid 1 and grid 3 at three streamwise locations,

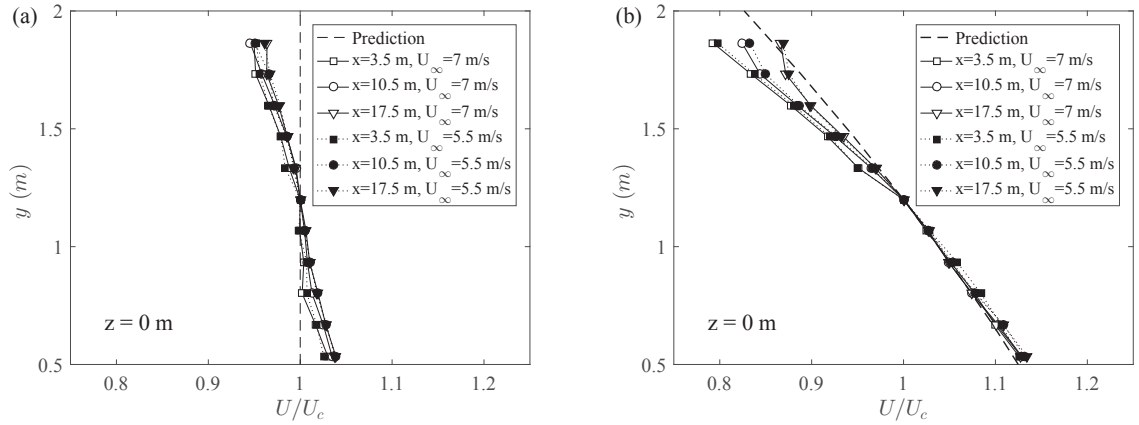

Figure 4.14: Vertical profiles of normalized mean velocity U/U_c, where U_c is the centerline velocity, measured at $z = 0\,\mathrm{m}$, $U_\infty = 5.5\,\mathrm{m/s}$ (filled symbols) and $U_\infty = 7\,\mathrm{m/s}$ (empty symbols) for (a) grid 1 and (b) grid 3, respectively.

i.e. $x = 3.5\,\mathrm{m}$, $x = 10.5\,\mathrm{mm}$, and $x = 17.5\,\mathrm{m}$, are given in figure 4.14, normalized by the centerline velocity U_c. Grid 1 is designed to produce a uniform flow, and the measured velocity at different y locations are all within $\pm 5\%$ of the calculated value as given in figure 4.14 (a). This is also in agreement with the observations of section 3.2.1, where the vertical profiles are self-preserved at different streamwise locations.

The profiles measured behind grid 3 are given in figure 4.14 (b). The deviations of the measured mean velocities from the calculated profile are all within $\pm 5\%$, which is reasonable considering the inhomogeneity of the background mean flow profile as shown in figure 4.7 (a). The mean shear rates of the vertical profiles averaged at three locations with $U_\infty = 7\,\mathrm{m/s}$ are $|\overline{\partial U/\partial y}| = 0.40\,\mathrm{s}^{-1}$, and $1.49\,\mathrm{s}^{-1}$ for grid 1 and grid 3, respectively. Measurements with $U_\infty = 5.5\,\mathrm{m/s}$ at the same locations are also presented in figure 4.14 (a) and (b) for grid 1 and grid 3, respectively, and the collapse of the profiles suggest that the mean velocity is independent of the Reynolds number effect.

The vertical profiles measured at $z = -1.2\,\mathrm{m}$ with $U_\infty = 7\,\mathrm{m/s}$ are presented in figure 4.15. This is the location behind the openings of the grid, as illustrated in figure 4.13. Comparing to the results at $z = 0\,\mathrm{m}$ from figure 4.14, the deviations from the predicted values seem larger for both grids. Nevertheless, the differences are well within $\pm 10\%$.

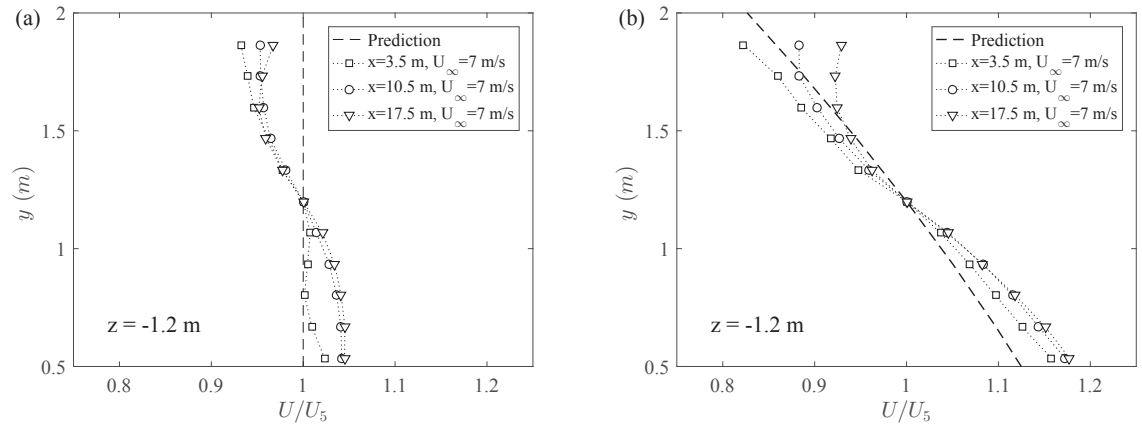

Figure 4.15: Vertical profiles of normalized mean velocity U/U_5, where U_5 is the mean velocity at layer 5 ($y = 1200\,\text{mm}$), measured at $z = -1.2\,\text{m}$, $U_\infty = 7\,\text{m/s}$ for (a) grid 1 and (b) grid 3, respectively.

The wave-like deviation observed in figure 4.15 is attributed to the non-uniformity of the background flow at $z = -1.2\,\text{m}$, as shown in figure 4.10 (a), where the mean velocity appears to be faster at smaller y, and slower at larger y. To confirm this conclusion, the vertical profiles at $z = -1.2\,\text{m}$ measured without the grid are extracted and compared with measurements at the same location with grid 1. The results are given in figure 4.16. The variation of the mean velocity seems correlated, and therefore supports the previous explanation of the deviations observed in figure 4.15.

In figure 4.17, the streamwise profiles of the normalized mean velocity U/U_∞ of grid 1 and grid 3 are presented, measured at $y = 668\,\text{mm}$, $y = 1200\,\text{mm}$, and $y = 1732\,\text{mm}$, respectively. For both grids, the values of U/U_∞ increases by approximately 3% over the measurement domain. The gradients of the streamwise velocity along the centerline at $U_\infty = 7\,\text{m/s}$ are calculated as $\overline{\partial U/\partial x} = 0.02\,\text{s}^{-1}$, and $\overline{\partial U/\partial x} = 0.01\,\text{s}^{-1}$ for grid 1 and grid 3, respectively. The measurements at $U_\infty = 5.5\,\text{m/s}$ along the centerline are also shown in figure 4.17 (filled symbols). The centerline profiles at both free stream velocities collapse, which is in agreement with the conclusion that the mean velocity is independent of the Reynolds number effect.

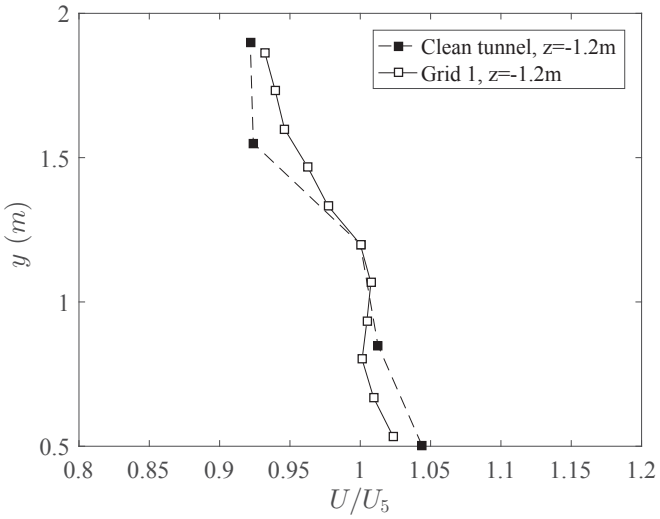

Figure 4.16: Comparison of the vertical profiles of U/U_5, where U_5 is the mean velocity at layer 5 ($y = 1200\,\mathrm{mm}$) measured at $z = -1.2\,\mathrm{m}$, with (empty symbols) and without (filled symbols) grid 1.

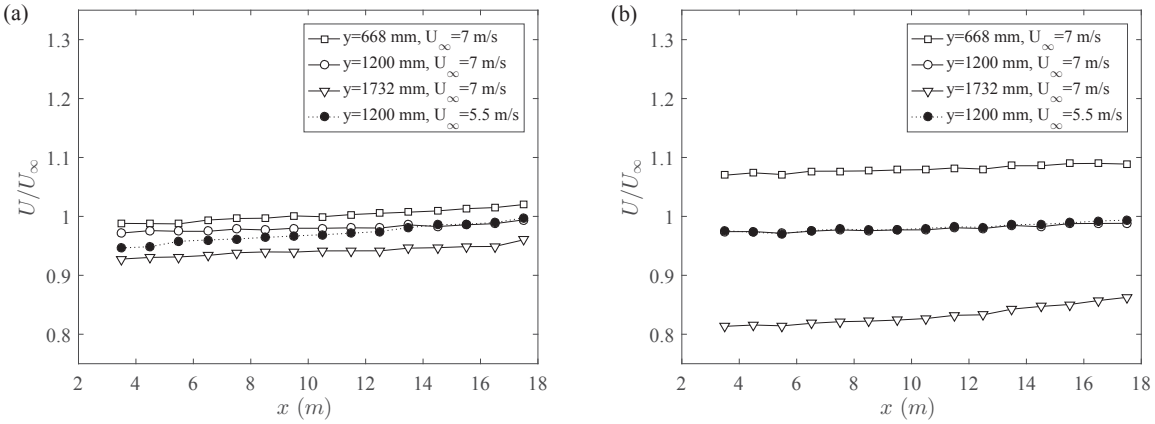

Figure 4.17: Streamwise profiles of normalized mean velocity U/U_∞ at three y locations for (a) grid 1 and (b) grid 3, respectively, at $U_\infty = 7\,\mathrm{m/s}$ (empty symbols). The centerline profiles measured at $U_\infty = 5.5\,\mathrm{m/s}$ are shown in filled symbols.

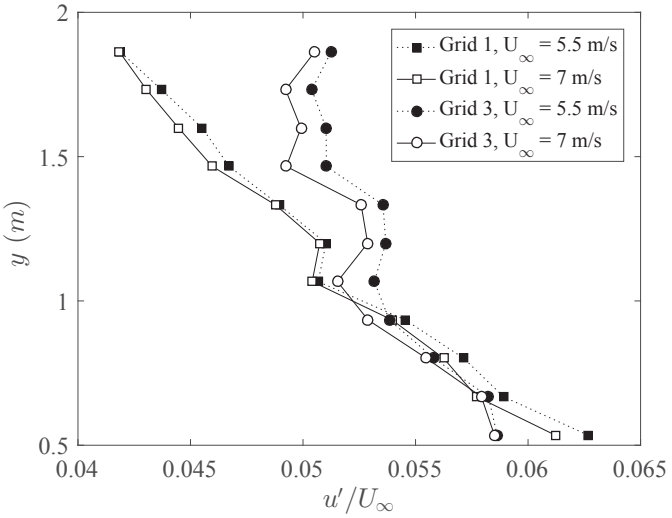

Figure 4.18: Vertical profiles of u'/U_∞ measured at $x = 3.5\,\text{m}$, $z = 0\,\text{m}$ with different free stream velocities for grid 1 and grid 3.

4.2.2 Turbulence intensity

In this section, the streamwise turbulence intensity profiles along the vertical and streamwise directions are presented. The vertical profiles of u'/U_∞ measured at $x = 3.5\,\text{m}$ and $z = 0\,\text{m}$ are given in figure 4.18 at $U_\infty = 7\,\text{m/s}$ (empty symbols) and $U_\infty = 5.5\,\text{m/s}$ (filled symbols). The profiles at different free stream velocities seem to collapse within the uncertainty of $5\%U_\infty$. The turbulence level reaches approximately 6% at $y = 535\,\text{mm}$, and gradually decreases with increasing y location, which is consistent with the observations in section 3.2.2.

Following the discussion in section 3.2.2, the scaled turbulence intensities along the y direction scale with x_*^{peak} in a power law, such that $(u'/U_n)^2\beta^2(C_D w_n/x_*^{peak})^{-1} \sim (x_*^{peak})^\gamma$, where U_n is the local mean velocity, $\beta^2 = 7.2$ is a constant characterizing the development of the wake for incoming flows with non-negligible turbulence level ($\sim 5\%$, see Symes and Fink, 1977), C_D, w_n, and x_*^{peak} are the drag coefficient, width of the vertical bar, and wake interaction length scale at layer n, respectively, and γ is a constant for the power law fitting. The results of the current measurements are given in figure 4.19. It is observed that these measurements follow the power law quite well, with fitting constants $\gamma = 0.80$

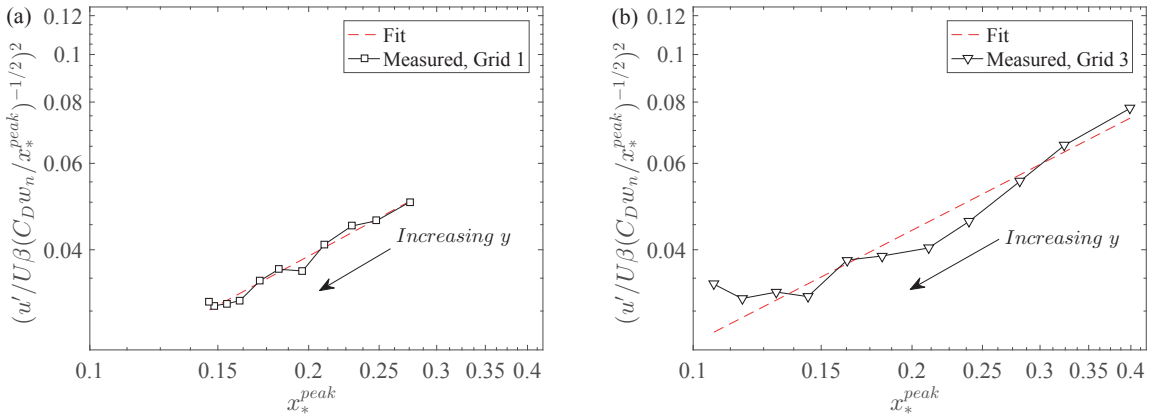

Figure 4.19: Scaling of the normalized turbulence intensity profiles $u'(y)$ measured at $x = 3.5\,\mathrm{m}$, $z = 0\,\mathrm{m}$ for (a) grid 1, (b) grid 3, respectively.

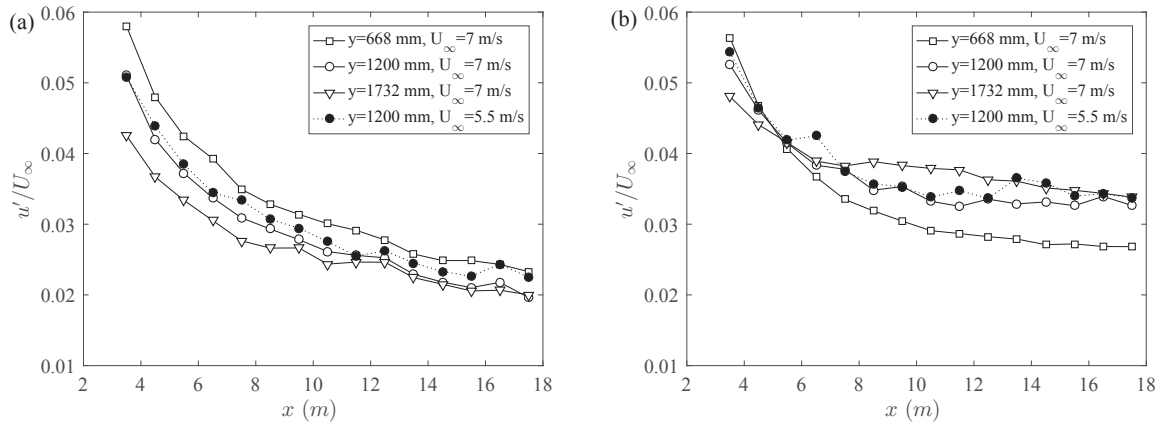

Figure 4.20: Streamwise profiles of normalized turbulence intensity u'/U_∞ at $z = 0\,\mathrm{m}$ and three y locations for (a) grid 1 and (b) grid 3, respectively, at $U_\infty = 7\,\mathrm{m/s}$ (empty symbols). The centerline profiles measured at $U_\infty = 5.5\,\mathrm{m/s}$ are shown in filled symbols.

and 0.76 for grid 1 and grid 3, respectively. These values are different to the fitting constants reported in section 3.2.2, where $\gamma = 1.46$ and 1.14 were calculated, this is due to the fact that the value of the constant γ varies with the mean velocity, turbulence intensity and grid geometries.

The streamwise profiles of the turbulence intensities measured at $z = 0\,\mathrm{m}$ and different y locations behind grid 1 and grid 3 are shown in figure 4.20. For grid 1, the turbulence intensities at all y locations monotonically decay along the streamwise direction from $x = 3.5\,\mathrm{m}$ to $17.5\,\mathrm{m}$, which is consistent with the results in section 3.2.2.

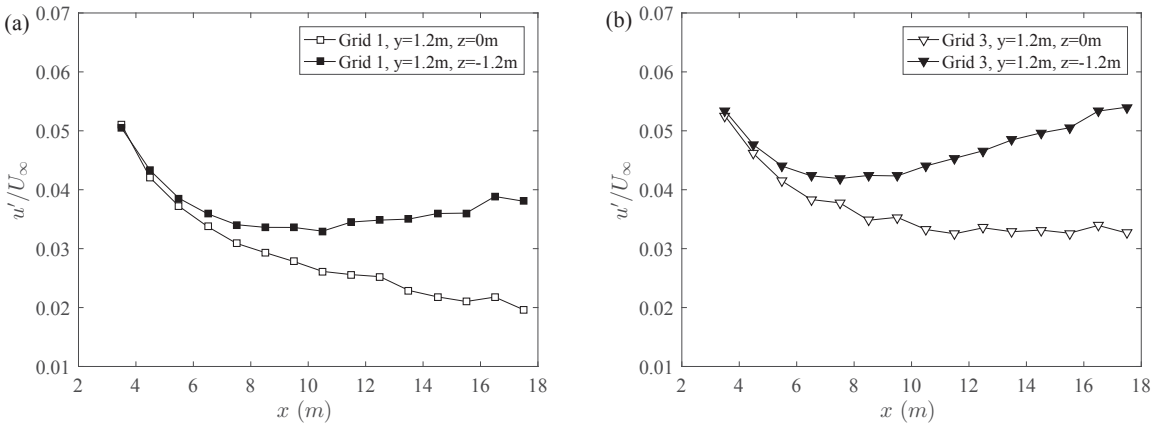

Figure 4.21: Comparison of streamwise profiles of normalized turbulence intensity u'/U_∞ at $y = 1200\,\text{mm}$ along the centerline (empty symbols) and at $z = -1.2\,\text{m}$ (filled symbols) for (a) grid 1 and (b) grid 3, respectively, at $U_\infty = 7\,\text{m/s}$.

For grid 3, the value of u'/U_∞ remains higher than that of grid 1. The centerline value decreases only from $x = 3.5\,\text{m}$ to $10\,\text{m}$, and stays approximately constant thereafter at a level of $u'/U_\infty \approx 3.5\%$. This is consistent with the observation in figure 3.8 (a), where the level of u'/U_∞ for grid 3 is higher than the other grids at the end of the measurement domain. Since the local drag coefficients of grid 1 and grid 3 are the same for the current measurement, as shown in figure 4.4, the higher turbulence intensity is explained by the higher shear rate of the turbulent flow generated by grid 3, such that the rate of turbulence production is increased, and the overall level of turbulence intensity decays more slowly. The centerline profiles measured at different free stream velocities seem to collapse as well, as shown in figure 4.20, which suggests that the streamwise evolution of the u'/U_∞ is independent of the Reynolds number, at least in the range investigated here $Re_D = 10000$ to 37000.

In figure 4.21, two streamwise profiles of the turbulence intensity u'/U_∞ at $z = -1.2\,\text{m}$ and $y = 1200\,\text{mm}$ are compared with the centerline profiles. The initial values (u'/U_∞ at $x = 3.5\,\text{m}$) of the turbulence intensities at different z locations are approximately the same, which seem to imply the transverse homogeneity of the flow at this streamwise location, but it has to be kept in mind that the background turbulence of the wind tunnel is not exactly homogeneous.

z	0 m	−1.2 m
Grid 1	$0.29\,\mathrm{s}^{-1}$	$0.76\,\mathrm{s}^{-1}$
Grid 3	$1.88\,\mathrm{s}^{-1}$	$2.14\,\mathrm{s}^{-1}$

Table 4.1: The local shear rate $|\partial U/\partial y|$ of the mean velocity profiles at $x = 3.5\,\mathrm{m}$, $y = 1.2\,\mathrm{m}$ for different grids and z locations.

However, the profiles of u'/U_∞ at $z = -1.2\,\mathrm{m}$ and $y = 1200\,\mathrm{mm}$ along the streamwise direction start to increase at approximately $x = 10\,\mathrm{m}$ and $x = 7\,\mathrm{m}$ for grid 1 and grid 3, respectively. This difference is consistent with some of the previous experiments where the turbulence intensity beyond a critical value of the dimensionless time scale τ_c^* (where $\tau^* \equiv (x/\overline{U_c})\,|S_n| = (x/\overline{U_c})\left|\overline{\partial U_n/\partial y}\right|$) remained constant in some cases (e.g. Rose, 1966; Champagne et al., 1970; Rose, 1970), and grew in others (e.g. Harris et al., 1977; Tavoularis and Corrsin, 1981; Rohr et al., 1988; Nedić and Tavoularis, 2016). This was explained by the ratio of turbulence production P to dissipation ϵ according to Tavoularis and Karnik (1989), such that the turbulence kinetic energy k grows exponentially when $P/\epsilon > 1$, and stays constant when $P/\epsilon \approx 1$. This is in agreement with the mean velocity profiles at $z = 0\,\mathrm{m}$ and $z = -1.2\,\mathrm{m}$, as shown in figure 4.14 and figure 4.15. The local shear rates $|\partial U/\partial y|$ at these locations are given in table 4.1. It is clear that the shear rate at $z = -1.2\,\mathrm{m}$ is much larger than that on the centerline, and is thus likely to be the cause of the growth of turbulence kinetic energy, and hence u'.

Figure 4.22 presents the streamwise evolution of the $\overline{u^2}/U_\infty^2$ against the dimensionless time scale $\tau \equiv [(x - x_*^{peak})/\overline{U_n}]\,|S_n|$ as introduced in section 3.2.4, where the wake interaction length scale x_*^{peak} is included. For grid 1, the dimensionless time scale is rather limited due to the small shear rate S_n. For grid 3, the value of $\overline{u^2}/U_\infty^2$ at $z = 0\,\mathrm{m}$ stays roughly constant at $\tau > 2$, while the value at $z = -1.2\,\mathrm{m}$ increases beyond the same location $\tau = 2$. It seems that the critical location of τ for a given grid is the same in this study, i.e. $\tau = 2$, for the case with constant or growing turbulence kinetic energy. In some previous

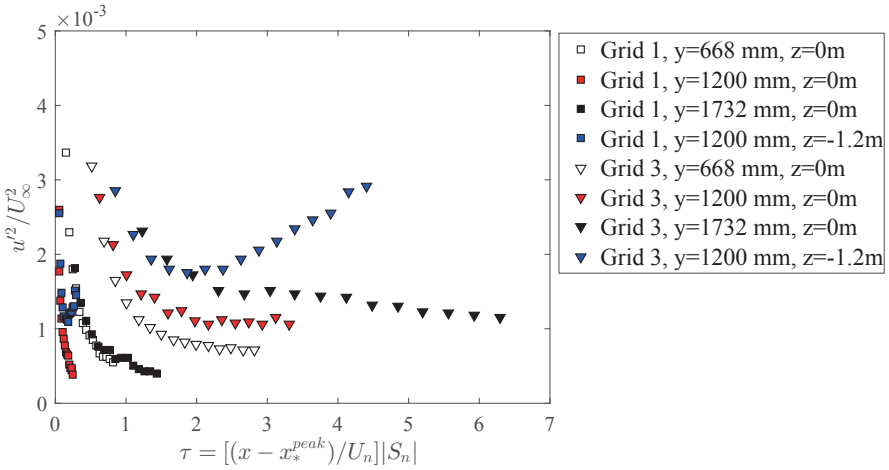

Figure 4.22: Streamwise profiles of $\overline{u^2}/U_\infty^2$ measured at different y and z locations with $U_\infty = 7\,\mathrm{m/s}$.

works, it has been shown that for the cases where $\overline{u^2}/U_c^2$ stays constant (Rose, 1966; Champagne et al., 1970; Rose, 1970), the development was fairly fast, reaching constant values at $\tau_c^* = 1.6$ to 3, while the critical values of τ_c^* are roughly $\tau_c^* = 4$ to 5 for cases with growing turbulence kinetic energy (Rose, 1966; Champagne et al., 1970; Rose, 1970). This seems to suggest that the critical value of τ is grid dependent, and such dependency of the grid geometry is compensated by including the x_*^{peak} in the definition of τ for the inhomogeneous multiscale grids, which explains the same critical value of $\tau = 2$ for two different types of streamwise evolution (constant or growing) of $\overline{u^2}/U_\infty^2$.

4.2.3 Integral length scale

In this section, the streamwise integral length scales at various locations are presented. The von Kármán spectrum model is used to compute the integral length scale using $L_{uu,x} = \pi E_{11}(0)/(2u'^2)$, as described in section 3.1.3. The streamwise evolution of the calculated $L_{uu,x}$ is shown in figure 4.23. In figure 4.23(a), a linear increase of $L_{uu,x}$ from $x = 3.5\,\mathrm{m}$ to $x = 12\,\mathrm{m}$ is observed for both grids. The increase of $L_{uu,x}$ seems to slow down between $x = 11\,\mathrm{m}$ to $17.5\,\mathrm{m}$. This is consistent with the observations in section 3.2.5.

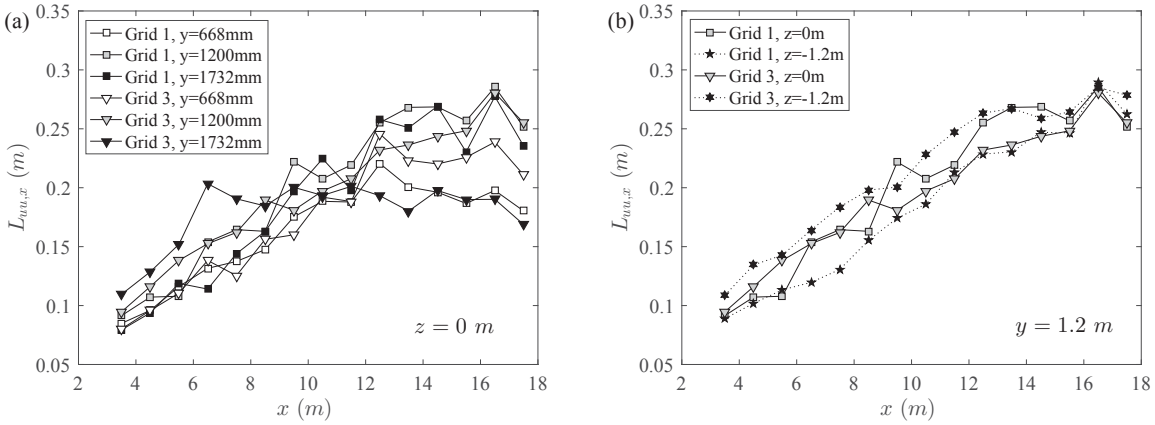

Figure 4.23: Longitudinal integral length scale $L_{uu,x}$ profiles for grid 1 and grid 3 at (a) different y locations and (b) different z locations with $U_\infty = 7\,\mathrm{m/s}$.

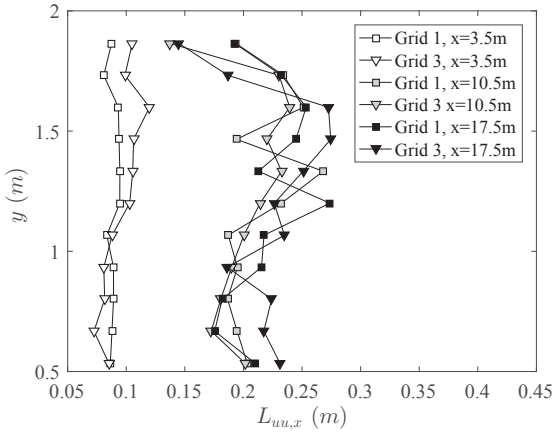

Figure 4.24: Longitudinal integral length scale $L_{uu,x}$ profiles for grid 1 and grid 3 along the y direction at $z = 0\,\mathrm{m}$ and three x locations with $U_\infty = 7\,\mathrm{m/s}$.

Figure 4.23(b) shows the streamwise evolution of $L_{uu,x}$ at $z = 0\,\mathrm{m}$ and $z = -1.2\,\mathrm{m}$. The profiles at these two transverse locations collapse quite well. This is interesting as the turbulence intensities at these two locations are quite different, as shown in figure 4.21. This observation might suggest that the evolution of the integral length scale $L_{uu,x}$ is primarily dependent on the external dimension/geometry of the grid, rather than bar dimensions.

The vertical profiles of $L_{uu,x}$ at $z = 0\,\mathrm{m}$ and different x locations are given in figure 4.24. The values seem to be constant along the y direction at all x locations. Further, the values of $L_{uu,x}$ at $x = 10.5\,\mathrm{m}$ and $17.5\,\mathrm{m}$ seem to collapse (perhaps slightly larger for the

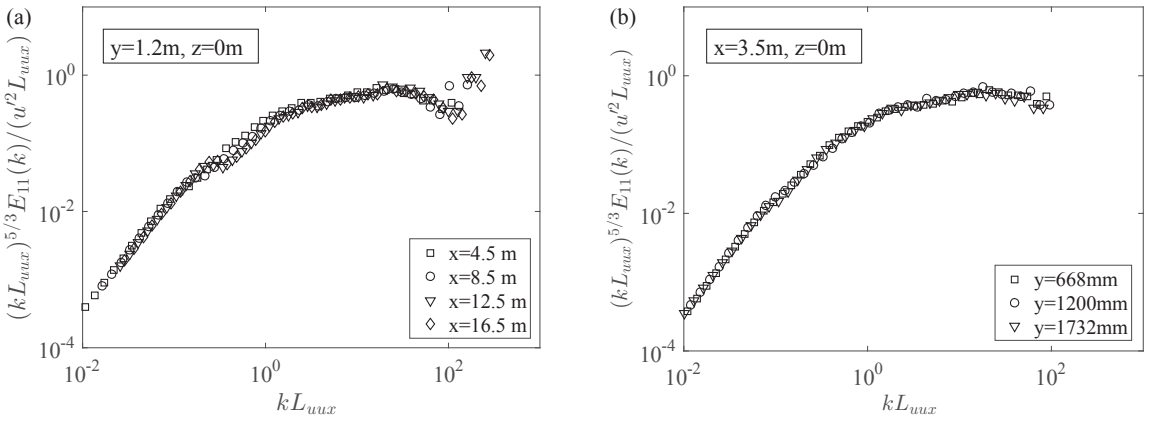

Figure 4.25: Example of normalized spectrum of grid 1 using u' and $L_{uu,x}$, measured at (a) different x locations and (b) different y locations with $U_\infty = 7\,\mathrm{m/s}$.

latter), which corresponds to the slower increase in the range $x = 12\,\mathrm{m}$ to $17.5\,\mathrm{m}$ observed in figure 4.23. This is also in agreement with the results discussed in section 3.2.5.

To close section 4.2, it is noted that the spectra measured at different x and y directions were also studied. In section 3.2.9, it was concluded that spectra measured at different x locations at the same relative location to the grid would collapse at all wave numbers when normalized using the external variables u' and $L_{uu,x}$, and that such a collapse ceases when spectra measured at different y locations are compared. Spectra measured for grid 1 are given in figure 4.25 along different x and y locations. As evident in figure 4.25 (b), even though there seems to be a collapse, the higher wave number may not collapse. Due to the lack of the dissipative range of the spectrum, however, the small wave number range of spectra always collapse when normalized using u' and $L_{uu,x}$, and therefore no comparison can be made.

4.3 Summary

In this chapter, the turbulent flow generated by two modified versions of the inhomogeneous multiscale grids proposed in Chapter 3 are investigated in a low-fidelity engineering wind tunnel using the Cobra probe. The grid was designed to have the same blockage

ratio profiles at different levels of the wind tunnel height. Based on the width of the grid bars, the Reynolds number $Re_D = w_n * U_\infty/\nu$ ranged from 10000 to 37000.

The mean velocity model after Taylor et al. (1949); McCarthy (1964) based on the local blockage ratio σ_n was shown to match the measurements, with an uncertainty attributed to non-uniformity of the background flow. The mean shear rate was measured as $0.40\,\mathrm{s}^{-1}$ and $1.49\,\mathrm{s}^{-1}$ for grid 1 and grid 3, respectively. The mean velocity profiles at different incoming flow velocities show that the mean flow is independent of the Reynolds number effect, and the shape of the profiles are self-preserved in the streamwise direction.

The scaling relation of the turbulence intensity profiles $u'(y)$ are verified using measurements at $x = 3.5\,\mathrm{m}$, such that $(u'/U_n)^2\beta^2(C_D w_n/x_*^{peak})^{-1} \sim (x_*^{peak})^\gamma$, where β is a constant, C_D, w_n, and x_*^{peak} are the drag coefficient, width of the vertical bar, and wake interaction length scale at layer n, respectively, and γ is a constant for the power law fitting. This confirms the conclusion in Chapter 3 that the shape of the turbulence intensity profile can be prescribed through the design of the wake interaction length scales x_*^{peak}.

The streamwise evolution of u'/U_∞ of grid 3 shows regions of constant turbulence and growing turbulence at different z locations relative to the grid. The growth of u'/U_∞ as shown in figure 4.21 is attributed to the higher local mean shear rate. The streamwise evolution of $\overline{u^2}/U_\infty^2$ against our proposed dimensionless time scale $\tau \equiv [(x - x_*^{peak})/\overline{U_n}]\,|S_n|$ shows that the critical point of τ is indeed the same, which seems to support the inclusion of the wake interaction length scale x_*^{peak} in the definition, as opposed to the previously used scale $\tau^* \equiv (x/\overline{U_c})\,|S_n| = (x/\overline{U_c})\left|\overline{\partial U_n/\partial y}\right|$, where $\overline{U_c}$ is the centerline velocity. The integral length scale is shown to increase monotonically along the x direction, with values that are roughly constant across the y direction, also in agreement with the conclusions in Chapter 3.

In summary, these observations altogether support our idea to generate bespoke turbulent shear flows with varying mean shear rate and turbulence intensity profiles by tailoring the geometry of the inhomogeneous multiscale grids. The proposed mean velocity model

and the scaling methods for turbulence intensities are verified in both experiments, and the evolution of the turbulence characteristics are consistent. As a next step, it would be interesting to explore the limit of such idea, i.e. what is the largest mean shear rate one can achieve using these grids, and what is the largest turbulence intensity one can produce by designing the dimension of the grid bars. With the answer to these questions, such grids can be readily applied to produce bespoke turbulent flows for a variety of applications.

Chapter 5

Conclusions and future works

In this thesis two classes of inhomogeneous multiscale grids were proposed and investigated experimentally using Hot-wire Anemometry, Particle Image Velocimetry, and pressure probes. These studies provides further understandings of the idea of tailoring turbulence field using fractal grids as proposed by Vassilicos and colleagues. The work was presented in three parts, and the main results are summarized in the following.

In the first part of the study, three rectangular fractal grids (RFG) were tested in three different facilities to compare with the turbulence field generated by the classical space-filling fractal grids (FSG). As one of the most important variable in characterizing the generated turbulence field, the wake interaction length scale x_*^{peak} was examined first. It is important because the value of x_*^{peak} in the turbulence generated by FSGs defines the streamwise location of maximum turbulence intensity. This length scale is therefore crucial in tailoring turbulent flows in a given wind tunnel, where maximum turbulence intensity is expected at certain streamwise location. For the RFGs, the previous definition of x_*^{peak} failed to give the correct streamwise location of maximum turbulence intensity. There are perhaps two reasons for this based on our observations. First, the spreading rate of the wake generated by grid bars is varied by the local velocity gradient due to the inhomogeneous grid geometry. Secondly, there are two distinctive x_*^{peak} in the RFG

generated turbulence anisotropic grid geometry, and the wakes are expected to meet at different streamwise locations on the centerline, which in all affects the actual turbulence peak location. Nevertheless, the actual turbulence intensity peak location is proportional to the wake interaction length scale, i.e. $x_{peak}/x_*^{peak} = constant \approx 1.4$ as long as the ratio of the largest grid bars in the two transverse direction remains the same.

Another difference with the FSG generated turbulence is the turbulence characteristics in the beginning of the decay region. In this region, approximately $1 < x/x_{peak} < 1.5$, the flow was found to be inhomogeneous and anisotropic. Both the integral length scale L_u and Taylor microscale λ decreases in this region along the streamwise direction, where the Reynolds number Re_λ decreases. This observation has not been reported in any previous studies of the fractal generated turbulence, and was therefore surprising at first. However, the ratio of the length scales L_u/λ remained roughly constant in this region for all the experiments, which corresponds to the non-equilibrium scaling relation $C_\epsilon \sim Re_0^{1/2}/Re_\lambda$ as proposed for the FSG generated turbulence. The relation $L_u/\lambda \approx constant$ was also confirmed by normalized spectra where all wave number ranges were collapsed using a single length scale.

In the second part of the study, a new class of inhomogeneous multiscale grids was proposed to generate turbulent shear flows with desired shape mean velocity and turbulence intensity profiles at the same time. The mean velocity model after Taylor et al. (1949); McCarthy (1964) based on the local blockage ratio σ_n was shown to match our measurements with mean shear rates from approximately $0\,\mathrm{s}^{-1}$ to $5\,\mathrm{s}^{-1}$. The drag coefficient of the vertical bars was found to affect the local mean velocity significantly, and a constant drag coefficient C_D is essential in the calculation of the mean velocity profile. The turbulence intensity level was found to scale with the wake interaction length scale x_*^{peak} such that at given streamwise location $x = x_m$, we have $(u'/U_n)^2\beta^2(C_D w_n/x_*^{peak})^{-1} \sim (x_m/x_*^{peak})^\gamma$, where U_n is the local at layer n, β is a constant, C_D, g_n, w_n are the drag coefficient, gap, and width of the vertical bars, respectively, at layer n, and γ is a dimensionless power law

exponent. With such scaling, one could prescribe the shape of the turbulence intensity profiles through the design of x_*^{peak}, which can be determined completely from the grid geometry. A general approach of grid design method is also presented. This sets out the framework of a possible grid design method based on optimization, and can be easily improved by including more constraints as new experimental results come out.

The mean velocity model and turbulence intensity scaling, and in general the design principles of the inhomogeneous multiscale grids was further tested in a low-fidelity engineering wind tunnel for its robustness. The mean velocity model was verified by correctly predicting turbulent shear flows with mean velocity profiles calculated from equations (3.3) to (3.5). The scaling relation of the turbulence intensity profiles $u'(y)$ were also verified. These results confirmed the conclusion in Chapter 3 that the shape of the turbulence intensity profile can be prescribed through the design of the wake interaction length scales x_*^{peak}.

In terms of the fundamentals of turbulent shear flows, a new dimensionless time scale was proposed in Chapter 3 that $\tau \equiv [(x - x_*^{peak})/\overline{U_n}]\,|S_n|$, where S_n is the local mean shear rate. This definition of τ includes the wake interaction length scale x_*^{peak} as the virtual origin, since x_*^{peak} marks the beginning of decay that varies with grid geometries. This dimensionless time scale τ successfully collapsed the Reynolds stress at different locations behind different grids at $\tau > 0.8$. The streamwise evolution of $\overline{u^2}/U_\infty^2$ against τ was also of interest as the critical location of τ determines where the turbulence kinetic energy starts growing or stays constant, for different ratios of production over dissipation P/ϵ. It has been shown that for the cases with constant turbulence kinetic energy, the development is fairly fast, reaching constant values at $\tau_c^* = 1.6$ to 3, while the critical values of τ_c^* are roughly $\tau_c^* = 4$ to 5 for cases with growing turbulence kinetic energy. The critical location of τ for the inhomogeneous multiscale grid is the same in the final part of the study. This seems to suggest that the critical value of τ is grid dependent, and such dependency of the grid geometry is compensated by including the x_*^{peak} in the definition of τ for the

inhomogeneous multiscale grids.

These results all together improves our understanding of the fractal/multiscale grid generated turbulence, and suggests a possible direction to design bespoke turbulent flow in a wind tunnel using a single passive grid. However, some questions still remain, and the following questions might be of interest.

(i) For the rectangular grids, how does the turbulence characteristics vary if the ratio of the largest bars of the RFG is changed? This ratio of large dimension is important in determining the x_*^{peak}, and therefore is expected to change the location of maximum turbulence intensity and the integral length scales.

(ii) If we further differentiate the x_*^{peak} calculated using the bar dimensions in the two transverse directions, does the region with decreasing length scales still exist in the decay region? If so, what exactly is the reason and how does each term in the t.k.e. equation look like, and how does the evolution differ from the rest of the decay region?

(iii) For turbulent shear flow studies, what is the maximum mean shear rate one can achieve using the inhomogeneous multiscale grids? What is the maximum turbulence intensity one can produce? Based on the current results, it seems also possible to produce a shear flow with increasing turbulence intensity and integral length scales, both of which would be desired in wind engineering testings. So it would be interesting to understand what is the minimum mean shear rate to produce growing turbulent kinetic energy. Since the growth of the turbulent kinetic energy is related to the P/ϵ ratio, it would be interesting to look at the other terms in the t.k.e. equation to improve the simplified model as proposed in section 3.2.5.

By answering these questions, this idea to produce bespoke turbulent flows with desired turbulent characteristics might be completed. The results will benefit the group of researchers interested in experimental studies of turbulence, and will of course improve the work flow in engineering applications where simulation of various turbulent flows is

needed.

Bibliography

A. Abdel-Rahman, C. Tropea, P. Slawson, and A. Strong. On temperature compensation in hot-wire anemometry. *Journal of Physics E: Scientific Instruments*, 20(3):315, 1987. ISSN 0022-3735.

R. A. Antonia. On estimating mean and instantaneous turbulent energy dissipation rates with hot wires. *Exp. Therm. Fluid Sci.*, 27(2):151–157, 2003. ISSN 0894-1777.

R. A. Antonia, H. S. Shafi, and Y. Zhu. A note on the vorticity spectrum. *Physics of Fluids*, 8(8):2196–2202, 1996. ISSN 1070-6631.

J. Armitt and J. Counihan. The simulation of the atmospheric boundary layer in a wind tunnel. *Atmospheric Environment*, 2(1):49–71, 1968. ISSN 0004-6981.

Kunlun Bai, Charles Meneveau, and Joseph Katz. Near-wake turbulent flow structure and mixing length downstream of a fractal tree. *Boundary-Layer Meteorology*, 143(2): 285–308, 2012. ISSN 0006-8314.

T. Balendra, D. A. Shah, K. L. Tey, and S. K. Kong. Evaluation of flow characteristics in the nus-hdb wind tunnel. *Journal of Wind Engineering and Industrial Aerodynamics*, 90(6):675–688, 2002. ISSN 0167-6105.

P. W. Bearman and D. M. Trueman. Investigation of flow around rectangular cylinders. *Aeronaut. Quart.*, 23(3):229–237, 1972. ISSN 0001-9259.

C. G. Bowers, D.H. Willits, and H.D. Bowen. Comparison of temperature correction methods for hot-wire anemometers. *T. ASAE*, 31(5):1552–1555, 1988. ISSN 0001-2351.

K. Bremhorst. Effect of fluid temperature on hot-wire anemometers and an improved method of temperature compensation and linearisation without use of small signal sensitivities. *J. Phys. E Sci. Instrum.*, 18(1):44, 1985. ISSN 0022-3735.

H.H. Bruun. *Hot-wire Anemometry: Principles and Signal Analysis*. Oxford science publications. Oxford University Press, 1995. ISBN 9780198563426.

Denis William Bryer and Ronald Charles Pankhurst. *Pressure-probe methods for determining wind speed and flow direction*. HMSO, 1971.

J. I. Cardesa, T. B. Nickels, and J. R. Dawson. 2D PIV measurements in the near field of grid turbulence using stitched fields from multiple cameras. *Exp. Fluids*, 52(6):1611–1627, 2012. ISSN 0723-4864.

HakkiErgun Cekli and Willem van de Water. Tailoring turbulence with an active grid. *Experiments in Fluids*, 49(2):409–416, 2010. ISSN 0723-4864.

J. E. Cermak. Laboratory simulation of the atmospheric boundary layer. *AIAA Journal*, 9(9):1746–1754, 1971. ISSN 0001-1452.

J. E. Cermak. Wind-tunnel development and trends in applications to civil engineering. *Journal of Wind Engineering and Industrial Aerodynamics*, 91(3):355–370, 2003. ISSN 0167-6105.

JE Cermak, VA Sandborn, Eo J Plate, GH Binder, and H Chuang. Simulation of atmospheric motion by wind-tunnel flows. Report, DTIC Document, 1966.

F. H. Champagne, V. G. Harris, and S. Corrsin. Experiments on nearly homogeneous turbulent shear flow. *Journal of Fluid Mechanics*, 41(01):81–139, 1970. ISSN 1469-7645.

J Chen, DF Fletcher, BS Haynes, and JD Hooper. Validation of the cobra probe using turbulence measurements in fully developed pipe flow. In *Proc. 13th Australasian Fluid Mech. Conf., Melbourne*, 1998.

J. Chen, B. S. Haynes, and D. F. Fletcher. Cobra probe measurements of mean velocities, reynolds stresses and higher-order velocity correlations in pipe flow. *Experimental Thermal and Fluid Science*, 21(4):206–217, 2000. ISSN 0894-1777.

Richard Henry Clarke, Arthur James Dyer, Robert R Brook, Derek G Reid, and Alexander J Troup. *The Wangara experiment: Boundary layer data*, volume 19. Division Meteorological Physics. CSIRO Australia, 1971.

D. C. Collis and M. J. Williams. Two-dimensional convection from heated wires at low reynolds numbers. *Journal of Fluid Mechanics*, 6(3):357–384, 1959. ISSN 0022-1120.

G. Comte-Bellot and S. Corrsin. The use of a contraction to improve the isotropy of grid-generated turbulence. *Journal of Fluid Mechanics*, 25(04):657–682, 1966.

G. Comte-Bellot and S. Corrsin. Simple eulerian time correlation of full-and narrow-band velocity signals in grid-generated, isotropic turbulence. *Journal of Fluid Mechanics*, 48 (02):273–337, 1971. ISSN 1469-7645.

N. J. Cook. On simulating the lower third of the urban adiabatic boundary layer in a wind tunnel. *Atmospheric Environment*, 7(7):691–705, 1973. ISSN 0004-6981.

N. J. Cook. Wind-tunnel simulation of the adiabatic atmospheric boundary layer by roughness, barrier and mixing-device methods. *Journal of Wind Engineering and Industrial Aerodynamics*, 3(23):157–176, 1978. ISSN 0167-6105.

W. G. Cornell. Losses in flow normal to plane screens. *Trans. ASME*, 80(4):791–799, 1958.

S Corrsin. Turbulence: experimental methods. *Handbuch der Physik*, 3:524–590, 1963.

J. Counihan. An improved method of simulating an atmospheric boundary layer in a wind tunnel. *Atmospheric Environment*, 3(2):197–214, 1969. ISSN 0004-6981.

J. Cuxart, C. Yage, G. Morales, E. Terradellas, J. Orbe, J. Calvo, A. Fernndez, M. R. Soler, C. Infante, P. Buenestado, A. Espinalt, H. E. Joergensen, J. M. Rees, J. Vil,

J. M. Redondo, I. R. Cantalapiedra, and L. Conangla. Stable atmospheric boundary-layer experiment in spain (sables 98): A report. *Boundary-Layer Meteorology*, 96(3): 337–370, 2000. ISSN 0006-8314.

AG Davenport. The relationship of wind structure to 71ind loading. paper 2. In *Symp. 16, Int. Conf. on Wind Effects on Buildings and Structures held at NPL. H.M.S.O., London*, 1963.

Alan G Davenport. The relationship of wind structure to wind loading. 1966.

Alan G Davenport. The application of the boundary layer wind tunnel to the prediction of wind loading. In *Proc. of Intl. Research Seminar on Wind Effects on Buildings and Structures*, volume 1, pages 201–230, 1967.

A. Dijk and F. T. M. Nieuwstadt. The calibration of (multi-) hot-wire probes. 1. temperature calibration. *Exp. Fluids*, 36(4):540–549, 2004. ISSN 0723-4864.

A. G. M. Driedonks. Models and observations of the growth of the atmospheric boundary layer. *Boundary-Layer Meteorology*, 23(3):283–306, 1982. ISSN 1573-1472.

Georg Eitel-Amor, Ramis rl, and Philipp Schlatter. Simulation and validation of a spatially evolving turbulent boundary layer up to re=8300. *International Journal of Heat and Fluid Flow*, 47(Supplement C):57–69, 2014. ISSN 0142-727X.

J.W Elder. Steady flow through non-uniform gauzes of arbitrary shape. *Journal of Fluid Mechanics*, 5(03):355–368, 1959. ISSN 1469-7645.

Cesar Farell and Arun K. S. Iyengar. Experiments on the wind tunnel simulation of atmospheric boundary layers. *Journal of Wind Engineering and Industrial Aerodynamics*, 79(12):11–35, 1999. ISSN 0167-6105.

M. Gad-El-Hak and S. Corrsin. Measurements of the nearly isotropic turbulence behind a uniform jet grid. *Journal of Fluid Mechanics*, 62(01):115–143, 1974.

Sandeep Garg and Z. Warhaft. On the small scale structure of simple shear flow. *Physics of Fluids*, 10(3):662–673, 1998.

J. R. Garratt. Review: the atmospheric boundary layer. *Earth-Science Reviews*, 37(1): 89–134, 1994. ISSN 0012-8252.

J. R. Garratt, G. D. Hess, W. L. Physick, and P. Bougeault. The atmospheric boundary layer advances in knowledge and application. *Boundary-Layer Meteorology*, 78(1):9–37, 1996. ISSN 1573-1472.

I. S. Gartshore and K. A. De Croos. Roughness element geometry required for wind tunnel simulations of the atmospheric wind. *Journal of Fluids Engineering*, 99(3): 480–485, 1977. ISSN 0098-2202.

W. K. George, P. D. Beuther, and A. Shabbir. Polynomial calibrations for hot wires in thermally varying flows. *Exp. Therm. Fluid Sci.*, 2(2):230–235, 1989. ISSN 0894-1777.

William K George. The self-preservation of turbulent flows and its relation to initial conditions and coherent structures. *Advances in turbulence*, pages 39–73, 1989.

R. Gomes-Fernandes, B. Ganapathisubramani, and J. C. Vassilicos. Particle image velocimetry study of fractal-generated turbulence. *Journal of Fluid Mechanics*, 711:306–336, 2012.

Susumu Goto and J. C. Vassilicos. Energy dissipation and flux laws for unsteady turbulence. *Physics Letters A*, 379(1617):1144–1148, 2015. ISSN 0375-9601.

Susumu Goto and J. C. Vassilicos. Local equilibrium hypothesis and taylors dissipation law. *Fluid Dynamics Research*, 48(2):021402, 2016a. ISSN 1873-7005.

Susumu Goto and J. C. Vassilicos. Unsteady turbulence cascades. *Physical Review E*, 94 (5):053108, 2016b.

V. G. Harris, J. A. H. Graham, and S. Corrsin. Further experiments in nearly homogeneous turbulent shear flow. *Journal of Fluid Mechanics*, 81(04):657–687, 1977. ISSN 1469-7645.

R. J. Hearst and P. Lavoie. Decay of turbulence generated by a square-fractal-element grid. *Journal of Fluid Mechanics*, 741:567–584, 2014. ISSN 1469-7645.

R. Jason Hearst and Bharathram Ganapathisubramani. Tailoring incoming shear and turbulence profiles for lab-scale wind turbines. *Wind Energy*, pages 1–15, 2017. ISSN 1099-1824.

J. D. Hooper and A. R. Musgrove. Reynolds stress, mean velocity, and dynamic static pressure measurement by a four-hole pressure probe. *Experimental Thermal and Fluid Science*, 15(4):375–383, 1997. ISSN 0894-1777.

JD Hooper and AR Musgrove. Multi-hole pressure probes for the determination of the total velocity vector in turbulent single-phase flow. In *4th International Symposium Transport Phenomena in Heat and Mass Transfer, The University of New South Wales, Sydney, Australia, ed. JA Reizes*, volume 4, pages 1364–1374, 1991.

Marcus Hultmark and Alexander J. Smits. Temperature corrections for constant temperature and constant current hot-wire anemometers. *Meas. Sci. Technol.*, 21(10):105404, 2010. ISSN 0957-0233.

D. Hurst and J. C. Vassilicos. Scalings and decay of fractal-generated turbulence. *Physics of Fluids*, 19(3):035103–31, 2007.

Juan C. Isaza, Ricardo Salazar, and Zellman Warhaft. On grid-generated turbulence in the near- and far field regions. *Journal of Fluid Mechanics*, 753:402–426, 2014. ISSN 1469-7645.

Martin Jensen and Niels Franck. *Model-scale tests in turbulent wind*. Danish Technical Press, 1963.

B. A. Kader and A. M. Yaglom. Mean fields and fluctuation moments in unstably stratified turbulent boundary layers. *Journal of Fluid Mechanics*, 212:637–662, 1990. ISSN 1469-7645.

J. C. Kaimal, J. C. Wyngaard, D. A. Haugen, O. R. Cot, Y. Izumi, S. J. Caughey, and C. J. Readings. Turbulence structure in the convective boundary layer. *Journal of the Atmospheric Sciences*, 33(11):2152–2169, 1976. ISSN 0022-4928.

G. Kanevce and S. Oka. Correcting hot-wire readings for influence of fluid temperature variations. *DISA information*, pages 21–24, 1973.

Hyung Suk Kang, Stuart Chester, and Charles Meneveau. Decaying turbulence in an active-grid-generated flow and comparisons with large-eddy simulation. *Journal of Fluid Mechanics*, 480:129–160, 2003a. ISSN 1469-7645.

Hyung Suk Kang, Stuart Chester, and Charles Meneveau. Decaying turbulence in an active-grid-generated flow and comparisons with large-eddy simulation. *Journal of Fluid Mechanics*, 480:129–160, 2003b. ISSN 1469-7645.

WG Kannuluik and EH Carman. The temperature dependence of the thermal conductivity of air. *Australian Journal of Chemistry*, 4(3):305–314, 1951.

U. Karnik and S. Tavoularis. Generation and manipulation of uniform shear with the use of screens. *Exp. Fluids*, 5(4):247–254, 1987. ISSN 1432-1114.

Pascal Knebel, Achim Kittel, and Joachim Peinke. Atmospheric wind field conditions generated by active grids. *Experiments in Fluids*, 51(2):471–481, 2011. ISSN 1432-1114.

S. Laizet, J. Nedi, and J. C. Vassilicos. The spatial origin of 5/3 spectra in grid-generated turbulence. *Physics of Fluids*, 27(6):065115, 2015. ISSN 1070-6631.

Sylvain Laizet and John Christos Vassilicos. Dns of fractal-generated turbulence. *Flow, turbulence and combustion*, 87(4):673–705, 2011.

E. M. Laws and J. L. Livesey. Flow through screens. *Annu. Rev. Fluid Mech.*, 10(1): 247–266, 1978. ISSN 0066-4189.

T. V. Lawson. Methods of producing velocity profiles in wind tunnels. *Atmos. Environ.*, 2(1):73–76, 1968.

S. C. Ling and C. A. Wan. Decay of isotropic turbulence generated by a mechanically agitated grid. *The Physics of Fluids*, 15(8):1363–1369, 1972. ISSN 0031-9171.

J. L. Livesey and E. M. Laws. Flow through non-uniform gauze screens. *Journal of Fluid Mechanics*, 59(04):737–743, 1973. ISSN 1469-7645.

F. Lohou, B. Campistron, A. Druilhet, P. Foster, and J.P. Pages. Turbulence and coherent organizations in the atmospheric boundary layer: A radar-aircraft experimental approach. *Boundary-Layer Meteorology*, 86(1):147–179, 1998. ISSN 1573-1472.

R. M. Lueptow, K. S. Breuer, and J. H. Haritonidis. Computer-aided calibration of x-probes using a look-up table. *Experiments in Fluids*, 6(2):115–118, 1988. ISSN 0723-4864.

J. L. Lumley. Some comments on turbulence. *Physics of Fluids A: Fluid Dynamics*, 4(2): 203–211, 1992. ISSN 0899-8213.

Hideharu Makita. Realization of a large-scale turbulence field in a small wind tunnel. *Fluid Dynamics Research*, 8(1-4):53, 1991. ISSN 1873-7005.

M. R. Maxey. The velocity skewness measured in grid turbulence. *Physics of Fluids*, 30 (4):935–938, 1987.

N. Mazellier and J. C. Vassilicos. Turbulence without richardson–kolmogorov cascade. *Physics of Fluids*, 22(7):075101–25, 2010.

B. Mazzi and J. C. Vassilicos. Fractal-generated turbulence. *Journal of Fluid Mechanics*, 502:65–87, 2004. ISSN 0022-1120.

B. Mazzi, F. Okkels, and J. C. Vassilicos. A shell-model approach to fractal-induced turbulence. *The European Physical Journal B - Condensed Matter and Complex Systems*, 28(2):243–251, 2002. ISSN 1434-6036.

J. H. McCarthy. Steady flow past non-uniform wire grids. *Journal of Fluid Mechanics*, 19(04):491–512, 1964. ISSN 1469-7645.

Richard T. McNider and Roger A. Pielke. Diurnal boundary-layer development over sloping terrain. *Journal of the Atmospheric Sciences*, 38(10):2198–2212, 1981.

G. Melina, P. J. K. Bruce, and J. C. Vassilicos. Vortex shedding effects in grid-generated turbulence. *Physical Review Fluids*, 1(4):044402, 2016.

J. Mi, M. Xu, and C. Du. Digital filter for hot-wire measurements of small-scale turbulence properties. *Meas. Sci. Technol.*, 22(12):125401, 2011. ISSN 0957-0233.

M. S. Mohamed and J. C. Larue. The decay power law in grid-generated turbulence. *Journal of Fluid Mechanics*, 219:195–214, 1990. ISSN 1469-7645.

A. S. Monin. The atmospheric boundary layer. *Annual Review of Fluid Mechanics*, 2(1): 225–250, 1970. ISSN 0066-4189.

G. L. Morrison. Effects of fluid property variations on the response of hot-wire anemometers. *Journal of Physics E: Scientific Instruments*, 7(6):434, 1974. ISSN 0022-3735.

P. J. Mulhearn and R. E. Luxton. The development of turbulence structure in a uniform shear flow. *Journal of Fluid Mechanics*, 68(03):577–590, 1975. ISSN 1469-7645.

AR Musgrove and JD Hooper. Pressure probe measurements of the turbulent stress distribution in a swirling jet. In *Proc. Third World Conf. Exp. Heat Transfer, Fluid Mechanical, and Thermodynamics*, volume 1, pages 172–179, 1993.

L. Mydlarski and Z. Warhaft. On the onset of high-reynolds-number grid-generated wind tunnel turbulence. *Journal of Fluid Mechanics*, 320:331–368, 1996a. ISSN 1469-7645.

L. Mydlarski and Z. Warhaft. On the onset of high-reynolds-number grid-generated wind tunnel turbulence. *Journal of Fluid Mechanics*, 320:331–368, 1996b. ISSN 1469-7645.

Y. Nakamura and Y. Tomonari. The effect of turbulence on the drags of rectangular prisms. *Japan Society of Aeronautical Space Sciences Transactions*, 19:82–86, 1976. ISSN 0549-3811.

J. Nedić and S. Tavoularis. Energy dissipation scaling in uniformly sheared turbulence. *Phys. Rev. E*, 93(3):033115, 2016.

M. Obligado, T. Dairay, and J. C. Vassilicos. Nonequilibrium scalings of turbulent wakes. *Physical Review Fluids*, 1(4):044409, 2016.

P. L. ONeill, D. Nicolaides, D. Honnery, and J. Soria. Autocorrelation functions and the determination of integral length with reference to experimental and numerical data. In *15th Australasian fluid mechanics conference*.

P. L. O'Neill, D. Nicolaides, D. Honnery, and J. Soria. Autocorrelation functions and the determination of integral length with reference to experimental and numerical data. In *Proc. 15th Australasian fluid mechanics conference, Sydney, Australia*, 2004.

P. R. Owen and H. K. Zienkiewicz. The production of uniform shear flow in a wind tunnel. *Journal of Fluid Mechanics*, 2(06):521–531, 1957. ISSN 1469-7645.

Hans A. Panofsky. The atmospheric boundary layer below 150 meters. *Annual Review of Fluid Mechanics*, 6(1):147–177, 1974. ISSN 0066-4189.

Alfredo Pea, Rogier Floors, and Sven-Erik Gryning. The hvsre tall wind-profile experiment: A description of wind profile observations in the atmospheric boundary layer. *Boundary-Layer Meteorology*, 150(1):69–89, 2014. ISSN 1573-1472.

B. R. Pearson. *Experiments on small-scale turbulence*. PhD thesis, University of Newcastle, 1999.

Stephen B Pope. *Turbulent flows*. IOP Publishing, 2001. ISBN 0957-0233.

C. J. Readings, D. A. Haugen, and J. C. Kaimal. The 1973 minnesota atmospheric boundary layer experiment. *Weather*, 29(8):309–312, 1974. ISSN 1477-8696.

H. K. Richards and J. B. Morton. Experimental investigation of turbulent shear flow with quadratic mean-velocity profiles. *Journal of Fluid Mechanics*, 73(01):165–188, 1976.

P. E. Roach. The generation of nearly isotropic turbulence by means of grids. *International Journal of Heat and Fluid Flow*, 8(2):82–92, 1987. ISSN 0142-727X.

A. G. Robins. Experimental model techniques for the investigation of the dispersion of chimney plumes. *Proceedings of the Institution of Mechanical Engineers*, 189(1):44–54, 1975. ISSN 0020-3483.

Eduardo Rodríguez-López, Paul J. K. Bruce, and Oliver R. H. Buxton. On the formation mechanisms of artificially generated high reynolds number turbulent boundary layers. *Boundary-Layer Meteorology*, 160(2):201–224, 2016. ISSN 1573-1472.

J. J. Rohr, E. C. Itsweire, K. N. Helland, and C. W. Van Atta. An investigation of the growth of turbulence in a uniform-mean-shear flow. *Journal of Fluid Mechanics*, 187: 1–33, 1988. ISSN 1469-7645.

W. G. Rose. Results of an attempt to generate a homogeneous turbulent shear flow. *Journal of Fluid Mechanics*, 25(01):97–120, 1966. ISSN 1469-7645.

W. G. Rose. Interaction of grid turbulence with a uniform mean shear. *Journal of Fluid Mechanics*, 44(04):767–779, 1970. ISSN 1469-7645.

Tsutomu Sanada. Comment on the dissipationrange spectrum in turbulent flows. *Physics of Fluids A: Fluid Dynamics*, 4(5):1086–1087, 1992. ISSN 0899-8213.

JRg Schumacher. Derivative moments in stationary homogeneous shear turbulence. *Journal of Fluid Mechanics*, 441:109–118, 2001. ISSN 0022-1120.

R. E. Seoud and J. C. Vassilicos. Dissipation and decay of fractal-generated turbulence. *Phy. Fluids*, 19(10):1–11, 2007.

G. S. Seyed and V. V. Srinivas. Hot-wire anemometry behaviour at very high frequencies. *Meas. Sci. Technol.*, 7(10):1297, 1996. ISSN 0957-0233.

X. Shen and Z. Warhaft. The anisotropy of the small scale structure in high reynolds number (re 1000) turbulent shear flow. *Physics of Fluids*, 12(11):2976–2989, 2000a.

X. Shen and Z. Warhaft. The anisotropy of the small scale structure in high reynolds number (r 1000) turbulent shear flow. *Physics of Fluids*, 12(11):2976–2989, 2000b.

Ian C Shepherd. A four hole pressure probe for fluid flow measurements in three dimensions. *Journal of Fluids Engineering*, 103(4):590–594, 1981. ISSN 0098-2202.

A. Shibl. Empirical expression for hot wire with corrections for temperature drift. *Wrme- und Stoffbertragung*, 21(6):329–332, 1987. ISSN 0042-9929.

L. F. G. Simmons and C. Salter. Experimental investigation and analysis of the velocity variations in turbulent flow. *Proceedings of the Royal Society of London. Series A*, 145 (854):212–234, 1934.

N. Sitaram and A. L. Treaster. A simplified method of using four-hole probes to measure three-dimensional flow fields. *Journal of Fluids Engineering*, 107(1):31–35, 1985. ISSN 0098-2202.

F. A. de Souza, V. D. Nguyen, and S. Tavoularis. The structure of highly sheared turbulence. *Journal of Fluid Mechanics*, 303:155–167, 1995. ISSN 1469-7645.

K. R. Sreenivasan. On the scaling of the turbulence energy dissipation rate. *Physics of Fluids*, 27(5):1048–1051, 1984. doi: 10.1063/1.864731.

Weitemeyer Stefan, Reinke Nico, Peinke Joachim, and Hlling Michael. Multi-scale generation of turbulence with fractal grids and an active grid. *Fluid Dynamics Research*, 45 (6):061407, 2013. ISSN 1873-7005.

Discetti Stefano, B. Ziskin Isaac, Astarita Tommaso, J. Adrian Ronald, and P. Prestridge Kathy. Piv measurements of anisotropy and inhomogeneity in decaying fractal generated turbulence. *Fluid Dynamics Research*, 45(6):061401, 2013. ISSN 1873-7005.

Roland B. Stull. *An introduction to boundary layer meteorology*, volume 13. Springer Science & Business Media, 2012. ISBN 9400930275.

G. Svensson, A. A. M. Holtslag, V. Kumar, T. Mauritsen, G. J. Steeneveld, W. M. Angevine, E. Bazile, A. Beljaars, E. I. F. de Bruijn, A. Cheng, L. Conangla, J. Cuxart, M. Ek, M. J. Falk, F. Freedman, H. Kitagawa, V. E. Larson, A. Lock, J. Mailhot, V. Masson, S. Park, J. Pleim, S. Sderberg, W. Weng, and M. Zampieri. Evaluation of the diurnal cycle in the atmospheric boundary layer over land as represented by a variety of single-column models: The second gabls experiment. *Boundary-Layer Meteorology*, 140(2):177–206, 2011. ISSN 1573-1472.

CR Symes and LE Fink. *Effects of external turbulence upon the flow past cylinders*, pages 86–102. Springer, 1977.

Y. Tassa and Y. Kamotani. Experiments on turbulence behind a grid with jet injection in downstream and upstream direction. *The Physics of Fluids*, 18(4):411–414, 1975. ISSN 0031-9171.

S. Tavoularis and U. Karnik. Further experiments on the evolution of turbulent stresses and scales in uniformly sheared turbulence. *Journal of Fluid Mechanics*, 204:457–478, 1989. ISSN 1469-7645.

Stavros Tavoularis and Stanley Corrsin. Experiments in nearly homogenous turbulent shear flow with a uniform mean temperature gradient. part 1. *Journal of Fluid Mechanics*, 104:311–347, 1981.

G. I. Taylor. Statistical theory of turbulence. *Proceedings of the Royal Society of London. Series A, Mathematical and Physical Sciences*, 151(873):421–444, 1935. ISSN 0080-4630.

G. I. Taylor, G. K. Batchelor, H. L. Dryden, and G. B. Schubauer. The effect of wire gauze on small disturbances in a uniform stream. *Q. J. Mech. Appl. Math.*, 2(1):1–29, 1949. doi: 10.1093/qjmam/2.1.1.

H. Tennekes and J. L. Lumley. *A first course in turbulence*. MIT press, 1972. ISBN 0262200198.

H. W. Teunissen. Simulation of the planetary boundary layer in a multiple-jet wind tunnel. *Atmospheric Environment (1967)*, 9(2):145–174, 1975. ISSN 0004-6981.

A. Thormann and C. Meneveau. Decay of homogeneous, nearly isotropic turbulence behind active fractal grids. *Physics of Fluids*, 26(2):025112, 2014.

Adrien Thormann and Charles Meneveau. Decaying turbulence in the presence of a shearless uniform kinetic energy gradient. *Journal of Turbulence*, 16(5):442–459, 2015.

A. A. Townsend. *The structure of turbulent shear flow*. Cambridge university press, 1980. ISBN 0521298199.

P. C. Valente and J. C. Vassilicos. The decay of turbulence generated by a class of multiscale grids. *Journal of Fluid Mechanics*, 687:300–340, 2011. ISSN 1469-7645.

P. C. Valente and J. C. Vassilicos. Universal dissipation scaling for nonequilibrium turbulence. *Physical Review Letters*, 108(21):214503, 2012.

P. C. Valente and J. C. Vassilicos. The non-equilibrium region of grid-generated decaying turbulence. *Journal of Fluid Mechanics*, 744:5–37, 2014. ISSN 1469-7645.

C. W. H. van Doorne and J. Westerweel. Measurement of laminar, transitional and turbulent pipe flow using stereoscopic-piv. *Experiments in Fluids*, 42(2):259–279, 2007. ISSN 1432-1114.

Christina Vanderwel and Stavros Tavoularis. Measurements of turbulent diffusion in uniformly sheared flow. *Journal of Fluid Mechanics*, 754:488–514, 2014.

J. C. Vassilicos. Dissipation in turbulent flows. *Annual Review of Fluid Mechanics*, 47: 95–114, 2015.

J Christos Vassilicos. *Intermittency in turbulent flows*. Cambridge University Press, 2001. ISBN 0521792215.

Theodore von Kármán. The fundamentals of the statistical theory of turbulence. *Journal of the Aeronautical Sciences*, 4(4):131–138, 1937.

DEJ Walshe. *Wind-excited oscillations of structures*. HM Stationery Office, 1972.

J. Westerweel, D. Dabiri, and M. Gharib. The effect of a discrete window offset on the accuracy of cross-correlation analysis of digital piv recordings. *Experiments in Fluids*, 23(1):20–28, 1997. ISSN 1432-1114.

B. Wieneke. Stereo-piv using self-calibration on particle images. *Experiments in Fluids*, 39(2):267–280, 2005. ISSN 1432-1114.

D. K. Wilson. A new model for turbulence spectra and correlations based on Meijer's G-functions. Technical Note ARL-TN-104, Army Research Laboratory, 1998.

I. Wygnanski, F. Champagne, and B. Marasli. On the large-scale structures in two-dimensional, small-deficit, turbulent wakes. *Journal of Fluid Mechanics*, 168:31–71, 1986.

J. Zhong, T. S. Huang, and R. J. Adrian. Extracting 3d vortices in turbulent fluid flow. *IEEE Transactions on Pattern Analysis and Machine Intelligence*, 20(2):193–199, 1998.

J. Zhou, R. J. Adrian, S. Balachandar, and T. M. Kendall. Mechanisms for generating coherent packets of hairpin vortices in channel flow. *Journal of Fluid Mechanics*, 387: 353–396, 1999. ISSN 0022-1120.

T Zhou, R Antonia, and L Chua. Performance of a probe for measuring turbulent energy and temperature dissipation rates. *Experiments in fluids*, 33(2):334–345, 2002. ISSN 0723-4864.

Yi Zhou, Kouji Nagata, Yasuhiko Sakai, Hiroki Suzuki, Yasumasa Ito, Osamu Terashima, and Toshiyuki Hayase. Relevance of turbulence behind the single square grid to turbulence generated by regular- and multiscale-grids. *Physics of Fluids*, 26(7):075105, 2014.

W. Zhu, R. van Hout, L. Luznik, H. S. Kang, J. Katz, and C. Meneveau. A comparison of piv measurements of canopy turbulence performed in the field and in a wind tunnel model. *Experiments in Fluids*, 41(2):309–318, 2006. ISSN 0723-4864.

Appendix A

A novel temperature calibration method

The voltage output fluctuation of a hot-wire can result from both a velocity fluctuation and a temperature fluctuation, so it is crucial to have a stable ambient fluid temperature for hot-wire measurements, or to have calibrations at different temperatures accompanying each data set. However, due to the lack of thermal control in the Honda wind tunnel, temperature variations as large as 5 °C were frequently detected. It was also impossible to calibrate before and after each data set, because removing the grid takes approximately 15 minutes and the ambient temperature would drop during that period of time. Such temperature difference causes drift of the voltage output that consequently gives biased mean velocity. A temperature compensation method is therefore needed to eliminate the influence of varying ambient temperature.

When the ambient temperature variation is small (i.e. $T_a - T_0 < 2\,^{\circ}\mathrm{C}$, where T_a is the ambient temperature, and T_0 is the reference temperature), the correction method proposed by Kanevce and Oka (1973); Bruun (1995) works well such that

$$E_{corr} = E_0 \left(\frac{T_w - T_a}{T_w - T_0} \right)^{0.5} \tag{A.1}$$

where E_0 is the measured voltage, E_{corr} is the corrected voltage, and T_w is the wire

operating temperature calculated from $R_w = R_{20}\,[1 + \alpha_{20}(T_w - T_{20})]$, where R_w and R_{20} are the hot-wire resistance at working temperature and 20 °C, respectively, and α_{20} is the temperature coefficient of the wire at 20 °C. This correction method fails, however, in the scenario for our Honda experiments where $T_a - T_0 > 2\,°\mathrm{C}$.

To correct for the voltage output at different temperatures, a heat transfer relation for a finite wire should be established first. The most commonly used form of such relation is proposed by Collis and Williams (1959) such that

$$Nu = A + BRe^n \tag{A.2}$$

where A, B, $n = 0.45 \sim 0.5$ are constants, $Nu = hd/\kappa$ is the Nusselt number, $Re = Ud/\nu$ is the Reynolds number, $h = q_w/(T_w - T_a)$ is the heat transfer coefficient, q_w is the heat transfer rate per unit area from the wire, and T_w and T_a are the wire and ambient temperatures, respectively, d is the wire diameter, κ is the thermal conductivity, and ν is the kinematic viscosity. Some of these quantities, i.e. h, κ, and ν are dependent on the ambient temperature, and thus the evaluation of equation A.2 relies on the estimation of these varying fluid properties at given temperature.

Several correction methods have been derived for hot-wires operated in the constant temperature mode based on equation A.2 (see Abdel-Rahman et al., 1987; Shibl, 1987; Bowers et al., 1988; George et al., 1989; Dijk and Nieuwstadt, 2004; Hultmark and Smits, 2010). To evaluate the temperature dependent quantities, various empirical expressions for the thermal conductivity κ and kinematic viscosity ν have been proposed. For instance,

$$\frac{\kappa}{\kappa_0} = \left(\frac{T}{T_0}\right)^a, \frac{\nu}{\nu_0} = \left(\frac{T}{T_0}\right)^b \tag{A.3}$$

as discussed by Collis and Williams (1959); Morrison (1974); Bruun (1995), where $0.8 <$

$a < 0.86$ and $1.76 < b < 1.9$, or

$$\kappa = 5.75 * 10^{-5}(1 + 0.0317T_a - 0.0000021T_a^2) \tag{A.4}$$

as proposed by Kannuluik and Carman (1951).

These methods rely completely on the estimation of the fluid properties, but the temperature at which they should be evaluated is not well defined (see Bremhorst, 1985; Bruun, 1995), even though the film temperature $T_f = (T_w + T_a)/2$ is often used. The calculated values depend on the selection of the power law constants a and b, and the evaluation of T_w. The compensated output of these reported methods failed to collapse the calibrations taken at different ambient temperatures T_a. Therefore, a simple temperature calibration procedure was developed as follows.

It starts with the heat transfer relation for a finite wire, as shown by Bruun (1995)

$$\frac{E_w^2}{R_w(T_w - T_a)} = A\kappa + \kappa(\frac{\rho}{\mu})^n BU^n \tag{A.5}$$

where A, B, n are constants, μ is the air dynamic viscosity, and ρ is the air density. Now if we accept the relations in equation A.3 with $a = 0.83$ and $b = 1.83$, the second coefficient becomes

$$\kappa_0 \left(\frac{T}{T_0}\right)^{0.83} \nu_0^{-n} \left(\frac{T}{T_0}\right)^{-1.83n}, \tag{A.6}$$

where $\nu = \mu/\rho$ is used. Since $n = 0.45 \sim 0.5$, if we take the mean value of $n = 0.475$, then $1.83n = 0.87$, the temperature dependency effectively cancels out, leaving only a constant coefficient $B^* = \kappa_0\nu_0^{-n}B$. For $A\kappa$, if we further assume that $T = T_f$ as discussed above, and that $T_w >> Ta$, then the variation of κ is negligible. Equation A.5 now becomes

$$\begin{aligned} E_0^2 &= (A^* + B^*U^n)(T_w - T_a) \\ &= A' + B'T_a \end{aligned} \tag{A.7}$$

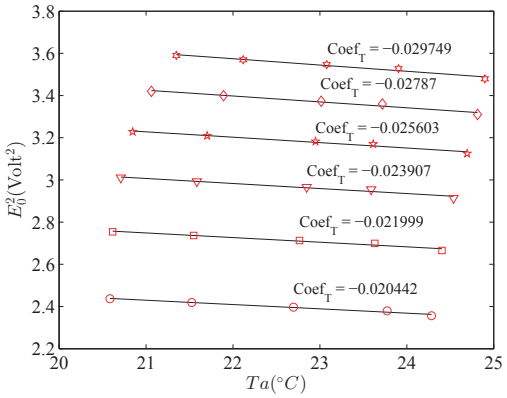

Figure A.1: Temperature dependency of E^2 at $U_\infty = 5, 8, 11, 14, 17, 20\,\mathrm{m\,s^{-1}}$.

where the output voltage E_0 is related to the hot wire voltage E_w by a constant factor related to the resistance of the hot wire probe and the internal bridge of the anemometer, and it is included in the constants A' and B'. Equation A.7 implies that for a given velocity, E_0^2 varies linearly to the ambient temperature T_a. This conclusion has been shown by e.g. Bremhorst (1985); Dijk and Nieuwstadt (2004), where Bremhorst (1985) showed a linear dependency of E_0^2 on T_a in the range 20 °C to 80 °C. Based on this observation, Bremhorst (1985) has also mentioned the possibility that the fluid properties should be evaluated at the wire temperature T_w, which naturally implies the linear dependency in equation A.7 for constant-temperature anemometers.

The calibration procedure starts with measurements of the output voltage E_0^2 at various temperatures with different free stream velocities. Voltage data is taken with the tunnel running at several velocities, and the temperature naturally increases with time. It is a common practice for large wind tunnels without temperature control as to stabilize the ambient temperature before taking measurements. Therefore, in practice, this method does not cost extra time.

One example of such measurement routine is given in figure A.1. It is clear that E_0^2 decreases linearly with T_a, with different slope $Coef_T = B'$ under different free stream velocities, which means that $Coef_T \sim f(U)$. These numbers are then fitted against velocities, which quantifies the relation of $Coef_T$ as a function of U, as shown in figure A.2.

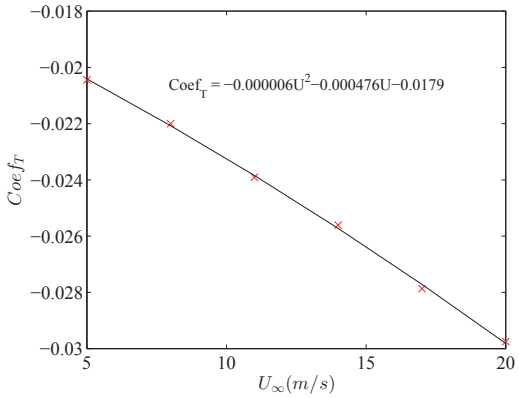

Figure A.2: Velocity dependency of $Coef_T$ at $U_\infty = 5, 8, 11, 14, 17, 20\,\mathrm{m\,s^{-1}}$, black curve shows the second order polynomial fit.

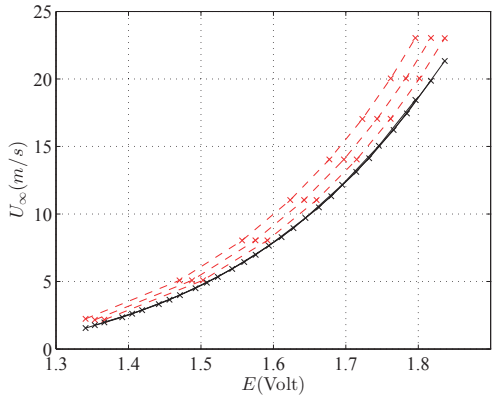

Figure A.3: Original calibration curves at different temperatures from 20.5 °C to 24.8 °C(red), and corrected curves (black).

This relation $Coef_T(U)$ is well represented by a second order polynomial, but note that the actual function depends on individual wires, which is expected since the heat transfer relation is known to be affected by the wire geometry.

To correct the measured voltage of the hot wire ${E_0}^2$, the specific $Coef_T$ is calculated by substituting the velocity U into $Coef_T \sim f(U)$. Then the corrected voltage ${E_{cor}}^2$ is calculated simply by

$$ {E_{cor}}^2 = {E_0}^2 - Coef_T \cdot (T_a - T_0) \tag{A.8} $$

where T_0 is the reference temperature, which is measured at the start of the routine.

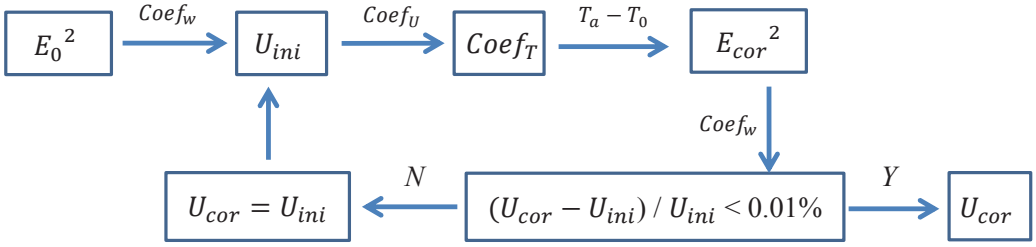

Figure A.4: Flow chart of temperature correction procedures for acquisition data.

Finally, calibration data taken at all velocities can be corrected following this procedure. Figure A.3 gives an example of the results, where all three red curves taken at different T_a collapse together after the correction (black lines). For a fixed voltage, the converted velocity difference at different temperature was reduced from 15% to a maximum of 1%. The final calibration coefficients for the hot wire are referred to as $Coef_w$.

Note, however, the correction procedure relies on the flow velocity U, which is known during calibrations, but unknown during data acquisition. This is solved by an iterative post-processing method as illustrated in figure A.4. The original data E_0 is converted to velocity U_{ini} using $Coef_w$ first, where U_{ini} serves as an initial guess of the local mean velocity. With this guessed velocity, the E_{cor} is then calculated and converted to velocity U_{cor} using the same procedure mentioned for calibration. After the first pass, U_{ini} and U_{cor} are compared to look at the difference. If the difference is larger than 0.01%, U_{ini} is substituted by U_{cor} and then sent back for another iteration, otherwise U_{cor} is passed on as the corrected velocity signal.

Appendix B

Effects of integration on the integral length scale

In order to calculate the longitudinal integral length scale L_u, the correlation function was examined. It is noticed that the auto-correlation function drops below zero and fluctuates around $R = 0$ as the separation distance increases. This phenomenon raises the question of the integration domain, which affects the calculation of L_u. O'Neill et al. (2004) discussed several methods using either the entire available domain, or up to where $R = R_{min}$, or up to the first zero-crossing if negative R is present, and they concluded that there may not be a clear relation between the integral length scale and the integration domain. For the discussion here, the first zero-crossing point is used for comparison.

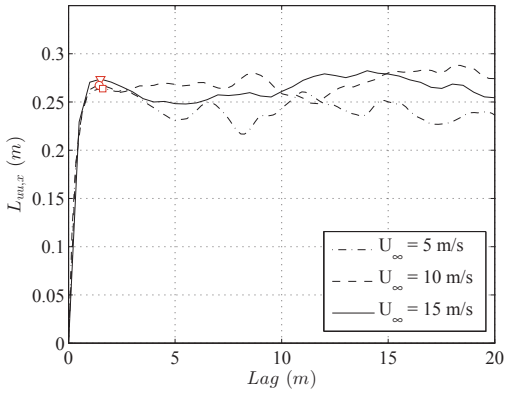

Figure B.1: Convergence of L_u with increasing integral domain. The symbols give the results by integrating the correlation function only up to the first zero-crossing.

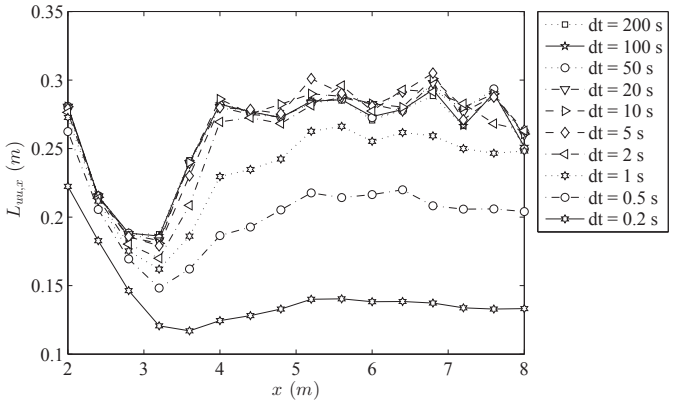

Figure B.2: Convergence of piecewise length in the calculation of L_u at $U_\infty = 10\,\mathrm{m\,s^{-1}}$.

Figure B.1 shows the variation of L_u as a function of the integration domain as well as the results by integrating only up to the first zero-crossing (red symbols). It is hard to argue whether the values integrated up to the first zero-crossing point are representative due to the large variations (almost 20%) with increasing integration domain.

Another popular method to calculate L_u is to divide the sample into smaller piecewise samples, calculate L_u for each piecewise sample by integrating up to the first zero-crossing point, and then take an average. This method, however, is sensitive to the selection of the sample piece length, as shown in figure B.2. It is clear that for pieces with dt smaller than 5 s, where dt is the sample time length for each piece, the results are converged. Also notice that the streamwise development of L_u is fluctuating more than expected, and the discrepancy of the results using different piecewise length at a given location is about 10%. This seems to imply the ambiguity of this integration method, as the integration domain cannot be well defined.